KIT SCIENTIFIC REPORTS 7549

Results of Severe Fuel Damage Experiment QUENCH-14 with Advanced Rod Cladding M5®

J. Stuckert, M. Große, U. Stegmaier, M. Steinbrück

KIT Scientific Publishing

J. Stuckert, M. Große, U. Stegmaier, M. Steinbrück

Results of Severe Fuel Damage Experiment QUENCH-14 with Advanced Rod Cladding M5®

Karlsruhe Institute of Technology
KIT SCIENTIFIC REPORTS 7549

Results of Severe Fuel Damage Experiment QUENCH-14 with Advanced Rod Cladding M5®

von
J. Stuckert,
M. Große,
U. Stegmaier,
M. Steinbrück

KIT Scientific Publishing

Report-Nr. KIT-SR 7549

Impressum

Karlsruher Institut für Technologie (KIT)
KIT Scientific Publishing
Straße am Forum 2
D-76131 Karlsruhe
www.ksp.kit.edu

KIT – Universität des Landes Baden-Württemberg und nationales
Forschungszentrum in der Helmholtz-Gemeinschaft

KIT Scientific Publishing 2010
Print on Demand

ISSN 1869-9669
ISBN 978-3-86644-535-2

Zusammenfassung

Ergebnisse des Schwere-Störfall-Experiments QUENCH-14 mit fortschrittlichem Hüllwerkstoff M5®

Die QUENCH-Experimente untersuchen zum einen den Wasserstoffquellterm, der aus Wassereinspeisung in einen überhitzten Leichtwasserreaktorkern nach Kühlmittelverlust resultiert, zum anderen das Hochtemperaturverhalten der Kernmaterialien unter transienten Bedingungen. Das typische QUENCH-Testbündel besteht aus 21 Brennstabsimulatoren mit einer Länge von ca. 2,5 m.

Im QUENCH-14 Experiment wurde speziell das Verhalten des M5® Hüllrohrmaterials auf die Bündeloxidation und das Flutverhalten untersucht, und zwar im Vergleich mit den früheren Tests QUENCH-06 (ISP-45), bei dem das Standardmaterial Zircaloy-4 zum Einsatz kam, und QUENCH-12, bei dem in VVER-Reaktoren eingesetztes E110 verwendet wurde. Die DWR-Bündelanordnung von QUENCH-14 mit einem einzelnen unbeheizten Stab, 20 beheizten Stäben und vier Eckstäben war ansonsten identisch zu der aus QUENCH-06. Der Test wurde im Prinzip nach demselben Ablauf wie QUENCH-06 gefahren, so dass die Auswirkungen des unterschiedlichen Hüllrohrmaterials direkt bestimmt werden können. Das Paul Scherrer Institut (Schweiz) hat mit den Codes SCDAPSIM, SCDAP/RELAP5 und MELCOR Vorausrechnungen durchgeführt.

Das Experiment begann mit einer Voroxidationsphase unter Dampf, die ~3000 s bei maximal ~1500 K Bündeltemperatur dauerte. Nach einer weiteren Temperatursteigerung auf eine maximale Bündeltemperatur von 2073 K wurde das Bündel mit 41 g/s Wasser von unten geflutet. Kurz nach dem Beginn des Flutens wurde die Höchsttemperatur von ~2300 K am Mantelrohr des Bündels (Shroud) gemessen. Die elektrische Leistung wurde während des Flutens auf einen Mittelwert von 2 W/cm gesenkt, um die Nachzerfallswärme zu simulieren. Innerhalb von 300 s nach Beginn des Flutens wurde die komplette Bündelkühlung erzielt.

Die Nachuntersuchungen des M5®-Bündels zeigten weder Breakawayoxidation der Hüllrohre noch merkliche Schmelzeverlagerungen zwischen den Stäben. Im Gegensatz dazu hatte der mit E110-Hüllrohren unter gleichen Bedingungen durchgeführte Versuch QUENCH-12 zu starken Auswirkungen des Breakawayeffekts an Hüllrohr und Shroudoberflächen während der Voroxidationsphase und zu lokalen Schmelzeverlagerungen zu Beginn des Flutens geführt.

Die Wasserstoffproduktion bis zum Fluten war mit denen von QUENCH-06 und QUENCH-12 vergleichbar. Während des Flutens wurden 6 g Wasserstoff freigesetzt, was mit QUENCH-06 (4 g) vergleichbar, gegenüber QUENCH-12 (24 g) jedoch viel weniger ist. Das unterschiedliche Verhalten der Zr1%Nb Legierungen untereinander (E110 und M5®) resultiert aus den unterschiedlichen Oxidschichteigenschaften.

Abstract

The QUENCH experiments are to investigate the hydrogen source term resulting from the water injection into an uncovered core of a Light-Water Reactor (LWR) as well as the high-temperature behavior of core materials under transient conditions. The typical QUENCH test bundle consists of 21 fuel rod simulators with a total length of approximately 2.5 m.

The QUENCH-14 experiment investigated the effect of M5® cladding material on bundle oxidation and core reflood, in comparison with the tests QUENCH-06 (ISP-45) that used standard Zircaloy-4 and QUENCH-12 that used VVER E110-claddings. The PWR bundle configuration of QUENCH-14 with a single unheated rod, 20 heated rods, and four corner rods was otherwise identical to QUENCH-06. The test was conducted in principle with the same protocol as QUENCH-06, so that the effects of the change of cladding material could be observed more easily. Pre-test calculations were performed by the Paul Scherrer Institut (Switzerland) using the SCDAPSIM, SCDAP/RELAP5 and MELCOR codes.

The experiment started with a pre-oxidation phase in steam, lasting ~3000 s at ~1500 K peak bundle temperature. After a further temperature increase to maximum bundle temperature of 2073 K the bundle was flooded with 41 g/s water from the bottom. The peak temperature of ~2300 K was measured on the bundle shroud, shortly after quench initiation. The electrical power was reduced to an average value of 2 W/cm during the reflood phase to simulate effective decay heat level. Complete bundle cooling was reached in 300 s after reflood initiation.

Post-test examinations showed neither breakaway cladding oxidation nor noticeable melt relocation between rods. Different from the QUENCH-14 (M5®) findings, the QUENCH-12 test with the E110 claddings performed under similar conditions had resulted in intensive breakaway effect at cladding and shroud surfaces during the pre-oxidation phase and local melt relocation on reflood initiation.

The hydrogen production in QUENCH-14 up to reflood was similar to QUENCH-06 and QUENCH-12 bundle tests. During reflood 6 g hydrogen were released which is similar to QUENCH-06 (4 g) but much less than during quench phase of QUENCH-12 (24 g). The reason for the different behavior of the Zr1%Nb cladding alloys is the different oxide scale properties of the materials.

Contents

Inhalt

Introduction 1

1 Description of the Test Facility 3

2 Test Bundle Instrumentation 5

3 Hydrogen Measurement Devices 6

4 Data Acquisition and Process Control 8

5 Test Conduct and Pertinent Results 8

6 Posttest Examination 10

6.1 QUENCH-14 Posttest Appearance Prior to Bundle Sectioning 10

6.2 Encapsulation and Sectioning of the Test Bundle 11

6.3 Metallographic Examination 11

6.4 Analysis of Hydrogen absorbed in Claddings an Corner Rods 13

6.4.1 Hot Extraction Analysis 13

6.4.2 Neutron Radiography 13

7 Summary and Conclusions 15

Acknowledgments 18

References 18

List of Tables

Table 1: QUENCH test matrix

Table 2: Design characteristics of the QUENCH-14 test bundle

Table 3: QUENCH-14; Electrical resistances of rods [mΩ]

Table 4: Diameters of the materials used for the QUENCH high-temperature thermocouples

Table 5: Main characteristics of the HfO_2 thermocouple insulator

Table 6: Main characteristics of the ZrO_2 pellet material, yttria-stabilized (type FZY)

Table 7: Properties of zirconia fiber insulating boards

Table 8: List of instrumentation for the QUENCH-14 test

Table 9: QUENCH-14; Bundle thermocouples positions

Table 10: QUENCH-14; Failure of thermocouples

Table 11: QUENCH-14; Water/steam balance

Table 12: QUENCH-14; Sequence of events

Table 13: QUENCH-14; Cross sections of the test bundle (without shroud) for metallographic examination

Table 14: QUENCH-14; Cross sections of the lower and upper shroud (two encapsulated pieces) for metallographic examination

List of Figures

Fig. 1: QUENCH Facility - Main components.

Fig. 2: Flow diagram of the QUENCH test facility.

Fig. 3: QUENCH Facility; Containment and test section.

Fig. 4: QUENCH-14; Test section with flow lines.

Fig. 5: QUENCH-14; Fuel rod simulator bundle (cross section) including rod type indications.

Fig. 6: QUENCH-14; Heated fuel rod simulator.

Fig. 7: QUENCH-14; Unheated fuel rod simulator.

Fig. 8: QUENCH-14; Test bundle; TC instrumentation and rod designation (top view).

Fig. 9: Axial temperature measurement locations in the QUENCH test section.

Fig. 10: QUENCH-14; High-temperature thermocouple.

Fig. 11: QUENCH-14; Concept for TC fastening at the test rod.

Fig. 12: QUENCH-14; Arrangement of the thermocouples inside the corner rods.

Fig. 13: QUENCH Facility; H_2 measurement with the GAM 300 Mass spectrometer.

Fig. 14: Mass spectrometer sampling position at the off-gas pipe of the QUENCH test facility.

Fig. 15: Hydrogen measurement with the CALDOS analyzer connected to the exhaust gas pipe of the QUENCH facility.

Fig. 16: QUENCH-14 test conduct (schematics of histories of bundle temperature, power, argon and steam flow rate and hydrogen production rate).

Fig. 17: QUENCH-14 test performance in comparison to the QUENCH-06 (Zry-4) test scenario.

Fig. 18: Comparison of temperature profiles at hottest elevation of 950 mm for bundles QUENCH-06 (Zry-4), QUENCH-12 (E110) and QUENCH-14 (M5®).

Fig. 19: QUENCH-14; Thermocouple readings at elevation 850 mm.

Fig. 20: Comparison of temperature radial scattering at hottest elevation of 950 mm for bundles QUENCH-06 (Zry-4), QUENCH-12 (E110) and QUENCH-14 (M5®) on beginning of transient (~6000 s).

Fig. 21: QUENCH-14; Thermocouple readings at elevation 950 mm during transient and reflood.

Fig. 22: QUENCH-14; Thermocouple readings at elevation 1050 mm during transient and reflood. Lower shroud temperatures due to absence of the ZrO_2 shroud insulation above 1024 mm.

Fig. 23: Comparison of axial bundle temperature profiles for QUENCH-06 (Zry-4), -12 (VVER), -14 (M5®).

Fig. 24: Comparison of axial shroud temperature profiles for QUENCH -06, QUENCH-12, QUENCH-14 with wall thickness of shroud 2.38, 2,25, and 3.3 mm respectively.

Fig. 25: Comparison of moderate temperature escalation at the end of transient and cooling status for bundle tests QUENCH-06, QUENCH-12 and QUENCH-14.

Fig. 26: QUENCH-14; feeding rate of quench pump (F 104) and rising of collapsed water front (L 501) during reflood phase.

Fig. 27: Temperature response during the QUENCH-14 reflood phase depicting TC wetting at different bundle elevations and a duration of complete bundle cooling of ~300 s (the same duration as for QUENCH-06 and QUENCH-12).

Fig. 28: QUENCH-14; reflood phase: cooling in 2-phase fluid above collapsed water surface.

Fig. 29: QUENCH-14; Appearance of withdrawn corner rods B, D, C, and A depicting intensive breakaway for E110 (rod C).

Fig. 30: QUENCH-14; Axial oxide layer thickness distribution of Zry-4 corner rods B (withdrawn at the end of pre-oxidation), D (at the end of the transient) and A (after the test), evaluated by metallography.

Fig. 31: Axial oxide layer profile of rod No. 16 of the QUENCH-14 test bundle (M5®) compared to the QUENCH-06 data (Zircaloy-4).

Fig. 32: QUENCH-14; ZrO_2 structure of solid corner rod B withdrawn at the end of preoxidation.

Fig. 33: QUENCH-14; ZrO_2 structure of solid corner rod D withdrawn at the end of transient.

Fig. 34: QUENCH-14; Comparison of ZrO_2 structure of instrumented corner rods A (Zry-4) and C (E110) withdrawn after the test; breakaway for external ZrO_2 sub-layer formed during preoxidation on surface of rod C.

Fig. 35: QUENCH-14; Post-test videoscope observations at the position of the withdrawn corner rod B. View from bottom.

Fig. 36: QUENCH-14; Post-test videoscope observations at the position of the withdrawn corner rod D. View from bottom.

Fig. 37: QUENCH-14; Posttest view of the test bundle at elevations 500-800 mm.

Fig. 38: QUENCH-14; Posttest view of the test bundle at elevations 800-1000 mm (cladding breaches caused by disassembly of test bundle and shroud).

Fig. 39: QUENCH-14; Posttest view of the test bundle at elevations 1000-1200 mm.

Fig. 40: QUENCH-14; debris buildup at spacer grid No. 4 (1050 mm).

Fig. 41: QUENCH-14; Posttest appearance of the lower part of the shroud (viewed from different azimuthal positions) at elevations -300 to 1000 mm and 600-1000 mm, respectively.

Fig. 42: QUENCH-14; Posttest view of the upper part of the shroud at elevations 1000-1300 mm.

Fig. 43: Appearance of test rod No. 16 after removed from the QUENCH-14 test bundle.

Fig. 44: QUENCH-14; Cladding rupture of fuel rod simulator No. 16 during handling.

Fig. 45: QUENCH-14; Microstructure of the cladding tube of rod No. 16 withdrawn after the test.

Fig. 46: QUENCH-14; Circumferential distribution of ZrO_2 thickness [µm] at different elevations of peripheral rod 16.

Fig. 47: QUENCH-14; Bundle cross sections at 550 mm, 570 mm, 636 mm and 650 mm (top view).

Fig. 48: QUENCH-14; Bundle cross sections at 734 mm, 750 mm, 834 mm and 850 mm (top view).

Fig. 49: QUENCH-14; Shroud cross sections at 885 mm, 900 mm, 925 mm and 950 mm (top view).

Fig. 50: QUENCH-14; Bundle cross sections at 900 mm, 934 mm, 950 mm and 1000 mm.

Fig. 51: QUENCH-14; Bundle cross sections at 1034 mm, 1050 mm, 1084 mm and 1100 mm (top view).

Fig. 52: QUENCH-14; Bundle cross sections at 1134 mm and 1150 mm (top view).

Fig. 53: QUENCH-14: Cross section at 636 mm bundle elevation; overview, oxidation state of rod No. 5.

Fig. 54: QUENCH-14; Cross section at 750 mm bundle elevation; overview, oxidation state of rod No. 2.

Fig. 55: QUENCH-14; Cross section at 850 mm bundle elevation; overview; oxidation state of rod No. 3.

Fig. 56: QUENCH-14; Cross section at elevation 850 mm depicting separately test rods 1-6.

Fig. 57: QUENCH-14; Cross section at elevation 850 mm depicting separately test rods 7-12.

Fig. 58: QUENCH-14; Cross section at elevation 850 mm depicting separately test rods 13-19.

Fig. 59: QUENCH-14; Cross section at elevation 850 mm depicting separately test rods 20, 21.

Fig. 60: QUENCH-14; Cross section at 850 mm bundle elevation; overview, oxidation state of rod No. 7.

Fig. 61: QUENCH-14; Thermocouples state at elevation 850 mm.

Fig. 62: QUENCH-14; Cross section at 900 mm bundle elevation; overview, oxidation state of rod No. 12.

Fig. 63: QUENCH-14; Elevation 900 mm; rods 1-6 with externally and internally oxidised cladding.

Fig. 64: QUENCH-14; Elevation 900 mm; rods 7-12 with externally and internally oxidised cladding.

Fig. 65: QUENCH-14; Elevation 900 mm; rods 13-19 with externally oxidised cladding and intact pellets.

Fig. 66: QUENCH-14; Elevation 900 mm; rods 20, 21 with externally and internally oxidised cladding.

Fig. 67: QUENCH-14; Cross section at 900 mm bundle elevation; overview; oxidation state of rod No. 9 with partially liquefied metal layer and development of internal oxide layer.

Fig. 68: QUENCH-14; 900 mm, structure of oxidised cladding of rod No. 20 with frozen melt of metal layer.

Fig. 69: Some fragments of cladding structures of the QUENCH-06 bundle at elevation 900 mm.

Fig. 70: QUENCH-14; EDX analysis of foaming material at surface of rod No.14 at elev. 900 mm: part of oxidised, melted and downwards relocated TFS 4/13 duplex sheath.

Fig. 71: QUENCH-14; Shroud cross section at 900 mm bundle elevation.

Fig. 72: QUENCH-14; Cross section at 950 mm bundle elevation; overview oxidation state of rod No. 3.

Fig. 73: QUENCH-14; Cross section at elevation 950 mm; rods 1-6; externally and internally oxidised cladding.

Fig. 74: QUENCH-14; Cross section at elevation 950 mm; rods 7-12 with externally and internally oxidised cladding.

Fig. 75: QUENCH-14; Cross section at elev. 950 mm; rods 13-19 with externally and internally oxidised cladding.

Fig. 76: QUENCH-14; Cross section at elevation 950 mm depicting separately test rods 20, 21.

Fig. 77: QUENCH-14; Cross section at 950 mm bundle elevation; interaction of metal melt with oxide layers at necking position between rods 1 and 2.

Fig. 78: QUENCH-14; Cross section at 950 mm bundle elevation; oxidation state of rod No. 3.

Fig. 79: QUENCH-14; EDX analysis of foaming material at surface of rod No.7 at elev. 950 mm: interaction of oxidised cladding tube with melt of failed TFS 8/13.

Fig. 80: QUENCH-14; EDX analysis of foaming material at surface of rod No.14 at elev. 950 mm: interaction of oxidised cladding tube with melt of failed TFS 4/13.

Fig. 81: QUENCH-14; Cross section at 1000 mm bundle elevation; overview, oxidation state of rod No. 2.

Fig. 82: QUENCH-14; Cross section at elev. 1000 mm; rods 1-6 with externally and internally oxidised cladding.

Fig. 83: QUENCH-14; Cross section at elev. 1000 mm; rods 7-12 with externally and internally oxidised cladding.

Fig. 84: QUENCH-14; Cross section at elev. 1000 mm; rods 13-19 with externally and internally oxidised cladding.

Fig. 85: QUENCH-14; Cross section at elevation 1000 mm depicting separately test rods 20, 21.

Fig. 86: QUENCH-14; Elevation 1000 mm, rod No. 2: interaction of melt with external oxide layer under steam starvation conditions.

Fig. 87: QUENCH-14; Cladding of rod No. 11 at 1000 mm bundle elevation: oxidised melt and internal oxide layer between 170° and 340°.

Fig. 88: QUENCH-14; Elevation 1000 mm; structure of oxidised cladding of rod No 11 with frozen and lost melt of metal layer.

Fig. 89: QUENCH-14; Cross section of rod No. 12 at elev. 1000 mm; interaction of oxidised cladding tube with relocated piece of Zry-4 shroud.

Fig. 90: QUENCH-14; EDX analysis of contact point between the Zry-4 shroud and the M5® cladding of rod 12 at elevation 1000 mm.

Fig. 91: Some fragments of cladding structures of the QUENCH-6 bundle at elevation 1000 mm.

Fig. 92: QUENCH-14; Cross section at elevation 1050 mm; oxidation state of rod No. 2 with moderate oxidised melt.

Fig. 93: QUENCH-14; Cross section at elevation 1050 mm; rods 1-6 externally and internally oxidised cladding.

Fig. 94: QUENCH-14; Cross section at elevation 1050 mm; rods 7-12 with externally and internally oxidised cladding.

Fig. 95: QUENCH-14; Cross section at elev. 1050 mm; rods 13-19 with externally and internally oxidised cladding.

Fig. 96: QUENCH-14; Cross section at elevation 1050 mm depicting separately test rods 20, 21.

Fig. 97: QUENCH-14; Cross section at elevation 1050 mm; oxidation state of rod No. 6 with slightly oxidised melt.

Fig. 98: QUENCH-14; Cross section at elevation 1050 mm; oxidation state of rod No. 20 without melt formation.

Fig. 99: QUENCH-14; Cross section at elevation 1100 mm; oxidation state of rod No. 3.

Fig. 100: QUENCH-14; Cross section at elevation 1100 mm; oxidation state of rod No. 8.

Fig. 101: QUENCH-14; Elevation 1100 mm; oxidation state of the Zry-4 spacer grid sheets at rod No. 8.

Fig. 102: QUENCH-14; Cross section at elevation 1100 mm; oxidation state of rod No. 3 (continuation).

Fig. 103: QUENCH-14; Cross section at elevation 1150 mm; oxidation state of rod No. 5.

Fig. 104: QUENCH-14; Oxide layer thickness at bundle elev. 570 mm (Cross section QUE-14-1).

Fig. 105: QUENCH-14; Oxide layer thickness at bundle elev. 636 mm (Cross section QUE-14-2).

Fig. 106: QUENCH-14; Oxide layer thickness at bundle elev. 750 mm (Cross section QUE-14-3).

Fig. 107: QUENCH-14; Oxide layer thickness at bundle elev. 850 mm (Cross section QUE-14-4).

Fig. 108: QUENCH-14; Oxide layer thickness at bundle elev. 900 mm (Cross section QUE-14-9).

Fig. 109: QUENCH-14; α-layers at bundle elevation 900 mm (Cross section QUE-14-9).

Fig. 110: QUENCH-14; Oxide layer thickness of the shroud at bundle elevation 925 mm (Cross section QUE-14-16)

Fig. 111: QUENCH-14; Oxide layer thickness at bundle elev. 950 mm (Cross section QUE-14-5).

Fig. 112: QUENCH-14; Oxide layer thickness at bundle elev. 1000 mm (Cross section QUE-14-10).

Fig. 113: QUENCH-14; α-layers at bundle elevation 1000 mm (Cross section QUE-14-10).

Fig. 114: QUENCH-14; Oxide layer thickness at bundle elev. 1050 mm (Cross section QUE-14-6).

Fig. 115: QUENCH-14; Oxide layer thickness at bundle elev. 1100 mm (Cross section QUE-14-7).

Fig. 116: QUENCH-14; Oxide layer thickness at bundle elev. 1150 mm (Cross section QUE-14-8).

Fig. 117: QUENCH-14; Axial distribution of summarized oxide thickness (external and internal oxide layers) for all rod simulators

Fig. 118: QUENCH-14; Axial distribution of oxide thicknesses for external and internal cladding oxide layers and shroud.

Fig. 119: Comparison of axial distribution of cladding external oxide thicknesses for the bundles QUENCH-06, QUENCH-12 and QUENCH-14.

Fig. 120: Hydrogen production according to mass-spectrometer measurements. Comparison between QUENCH-06, QUENCH-12 and QUENCH-14.

Fig. 121: Comparison of hydrogen uptake by claddings of QUENCH-14, QUENCH-12, and QUENCH-06 bundles; evaluation by hot extraction.

Fig. 122: QUENCH-14; Axial distribution of hydrogen absorbed in the Zry-4 corner rods at different experiment stages; evaluation by neutron radiography.

Fig. 123: QUENCH-14; Comparison of the hydrogen absorbed in the E110 and Zry-4 corner rods and M5® cladding tube of the rod simulator No.16, which were withdrawn from the bundle after the test. Evaluation by neutron radiography.

Fig. A-1 QUENCH-14; Eddy current measurement of oxide thickness at corner rods

Fig. A-2 QUENCH-14; Pre-test with gradual increase of electrical power and constant steam flow rate of ~3 g/s.

Fig. A-3 QUENCH-06; Thermocouples state at elevations 900 mm and 1000 mm.

Introduction

The most important management measure to terminate a severe accident transient in a Light Water Reactor (LWR) is the injection of water to cool the uncovered degraded core. Analysis of the TMI-2 [1] accident and the results of integral out-of-pile (CORA [2, 3]) and in-pile experiments (LOFT [4], PHEBUS [5]) have shown that before the water succeeds in cooling the fuel pins there may be an enhanced oxidation of the zirconium alloy cladding that in turn causes a sharp increase in temperature, hydrogen production and fission product release.

Besides, quenching is considered as a worst-case accident scenario regarding hydrogen release to the containment. For licensing and safety analyses it has to prove that the hydrogen release rate and total amount do not exceed limits for the considered power plant. The hydrogen generation rate must be known to design appropriately accident mitigation measures like passive autocatalytic recombiners and ignitors.

The physical and chemical phenomena of the hydrogen release are, however, not sufficiently well understood. The increased hydrogen production during quenching cannot be completely explained on the basis of the available Zircaloy/steam oxidation correlations [6]. In most of the code systems describing severe fuel damage, phenomena, e.g. melt oxidation and steam starvation prior to flooding, which lead to an enhanced oxidation and hydrogen generation are either not considered or only modeled in a simplified empirical manner.

In addition, no sophisticated models are available to predict correctly the thermal-hydraulic and the clad behavior of the quenching processes in the CORA and LOFT LP-FP-2 tests. An extensive experimental database is therefore needed as a basis for model development and code improvement.

The QUENCH program on the investigation of coolability and determination of the hydrogen source term has therefore been launched at the Forschungszentrum Karlsruhe with the following main objectives.

- The provision of an extensive experimental database for the development of detailed mechanistic models,
- The examination of the physico-chemical behavior of overheated fuel elements under different flooding conditions and at different stages of core degradation,
- The determination of cladding failure criteria, cracking of oxide layers, exposure of new metallic surfaces to steam,
- The investigation of the oxide layer degradation under steam starvation conditions and influence of this phenomenon on subsequent flooding,
- The investigation of the melt oxidation process,
- The determination of the hydrogen source term.

The QUENCH program began with small-scale experiments using short Zircaloy fuel rod segments [7-9]. On the basis of these results well-instrumented large-scale bundle experiments with fuel rod simulators under nearly adiabatic conditions are performed in the QUENCH facility of the Forschungszentrum Karlsruhe, now Karlsruhe Institute of Technology (KIT) [10]. The large-scale bundle experiments are more representative of prototypic reactor accident conditions than are the single-rod experiments. However, small-scale or "separate-effects" experiments are additionally needed to support the large-scale bundle experiments and model development in particular. Important parameters of the bundle test program (see Table 1) are: quench medium, i.e. water or steam, fluid injection rate, cladding oxide layer thickness, temperature at onset of flooding as well as the type of cladding, the availability of neutron absorber materials (AgInCd, B_4C) and the oxidizing atmosphere (e.g. air ingress).

The main objective of experiment QUENCH-14 was the investigation of the effect of M5® cladding material on bundle oxidation and core reflood, in comparison with tests QUENCH-06 (ISP-45) that used standard Zircaloy-4 and QUENCH-12 that used VVER E110-claddings. The PWR bundle configuration of QUENCH-14 with a single unheated rod, 20 heated rods, and four corner rods was otherwise identical to QUENCH-06. The QUENCH-14 experiment was successfully conducted at the Forschungszentrum Karlsruhe on 2nd July 2008. It had been preceded by a low-temperature (maximum of about 770 K) pre-test that characterized the transient bundle behavior (Fig. A-2).

The test scenario was based on the results of pre-test calculations performed by the Paul Scherrer Institute (PSI) using SCDAPSIM, SCDAP/RELAP5 and MELCOR, modified locally as necessary for M5® oxidation kinetics based on separate-effects data from the QUENCH program. The test was conducted in principle with the same protocol as QUENCH-06, so that the effects of the change of cladding material could be observed more easily.

1 Description of the Test Facility

The main components of the QUENCH test facility are presented in Fig. 1. The test section is enclosed by a safety containment with a wall thickness of 5.6 mm and an inner diameter of 801.8 mm. The facility can be operated in two modes: a forced-convection mode depicted in the flow diagram of Fig. 2 and a boil-off mode. In the forced-convection mode (relevant for QUENCH-14) superheated steam from the steam generator and superheater together with argon as a carrier gas enter the test bundle at the bottom (Figs. 3 and 4). The system pressure in the test section is about 0.2 MPa. The argon, steam and hydrogen produced in the zirconium-steam reaction flow upward inside the bundle and from the outlet at the top through a water-cooled off-gas pipe to the condenser where the remaining steam is separated from the non-condensable gases argon and hydrogen. The water cooling circuits for bundle head and off-gas pipe are temperature-controlled to guarantee that the steam/gas temperature is high enough so that condensation at the test section outlet and inside the off-gas pipe can be avoided. The temperature at the bundle head is kept at 348 K, and the flow rate of the cooling water is ~250 g/s. The off-gas pipe consists of a water-cooled inner pipe with a countercurrent flow and a flow rate of ~370 g/s. The water inlet temperature is controlled at 393 K. Between the off-gas pipe and inner cooling jacket there is stagnant off-gas. The main dimensions of the tubes that make up the off-gas pipe are:

Inner pipe:	outer diameter 139.7 mm, wall thickness 4.5 mm
	total length 3256 mm, material: stainless steel
Inner cooling jacket:	outer diameter 154 mm, wall thickness 2 mm,
	material: stainless steel
Outer cooling jacket:	outer diameter 168.3 mm, wall thickness 5 mm,
	material: stainless steel

The quenching water is injected through a separate line marked “bottom quenching” in Fig. 4.

The design characteristics of the test bundle are given in Table 2. The test bundle is made up of 21 fuel rod simulators, each with a length of approximately 2.5 m, and of four corner rods (see cross section in Fig. 5). The fuel rod simulators (Figs. 6 and 7) are held in their positions by five grid spacers, four of Zircaloy-4, and one of Inconel 718 in the lower bundle zone. All test rods, excluding the rod in the bundle center, are heated electrically over a length of 1024 mm and are filled with Kr at a pressure of approx. 0.22 MPa. The heated rods (Fig. 6) were connected to a controlled feeding system that compensated minor gas losses and allowed observation of a first cladding failure as well as a progression of rod failure. The rod cladding of the heated and unheated fuel rod simulator is M5® (industrial product made by AREVA) with 10.75 mm outside diameter and 0.725 mm wall thickness (see also Table 2).

Tungsten heating elements of 6 mm diameter are installed in the center of the heated rods and are surrounded by annular ZrO_2 pellets. The physical properties of the ZrO_2 pellets are

described in Table 6. The tungsten heaters (chemical clean tungsten) are connected to electrodes made of molybdenum (chemical clean molybdenum) and copper (material 2.1293 with Cr 0.8, Zr 0.08 and balance Cu) at each end of the heater. The molybdenum and copper electrodes are joined by high-frequency/high-temperature brazing under vacuum ($2x10^{-3}$ mbar) using an AuNi 18 powder (particle size <105 µm). The electrical resistance of the internal rod heating system, combined from W heater and Mo-(Cu alloy) electrodes, was measured before (at the end of bundle assembling) and after the test (Table 3). For electrical insulation the surfaces of both types of electrodes are plasma-coated with 0.2 mm ZrO_2. To protect the copper electrodes and the O-ring-sealed wall penetrations against excessive heat they are water-cooled (lower and upper cooling chambers filled with demineralized water). The copper electrodes are connected to the DC electric power supply by means of special sliding contacts at the top and bottom. The total heating power available is 70 kW. The distribution of the electric power within the two groups is as follows: about 40 % of the power is released into the inner rod circuit consisting of eight fuel rod simulators (in parallel connection) and 60 % in the outer rod circuit (12 fuel rod simulators in parallel connection). The measured electric resistance of a single heater (W+Mo+Cu sections) is 3 mΩ at room temperature. This value increases significantly with temperature. The additional resistance of the external electric circuit between the axial end of the single heater and the connection to the generator (sliding contacts, cables, and bolts) is 3.13 mΩ for the innner rod group and 4.35 mΩ for the outer rod group. These values can be taken as constant because the external electric circuit remains at ambient temperature throughout the experiment.

The lower boundary for the lower cooling chamber is a sealing plate made of stainless steel with plastic inlays for electrical insulation, sealed toward the system by O-shaped rings. The upper boundary of the lower cooling chamber is a sealing plate of stainless steel. An insulation plate made of plastic (PEEK) forms the top of the upper cooling chamber, and a sealing plate of Al_2O_3, functioning as a heat-protection shield, is the lower boundary of the upper cooling chamber (see Fig. 6).

In the region below the upper Al_2O_3 plate the copper electrode is connected firmly to the cladding. This is done by rotary swaging the cladding onto the electrode. In the swaging region a sleeve of boron nitride is put between electrode and cladding for electrical insulation. The axial position of the fuel rod simulator in the test bundle is fixed by a groove and a locking ring in the top Cu electrodes. Referred to the test bundle the fixing point of the fuel rod simulators is located directly above the upper edge of the upper insulation plate. So, during operation the fuel rod simulators are allowed to expand downwards. Clearance for expansion of the test rods is provided in the region of the lower sealing plate. Also in this region, relative movement between cladding and internal heater/electrode can take place.

The test bundle is surrounded by a 3.25 mm thick shroud (80 mm ID) made of Zircaloy-4 with a 37 mm thick ZrO_2 fiber insulation (physical properties are given in Table 7) and an annular cooling jacket made of Inconel 600 (inner tube) and stainless steel (outer tube; see Fig. 5). The annulus between shroud and cooling jacket was filled (after several cycles of degasing) with stagnant argon of 0.22 MPa and was connected to a flow-controlled argon feeding system in order to prevent steam access to the annulus after shroud failure. The 6.7 mm annulus of the cooling jacket is cooled by an argon flow. Above the heated zone, i.e. above

the 1024 mm elevation there is no ZrO_2 fiber insulation to allow for higher radial heat losses. This region of the cooling jacket is cooled by a water flow (Figs. 3 and 4). Both the lack of ZrO_2 insulation above the heated region and the water cooling force the axial temperature maximum downward.

Insertion of four corner rods avoids an atypically large flow cross section at the outer positions and hence helps to obtain a rather uniform radial temperature profile. There are four corner rods installed in the bundle. Two of them, i.e. rods “A” and “C” are made of a solid rod at the top and a tube at the bottom and are used for thermocouple instrumentation. Corner rod A is a Zircaloy-4 rod whereas corner rod C is made of E110 (Zr1%Nb). The other two rods, i.e. rods “B” and “D” (solid Zircaloy-4 rods of 6 mm diameter) are particularly determined to be withdrawn from the bundle to check the amount of ZrO_2 oxidation at specific times. In QUENCH-14, for the first time, all four corner rods were used for analysis of the oxide layer thickness. Rod B was pulled out of the bundle before transient and rod D before quenching; rods A and C were removed after test termination. It has to be noted that there was no M5 material available for a corner rod design so that the layer thickness measured at the corner rods cannot be used quantitatively as test bundle data.

2 Test Bundle Instrumentation

The test bundle was instrumented with sheathed thermocouples (TC) attached to the rod claddings at 17 different elevations between -250 mm and 1350 mm and at different orientations according to Figs. 8 and 9. The elevations of the surface-mounted shroud thermocouples are from -250 mm to 1250 mm. In the lower bundle region, i.e. up to the 550 mm elevation, NiCr/Ni thermocouples (1 mm diameter, stainless steel sheath 1.4541 (X6CrNiTi18-10), MgO insulation) are used for temperature measurement of rod cladding and shroud as is illustrated in Fig. 9. The thermocouples of the hot zone are high-temperature thermocouples with W-5Re/W-26Re wires, HfO_2 insulation, and a duplex sheath of tantalum (internal)/zirconium with an outside diameter of 2.2-2.3 mm (see Table 4 and for final dimensions after the sheath treatment Fig. 10). Main physical properties of the HfO_2 insulation are given in Table 5.

The thermocouple attachment technique for the surface-mounted high-temperature TCs is illustrated in Fig. 11. The TC tip is held in place by two clamps of zirconium (0.2 mm thick). As these clamps are prone to oxidation and embrittlement in a steam environment an Ir-Rh wire of 0.25 mm diameter is additionally used for fixation in the experiments with pre-oxidation, as was the case in test QUENCH-14. The compensation leads of the thermocouples from the -250 mm to the 850 mm level leave the test section at the bottom of the test section whereas those of the TCs above 850 mm are routed out of the top of the test section to prevent TC cables to pass the hot zone. Additionally, the cables of shroud thermocouples (designated TSH xx/x “I”) were routed toward outside the shroud insulation to avoid heat transfer from the shroud into the TC cable, apart from the TC junction.

The thermocouples attached to the outer surface of the rod cladding at elevations between -250 and 1350 mm are designated “TFS” for all heated rods. “TCRC” is the designation for the centerline central-rod high-temperature thermocouples.

The shroud thermocouples (designation “TSH”) are mounted at the outer surface between -250 mm and 1250 mm. The thermocouples that are installed inside the Zircaloy instrumentation rods at the two corner positions of the bundle (positions A and C) are designated “TIT” (see Fig. 12). The thermocouples of the cooling jacket are installed inside the wall of the inner cooling tube (from -250 mm to 1150 mm, designation “TCI”) and at the outer surface of the outer cooling tube (from -250 mm to 950 mm, designation “TCO”).

The thermocouples in the lower bundle region, i.e. up to 550 mm elevation, NiCr/Ni thermocouples with stainless steel sheath/MgO insulation and an outside diameter of 1.0 mm are used for measurements of the rod cladding, rod centerline and shroud temperatures. The thermocouples in the hot zone and above are high-temperature thermocouples with W5Re/W26Re wires, HfO_2 insulation, and a duplex sheath of tantalum (inside) and Zircaloy (outside) with an outside diameter of about 2.2-2.3 mm (Fig. 10). The “TIT” thermocouples are also of the high-temperature type. The thermocouples of the cooling jacket (TCI and TCO) are 1 mm NiCr/Ni thermocouples with stainless steel sheath for all levels.

A list of all instruments for experiment QUENCH-14 installed in the test section and at the test loop is given in Table 8. A distribution of the thermocouples along the bundle is shown in Table 9. The thermocouples that failed prior or during the test are listed in Table 10.

The flow rates of noble gases (Ar, Kr) are regulated with the BRONKHORST flow controllers. Steam and water flows are controlled with the SIEMENS flow controllers. Numerous pressure transmitters from WIKA measure absolute and differential pressures along the gas supply system, at inlet and outlet of the test section. Evaluation of different gauges has allowed to estimate the water-steam balance (Table 11).

3 Hydrogen Measurement Devices

The released hydrogen is analyzed by two different measurement systems: (1) a Balzers mass spectrometer (MS) “GAM 300” (Fig. 13) and (2) a hydrogen detection system ”Caldos 7 G” (Fig. 15) located in a bypass to the off-gas line downstream the condenser. Due to their different locations in the facility the mass spectrometer “GAM 300” responds almost immediately (less than 5 s) to a change in the gas composition whereas the Caldos device has a delay time of about 80-100 s.

The mass spectrometer “BALZERS GAM 300“ used is a completely computer-controlled quadrupole MS with an 8 mm rod system which allows certain quantitative measurement of gas concentrations down to about 10 ppm. For the MS measurement a sampling tube is inserted in the off-gas pipe located approx. 2.7 m downstream from the test section outlet (see Fig. 2 and 4). It has several holes at different elevations to guarantee that the sampling of the gas to be analyzed is representative (see Fig. 14). To avoid steam condensation in the gas pipes between the sampling position and the MS the temperature of the gas at the MS inlet is controlled by heating tapes to be between 110 and 150 °C (the upper operating temperature of the MS inlet valves). This allows the MS to analyze the steam production rate. Besides, the concentrations of the following species were continuously measured by the mass spectrometer during all test phases: argon, hydrogen, steam, nitrogen, oxygen, and

helium. The fuel rod simulators are filled with krypton which can be used as an indicator for a cladding failure. Additionally, the MS is used to control the atmosphere in the facility, e.g., to monitor the gas composition at the beginning of the test.

The temperature and pressure of the analyzed gas are measured near the inlet valve of the MS. The MS is calibrated for hydrogen, oxygen and nitrogen with well-defined argon/gas mixtures and for steam with mixtures of argon and steam supplied by a Bronkhorst controlled evaporator mixing (CEM) device. The MS off-gas is released into the atmosphere because the amount of hydrogen taken out of the system is negligible. A heated measuring gas pump was used to ensure a continuous flow of the steam-gas mixture from the off-gas pipe to the mass spectrometer.

The principle of measurement of the Caldos system is based on the different heat conductivities of different gases. The Caldos device is calibrated for the hydrogen-argon gas mixture. To avoid any moisture in the analyzed gas a gas cooler, which is controlled at 276 K, is connected to the gas analyzer (see also Fig. 15). The response time of the gas analyzer is documented by the manufacturer to be 2 s, i.e. a time in which 90 % of the final value should be reached. In contrast to the mass spectrometer the Caldos device only measures the hydrogen content. Gases other than H_2 cannot be analyzed by this system.

For the Caldos device as well as for the MS the hydrogen mass flow rate is calculated by referring the measured H_2 concentration to the known argon mass flow rate according to equation (1):

$$\dot{m}_{H_2} = \frac{M_{H_2}}{M_{Ar}} \cdot \frac{C_{H_2}}{C_{Ar}} \cdot \dot{m}_{Ar} \tag{1}$$

with M representing the molecular masses, C the concentrations in vol-% and $\dot{m}$ the mass flow rates of the corresponding gases.

With an argon-hydrogen (two-component) mixture that in fact exists at the location of the Caldos analyzer equation (1) can be written as follows

$$\dot{m}_{H_2} = \frac{M_{H_2}}{M_{Ar}} \cdot \frac{C_{H_2}}{100 - C_{H_2}} \cdot \dot{m}_{Ar} \tag{2}$$

4 Data Acquisition and Process Control

A computer-based control and data acquisition system is used in the QUENCH facility. Data acquisition, data storage, online visualization as well as process control, control engineering and system protection are accomplished by three computer systems that are linked in a network.

The data acquisition system allows recording of about 200 measurement channels at a maximum frequency of 25 Hz per channel. The experimental data and the date and time of the data acquisition are stored as raw data in binary format. After the experiment the raw data are converted into SI units and stored as ASCII data.

For process control, a system flow chart with the most important actual measurement values is displayed on the computer screen. Furthermore, the operating mode of the active components (pumps, steam generator, superheater, DC power system, valves) is indicated. Blocking systems and limit switches ensure safe plant operation. Operating test phases, e.g. heating or quenching phases, are pre-programmed and can be started on demand during the experiment. The parameter settings of the control circuits and devices can be modified online.

Online visualization allows to observe and to document the current values of selected measurement positions in the form of tables or plots. Eight diagrams with six curves each can be displayed as graphs. This means that altogether 48 measurement channels can be selected and displayed online during the course of the experiment.

The data of the main data acquisition system and of the mass spectrometers were stored on different computers. Both computers were synchronized. The data of the main acquisition system were stored at a frequency of 1 Hz. The mass spectrometer data were recorded at a frequency of approx. 0.33 Hz during the entire test.

5 Test Conduct and Pertinent Results

A listing of the major events during the QUENCH-14 experiment is given in Table 12. The QUENCH-14 test phases were as follows (Fig. 16):

	Heatup to ~873 K. Facility checks.
Phase I	**Stabilization** at ~873 K.
Phase II	Heatup with ~0.3-0.6 K/s to ~1500 K.
Phase III	**Pre-oxidation** of the test bundle in a flow of 3 g/s of superheated steam and 3 g/s argon for ~3000 s at relatively constant peak temperature of ~1500 K. Withdrawal of corner rod B at the end.
Phase IV	**Transient** heatup with 0.3…2.0 K/s from ~1500 to ~2050 K in a flow of 3 g/s of superheated steam and 3 g/s argon. Withdrawal of corner rod D ~30 s before quench initiation.
Phase V	**Quenching** of the bundle by a flow of ~41 g/s of water.

The test was conducted in principle with the same protocol as QUENCH-06 (Fig. 17) and similar temperature history as QUENCH-12 (Fig. 18). Typical readings of the high temperature thermocouples are shown for the elevation 850 mm in Fig. 19. The experiment started with an application of electrical bundle power of ca. 3.8 kW, which was ramped step-wise to ~11 kW to achieve the desired pre-oxidation temperature at bundle peak position of ~1500 K, in a flow of 3.0 g/s argon and 3.0 g/s steam. Pre-oxidation was lasted ~3000 s; a first corner rod, i.e. rod B, was withdrawn about 50 s before end of preoxidation to check the oxidation level.

The power was then ramped at a rate of 6.2 W/s to cause a temperature increase until the desired maximum bundle temperature of ~2050 K which was reached after about 1200 s. The radial temperature scattering at hottest elevation of 950 mm on the beginning of the transient phase is shown in Fig. 20 in comparison to the tests QUENCH-06 and QUENCH-12. The temperatures at the end of the transient phase are shown in Figs. 21 and 22 for the bundle elevations 950 and 1050 mm correspondingly. The axial temperature distributions at the start and the end of the transient phase are shown in Fig. 23 (rod temperatures) and Fig. 24 (shroud temperatures) as comparison between three bundle tests. A second corner rod, i.e. rod D, was withdrawn about 30 s before quench initiation, when the maximum bundle temperature was nearly 2000 K.

The quench criterion and reflood rate were identical to those in QUENCH-06 and QUENCH-12 (Fig. 25). Reflood with 41 g/s water at room temperature was initiated, following fast water injection to fill the lower plenum (Fig. 26). The value of 41 g/s corresponds to effective 1.3 g/s/rod with consideration of shroud and corner rods (indeed the total perimeter of shroud (251 mm) and four corner rods (75 mm) corresponds to perimeter of 10 additional fuel rod simulators, i.e. the flow rate per rod is 41/(21+10)=1.3). The electrical power was reduced to 3.9 kW during the reflood phase, approximating effective decay heat levels. Following reflood initiation a negligible temperature excursion was observed. The peak temperature reached, ~2300 K, was measured on the shroud, shortly after the quench initiation. Complete bundle cooling was reached in 300 s after reflood initiation (Fig. 27). Comparison of the collapse water front position with reaction of thermocouples on the full wetting by 2-phase fluent allows determine the size evolution of this fluent zone (Fig. 28). The maximum height of 2-phase fluent was 550 mm, which was measured when collapse water front reached the elevation of ~600 mm.

The hydrogen production measured with mass spectrometer was ~34 g in the pre-oxidation and transient phases, and ca. 6 g in the quench phase; the total amounts released being similar to those in QUENCH-06, i.e. 32 g and 4 g [11], respectively, but less compared to QUENCH-12 with H_2 amounts of 34 and 24 g, respectively [12] (Fig. 120).

Shroud failure was indicated (change of the Ar flow rate into annulus between shroud and cooling jacket from 0 to 1.2 g/s) at around the initiation of reflood; while heated rod failure was observed (indication of Kr by mass spectrometer) towards the end of the transient phase. The remaining two corner rods, i.e. rods A (Zry-4) and C (E110), were withdrawn after the test, again to check oxide levels and hydrogen absorption by neutron radiography. Only corner rod C exhibits breakaway oxidation, which was observed between 500 and 1300 mm (Fig. 29).

6 Posttest Examination

6.1 QUENCH-14 Posttest Appearance Prior to Bundle Sectioning

In QUENCH-14, for the first time, all four corner rods were used for analysis of the oxide layer thickness. The peak oxide layer thicknesses for three Zircaloy-4 rods (A, B and D) were measured metallographically at elevation ~950 mm with the following values: 170 µm at the end of the pre-oxidation phase (rod B), 470 µm before reflood (rod D) and about 630 µm after the test (rod A). Fig. 30 shows the axial distribution of the oxide layer thickness for these corner rods. The estimation of the oxide thicknesses by means of the eddy-current measurements shows that this express method has relative high measurement error for the oxide layers thicker than 200 µm (Fig. A-1). The metallographic comparison of two different corner rods withdrawn after the test shows clear influence of the breakaway oxidation for the rod C made from E110 alloy at elevations between 650 and 1050 mm (Figs. 32 - 34). Inspection of the rod No. 16, which was not instrumented and was removed from the QUENCH-14 bundle prior to encapsulation of the test bundle, shows no breakaway effect (Figs. 43 – 46). The comparison of the axial distribution of the oxide layer thickness for rods No. 16 of bundles QUENCH-14 and QUENCH-06 shows that at bundle elevations with possible breakaway conditions the oxide layer thickness of the M5® alloy is less than for the Zry-4 alloy (Fig. 31).

Before disassembly of the QUENCH-14 shroud/test bundle unit the empty channels of corner rods were used for visual inspection. The post-test endoscopic investigations of the bundle were performed with an OLYMPUS IPLEX videoscope inserted at the empty positions of the two withdrawn corner rods B and D. The post-test endoscopy showed neither breakaway cladding oxidation nor noticeable melt formation (Figs. 35 – 36).

For the first time the shroud was taken off the test bundle so that the test rods could be viewed in detail and the appearance could be documented by photography (Figs. 37 – 39). The posttest appearance of the QUENCH-14 bundle supports the findings of the separate-effects tests with short specimens that even at elevated temperatures there is less spalling of the oxide scale for M5® compared to Zircaloy-4. At the surface of the QUENCH-14 rod claddings traces of interaction between claddings and pieces of ruptured spacer grids relocated from elevation1050 mm (Fig. 38) were observed. Also traces of eutectic interaction with steel debris were observed at the surface of some rod claddings (Fig. 40). Handling of the test bundle during disassembly caused cladding rupture between 850 and 900 mm elevation. The ruptures occurred at the transition zone from moderate to strong oxidation due to a strong embrittlement. Strongest oxidation took place in the hot region between 900 and 1100 mm.

During disassembly the shroud broke apart into two pieces at around 950-1000 mm elevation (Figs. 41 – 42). The outside surface of the shroud appeared unaffected up to elevation 600-650 mm. Changes in the color are evident between 650 and 850 mm. From 850 mm upward the shroud is deformed due to a temperature beyond melting of β-Zr and reaction with the ZrO_2 fiber insulation (oxidation-reduction process). The upper part of the shroud, i.e. from 1000 to 1300 mm, appears severely oxidized but not molten.

6.2 Encapsulation and Sectioning of the Test Bundle

After separately photographing test bundle and shroud, the test bundle and the two shroud pieces were encapsulated in epoxy resin. For encapsulation the test bundle and shroud are set up vertically. Prior to filling, a cap is placed over the bottom of the copper electrodes and a low-melting metal alloy (similar to Wood's metal containing 48 % Bi, 18 % Pb, 23 % In, 11 % Sn; density of ~10 kg/dm^3; melting point of 331 K) is used to seal the bottom of the bundle. The low-melting metal is also used for sealing the bundle foot so that it can be re-used for the next experiment. For this purpose an inner cage is inserted into the bundle foot from the bottom. Filling of this auxiliary structure is from above the bundle foot, i.e. through holes in the shroud at elevations above –300 mm. Then a Plexiglas® tube as mould with an inner diameter of 90 mm is put over the test bundle and fixed at the flange of the bundle foot by glue. A Plexiglas® tube with an inner diameter of 140 mm was used to encapsulate the shroud.

Encapsulation of the bundle is performed by filling the mould with the epoxy resin (Bakelite EPR 0273 with the pertinent hardener Bakelite EPH 350) from the bundle foot over the entire bundle length. The epoxying process generally shows a little heating due to the exothermal heat that develops during the curing stage and some shrinkage effect. After epoxying the bundle the resin is allowed to harden for one week. Sectioning of the bundle is done by a saw with a diamond blade approximately 3 mm thick and with an OD of 500 mm. The elevations of the cross sections used for metallographic analyses are listed in Tables 13 and 14. Figs. 47 - 52 present an overview of the QUENCH-14 cross sections available. They are described and interpreted in the subsequent sections.

6.3 Metallographic Examination

Bundle cross-section at elevation 636 mm (Fig. 53): The morphology of the cladding oxide layer is typical for the long-term oxidation at moderate temperatures less than 1473 K. Homogeneous monoclinic oxide is formed, underlayed by brittle and relatively wide hexagonal alpha-Zr stabilized by oxygen.

Bundle cross-section at elevation 750 mm (Fig. 54): The structure of cladding oxide layer is quite friable due to micro cracks development. The radial micro cracks are developed under influence of shrink stresses during phase transition between monoclinic and tetragonal phases of zirconium oxide at T~1473 K. This was the reason for removal of parts of columnar grains during grinding and polishing processes.

Bundle cross-section at elevation 850 mm (Fig. 55): A columnar structure of the oxide layer is well observed. A part of the oxide layer at the boundary to α-Zr(O) reveals formation of the cubic ZrO_{2-x} crystal structure at temperatures above 1773 K. One thermocouple (TFS 3/12) at this elevation was decoupled from the rod cladding (the corresponding thermocouple reading given in Fig. 19 shows temperature decrease during preoxidation). An overview of individual rod cross-sections, which are given in Figs. 56 – 59, shows formation of cracks going through claddings and being slightly oxidized (Fig. 60). No crack formation in the pellets was observed. The status of the thermocouple sheath oxidation is pictured in Fig. 61. The external Zr sheath was practically completely oxidized for the cladding surface thermocouples; the internal Ta sheath was locally attacked by steam with formation of Ta_2O_5.

However, both sheaths of the TCRC thermocouple inside the central rod remained intact. For comparison, the thermocouples status of the QUENCH-06 bundle is given in Fig. A-3.

Bundle cross-section at elevation 900 mm (Fig. 62): A part of the oxide layer at the boundary to α-Zr(O) reveals formation of cubic ZrO_{2-x} phase at temperatures above 1773 K with typical metal precipitates developed during cool down. The overview of individual rod cross-sections, which is given in Figs. 63 – 66, shows formation of pre-reflood and post-reflood cracks going through claddings, circumferential internal oxidation of claddings (for five rods No. 7 - No. 9, No. 20 and No. 21) and frozen oxidized Ta-containing melt from damaged thermocouples (for two rods No. 7 and No. 14). Pellets of six rods (No. 1, No. 2, No. 9, No. 10, No. 20 and No. 21) showed formation of radial cracks. The metal part of internally oxidized claddings was molten and showed formation of ceramic precipitates inside the melt (Figs. 67 and 68). Because the pellets at the boundary to the internal cladding oxide showed no reduction structure (no metal precipitates inside the ceramic), it can be concluded that the internal oxide layer developed due to the interaction between melt and steam, which penetrated through the cladding cracks. Similar observations of internal oxide formation were made for the QUENCH-06 bundle (Fig. 69). Fig. 70 shows the typical structure of Ta-containing oxidized melt from a damaged thermocouple (melting point of Ta_2O_5 is ~2150 K). A shroud segment with molten Zry-4, which has interacted with the ZrO_2 thermal insulation, is shown in Fig. 71.

Bundle cross-section at elevation 950 mm (Fig. 72): A very intensive cladding oxidation occurred at this elevation. An overview of individual rod cross-sections, which is given in Figs. 73 – 76, shows only remnants of very thin metal layers or even their complete absence. All ZrO_2 pellets reveal the formation of cracks. The characteristic necking mechanism at the contact between the rods with the accompanied melt oxidation is depicted in Fig. 77. A typical cladding oxidation status is shown in Fig. 78. Similar to the elevation 900 mm the wetting of rods No. 7 and No. 14 with Ta-containing melt from damaged thermocouples was observed. The SEM/EDX analysis of Ta-containing melt is presented in Figs. 79 and 80.

Bundle cross-section at elevation 1000 mm (Fig. 81): Similar to the elevation 950 mm a very intensive external and internal cladding oxidation with the formation and oxidation of melt enclosed between these oxide layers was occurred. The overview of individual rod cross-sections given in Figs. 82 – 85 shows voids developed between the oxide layer and the pellet due to melt relocation. Fig. 86 documents a relatively thick partially oxidized melt at the contact location between the rods No. 2 and No. 1: the melt was not completely oxidized because of steam starvation at this contact point. The map of circumferential layer structure with oxidized melt and internal oxide layer is pictured in Fig. 87 for the rod No. 11; selected details of the oxide cladding are presented in Fig. 88. For comparison, similar fragments of cladding structures of the QUENCH-06 bundle are given in Fig. 91. Figs. 89 and 90 show the optical and SEM observations of local interaction between the M5 cladding and the Zry-4 shroud piece.

Figs. 92 – 102 illustrate melt formation, partially melt relocation and melt oxidation at elevations 1050 and 1100 mm with molybdenum electrodes. Fig. 101 shows results of oxidation and melting of the Zry-4 spacer grid relocated from upper elevation.

No melt formation and only moderate cladding oxidation were observed at elevation 1150 mm (Fig. 103).

Results of post-test measurements of oxide layer thickness (and α-Zr(O) layer thickness for elevations 900 and 1000 mm) are summarized in Figs. 104 to 116. Corresponding axial distribution of averaged bundle oxidation degree are depicted in Figs. 117 and 118. Fig. 119 shows the comparison of axial ZrO_2 layer thickness distributions for bundle tests QUENCH-14, QUENCH-12 and QUENCH-06. The curve shapes are very similar among each other with the highest oxide thicknesses at elevation 950 mm. The maximum value of oxide thickness of Zircaloy-4 used in QUENCH-06 is lower than after tests QUENCH-12 and QUENCH-14 with niobium bearing alloys E110 and M5®. This is in accordance with results of separate-effect tests showing higher activation energies of the oxidation rates of Zr-Nb alloys which result in higher oxidation rates at temperatures above 1650 K [13, 14].

6.4 Analysis of Hydrogen absorbed in Claddings an Corner Rods

6.4.1 Hot Extraction Analysis

The hydrogen content in cladding segments of 20 mm length were determined by hot extraction. The specimens were put in the “LAVA” furnace at room temperature. The furnace was evacuated and flushed by Ar. Then the specimens were heated up in flowing Ar to a temperature of 1773 K. After annealing for 30 min at this temperature the specimens were cooled down to room temperature in the furnace. The hydrogen concentration in the off-gas was measured by the mass spectrometer “GAM300”. The integration of the hydrogen flux over the annealing time gives the amount of hydrogen extracted from the specimen.

The maximum hydrogen content of 2.2 at% was measured at the QUENCH-14 bundle elevation of 925 mm. Measurement results of hydrogen uptake by claddings of bundles QUENCH-14, QUENCH-12 and QUENCH-06 are given in Fig. 121. It can be seen that hydrogen uptake by the M5® cladding alloy (QUENCH-14) was noticeably lower than for the Zircaloy-4 cladding alloy (QUENCH-06) and significantly lower than for the E110 alloy. This confirms results of separate-effects tests. The explanation of this behavior is given in the next session.

6.4.2 Neutron Radiography

Neutron radiography experiments provide the possibility of a fast, non-destructive and quantitative determination of the hydrogen content with a spatial resolution up to 25 µm. In [15] the experimental setup was optimized and the calibration of the dependence of macroscopic total neutron cross section on hydrogen content was given.

The method was applied to determine quantitatively the hydrogen absorbed in the corner rods A (Zircaloy-4), C (E110) and the cladding rod 16 (M5®) of the QUENCH-14 bundle. The measurements were performed at the cold neutron radiography facility ICON (SINQ, PSI, Switzerland) [16] with a camera length L/d of 350. L is the aperture to sample distance and d the aperture opening size. The neutron radiographs were recorded by a camera system, specially developed for neutron micro-tomography applications. It consists of an ultra-thin Gadox scintillator (thickness 10 µm), a lens without any optical distortions (diameter:

155 mm, height: 620 mm mass: 30 kg) and the high resolution 1:1 magnification CCD camera ANDOR DV436 (Peltier cooled, pixel size 13.5 µm, field of view: 28 mm x 28 mm, 2048 x 2048 pixels, 16 bit). Due to the camera system has an active window with a size of 28 mm x 28 mm the rods were scanned with a step size of 20 mm.

The data were analyzed with the “ImageJ” software package. The measurements were normalized with an open beam frame and corrected for dark current. With an axial step size of 20 mm the intensity distribution of the position perpendicular to the rod axis was determined by integration over an axial width of 1 mm. In the region attenuated by the rods the intensity distribution can be described by the Eqs. (*3*) and (*4*). The transmission *T* of the neutron beam behind the specimen is given by:

$$T = \frac{I - I_B}{I_o - I_B} = \exp(-\Sigma_{total} \cdot s) \tag{3}$$

I is the intensity behind the specimen, I_0 the primary beam intensity, I_B the background intensity measured behind a Cd specimen with comparable dimension, Σ_{total} the macroscopic total neutron cross section of the material and *s* the path length through the specimen. As hydrogen is added to the Zircaloy-4, Σ_{total} can be given as:

$$N_H \sigma_{total,H} + \Sigma_{total,Zry-4} \tag{4}$$

$\Sigma_{total,Zry-4}$ is the total macroscopic neutron cross section of the dehydrated Zircaloy-4 specimen N_H the hydrogen atom number density and $\sigma_{total,H}$ the total microscopic cross section of hydrogen. For an illumination in radial direction the path length *s* through a rod shaped specimen is given by the complex equation:

$$s = \Re\left(\sqrt{d^2 - (x - x_0)^2}\ \right) \tag{5}$$

$$s = \Re\left(\sqrt{r_o^2 - (x - x_0)^2} - \sqrt{r_i^2 - (x - x_0)^2}\right) \tag{6}$$

$\Re$ is the real part of the complex term, *x* the actual radial position, x_0 the radial middle position of the specimen, *d* the rod diameter, r_o and r_i the outer and inner radius, respectively. Due to the fact that the intensity fit at the sample edges is very sensitive for the sample alignment, only the middle positions were used for the analysis where $s \approx d$ = 6 mm for the corner rods and $s \approx d_o - d_i$ = 1.5 mm for the cladding tube.

Since the total cross section of hydrogen-free Zr-Nb alloy is very close to the cross section of hydrogen-free Zircaloy-4 (Zr-Sn), the hydrogen atomic concentration c_H^m in at.% is given according to [15] by:

$$c_H^m = \frac{\dfrac{\Sigma_{total} - 0.21\ cm^{-1}}{2.90\ cm^{-1}}}{\dfrac{\Sigma_{total} - 0.21\ cm^{-1}}{2.90\ cm^{-1}} + 1} \tag{7}$$

Fig. 122 gives the axial distributions of the hydrogen concentrations in the three investigated corner rods determined by eq. (*7*) and compares the hydrogen concentrations in the Zircaloy-4 corner rods withdrawn after different stages of the QUENCH-14 test. The hydrogen concentration in the Zircaloy-4 corner rods is low after the pre-oxidation phase (maximal value: 1.25 at.% ≈ 140 wppm at about z ≈ 950 mm). Before reflood maximal hydrogen concentrations of 3.1 at.% (≈ 340 wppm) at z = 970 mm and 3.0 at.% (≈ 330 wppm) at z = 1145 mm were reached.

The quenching results in an additional strong hydrogen uptake, at least for Zircaloy-4. Values up to 7.5 at.% (≈ 830 wppm) were measured. However, the lost material between 922 and 1005 mm could have a higher hydrogen concentration.

Strong differences between the applied cladding materials were found. Fig. 123 compares the Zircaloy-4 corner rod A, the E110 corner rod C and the M5® cladding tube 16 withdrawn after the test. At axial positions, where breakaway occurs, the E110 contains about one order of magnitude more hydrogen than the other two materials. In addition, the general axial distribution is changed by the breakaway effect. Whereas the maximal hydrogen concentrations in Zircaloy-4 and M5™ were found at the hottest position (z ≈ 950 mm) local maxima in E110 were found at about z ≈ 1100 mm, 900 mm and 600 mm. The results obtained at the corner rod C confirm the outcome of the QUENCH-12 test. Here comparably high hydrogen concentrations were determined in the E110 control rods.

7 Summary and Conclusions

QUENCH-14 was the third of four tests investigating the influence of the cladding alloy on the oxidation and degradation of fuel rod bundles during severe accident sequences and in particular during reflood of the core. The fourth test of the QUENCH-ACM (Advanced Cladding Materials) series was QUENCH-15 performed with ZIRLO™ in 2009.

Although significant differences between the various alloys have been found in separate-effects tests especially at temperatures below 1350 K, the influence on integral bundle behaviour during typical accident transients seems to be less significant. The strong differences seen in the SETs are mainly caused by different susceptibility of the alloys to breakaway oxidation which leads to reduction or even loss of protective effect of oxide scales and accelerated oxidation kinetics after a certain time.

The superior oxidation resistance of M5® at operation conditions is also seen at higher temperatures typical for accident scenarios. M5® revealed low oxidation over wide temperature ranges and the lowest hydrogen uptake in comparison to Zircaloy-4 and E110. This was seen in test-to-test comparisons and additionally by comparison of the corner rods made of Zry-4 and E110 with a withdrawn M5® cladding tube after test QUENCH-14.

Only at very high temperatures above 1650 K Zircaloy-4 revealed lower oxidation rates than the niobium bearing alloys. In the transient QUENCH scenario, the combination of lower oxidation rate of M5® at temperatures below 1650 K resulting in a thinner protective oxide layer compared to Zry-4, on the one hand, and a higher oxidation rate at enhanced

temperatures, on the other hand, may lead to accelerated oxidation kinetics of Nb bearing alloys in the late transient phase.

The essential results of the QUENCH-14 experiment can be summarized as follows.

- The QUENCH-14 experiment investigated the effect of niobium-bearing M5® cladding material on bundle oxidation and core reflood, in comparison with test QUENCH-06 (ISP-45) that used standard Zircaloy-4, and QUENCH-12 (ISTC 1648.2) that used niobium-bearing E110 alloy.

- The evolution of the axial peak of oxide layer thickness during the test was evaluated with three Zircaloy-4 corner rods, which were withdrawn (1) 10 s before initiation of the transient phase, (2) 30 s before reflood initiation, (3) after the test. The fourth corner rod made of the E110 alloy, which was withdrawn also after the test, showed intensive breakaway oxidation.

- The pre-oxidation phase at a peak bundle temperature of ~1500 K (elevation 950 mm) lasted ~3000 s. The maximum oxide layer thickness at the first withdrawn corner rod was 170 µm.

- During the transient phase the electric power was ramped from 540 to 940 W/rod at a rate of 0.3 W/s/rod. The desired maximum bundle temperature of 2073 K was reached after about 1200 s. For the maximum oxide layer thickness at the withdrawn second corner rod the result of metallographic measurement was 470 µm. The first test rod failure was observed about 15 s before reflood initiation.

- Following a fast water injection to quickly fill the lower volume, reflooding of the bundle by water injection at 41 g/s (corresponds to effective 1.3 g/s/rod with consideration of shroud and corner rods) was initiated, and the electrical power was reduced to an average decay heat level of 2 W/cm. Shroud failure was detected a few seconds after reflood initiation. The bundle cooling to 400 K took about 300 s. The maximum oxide layer thickness at the third corner rod, withdrawn after the test, was 630 µm according to metallographic investigation.

- The maximum height of the 2-phase fluent was 550 mm, which was measured when the collapsed water front reached the elevation of ~600 mm.

- Post-test investigations of the bundle showed neither breakaway oxidation of M5® cladding nor melt relocation. Ten bundle cross sections between elevations 550 and 1150 mm were metallographically evaluated. Some melting of the cladding occurred at elevations between 900 and 1100 mm but the molten cladding material remained between pellets and external cladding oxide layer. The maximum oxide layer thickness obtained by averaging of data for 21 claddings was found at elevation 950 mm; corresponding value is 860 µm. The maximum averaged shroud oxide thickness of 590 µm was measured also at elevation 950 mm.

- The formation of an internal oxide layer (between pellet and molten cladding metal) was observed for some rods at elevations 900 and 1000 mm. The development of this layer was interpreted mainly as result of interaction between internal cladding surface and steam which penetrated through the cladding cracks, because no reduction of the ZrO_2 pellet material was observed. The maximum thickness of internal oxide layer reached 200 µm at elevation 1000 mm.

- The measured hydrogen production during the QUENCH-14 test was 34 g in the pre-oxidation and transient phases and 6 g in the quench phase being similar to those in QUENCH-06, i.e. 32 g and 4 g, respectively. Corresponding values for QUENCH-12 were 32 and 24 g. The reasons for such very different hydrogen production during the quench phase of tests QUENCH-12 and QUENCH-14 were (1) the degradation of oxide layers caused by the breakaway effect in case of the QUENCH-12 bundle and the absence of this effect for the QUENCH-14 bundle, and (2) oxidation of the melt relocated between rods during quenching of the QUENCH-12 bundle.

- The distributions of the hydrogen concentrations in the corner rods A, B, D (all Zircaloy-4) and C (E110), as well as in the cladding tube 16 were measured by means of neutron radiography. The Zircaloy-4 corner rods withdrawn at different stages of the test show that in this alloy the most hydrogen was absorbed during quenching. Strong differences in the hydrogen uptake were found for the different applied alloys. The high hydrogen uptake susceptibility of E110 due to the breakaway effect found in the QUENCH-12 test was confirmed. The hydrogen concentration in this alloy is about one order of magnitude higher than in Zry-4 or M5®.

The experiment QUENCH-15 with Zirlo™ cladding alloy concluded the QUENCH-ACM series in 2009. A final report is expected to be released in 2011. Further QUENCH bundle tests will investigate typical LOCA conditions of German NPPs (QUENCH-LOCA) and the formation and coolability of debris in the core (QUENCH-Debris).

Acknowledgments

The broad support needed for preparation, execution, and evaluation of the QUENCH-14 experiment is gratefully acknowledged. In particular, the authors would like to thank Mr. J. Moch for the assembly including instrumentation as well as disassembly and encapsulation of the test bundle, Mr. S. Horn for the preparation and measurement of hydrogen with the “Caldos” analyzer and the various support, Mrs. J. Laier for processing the test data, Mrs. U. Peters for the determination of extent of oxidation of the corner rods and the photographic documentation of the cross sections, Mr. L. Anselment for cutting the epoxied test bundle and shroud, Mrs. M. Heck for her detailed draft review.

The determination of the test protocol was based on numerous calculations with SCDAP/RELAP5 and SCDAPSIM performed by Drs. J. Birchley and T. Haste, Paul Scherrer Institute (PSI), Switzerland.

References

[1] J.M. Broughton, P. Kuan, and D.A. Petti, “A Scenario of the Three Mile Island Unit 2 Accident,” Nuclear Technology, 87, 34, 1989.

[2] P. Hofmann, S. Hagen, V. Noack, G. Schanz, L. Sepold, “Chemical-Physical Behavior of Light Water Reactor Core Components Tested under Severe Reactor Accident Conditions in the CORA Facility,” Nuclear Technology, vol. 118, 1997, p. 200.

[3] S. Hagen, P. Hofmann, V. Noack, L. Sepold, G. Schanz, G. Schumacher, “Comparison of the Quench Experiments CORA-12, CORA-13, CORA-17,” FZKA 5679, Forschungszentrum Karlsruhe, 1996.

[4] S.M. Modro and M.L. Carboneau, “The LP-FP-2 Severe Fuel Damage Scenario; Discussion of the Relative Influence of the Transient and Reflood Phase in Affecting the Final Condition of the Bundle,” OECD/LOFT Final Event, ISBN 92-64-03339-4, 1991, p. 388.

[5] B. Clement, N. Hanniet/Girault, G. Repetto, D. Jacquemain, A.V. Jones, M.P. Kissane, P. von der Hardt, “LWR Severe Accident Simulation: Synthesis of the Results and Interpretation of the First Phebus FP Experiment FPT0,” Nuclear Engineering and Design, 2003.

[6] L. Sepold, A. Miassoedov, G. Schanz, U. Stegmaier, M. Steinbrück, J. Stuckert, C. Homann, “Hydrogen Generation in Reflooding Experiments with LWR-type Rod Bundles (QUENCH Program),” Journal Nuclear Technology, Vol. 147, Aug. 2004, pp. 202-214.

[7] P. Hofmann, V. Noack, M.S. Veshchunov, A.V. Berdyshev, A.V. Boldyrev, L.V. Matweev, A.V. Palagin, V.E. Shestak, “Physico-Chemical Behavior of Zircaloy Fuel

Rod Cladding Tubes During LWR Severe Accident Reflood," FZKA 5846, Forschungszentrum Karlsruhe, 1997.

[8] P. Hofmann, A. Miassoedov, L. Steinbock, M. Steinbrück, A.V. Berdyshev, A.V. Boldyrev, A.V. Palagin, V.E. Shestak, M. Veshchunov, "Quench Behavior of Zircaloy Fuel Rod Cladding Tubes. Small-Scale Experiments and Modeling of the Quench Phenomena," FZKA 6208, Forschungszentrum Karlsruhe, 1999.

[9] J. Stuckert, M. Steinbrück, U. Stegmaier, "Single Rod Quench Tests with Zr-1Nb. Comparison with Zircaloy-4 Cladding Tests and Modelling," FZKA 6604, Forschungszentrum Karlsruhe, 2001.

[10] L. Sepold, W. Hering, G. Schanz, W. Scholtyssek, M. Steinbrück, J. Stuckert. Severe fuel damage experiments performed in the QUENCH facility with 21-rod bundles of LWR-type. Nuclear Engineering and Design, 237 (22), November 2007, p. 2157–2164.

[11] L. Sepold, W. Hering, C. Homann, A. Miassoedov, G. Schanz, U. Stegmaier, M. Steinbrück, H. Steiner, J. Stuckert, "Experimental and Computational Results of the QUENCH-06 Test (OECD ISP-45)," FZKA 6664, Forschungszentrum Karlsruhe, February 2004.

[12] J. Stuckert, J. Birchley, M. Grosse, T. Haste, L. Sepold, M. Steinbrück. Experimental and Post-Test Calculation Results of the Integral Reflood Test QUENCH-12 with a VVER-type Bundle. Annals of Nuclear Energy, 36 (2009), 183-192.

[13] M. Steinbrück, Oxidation of Zirconium Alloys in Oxygen at High Temperatures up to 1600°C, Oxid. Met. 70 (2008), 317-329

[14] M. Große, Comparison of the high-temperature steam oxidation kinetics of advanced cladding materials, Nucl. Technol. 170 (2010), 272-279

[15] M. Grosse, E. Lehmann, P. Vontobel, M. Steinbrueck. Nucl. Instr. & Methods in Phys. Res. A 566 (2006), 739.

[16] G. Kühne, G. Frei, E. Lehmann, P. Vontobel. Nucl. Instr. & Meth. in Phys. Res. A 542 (1-3) (2005), 264.

Table 1: QUENCH Test Matrix

Test	Quench medium and injection rate	Temp. at onset of flooding[1)]	Max. ZrO_2 before transient[2)]	Max. ZrO_2 (*X s*) before flooding[2)]	Posttest average ZrO_2 thickness[3)]	H_2 production before / during cooldown	Remarks, objectives
QUENCH-00 Oct. 9 - 16, 97	Water 80 g/s	≈ 1800 K			completely oxidized		Commissioning tests.
QUENCH-01 Febr 26, 98	Water 52 g/s	≈ 1830 K	312 µm		500 µm at 913 mm	36 / 3	COBE Project; partial fragmentation of pre-oxidized cladding.
QUENCH-02 July 7, 98	Water 47 g/s	≈ 2400 K			completely oxidized	20 / 140	COBE Project; no additional pre-oxidation; quenching from high temperatures.
QUENCH-03 January 20, 99	Water 40 g/s	≈ 2350 K			completely oxidized	18 / 120	No additional pre-oxidation, quenching from high temperatures.
QUENCH-04 June 30, 99	Steam 50 g/s	≈ 2160 K	82 µm		280 µm	10 / 2	Cool-down behavior of slightly pre-oxidized cladding by cold steam injection.
QUENCH-05 March 29, 2000	Steam 48 g/s	≈ 2020 K	160 µm		420 µm	25 / 2	Cool-down behavior of pre-oxidized cladding by cold steam injection.
QUENCH-06 Dec 13 2000	Water 42 g/s	≈ 2060 K	207 µm[5)]	300 µm, (60 s), SVECHA modeling	670 µm[4)]	32 / 4	OECD-ISP 45; prediction of H_2 source term by different code systems.
QUENCH-07 July 25, 2001	Steam 15 g/s	≈ 2100 K	230 µm		completely oxidized	66 / 120	COLOSS Project; impact of B_4C absorber rod failure on H_2, CO, CO_2, and CH_4 generation.

Test	Quench medium and injection rate	Temp. at onset of flooding[1)]	Max. ZrO_2 before transient[2)]	Max. ZrO_2 (X s) before flooding[2)]	Posttest average ZrO_2 thickness[3)]	H_2 production before / during cooldown	Remarks, objectives
QUENCH-09 July 3, 2002	Steam 49 g/s	≈ 2100 K			completely oxidized	60 / 400	As QUENCH-07, steam-starved conditions prior to cooldown.
QUENCH-08 July 24, 2003	Steam 15 g/s	≈ 2090 K	274 µm		completely oxidized	46 / 38	As QUENCH-07, no absorber rod
QUENCH-10 July 21, 2004	Water 50 g/s	≈ 2200 K	514 µm	613 µm (at 850 mm)	completely oxidized	48 / 5	LACOMERA Project; Air ingress.
QUENCH-11 Dec 08, 2005	Water 18 g/s	≈ 2040 K		170 µm	completely oxidized	9 / 132	LACOMERA Project; Boil-off.
QUENCH-12 Sept 27, 2006	Water 48 g/s	≈ 2100 K	160 µm, breakaway	300 µm, (110 s), breakaway	completely oxidized	34 / 24	ISTC Project No. 1648.2; VVER bundle with E110 claddings
QUENCH-13 Nov 7, 2007	Water 52 g/s	≈ 1820 K		400 µm, after AgInCd rod failure	750 µm	42 / 1	SARNET; impact of AgInCd absorber rod failure on aerosol generation.
QUENCH-14 July 2, 2008	Water 41 g/s	≈ 2100 K	170 µm[6)]	470 µm[6)], (30 s)	840 µm[4)]	34/6	ACM series: M5® cladding

1) Maximum measured bundle temperature at 950 mm elevation.

2) Measured at the withdrawn corner rod at 950 mm elevation.

3) Measured posttest at the bundle elevation of maximum temperature, i.e. 950 mm.

4) Some claddings were completely oxidized at 950 mm elevation.

5) Oxide thickness during transient phase.

6) Zircaloy-4 corner rods (no M5® values available).

Revised: February 2010

Table 2: Design characteristics of the QUENCH-14 test bundle

Bundle type		PWR
Bundle size		21 rods
Number	heated / unheated	20 / 1
Pitch		14.3 mm
Coolant channel area		30.1 cm^2
Hydraulic diameter		11.6 mm
Rod outside diameter		10.75 mm
Cladding material		M5® (Zr-1Nb-0.125O)*
Cladding thickness		0.725 mm
Rod length	heated rod (levels) unheated rod (levels)	2480 mm (-690 to 1790 mm) 2842 mm (-827 to 2015 mm, incl. extension piece)
Internal rod pressure (gas)		0.22 MPa abs. (Kr)
Heater material		Tungsten (W)
Heater length		1024 mm
Heater diameter		6 mm
Annular pellet	material heated rod unheated rod	ZrO_2;Y_2O_3-stabilized ∅ 9.15/6.15 mm; L=11 mm ∅ 9.15/2.5 mm; L=11 mm
Pellet stack	heated rod unheated rod	0 mm to ~1020 mm 0 mm to 1553 mm
Corner rod (4)	material instrumented (A, C) not instrumented (B, D)	Rod A, B, D: Zircaloy-4; rod C: E110 tube ∅ 6x0.9 (bottom: -1140 mm) rod ∅ 6 mm (top: +1300 mm) rod ∅ 6 mm (-1350 to +1155 mm)
Grid spacer	material length sheet thickness elevation of lower edge	Zircaloy-4, Inconel 718 Zry 42 mm, Inc 38 mm 0.5 mm Inc: -200 mm; Zry: 50, 550, 1050, 1410 mm
Shroud	material wall thickness outside diameter length (extension)	Zircaloy-4 3.25 mm 86.50 mm 1600 mm (-300 to 1300 mm)
Shroud insulation	material insulation thickness elevation	ZrO_2 fiber ~ 37 mm -300 to ~1000 mm
Molybdenum-copper electrodes	length of upper electrodes length of lower electrodes diameter of electrodes: prior to coating after coating with ZrO_2	766 mm (576 Mo, 190 mm Cu) 690 mm (300 Mo, 390 mm Cu) 8.6 mm 9.0 mm
Cooling jacket	Material: inner/outer tube inner tube outer tube	Inconel 600 (2.4816) / SS (1.4571) ∅ 158.3 / 168.3 mm ∅ 181.7 / 193.7 mm

*) AREVA product

Table 3: QUENCH-14; Electrical resistances of rods [mΩ] at 20 °C

Internal circuit with 8 rods

rod	2	3	4	5	6	7	8	9	Ave-rage	8 rods parallel
pre-test	3.1	3.0	3.2	3.0	2.9	3.2	3.3	3.3	3.1	0.39
post-test	3.3	3.3	3.3	3.3	3.3	3.3	3.4	3.3	3.3	0.41

Note: Measured values include the resistance of slide contacts R_s=0.73 mΩ

External circuit with 12 rods

rod	10	11	12	13	14	15	16	17	18	19	20	21	ave-rage	12 rods parallel
pre-test	3.8	3.4	3.3	3.3	3.6	3.3	3.7	3.2	3.2	3.3	3.2	5.1	3.5	0.29
post-test	3.3	3.3	3.2	3.3	3.3	3.3	3.4	3.3	3.2	3.2	3.3	3.2	3.3	0.27

Note: Measured values include the resistance of slide contacts R_s=0.75 mΩ

Each circuit connected to the DC generator with 4 parallel bonded cables. The resistance of each cable is R_c=1.2 mΩ. Therefore, the external (outside) resistance corresponding to each heated rod (indicated by SCDAP/RELAP as **fxwid**) is $R_{ie}=R_s+8*R_c/4$=3.13 mΩ for the inner rod group and $R_{oe}=R_s+12*R_c/4$=4.35 mΩ for the outer rod group.

Table 4: Diameters of the materials used for the QUENCH high-temperature thermocouples [mm]

Material	As-received	Final
W/Re wires	0.254	
HfO_2 insulation OD (see drawing below)	1.1	
Ta tube OD / ID	2.15 / 1.65	1.4 / 0.94
Zr tube OD / ID	2.5 / 1.65 ± 0.05	2.2-2.3 / ~1.4

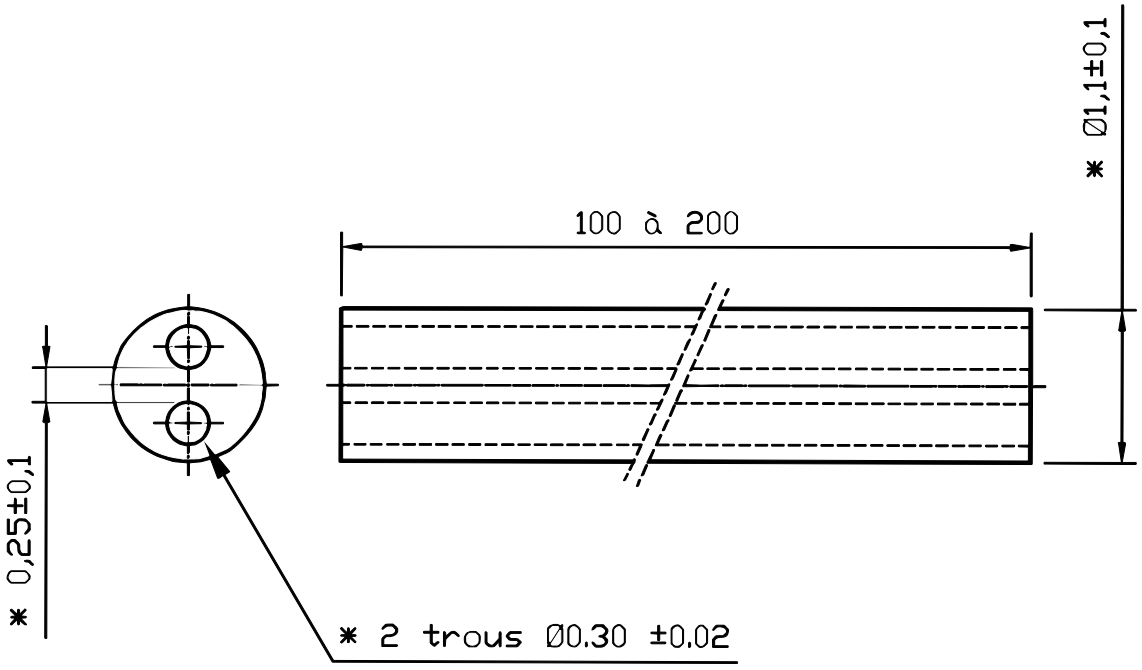

Table 5: Main characteristics of the HfO_2 thermocouple insulator

Property	Data
Composition of basic material	99 % HfO_2
Melting temperature	2840 °C
Max. use temperature	2500 °C
Density	8.4 g/cm^3
Thermal conductivity at 20-1000 °C	1.14 W/m K
Linear expansion	5.8 x 10^{-6}/K

According to Saint-Gobain ceramics, 1997

Table 6: Main characteristics of the ZrO_2 pellet material, yttria-stabilized (type FZY)

Property		Data
Density		5.5-5.8 g/cm^3
Open porosity		0
Mean grain size		50 µm
Hardness (Knoop, 100 g)		17000 N/mm^2
Yield strength under compression		2000 N/mm^2
Bending strength		350 N/mm^2
Elastic modulus		165 GPa
Specific heat at 20 °C		400 J/kg K
Thermal conductivity at 100 °C		2.5 W/m K
Linear expansion, 20-1000 °C		10.5 x 10^{-6}/K
Specific electric resistance	at 20 °C	10^{10} Ω cm
	at 500 °C	5000 Ω cm
	at 1000 °C	50 Ω cm

According to FRIATEC, Mannheim

Table 7: Properties* of zirconia fiber insulating boards

Chemical composition

Oxide	ZrO_2	Y_2O_3	HfO_2	TiO_2	SiO_2	CaO	MgO	Fe_2O_3	Al_2O_3	Na_2O
typical wt%	88	10	2	0.14	0.12	0.09	0.03	0.04	0.01	0.01

Physical properties

bulk density	porosity	shrinkage		thermal expansion coefficient @298-1453K	melting point	max service temperature	flexural strength	compressive strength @10% compression
		(1 hour @1925 K)	(24 hours @1925 K)					
g/cm³	%	%		1/K	K	K	MPa	MPa
0.48	92	1.2	2.8	$10.7*10^{-6}$	2866	2500	0.59	0.29

Thermal conductivity

temperature, K	673	1073	1373	1673	1923
conductivity, W/(m*K)	0.08	0.11	0.14	0.19	0.24

Specific heat capacity

temperature, K	366	2644
specific heat capacity, J/(kg*K)	544	754

**According to specifications of manufacturer ZIRCAR PRODUCTS on the ZYFB3 material*

Table 8: List of instrumentation for the QUENCH-14 test

Chan	Designation	Instrument, location	Unit
0	**TFS 18/17**	TC (W/Re), surface of fuel rod simulator 18, group 4, 1350 mm	K
1	**TFS 13/17**	TC (W/Re), surface of fuel rod simulator 13, group 4, 1350 mm	K
2	**TFS 7/16**	TC (W/Re), surface of fuel rod simulator 7, group 5, 1250 mm	K
3	**TFS 3/16**	TC (W/Re), surface of fuel rod simulator 3, group 5, 1250 mm	K
4	**TFS 15/15**	TC (W/Re), surface of fuel rod simulator 15, group 5, 1150 mm	K
5	**TSH 16/180**	TC (W/Re), shroud outer surface, 1250 mm, 291°, behind shroud insulation	K
6		TC (W/Re), Reserve	K
7	**TFS 20/14**	TC (W/Re), surface of fuel rod simulator 20, group 5, 1050 mm	K
8	**TFS 14/14**	TC (W/Re), surface of fuel rod simulator 14, group 5, 1050 mm	K
9	**TFS 6/14**	TC (W/Re), surface of fuel rod simulator 6, group 2, 1050 mm	K
10	**TFS 2/14**	TC (W/Re), surface of fuel rod simulator 2, group 2, 1050 mm	K
11	**TFS 19/13**	TC (W/Re), surface of fuel rod simulator 19, group 4, 950 mm	K
12	**TIT A/13**	TC (W/Re), center line of corner rod A, 950 mm	K
13	**TFS 11/13**	TC (W/Re), surface of fuel rod simulator 11, group 5, 950 mm	K
14	**TFS 8/13**	TC (W/Re), surface of fuel rod simulator 8, group 2, 950 mm	K
15	**TFS 4/13**	TC (W/Re), surface of fuel rod simulator 4, group 2, 950 mm	K
16	**TFS 9/15**	TC (W/Re), surface of fuel rod simulator 9, group 3, 1150 mm	K
17	**TSH 15/0**	TC (W/Re), shroud outer surface, 1150 mm, 21°	K
18	**TSH 15/180**	TC (W/Re), shroud outer surface, 1150 mm, 201°	K
19	**TSH 16/0**	TC (W/Re), shroud outer surface, 1250 mm, 21°, behind shroud insulation	
20	**TSH 14/270**	TC (W/Re), shroud outer surface, 1050 mm, 289°, behind shroud insulation	K
21	**TSH 14/90**	TC (W/Re), shroud outer surface, 1050 mm, 11°, behind shroud insulation	K
22	TFS 20/9	TC (NiCr/Ni), surface of fuel rod simulator 20, 550 mm	K
23	TFS 17/9	TC (NiCr/Ni), surface of fuel rod simulator 17, 550 mm	K
24	F 902	Reserve	
25	Fm 401	Argon gas mass flow rate, (20 mA)	g/s
26..32		TC (W/Re), Reserve	K
33	**TCRC 13**	TC (W/Re), centerline of central rod, 950 mm	K
34		Reserve	K
35	TSH 4/270	TC (NiCr/Ni), shroud outer surface, 50 mm, 291°	K
36	TSH 5/0	TC (NiCr/Ni), shroud outer surface, 150 mm, 21°	K

Chan	Designation	Instrument, location	Unit
37	**TFS 5/15**	TC (W/Re), surface of fuel rod simulator 5, 1150 mm	K
38	TFS 11/9	TC (NiCr/Ni), surface of fuel rod simulator 11, group 5, 550 mm	K
39	TFS 8/9	TC (NiCr/Ni), surface of fuel rod simulator 8, group 2, 550 mm	K
40	**TCRC 12**	TC (W/Re), centerline of central rod, 850 mm	
41	**TFS 6/10**	TC (W/Re), surface of fuel rod simulator 6, 650 mm	K
42	TFS 4/9	TC (NiCr/Ni), surface of fuel rod simulator 4, group 2, 550 mm	K
43	TCR 9	TC (NiCr/Ni), surface of fuel rod simulator 1, 550 mm	K
44	TFS 13/8	TC (NiCr/Ni), surface of fuel rod simulator 12, group 4, 450 mm	K
45	TFS 9/8	TC (NiCr/Ni), surface of fuel rod simulator 9, group 3, 450 mm	K
46	TFS 4/8	TC (NiCr/Ni), surface of fuel rod simulator 4, group 2, 450 mm	K
47	**TFS 17/13**	TC (W/Re), surface of fuel rod simulator 17, 950 mm	K
48	**TFS 2/10**	TC (W/Re), surface of fuel rod simulator 2, 650 mm	K
49	**TSH 11/180**	TC (W/Re), shroud outer surface, 750 mm, behind shroud insulation	K
50	**TIT C/12**	TC (W/Re), center line of corner rod C, 850 mm	
51		TC (W/Re), Reserve	K
52	**TFS 3/12**	TC (W/Re), surface of fuel rod simulator 3, 850 mm	K
53	**TSH 12/180**	TC (W/Re), shroud outer surface, 850 mm, behind shroud insulation	K
54	**TSH 11/0**	TC (W/Re), shroud outer surface, 750 mm, 21°, behind shroud insulation	K
55	**TSH 13/90**	TC (W/Re), shroud outer surface, 950 mm, behind shroud insulation	K
56	**TFS 9/11**	TC (W/Re) surface of fuel rod simulator 9, 750 mm	K
57	**TFS 5/11**	TC (W/Re) surface of fuel rod simulator 5, 750 mm	K
58	TSH 6/270	TC (NiCr/Ni), shroud outer surface, 250 mm, 281°	K
59	**TFS 10/12**	TC (W/Re) surface of fuel rod simulator 10, group 4, 850 mm	K
60		TC (W/Re) Reserve	K
61	T 206	Temperature upstream steam flow instrument location 1 g/s	K
62	P 206	Reserve	
63	F 206	Reserve	
64	T 402 b	TC (NiCr/Ni), Ar super heater	K
65	**TFS 10/12**	TC (W/Re), surface of fuel rod simulator 10, 850 mm	K
66	**TSH 13/270**	TC (W/Re), shroud outer surface, 950 mm, behind shroud insulation	K
67	**TSH 12/0**	TC (W/Re) shroud outer surface, 850 mm, 11°, behind shroud insulation	K

Chan	Designation	Instrument, location	Unit
68	T 512	TC (NiCr/Ni), gas temperature bundle outlet	K
69		TC (W/Re) Reserve	K
70	**TFS 7/12**	TC (W/Re) surface of fuel rod simulator 7, group 3, 850 mm	K
71	*Ref. T01*	*Temperature of measuring crate 1 (reference temperature)*	K
72	TFS 12/7	TC (NiCr/Ni), surface of fuel rod simulator 12, group 5, 350 mm	K
73	TCR 7	TC (NiCr/Ni), surface of fuel rod simulator 1, 350 mm	K
74	TFS 15/6	TC (NiCr/Ni), surface of fuel rod simulator 15, group 5, 250 mm	K
75	TFS 9/6	TC (NiCr/Ni), surface of fuel rod simulator 9, group 3, 250 mm	K
76	TFS 17/5	TC (NiCr/Ni), surface of fuel rod simulator 17, group 4, 150 mm	K
77	TFS 2/5	TC (NiCr/Ni), surface of fuel rod simulator 2, group 2, 150 mm	K
78	TSH 10/90	TC (NiCr/Ni), shroud outer surface, 650 mm,109°	K
79	TSH 10/270	TC (NiCr/Ni), shroud outer surface, 650 mm, 289°	K
80	TSH 9/0	TC (NiCr/Ni), shroud outer surface, 550 mm, 11°	K
81	TSH 9/180	TC (NiCr/Ni), shroud outer surface, 550 mm, 191°	K
82	TSH 8/90	TC (NiCr/Ni), shroud outer surface, 450 mm, 109°	K
83	TSH 8/270	TC (NiCr/Ni), shroud outer surface, 450 mm, 289°	K
84	TSH 7/0	TC (NiCr/Ni), shroud outer surface, 350 mm, 11°	K
85	TSH 7/180	TC (NiCr/Ni), shroud outer surface, 350 mm, 191°	K
86	TSH 6/90	TC (NiCr/Ni), shroud outer surface, 250 mm, 109°	K
87	TSH 5/180	TC (NiCr/Ni),	K
88	TSH 4/90	TC (NiCr/Ni), shroud outer surface, 50 mm, 109°	K
89	TSH 3/180	TC (NiCr/Ni), shroud outer surface, -50 mm, 191°	K
90	TSH 1/0	TC (NiCr/Ni), shroud outer surface, -250 mm, 11°	K
91	TCI 9/270	TC (NiCr/Ni), cooling jacket inner tube wall, 550 mm, 270°	K
92	TCI 10/270	TC (NiCr/Ni), cooling jacket inner tube wall, 650 mm, 270°	K
93	TCI 11/270	TC (NiCr/Ni), cooling jacket inner tube wall, 750 mm, 270°	K
94	TCI 13/270	TC (NiCr/Ni), cooling jacket inner tube wall, 950 mm, 270°	K
95	TFS 20/4	TC (NiCr/Ni), surface of fuel rod simulator 20, group 5, 50 mm	K
96	TCI 1/180	TC (NiCr/Ni), cooling jacket inner tube wall, -250 mm, 180°	K
97	TCI 4/180	TC (NiCr/Ni), cooling jacket inner tube wall, 50 mm, 180°	K
98	TCI 7/180	TC (NiCr/Ni), cooling jacket inner tube wall, 350 mm, 180°	K
99	TCI 11/180	TC (NiCr/Ni), cooling jacket inner tube wall, 750 mm, 180°	K
100	TCI 12/180	TC (NiCr/Ni), cooling jacket inner tube wall, 850 mm, 180°	K
101	TCI 13/180	TC (NiCr/Ni), cooling jacket inner tube wall, 950 mm, 180°	K
102	TCI 15/180	TC (NiCr/Ni), cooling jacket inner tube wall, 1150 mm, 180°	K

Chan	Designation	Instrument, location	Unit
103	T 002	TC (NiCr/Ni), cooling water, inlet of off-gas tube	K
104	TCI 9/90	TC (NiCr/Ni), cooling jacket inner tube wall, 550 mm, 90°	K
105	TCI 10/90	TC (NiCr/Ni), cooling jacket inner tube wall, 650 mm, 90°	K
106	TCI 11/90	TC (NiCr/Ni), cooling jacket inner tube wall, 750 mm, 90°	K
107	TCI 13/90	TC (NiCr/Ni), cooling jacket inner tube wall, 950 mm, 90°	K
108	TFS 12/4	TC (NiCr/Ni), surface of fuel rod simulator 12, group 5, 50 mm	K
109	TCI 1/0	TC (NiCr/Ni), cooling jacket inner tube wall, -250 mm, 0°	K
110	TCI 4/0	TC (NiCr/Ni), cooling jacket inner tube wall, 50 mm, 0°	K
111	TCI 7/0	TC (NiCr/Ni), cooling jacket inner tube wall, 350 mm, 0°	K
112	TCI 11/0	TC (NiCr/Ni), cooling jacket inner tube wall, 750 mm, 0°	K
113	TCI 12/0	TC (NiCr/Ni), cooling jacket inner tube wall, 850 mm, 0°	K
114	TCI 13/0	TC (NiCr/Ni), cooling jacket inner tube wall, 950 mm, 0°	K
115	TCI 15/0	TC (NiCr/Ni), cooling jacket inner tube wall, 1150 mm, 0°	K
116	T 003	TC (NiCr/Ni), cooling water, outlet of off-gas tube	K
117	T 309	TC (NiCr/Ni), Ar bundle top	K
118	TFS 6/2	TC (NiCr/Ni), surface of fuel rod simulator 6, -150 mm	K
119	TFS 7/3	TC (NiCr/Ni), surface of fuel rod simulator 7, group 3, -50 mm	K
120	TCO 1/0	TC (NiCr/Ni), cooling jacket outer tube surface, -250 mm, 0°	K
121	TCO 7/0	TC (NiCr/Ni), cooling jacket outer tube surface, 350 mm, 0°	K
122	TCO 13/0	TC (NiCr/Ni), cooling jacket outer tube surface, 950 mm, 0°	K
123	T 601	Temperature off-gas, 2660 mm from test section outlet (flange)	K
124	T 513	Temperature bundle head top (wall)	K
125	T 514	Temperature bundle head, cooling water inlet	K
126	T 307	TC (NiCr/Ni), inner surface of inlet of off-gas pipe	K
127	TSH 2/90	TC (NiCr/Ni), shroud outer surface, -150 mm, 111°	K
128	T 104	Temperature quench water	K
129	T 201	Temperature steam generator heating pipe	K
130	TFS 4/1 F	TC (NiCr/Ni),, fluid temperature at fuel rod simulator 4, -250 mm	K
131	T 205	Temperature upstream steam flow instrument location 10 g/s	K
132	T 301A	Temperature downstream superheater	K
133	T 302	Temperature superheater heating pipe	K
134	T 303	Temperature upstream total flow instrument location	K
135	T 401	Temperature upstream Ar flow instrument (orifice) location	K
136	T 403	Temperature of Ar at inlet cooling jacket	K

Chan	Designation	Instrument, location	Unit
137	T 404	Temperature of Ar at outlet cooling jacket	K
138	T 501	Temperature in containment (near from bundle head)	K
139	T 502	Temperature at outer surface of containment, 0°, 2.4 m	K
140	T 503	Temperature at outer surface of containment, 270°, 2.2 m	K
141	T 504	Temperature at outer surface of containment, 270°, 3.2 m	K
142	T 505	Temperature at outer surface of containment, 90°, 3.2 m	K
143	T 506	Temperature at outer surface of containment, 270°, 3.6 m	K
144	T 507	Temperature at outer surface of containment, 90°, 3.6 m	K
145	T 508	Temperature at outer surface of containment, 180°, 4.0 m	K
146	T 310	TC (NiCr/Ni), aerosol extraction tube in off-gas pipe	K
147	T 510	Temperature at outer surface of containment, 270°, 4.4 m	K
148	T 511	Gas temperature at bundle inlet	K
149	T 901	Temperature upstream off-gas flow instrument F 901	K
150	T 304	Temperature of pipe surface at valve V 302	K
151	*Ref. T02*	*Temperature of measuring crate 2 (reference temperature)*	K
152	P 201	Pressure steam generator	bar
153	P 204	Reserve	
154	P 205	Pressure at steam flow instrument location 10 g/s	bar
155	P 303	Pressure upstream total flow instrument (orifice) location	bar
156	P 401	Pressure upstream gas flow instrument location	bar
157	P 511	Pressure at bundle inlet	bar
158	P 512	Pressure at bundle outlet	bar
159	P 601	Pressure upstream off-gas flow instrument (orifice) F 601	bar
160	P 901	Pressure He supply for unheated rods	bar
161	L 201	Liquid level steam generator	mm
162	L 501	Liquid level quench water	mm
163	L 701	Liquid level condensation vessel	mm
164	Q 901	H_2 concentration, off-gas (Caldos)	$\%H_2$
165	P 411	Pressure Kr supply for heated rods	bar
166	P 403	Pressure Ar cooling of cooling jacket	bar
167	P 406	Pressure insulation shroud/cooling jacket	bar
168	Fm 104	Flow rate quench water	g/s
169	F 204	Reserve	
170	Fm 205	Flow rate steam 10 g/s	g/s
171	F 303	Flow rate at bundle inlet (steam + argon), orifice	mbar

Chan	Designation	Instrument, location	Unit
172	F 401	Reserve	
173	Fm 403	Flow rate cooling gas	g/s
174	F 601	Flow rate off-gas (orifice), 2000 mm from test section outlet (flange)	mbar
175	Fm 406	Flow rate argon into room between shroud and cooling jacket	g/s
176	E 201	Electric current steam generator	A
177	E 301	Electric current superheater	A
178	E 501	Electric current inner ring of fuel rod simulators	A
179	E 502	Electric current outer ring of fuel rod simulators	A
180	E 503	Electric voltage inner ring of fuel rod simulators	V
181	E 504	Electric voltage outer ring of fuel rod simulators	V
182	Hub_V302	Gas supply valve lift	%
183	*Ref. T03*	*Temperature of buffer amplifier (reference temperature)*	K
184….. 199		Binary inputs	
200….. 215		Analog outputs	
250	E 505	Electric power inner ring of fuel rod simulators	W
251	E 506	Electric power outer ring of fuel rod simulators	W
252	EP	Gross electrical power	kW

Indications:

TFS – high-temperature TC at the rod surface,

TFS - low-temperature TC at the rod surface;

TCR – low-temperature TC at the rod surface;

TSH - high-temperature TC at outer surface of shroud;

TSH - low-temperature TC at outer surface of shroud;

[ ] - gauge outside of containment.

Groups of the rods:

group 1: rod 1 (central unheated rod);
group 2: rods 2, 4, 6, 8 (first ring of the heated rods);
group 3: rods 3, 5, 7, 9 (first ring of the heated rods);
group 4: rods 10, 13, 16, 19 (second ring of the heated rods);
group 5: rods 11, 12, 14, 15, 17, 18, 20, 21 (second ring of the heated rods).

Table 9: QUENCH-14; Bundle thermocouples positions

Elevation, mm	-250	-150	-50	50	150	250	350	450	550	650	750	850	950	1050	1150	1250	1350
Rod/Elevation	1	2	3	4	5	6	7	8	9	10	11	12	13	14	15	16	17
1							N		N			W	W				
2					N					W				W			
3												W				W	
4	N							N	N				W				
5											W				W		
6		N								W				W			
7			N									W				W	
8									N				W				
9						N		N			W				W		
10												W					
11									N				W				
12				N			N										
13								N									W
14														W			
15						N									W		
16																	
17					N				N				W				
18																	W
19													W				
20				N					N					W			
21																	
Number per elevation	1	1	1	2	2	2	2	3	6	2	2	3+1	5+1	4	3	2	2

TCs to bundle bottom

TCs to bundle top (16 W/Re surface + 2 W/Re internal)

	Heated rods (20)
	Unheated rods (1)
N	NiCr/Ni (20 TCs)
W	W/Re (23 TCs)
W	internal TC (2 TCs)

Table 10: QUENCH-14; Failure of thermocouples

Thermocouple	Elevation [mm]	Time at failure [s]	Failure temperature [K]
TFS 4/13	950	6737	1538.3
TFS 8/13	950	6866	1633.9
TFS 11/13	950	6945	1556.5
TFS 3/12	850	7030	1499.9
TFS 2/14	1050	7046	1609.6
TFS 9/15	1150	7187	1456.9
TFS 6/14	1050	7120	1670
TFS 20/14	1050	7299	1590
TFS 7/12	850	7362	352.8
TFS 19/13	950	7397	305.2

Table 11: QUENCH-14; Water/steam balance

Accumulated mass of water [g]	
Total steam injected (Fm 205)	22320
Total quench water injected (F 104)	15391
Quench water from fast injection system	4000
Total used water	**41711**
Condensed water collected (L 701)*: 2128.9 mm	30443
Water/steam consumed by Zr oxidation (40 g H_2)	360
Water found posttest in the test bundle	5740
Water found posttest retained in the ZrO_2 fiber insulation**	4614
Water found posttest in the annulus of the upper plenum	450
Total water collected posttest as condensate	**41607**

*) water column of 1 mm corresponds to 14.3 g

**) posttest insulation weight (between -300 mm and 1000 mm): 13614 g; weight of the dry insulation (10 annuli): 10 x 900 g = 9000 g

Table 12: QUENCH-14; Sequence of events

Time [s]	Event
02.07.2008 0 (11:16:21 h)	Start data recording, TCRC 13: 895 K, TIT A/1 3: 862 K, el. power at 3.86 kW.
1964	Plateau of electrical power of 10.8 kW reached. TCRC 13: 1408 K.
3110	Beginning of pre-oxidation phase. TIT A/13: 1473 K; TCRC 13: 1514 K.
5958	Corner rod B removed from bundle (reaction of TFS 5/11).
6010	Transient start with electrical power rate of 6.195 W/s.
7180	Start of moderate temperature escalation at elevations from 850 to 1350 mm.
7184	Corner rod D removed from bundle (reaction of TFS 9/11).
7200	First failure of fuel rod simulators (P 411 and MS).
7214	Initiation of fast water injection. Volume of injected water ~4 l.
7217	Start of quench water flow (F 104), water at -250 mm (TFS 4/1).
7215	Temperature maximum reached: TSH 13/270 = 2249 K; TCRC 13 = 2109 K.
7224	Shroud failure (F 406).
7236	Electrical power reduction from 18.7 kW.
7252	Electrical power at 3.9 kW (simulation of decay heat).
7472	Water level (L 501) at elevation 950 mm (approximate position of shroud breach).
7600	Quench pump shutoff. Maximum of water level reached: L 501= 1160 mm. Electrical power shutoff.
7646	Water level decreased to the shroud breach position of 950 mm.
11307	End of data recording.
	Corner rods A and C removed from bundle after test termination.
03.07.2008, 11:00 h	L 501 = 872 mm, L 701 = 639 mm.

Table 13: QUENCH-14; Cross sections of the test bundle (without shroud) for metallographic examination

Sample	Sample length (mm)	Axial position (mm)		Remarks
		bottom	top	
			546	Remainder
Cut	4	546	550	
QUE-14-1	20	550	**570**	Spacer 3, 570 mm polished
Cut	4	570	574	
QUE-14-a	56	574	630	
Cut	4	630	634	
QUE-14-2	16	**636**	650	636 mm polished
Cut	4	650	654	
QUE-14-b	76	654	730	
Cut	4	730	734	
QUE-14-3	16	734	**750**	TC elevation 11, 750 mm polished
Cut	4	750	754	
QUE-14-c	76	754	830	
Cut	4	830	834	
QUE-14-4	16	834	**850**	TC elevation 12, 850 mm polished
Cut	4	850	854	
QUE-14-d	42	854	896	
Cut	4	896	900	
QUE-14-9	30	**900**	930	900 mm polished
Cut	4	930	934	
QUE-14-5	16	934	**950**	TC elevation 13, 950 mm polished
Cut	4	950	954	
QUE-14-e	42	954	996	
Cut	4	996	1000	
QUE-14-10	30	**1000**	1030	1000 mm polished
Cut	4	1030	1034	
QUE-14-6	16	1034	**1050**	TC elevation 14, 1050 mm polished
Cut	4	1050	1054	
QUE-14-f	26	1054	1080	
Cut	4	1080	1084	
QUE-14-7	16	1084	**1100**	1100 mm polished
Cut	4	1100	1104	
QUE-14-g	26	1104	1130	
Cut	4	1030	1034	
QUE-14-8	16	1134	**1150**	TC elevation 15, 1150 mm polished
Cut	4	1150	1154	
		1154		Remainder

Table 14: QUENCH-14; Cross sections of the lower and upper shroud (two encapsulated pieces) for metallographic examination

Sample	Sample length (mm)	Axial position (mm)		Remarks
		bottom	top	
			630	Remainder
Cut	4	630	634	
QUE-14-18	16	634	**650**	TC elevation 10, 650 mm grinded
Cut	4	650	654	
QUE-14-z	76	654	730	
Cut	4	730	734	
QUE-14-12	16	734	**750**	TC elevation 11, 750 mm grinded
Cut	4	750	754	
QUE-14-u	76	754	830	
Cut	4	830	834	
QUE-14-13	16	834	**850**	TC elevation 12, 850 mm grinded
Cut	4	850	854	
QUE-14-v	26	854	880	
Cut	4	880	884	
QUE-14-11	16	884	**900**	900 mm polished
Cut	4	900	904	
QUE-14-16	21	904	**925**	925 mm grinded
Cut	4	925	929	
QUE-14-17	20	929	**950**	TC elevation 13, 950 mm grinded
Cut	4	950	954	
QUE-14-x	76	954	1030	
Cut	4	1030	1034	
QUE-14-14	16	1034	**1050**	TC elevation 14, 1050 mm grinded
Cut	4	1050	1054	
QUE-14-w	76	1054	1130	
Cut	4	1130	1134	
QUE-14-15	16	1134	**1150**	TC elevation 15, 1150 mm grinded
Cut	4	1150	1154	
		1154		Disposal

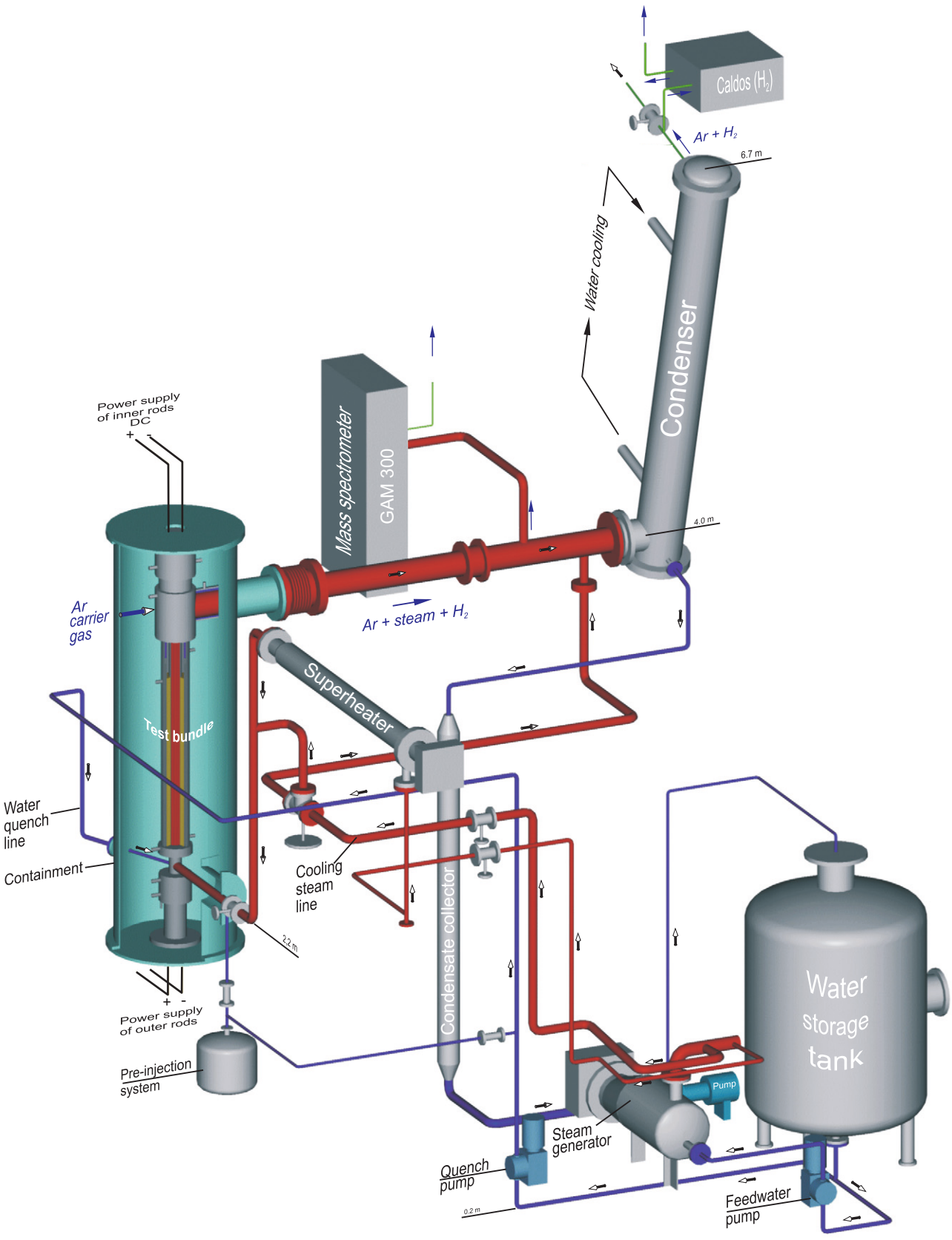

Fig 1-QUE14-Gesamtanlage.cdr
27.04.10 - IMF

Fig. 1: QUENCH Facility - Main components.

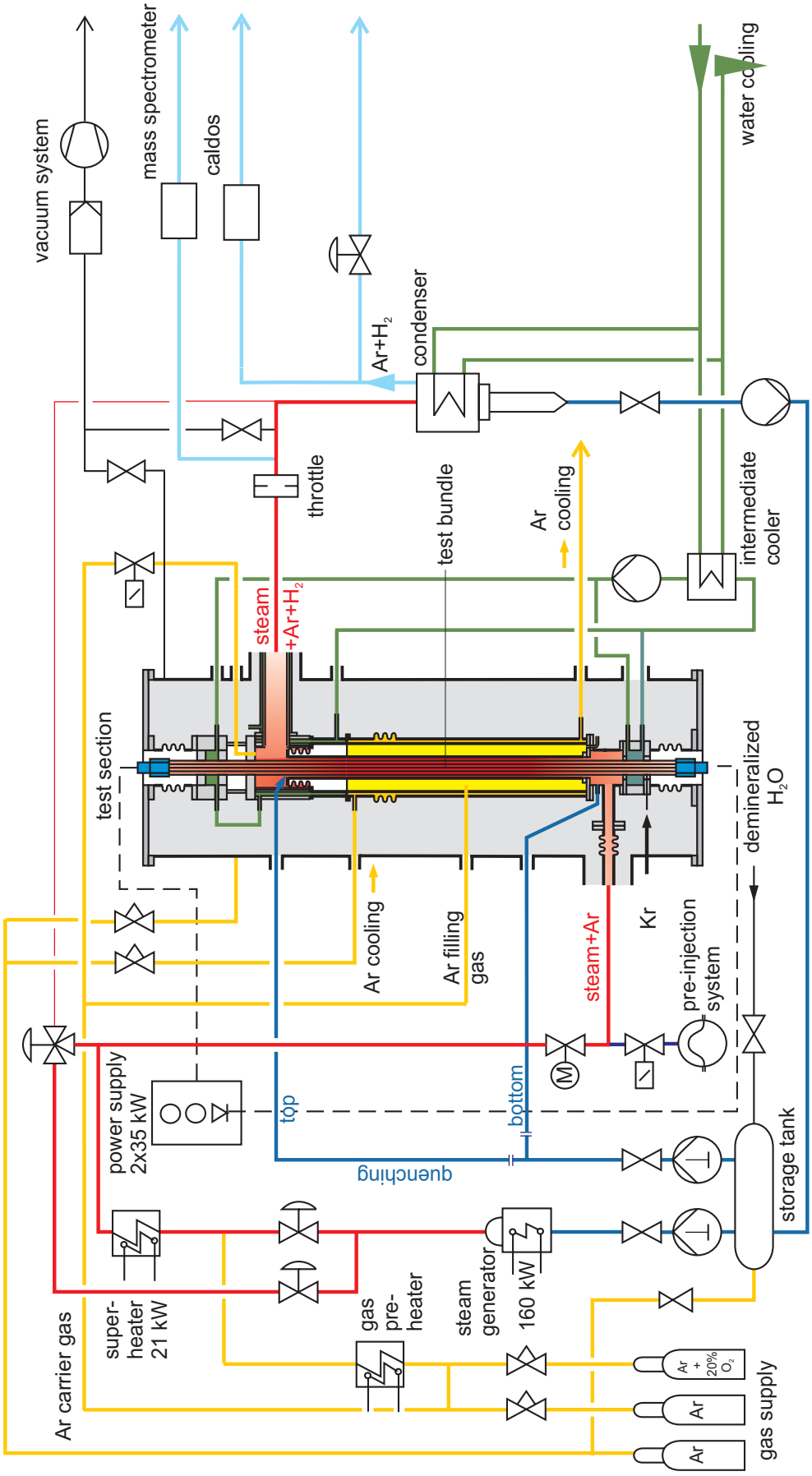

Fig.2-QUE14-Flow diagram.cdr
27.04.10 - IMF

Fig. 2: Flow diagram of the QUENCH test facility.

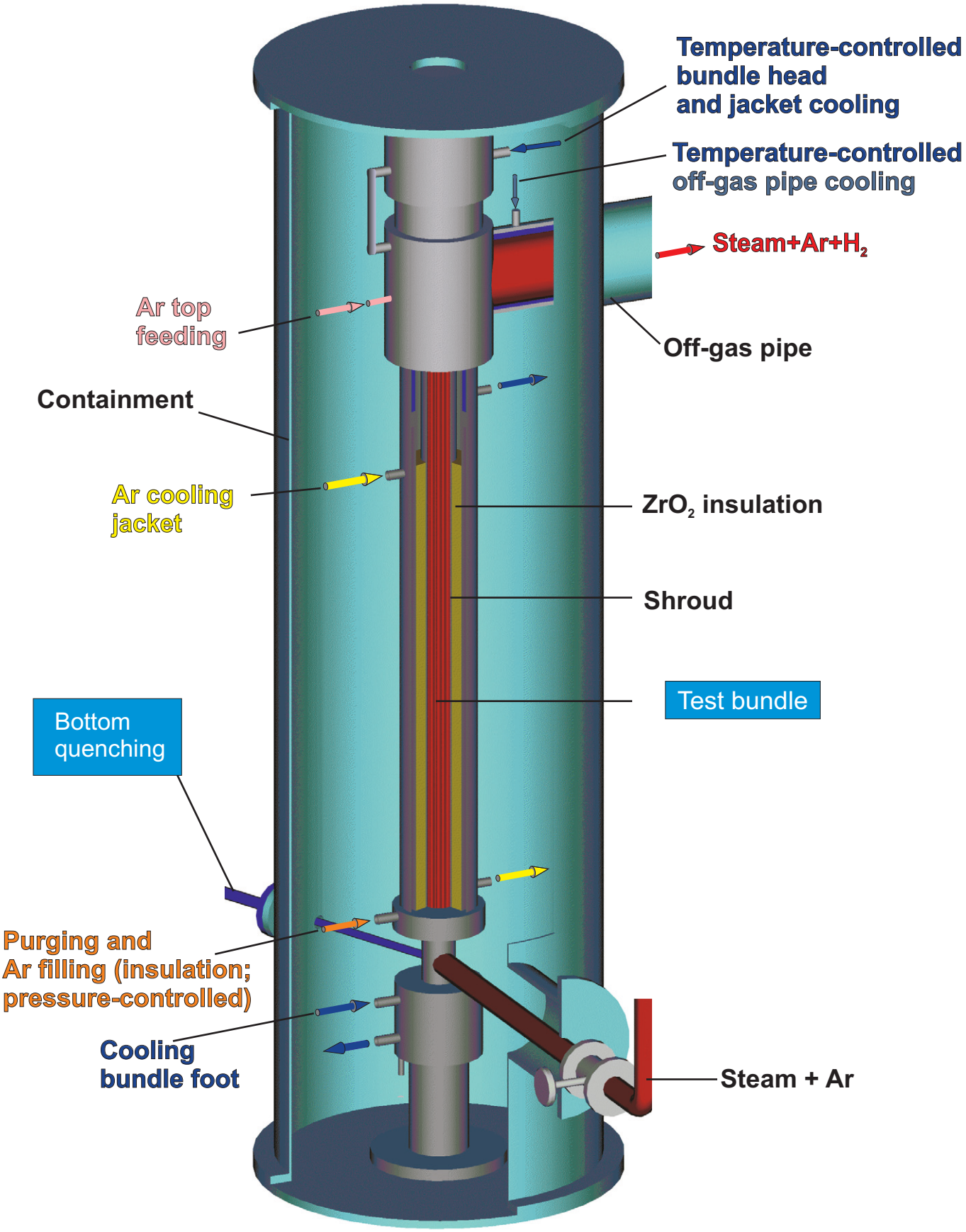

Fig. 3: QUENCH Facility; Containment and test section.

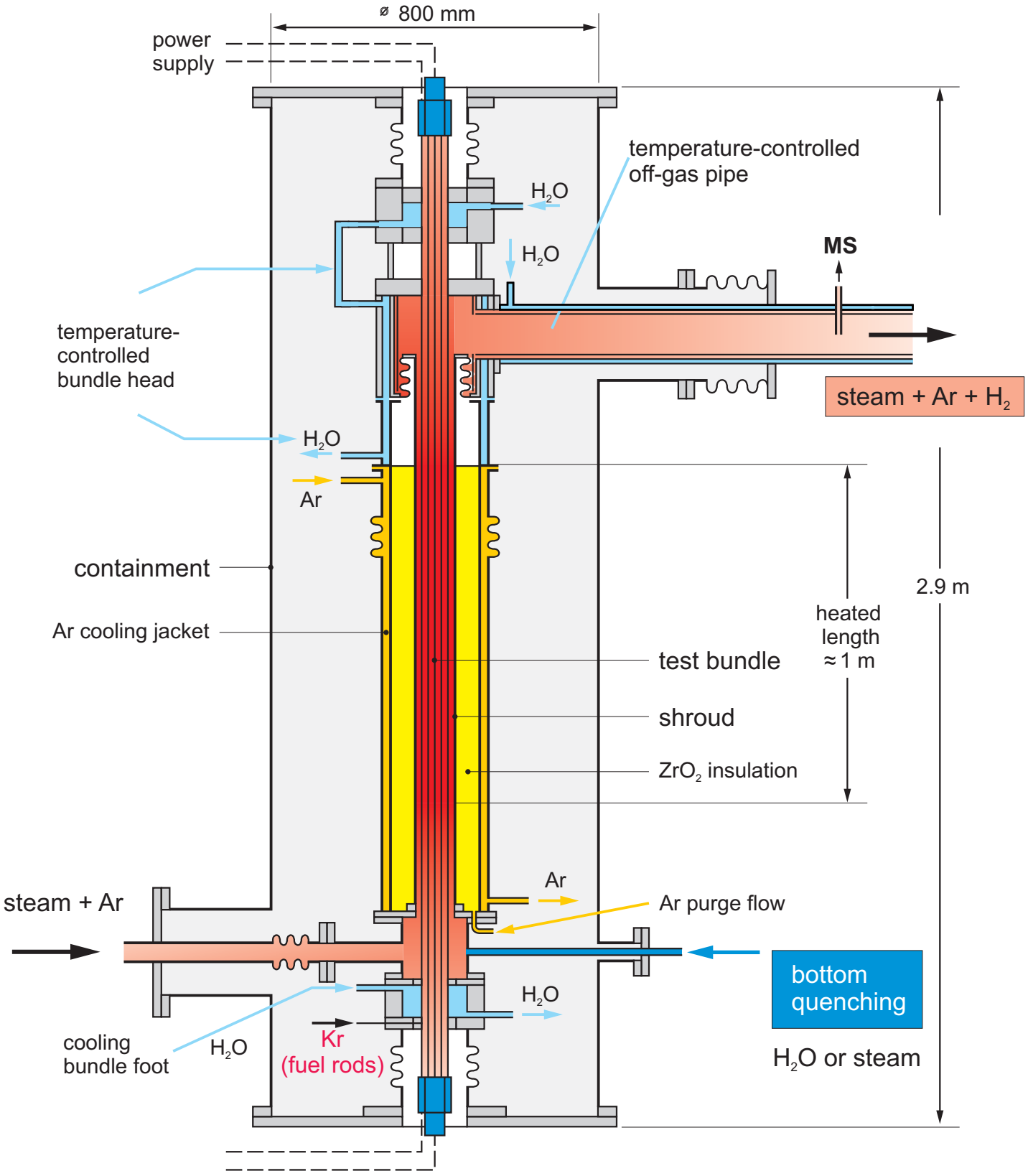

Fig. 4: QUENCH-14; Test section with flow lines.

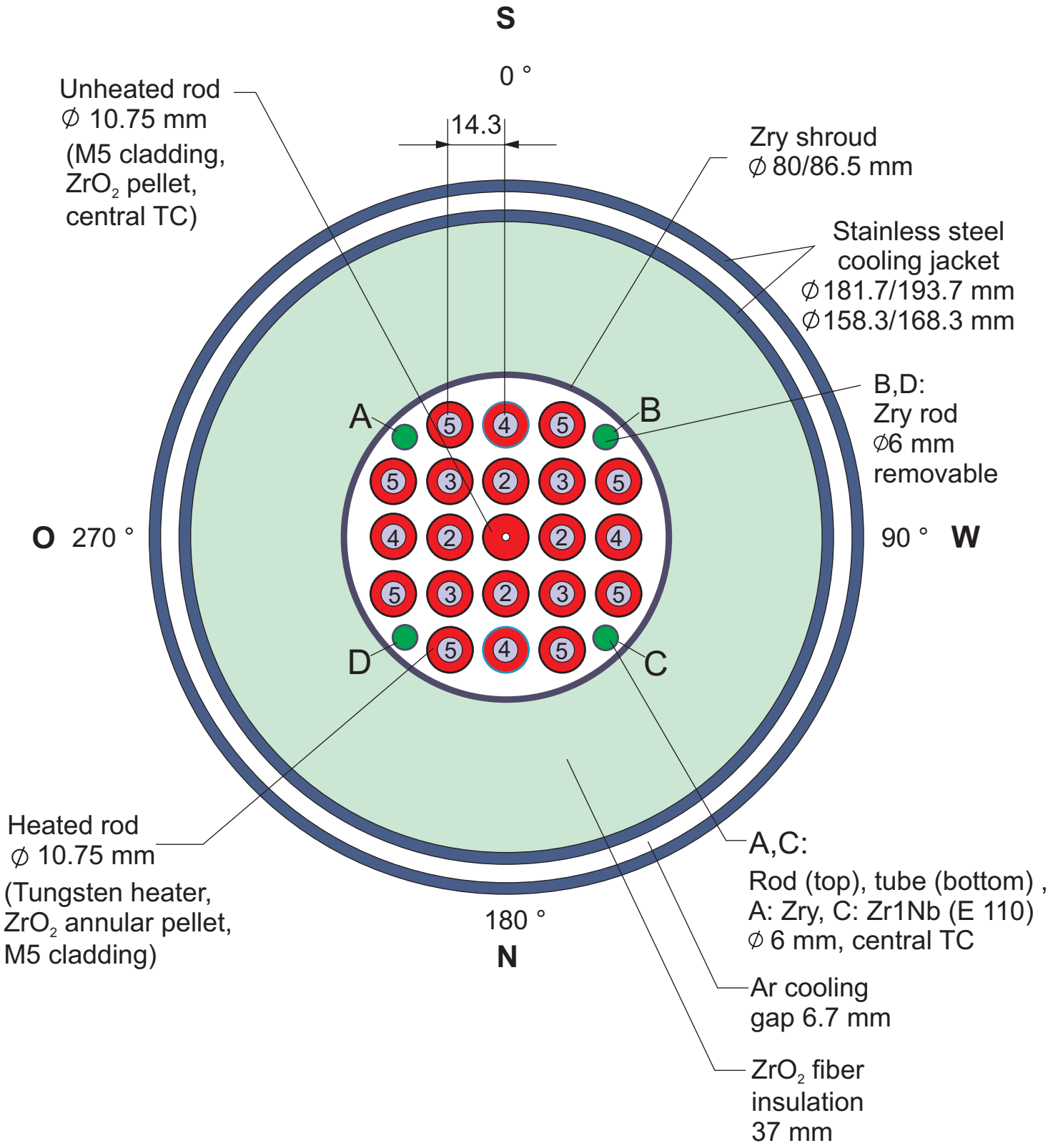

Fig.5-QUE14 Cross section.cdr
18.12.08 - IMF

Fig. 5: QUENCH-14; Fuel rod simulator bundle (cross section, top view) including rod type indications.

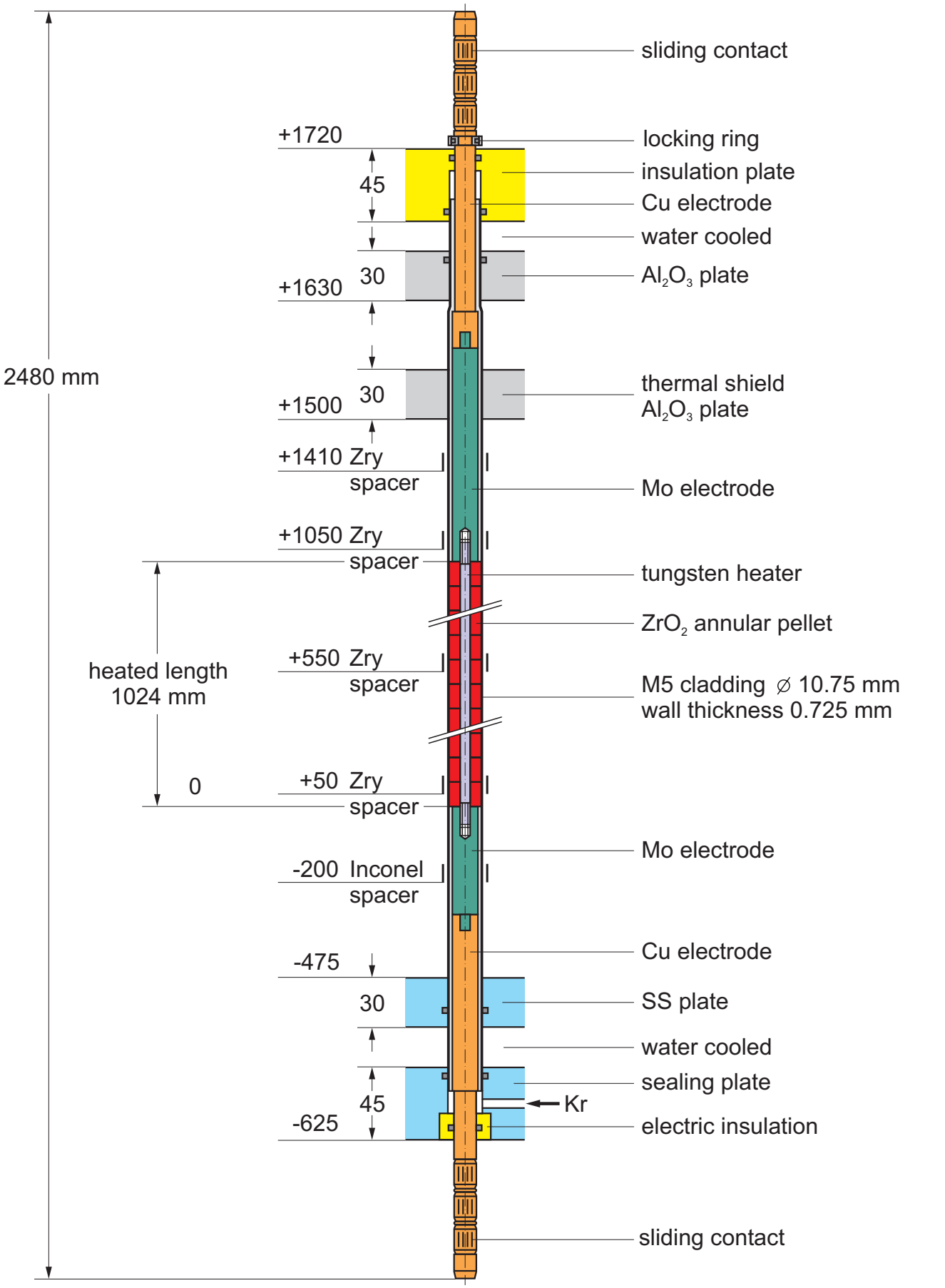

Fig.6-QUE14-Heated fuel rod sim.cdr
16.07.08 - IMF

Fig. 6: Heated fuel rod simulator.

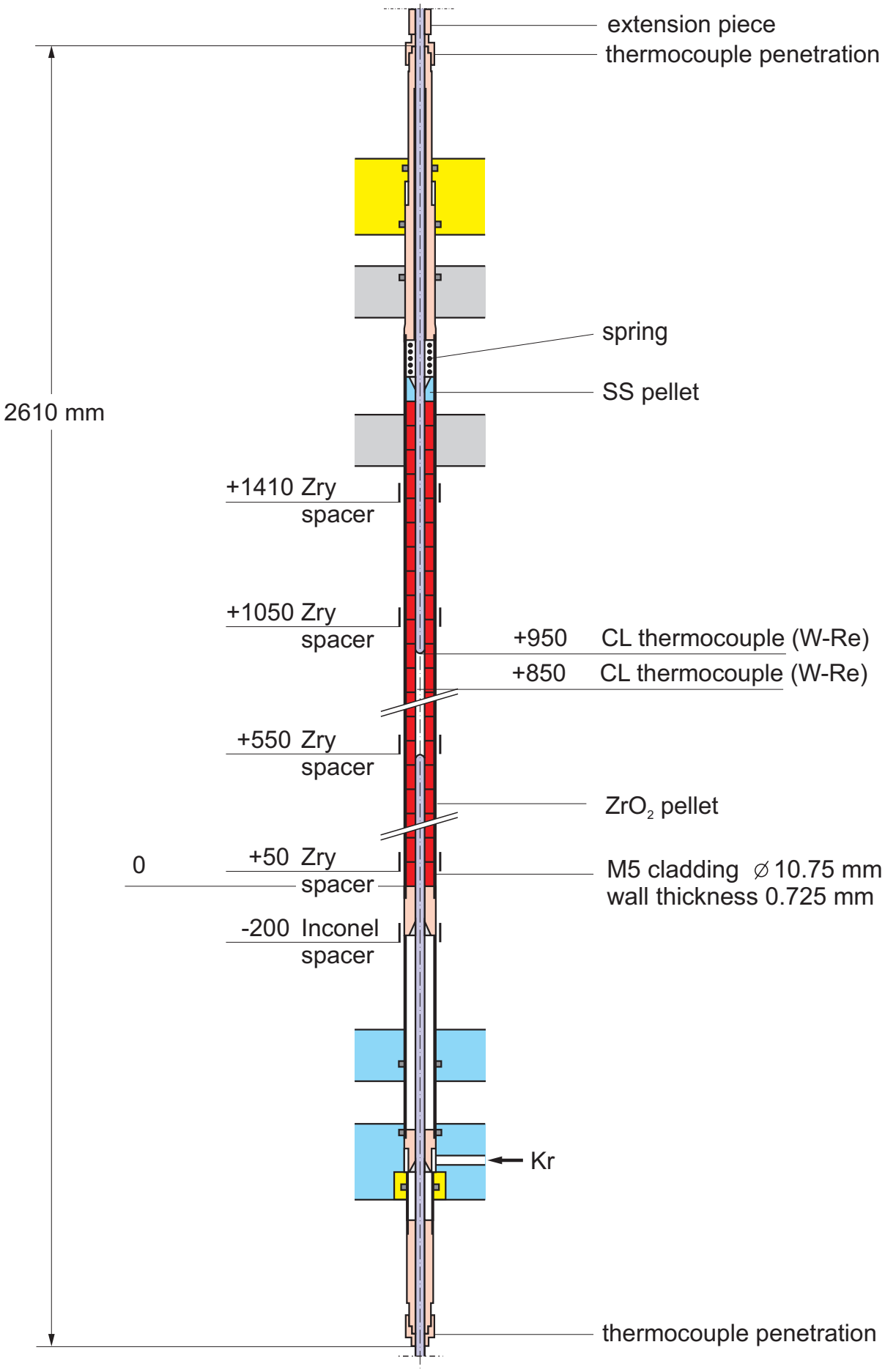

Fig. 7 : Unheated fuel rod simulator.

Fig. 7-QUE14 Unheated fuel rod sim.cdr
01.10.08 - IMF

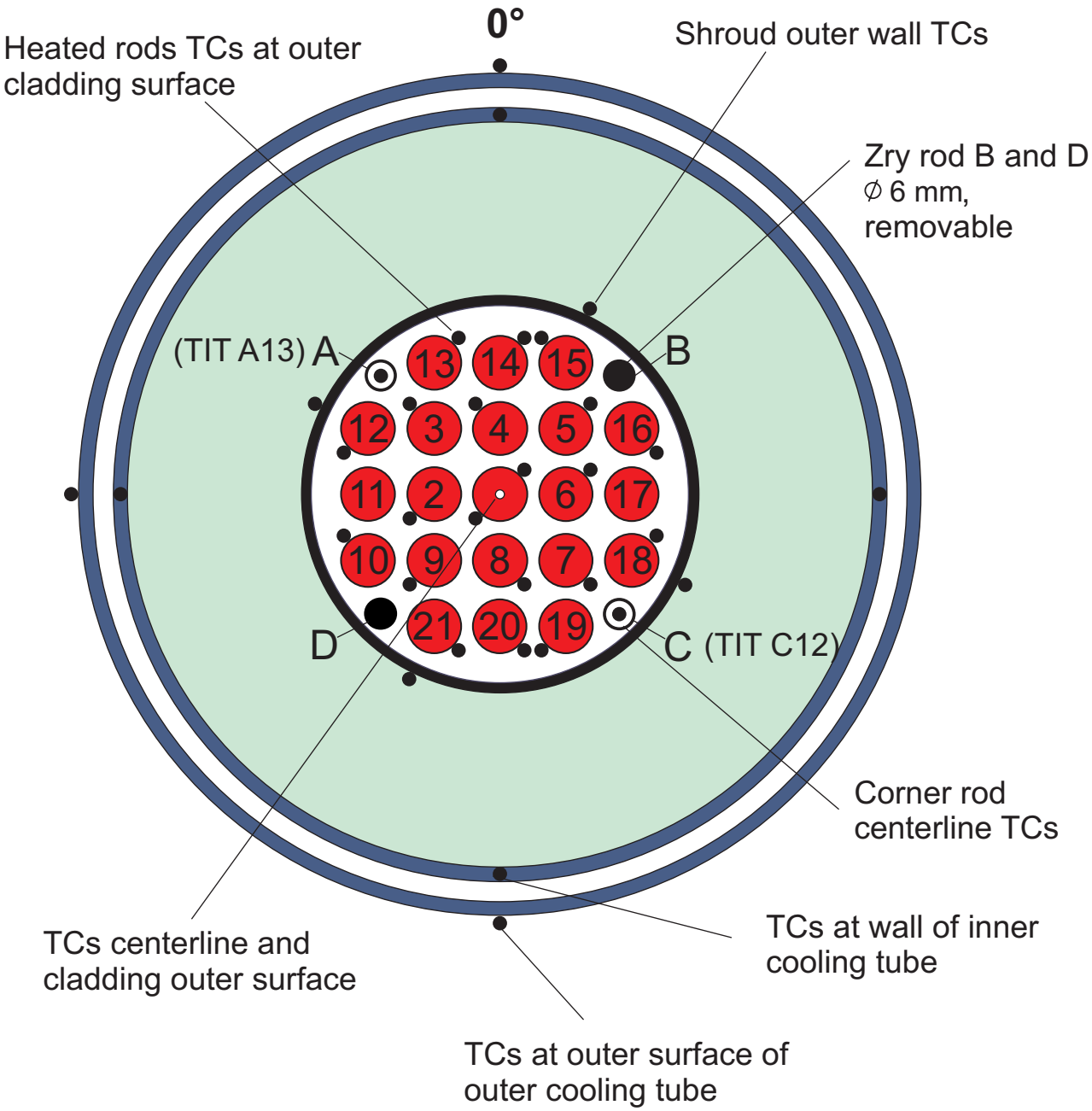

Fig.8-QUE14 TC instr.cdr
16.07.08 - IMF

Fig. 8: QUENCH-14; Test bundle; TC instrumentation and rod designation (top view).

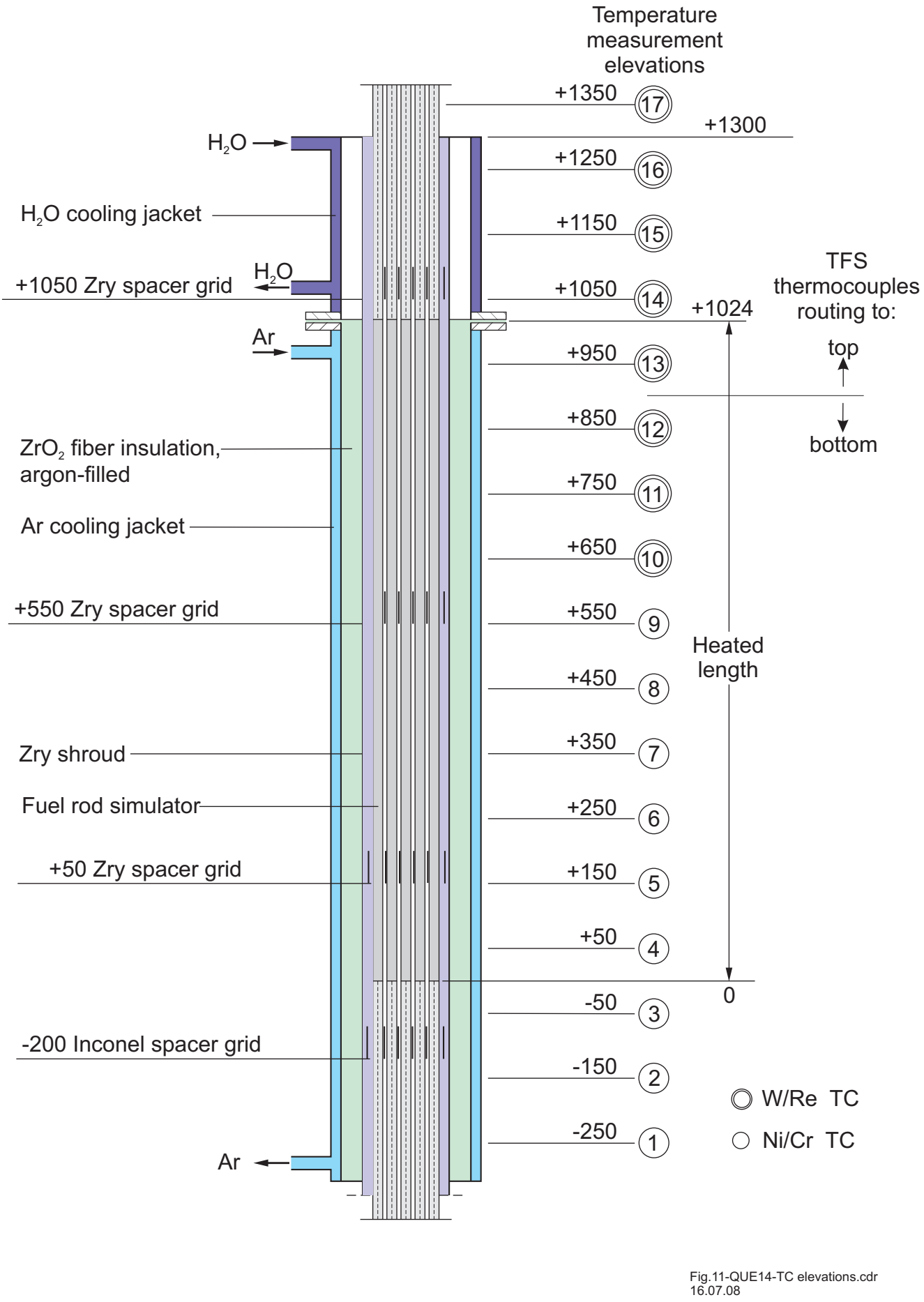

Fig. 9: Axial temperature measurement locations in the QUENCH test section.

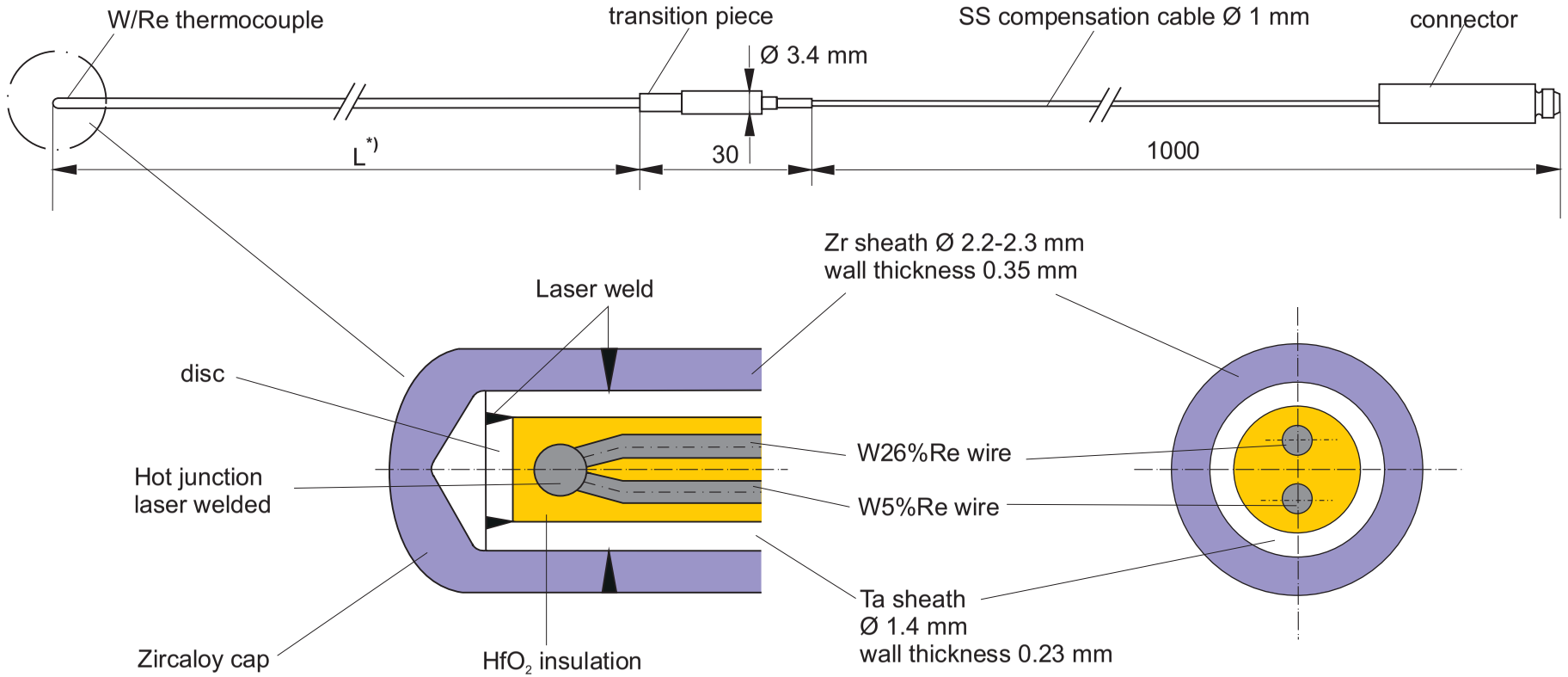

*) L: high-temperature section length dependent on the TC position in the test bundle: 500-1700 mm

Fig.10-QUE14-High-temp thermocouple.cdr
16.07.08 - IMF

Fig. 10: QUENCH; High-temperature thermocouple.

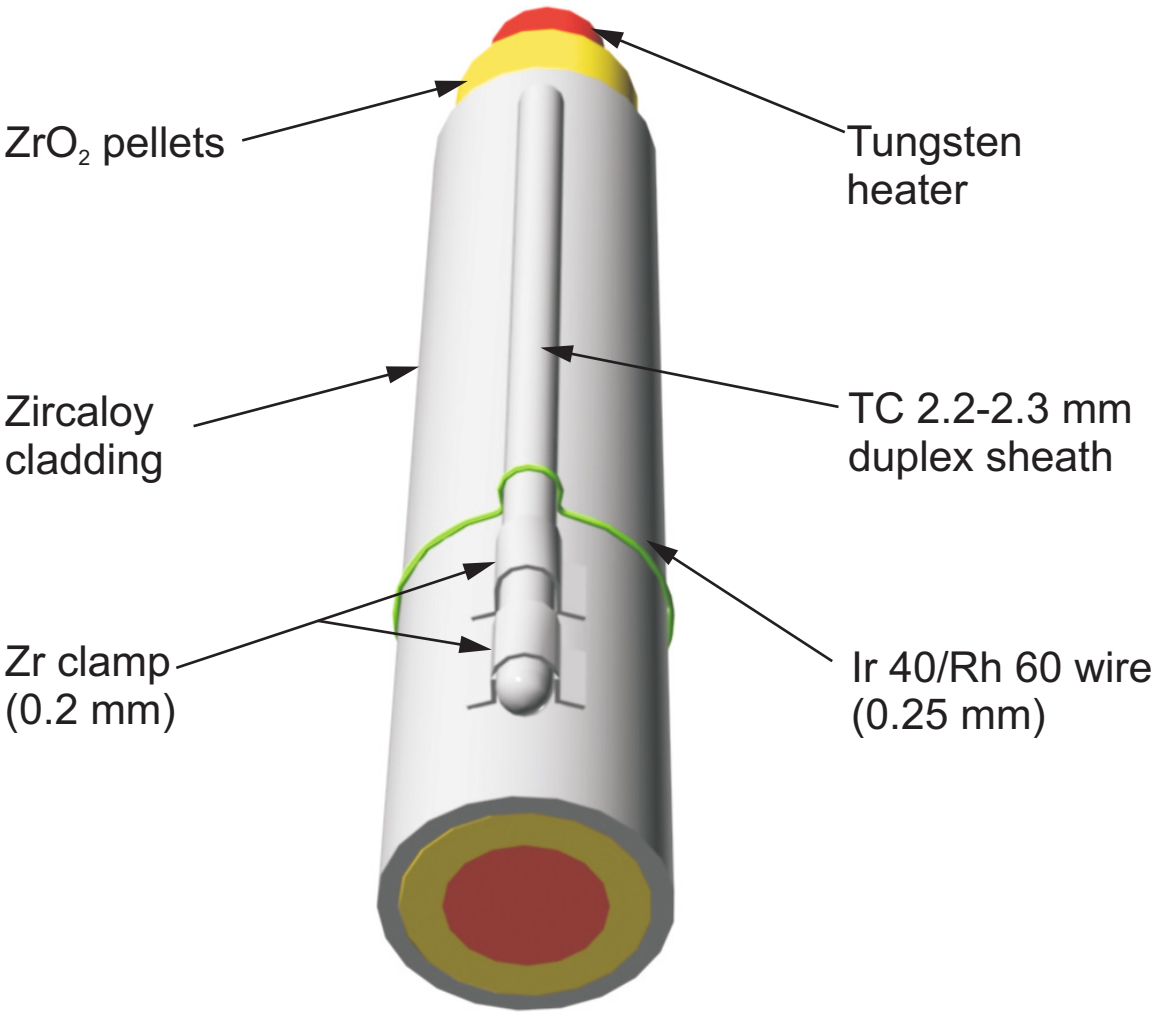

Fig 11-QUE14-TC Fastening3.cdr
18.12.08 - IMF

Fig. 11: QUENCH-14; Concept for TC fastening at the test rod.

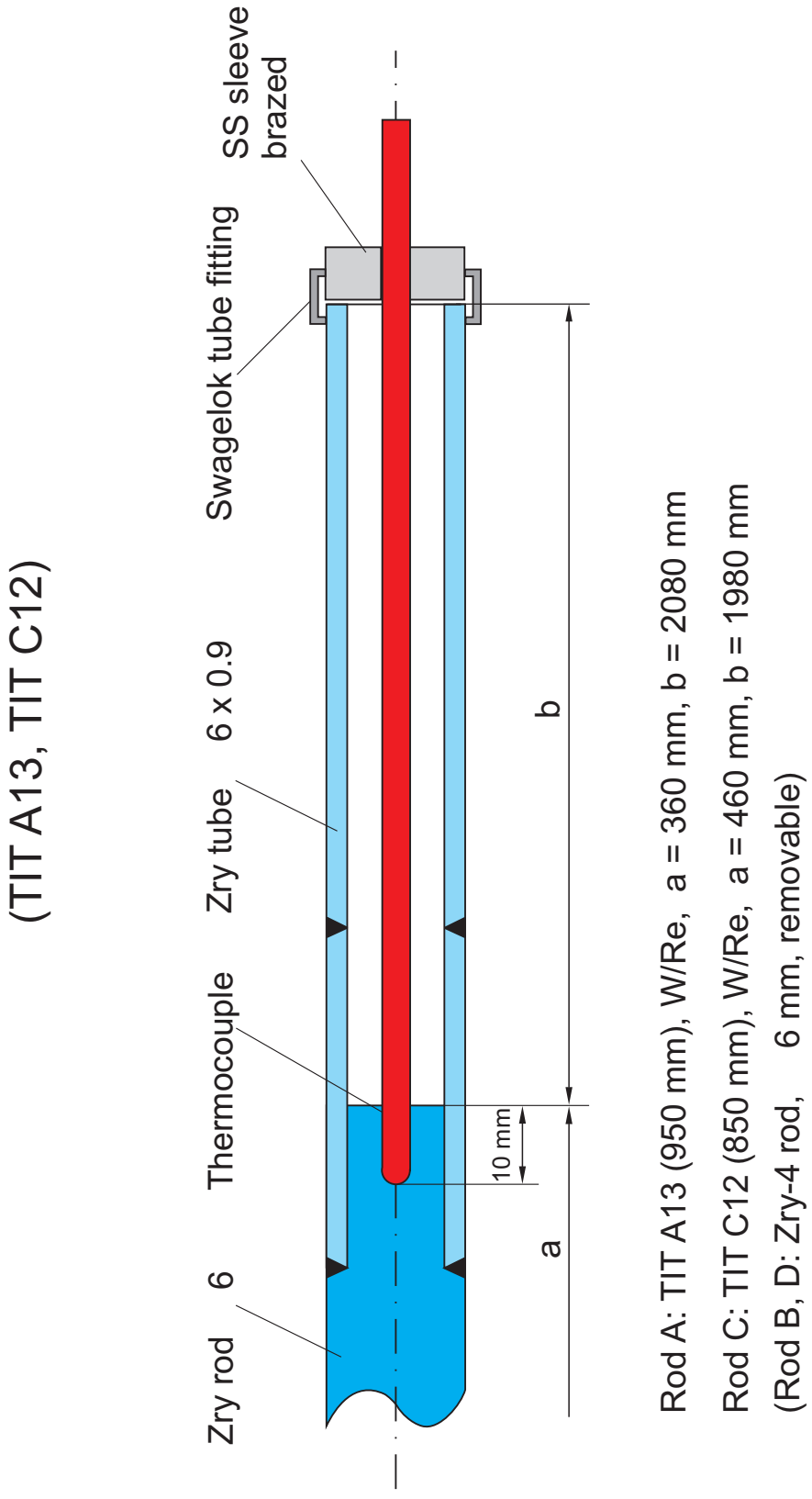

Fig 12-QUE14-TC in corner rod.cdr
01.10.08 - IMF

Fig. 12: QUENCH-14; Arrangement of the thermocouples inside the corner rods.

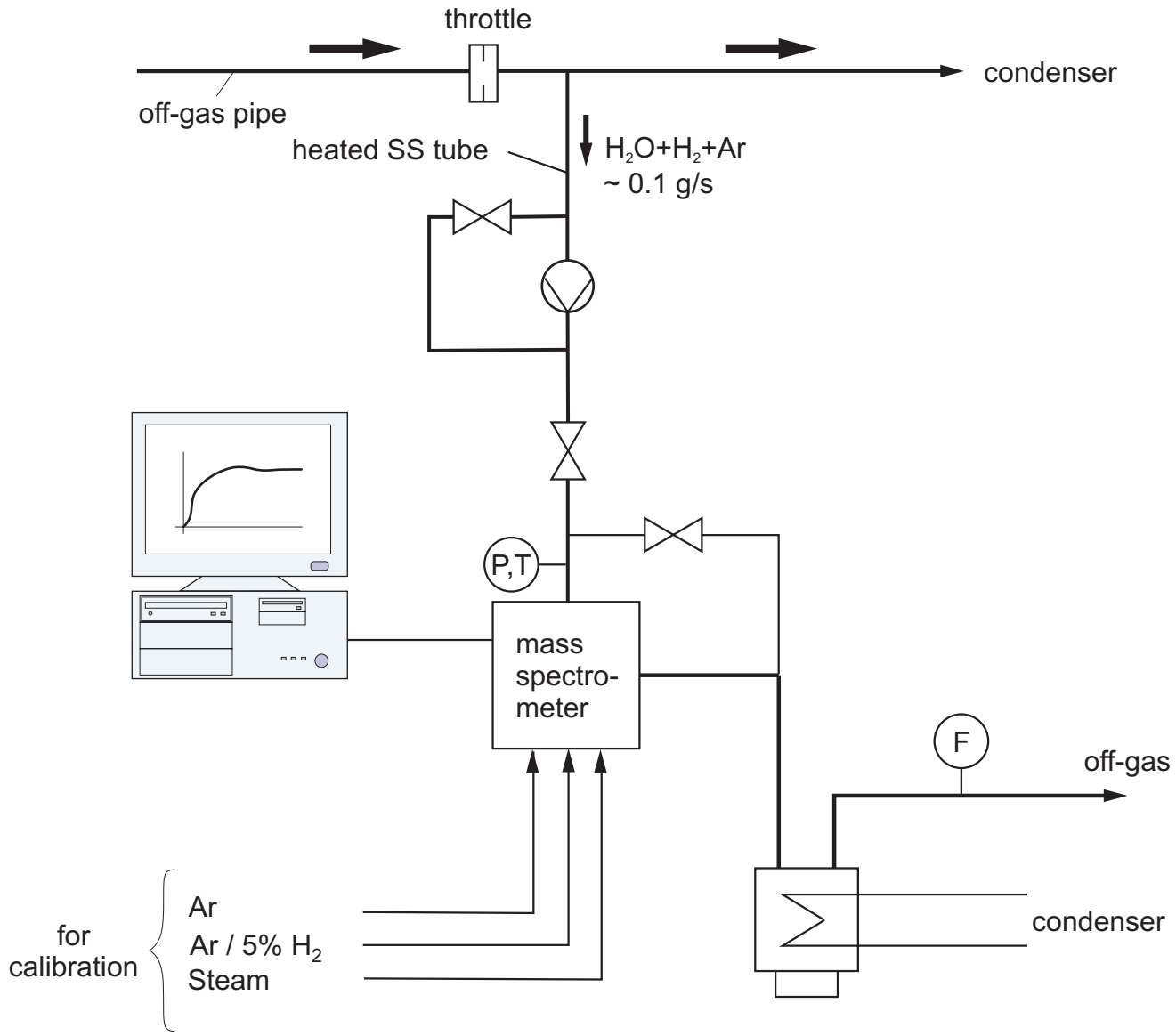

Fig.13-QUE14-MS Quench facility.cdr
16.07.08 - IMF

Fig. 13: QUENCH Facility; H_2 measurement with the GAM 300 mass spectrometer.

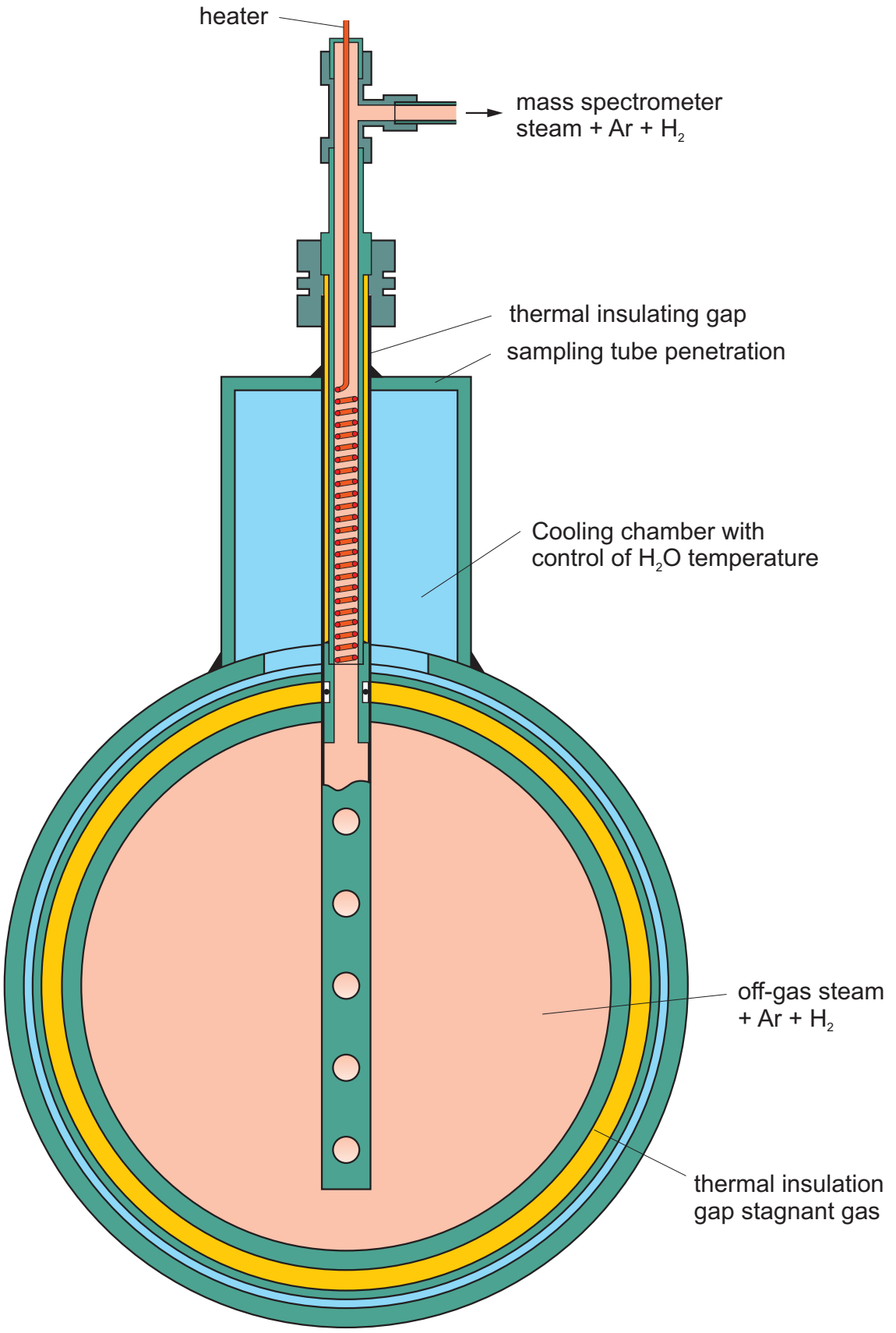

Fig 14-QUE14 MS sampling position new.cdr
16.07.08 - IMF

Fig. 14: Mass spectrometer sampling position at the off-gas pipe of the QUENCH test facility.

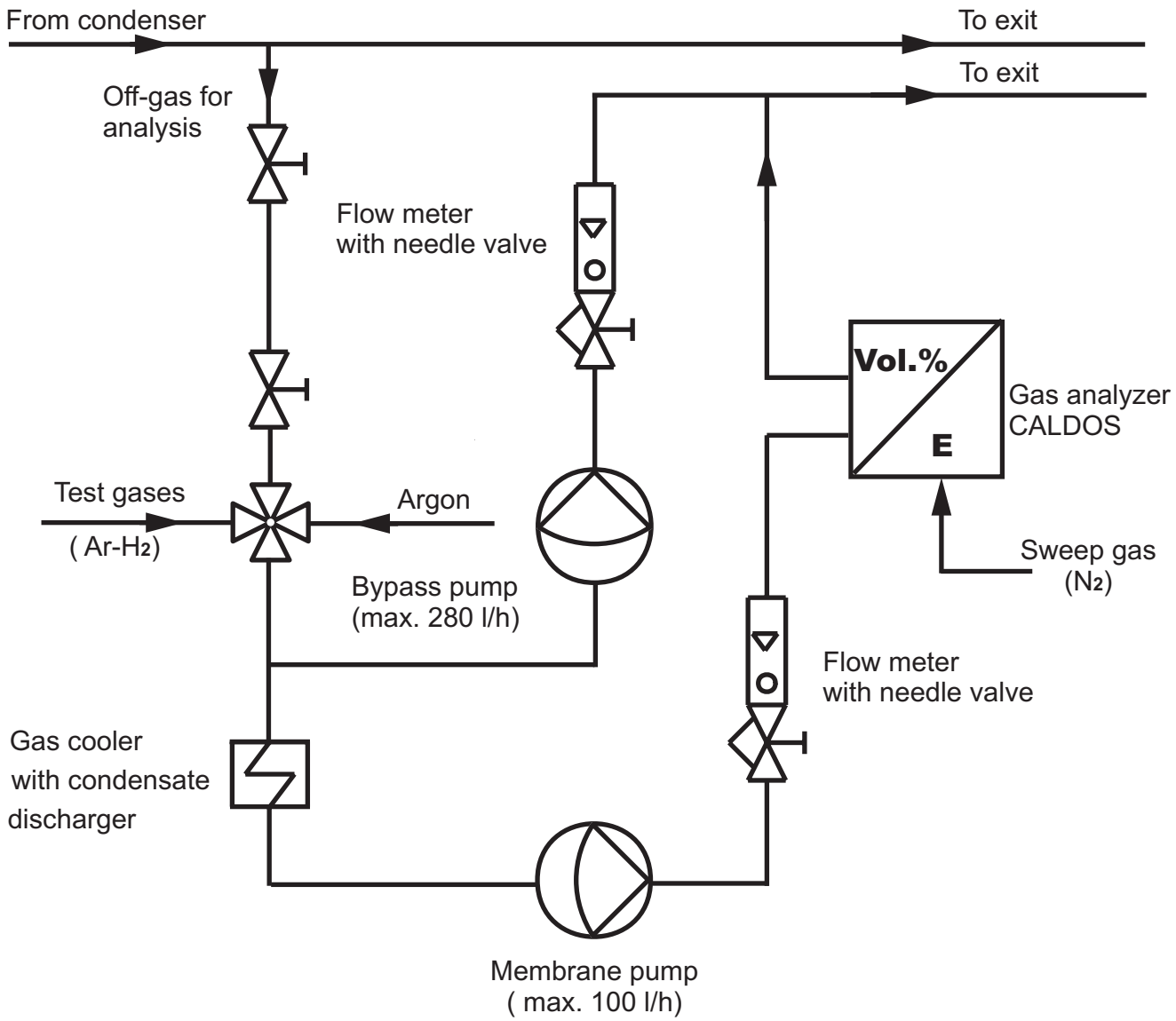

Fig 15 QUE14 Caldos Schema (ab QUE04).cdr
16.07.08 - IMF

Fig. 15: Hydrogen measurement with the CALDOS analyzer connected to the exhaust gas pipe of the QUENCH facility.

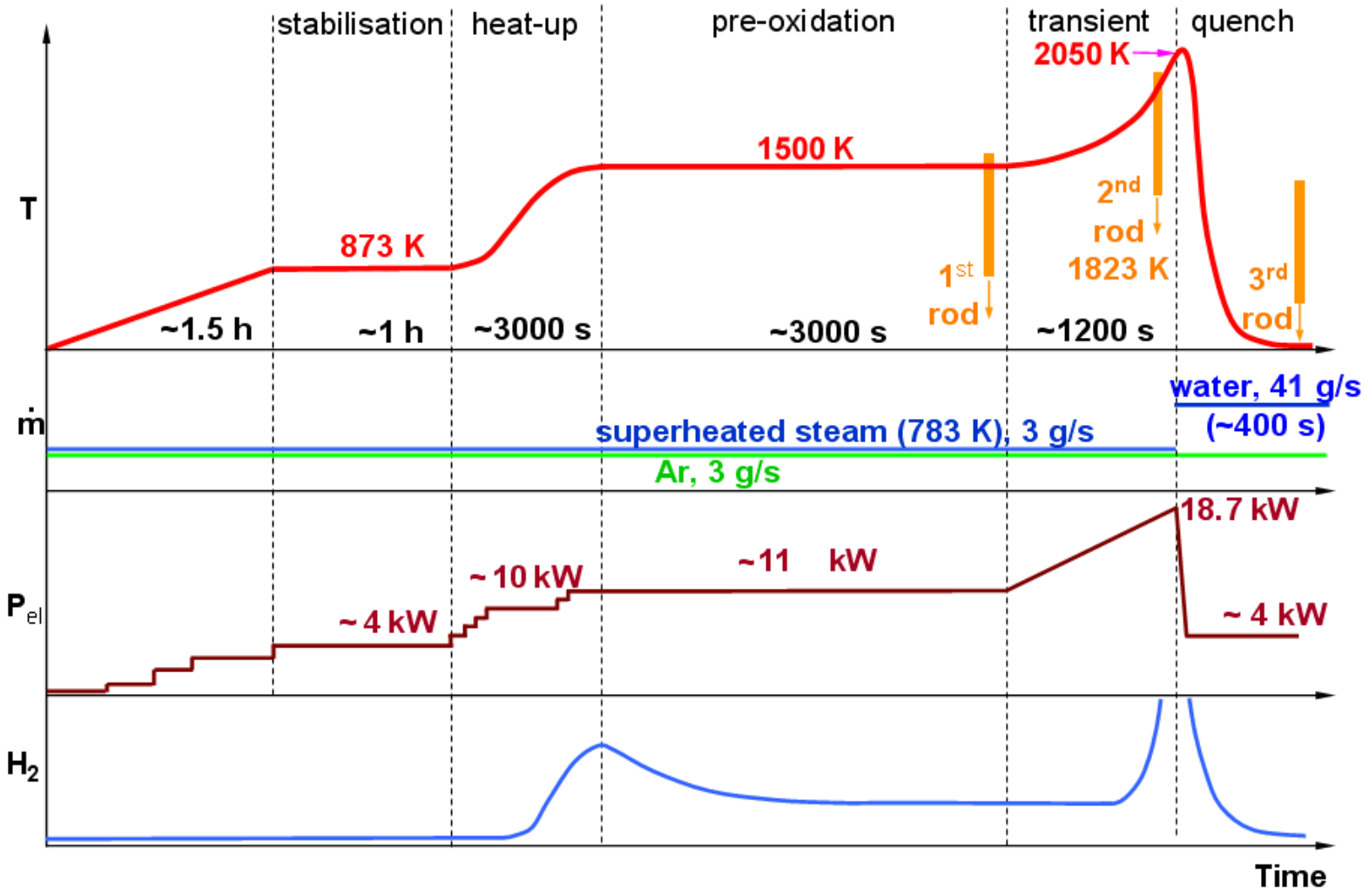

Fig. 16: QUENCH-14 test conduct (schematics of histories of bundle temperature, power, argon and steam flow rate and hydrogen production rate).

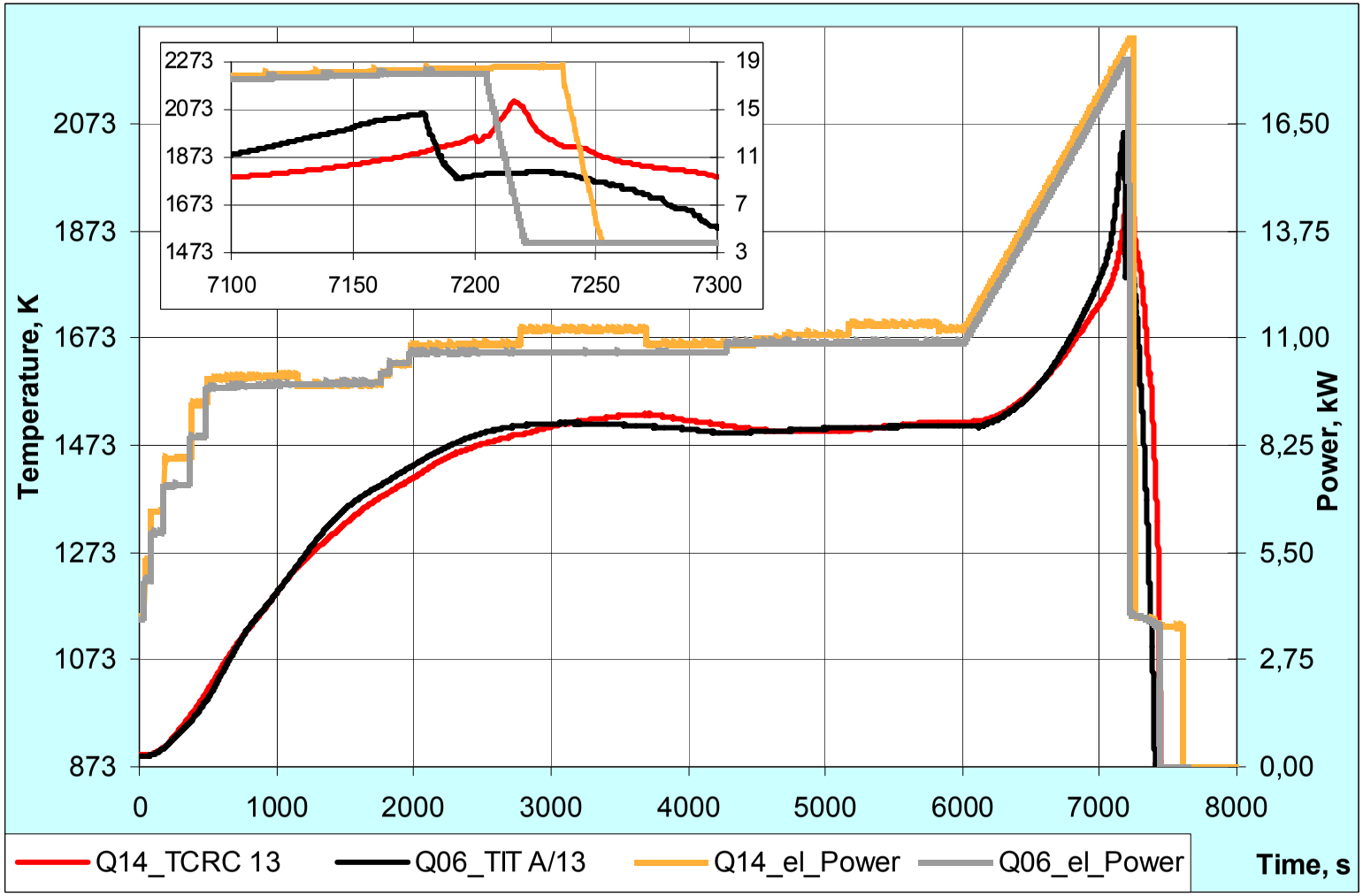

Fig. 17: QUENCH-14 test performance in comparison to the QUENCH-06 (Zry-4) test scenario.

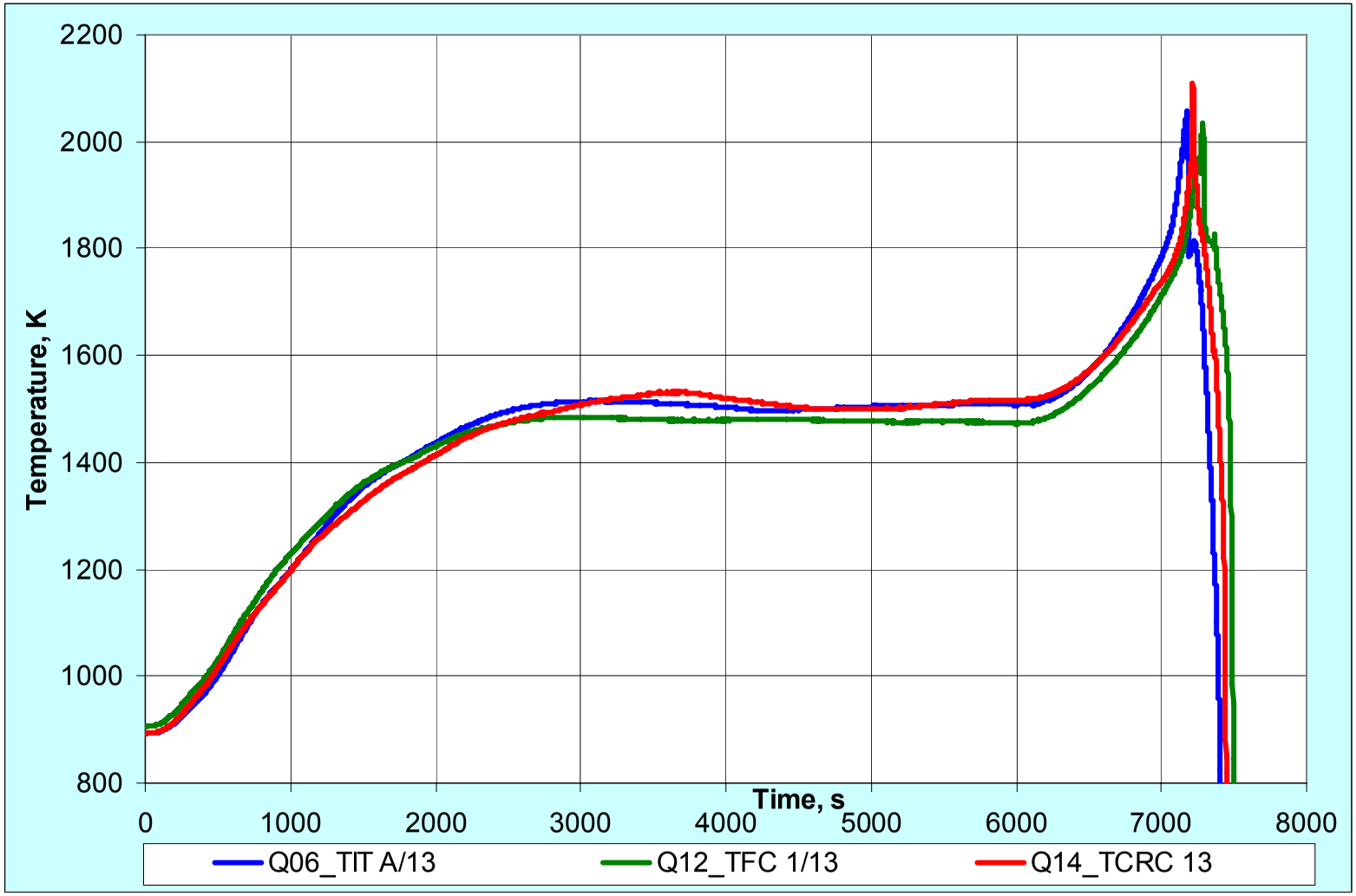

Fig. 18: Comparison of temperature profiles at hottest elevation of 950 mm for bundles QUENCH-06 (Zry-4), QUENCH-12 (E110) and QUENCH-14 (M5).

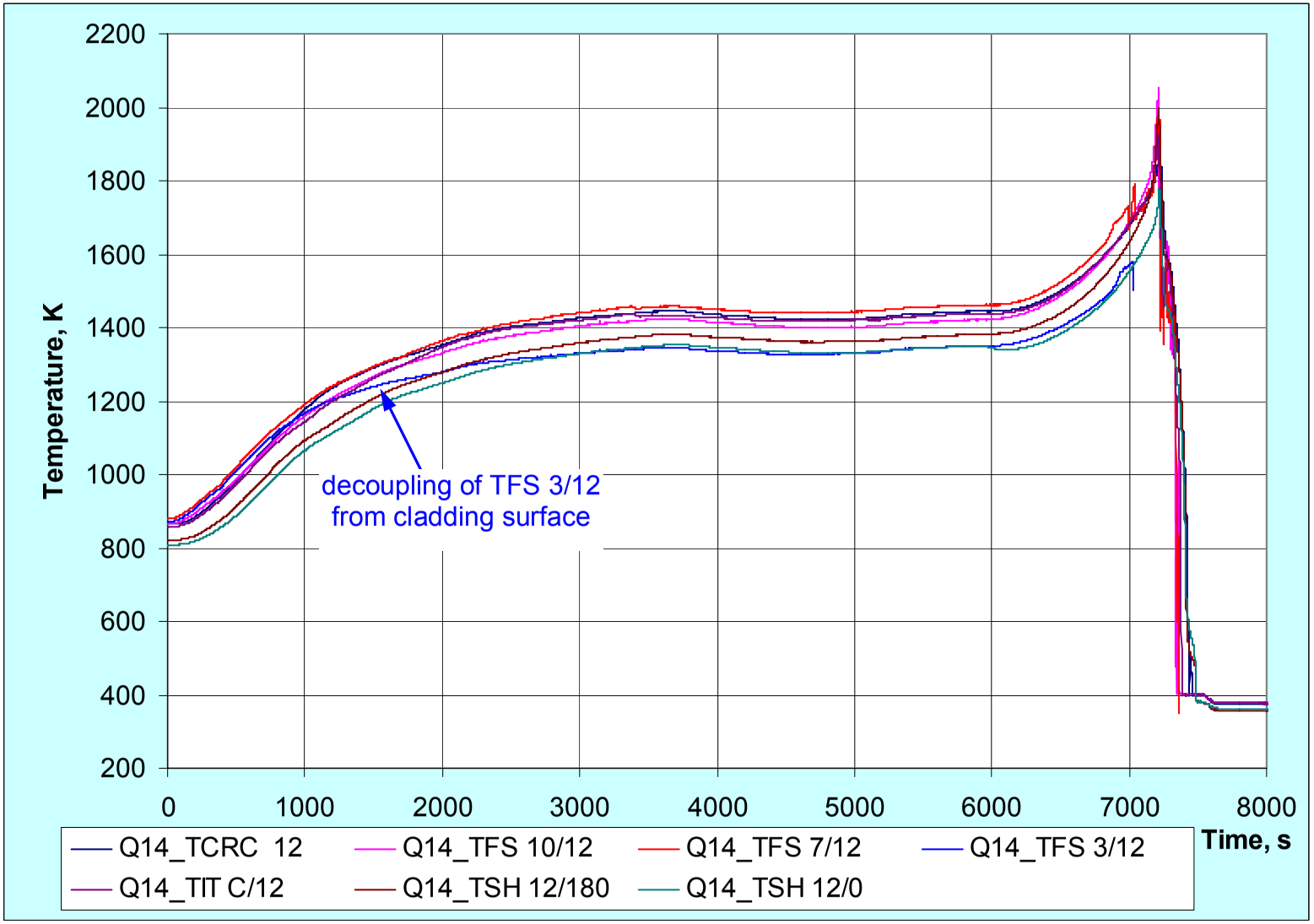

Fig. 19: QUENCH-14; Thermocouple readings at elevation 850 mm.

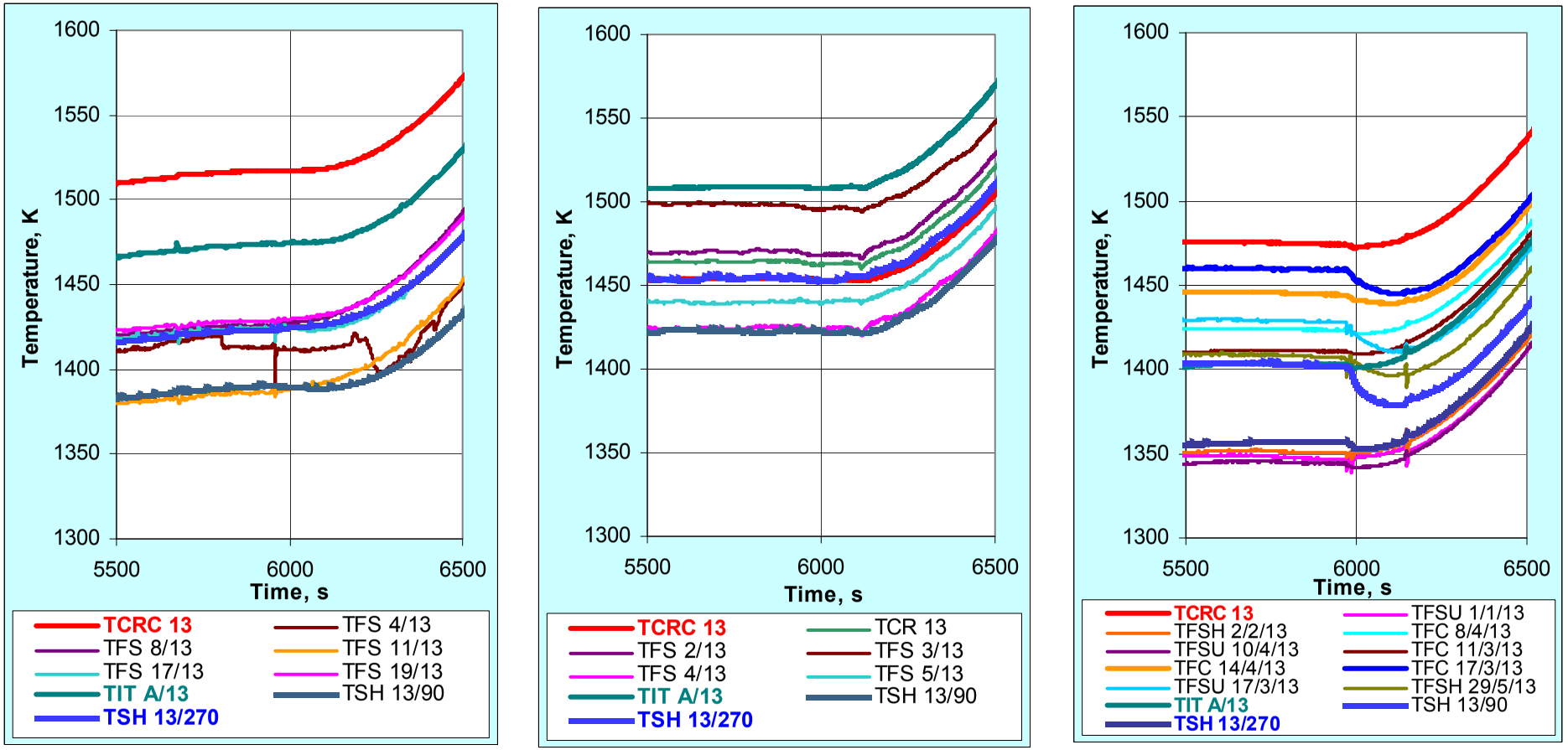

QUENCH-14:
T_{av} = 1432 K
ΔT = ± 28 K

QUENCH-06:
T_{av} = 1459 K
ΔT = ± 22 K

QUENCH-12:
T_{av} = 1400 K
ΔT = ± 33 K

Fig. 20: Comparison of temperature radial scattering at hottest elevation of 950 mm for bundles QUENCH-06 (Zry-4), QUENCH-12 (E110) and QUENCH-14 (M5®) on beginning of transient (~6000 s).

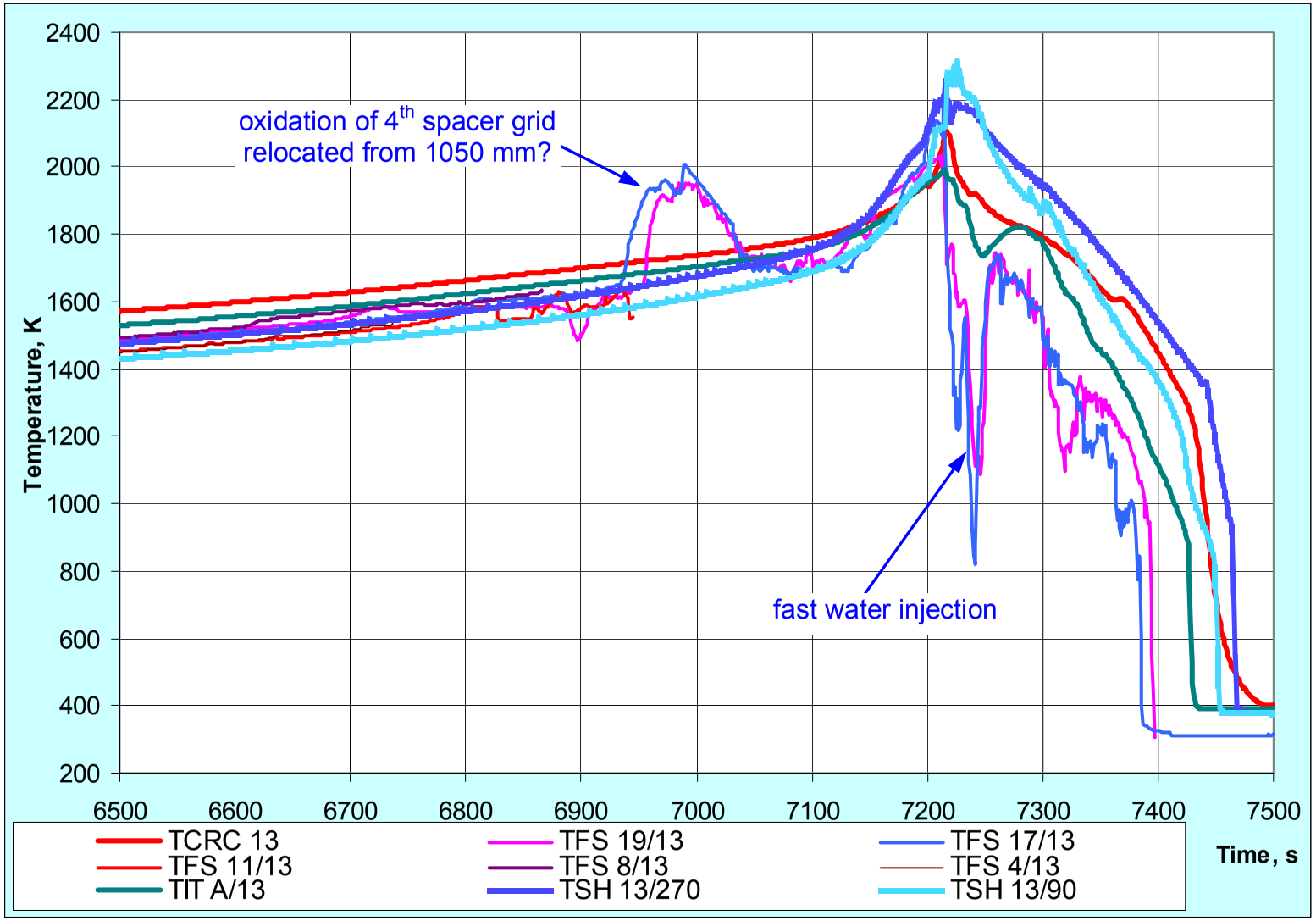

Fig. 21: QUENCH-14; Thermocouple readings at elevation 950 mm during transient and reflood.

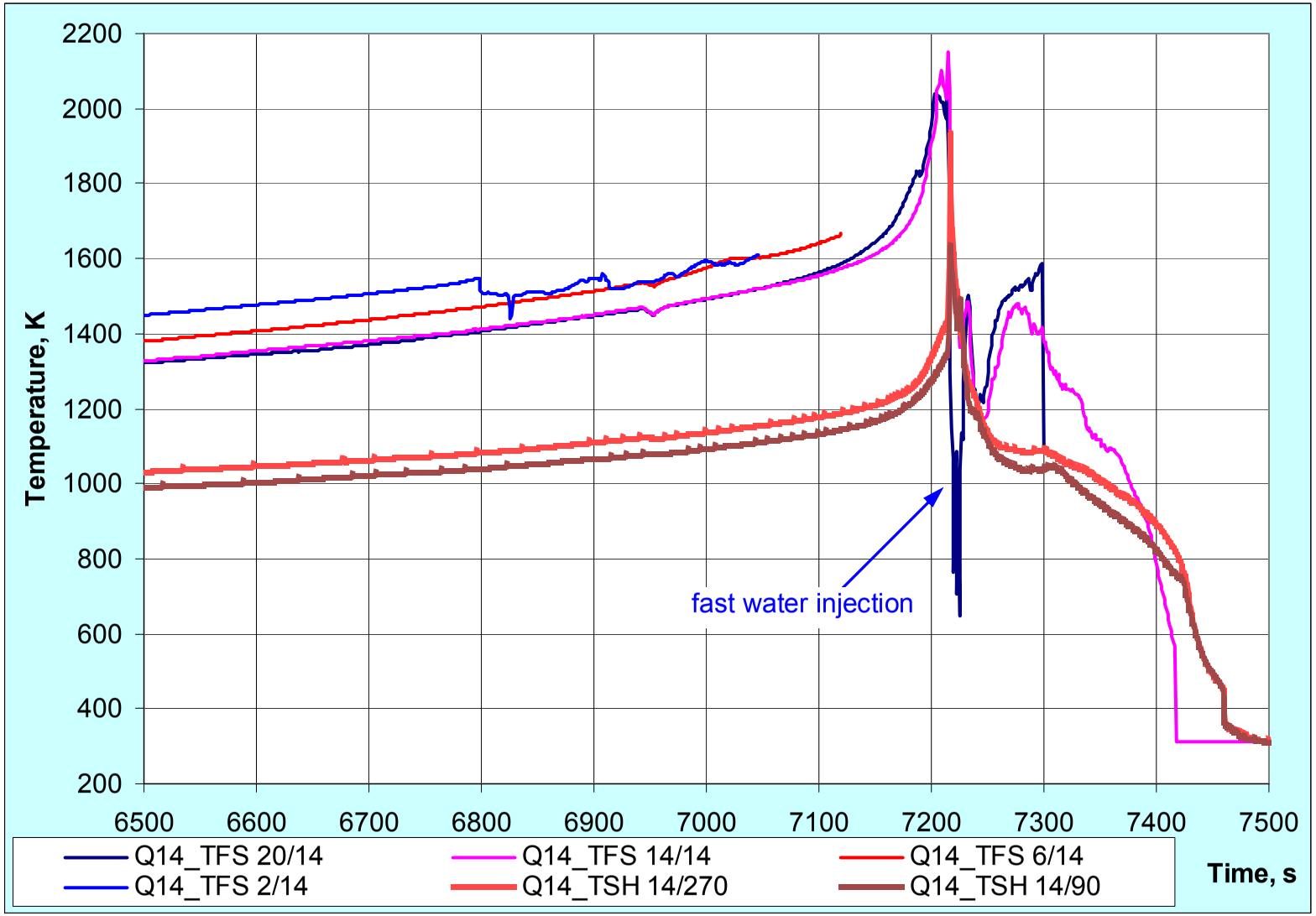

Fig. 22: QUENCH-14; Thermocouple readings at elevation 1050 mm during transient and reflood. Lower shroud temperatures due to absence of the ZrO_2 shroud insulation above 1024 mm.

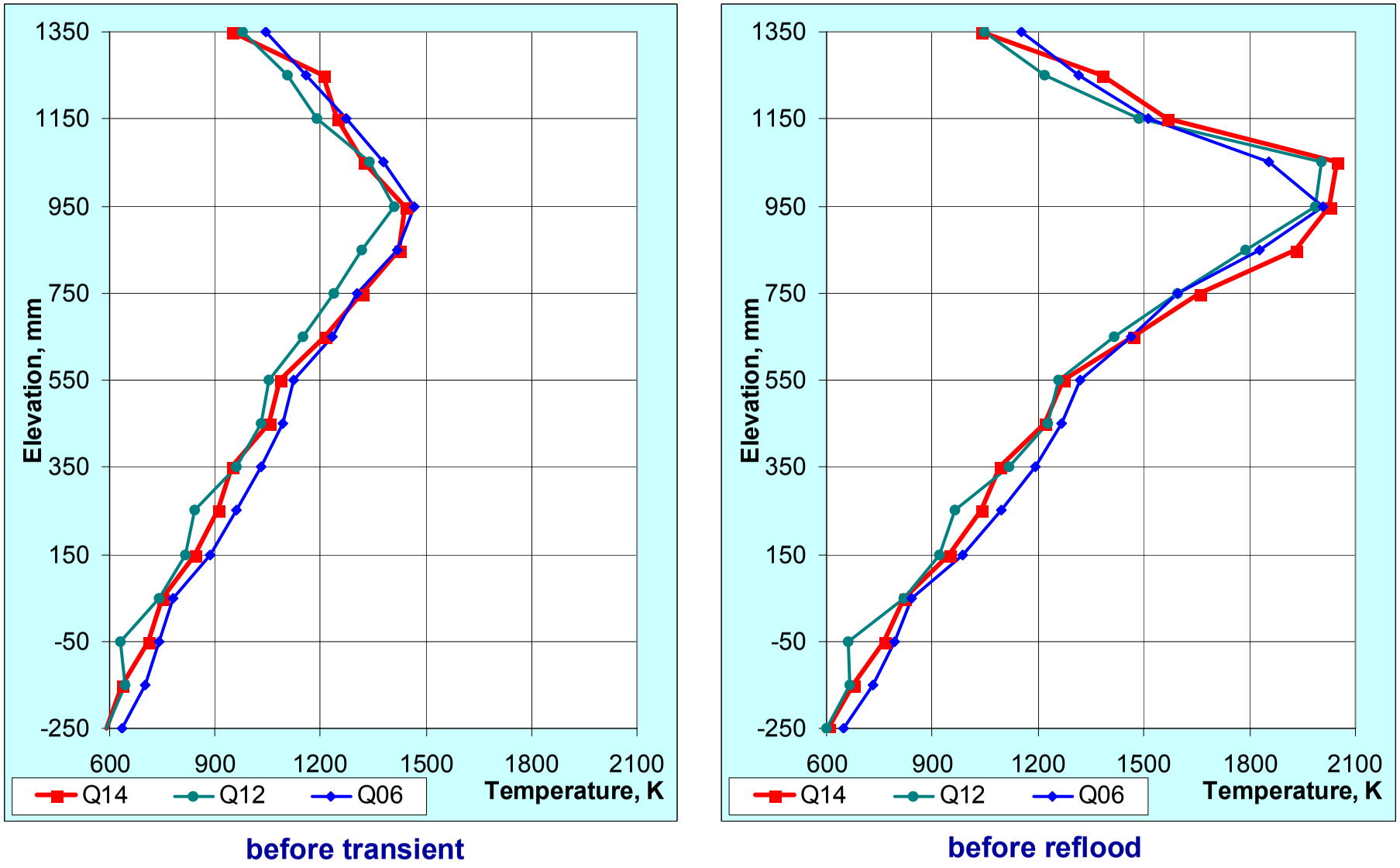

Fig. 23: Comparison of axial bundle temperature profiles for QUENCH-06 (Zry-4), -12 (VVER), -14 (M5®).

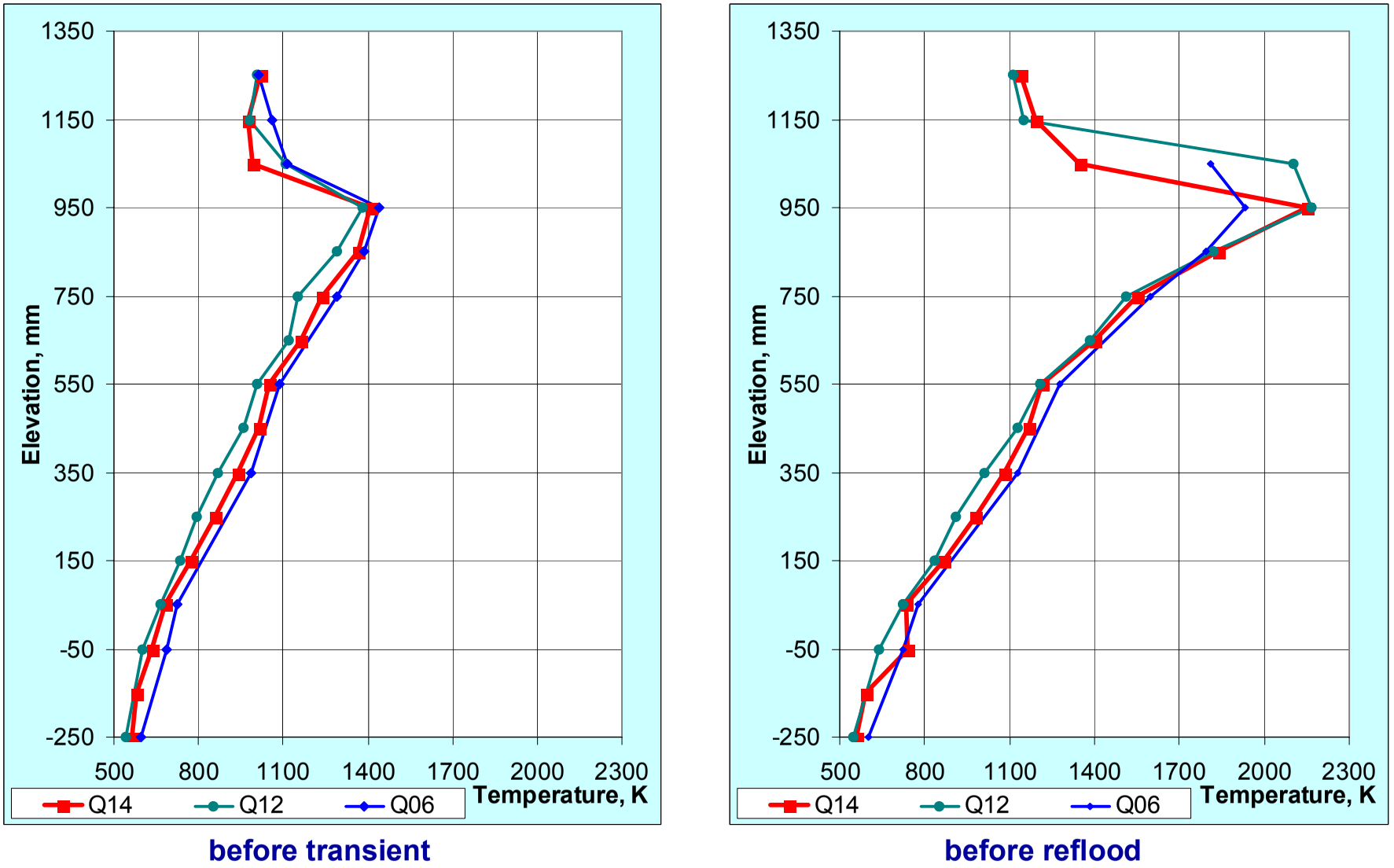

Fig. 24: Comparison of axial shroud temperature profiles for QUENCH-06, QUENCH-12, QUENCH-14 with wall thickness of shroud 2.38, 2.25, and 3.3 mm, respectively.

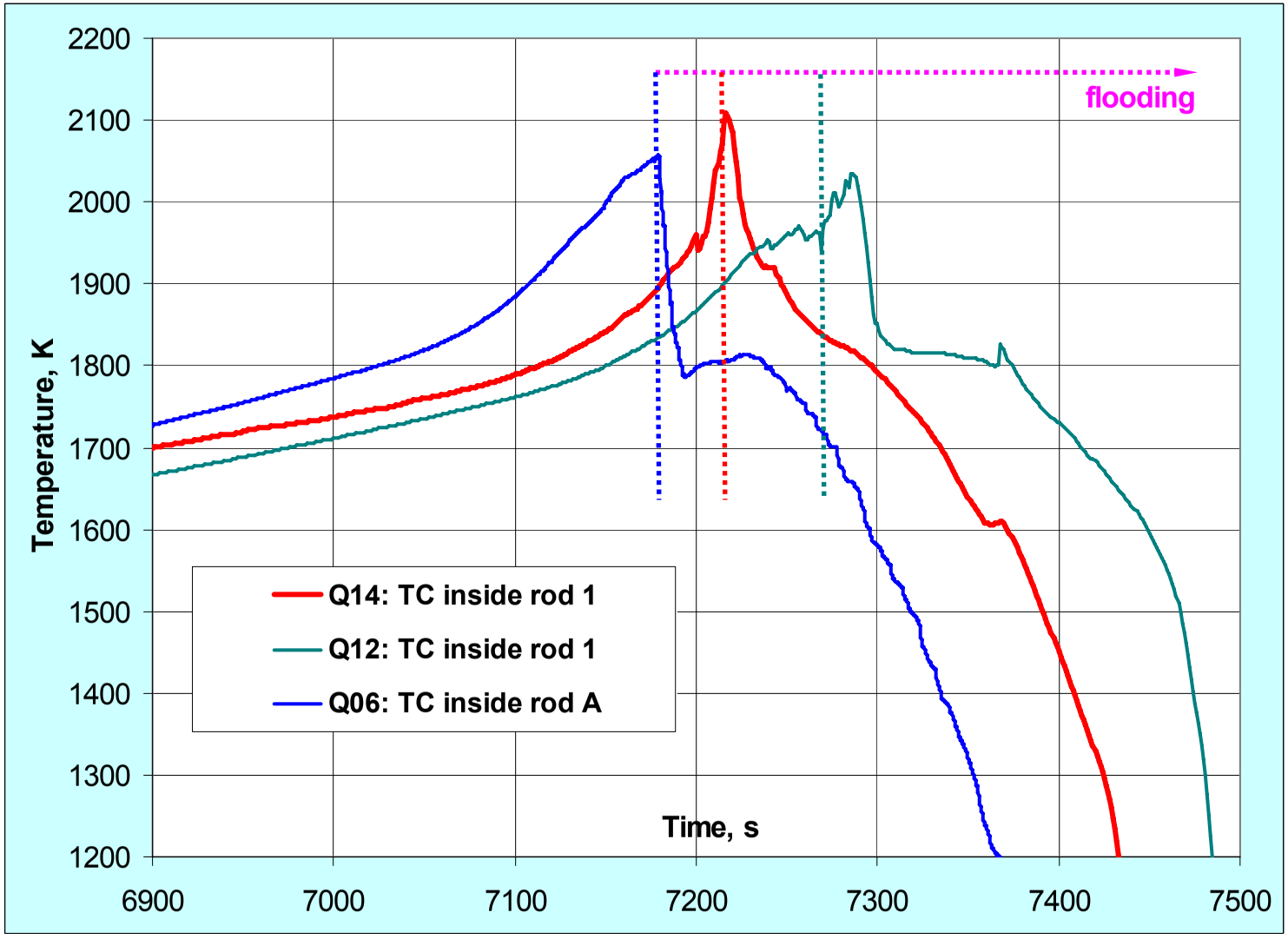

Fig. 25: Comparison of moderate temperature escalation at the end of transient and cooling status for bundle tests QUENCH-06, QUENCH-12 and QUENCH-14.

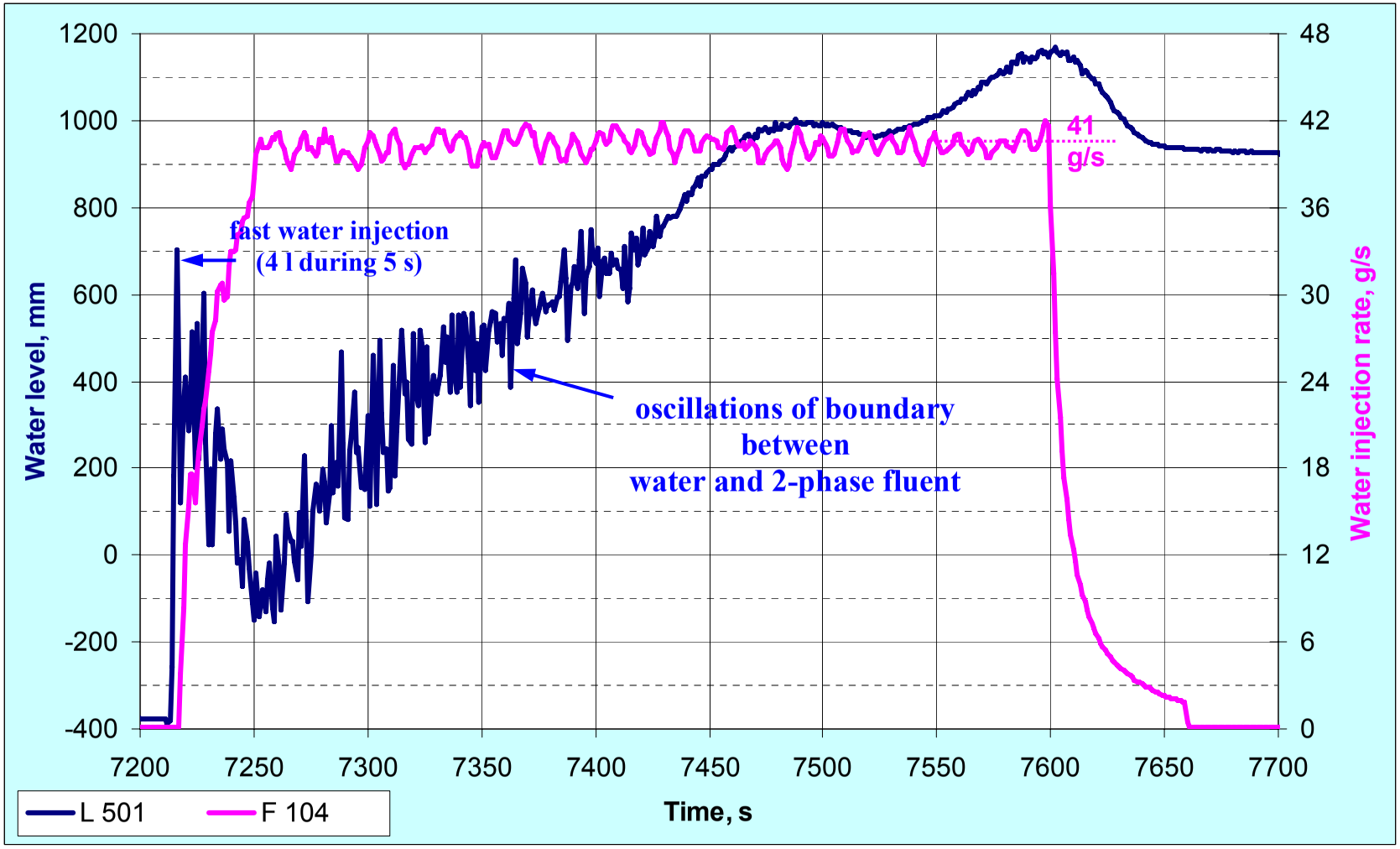

Fig. 26: QUENCH-14; feeding rate of quench pump (F 104) and rising of collapsed water front (L 501) during reflood phase.

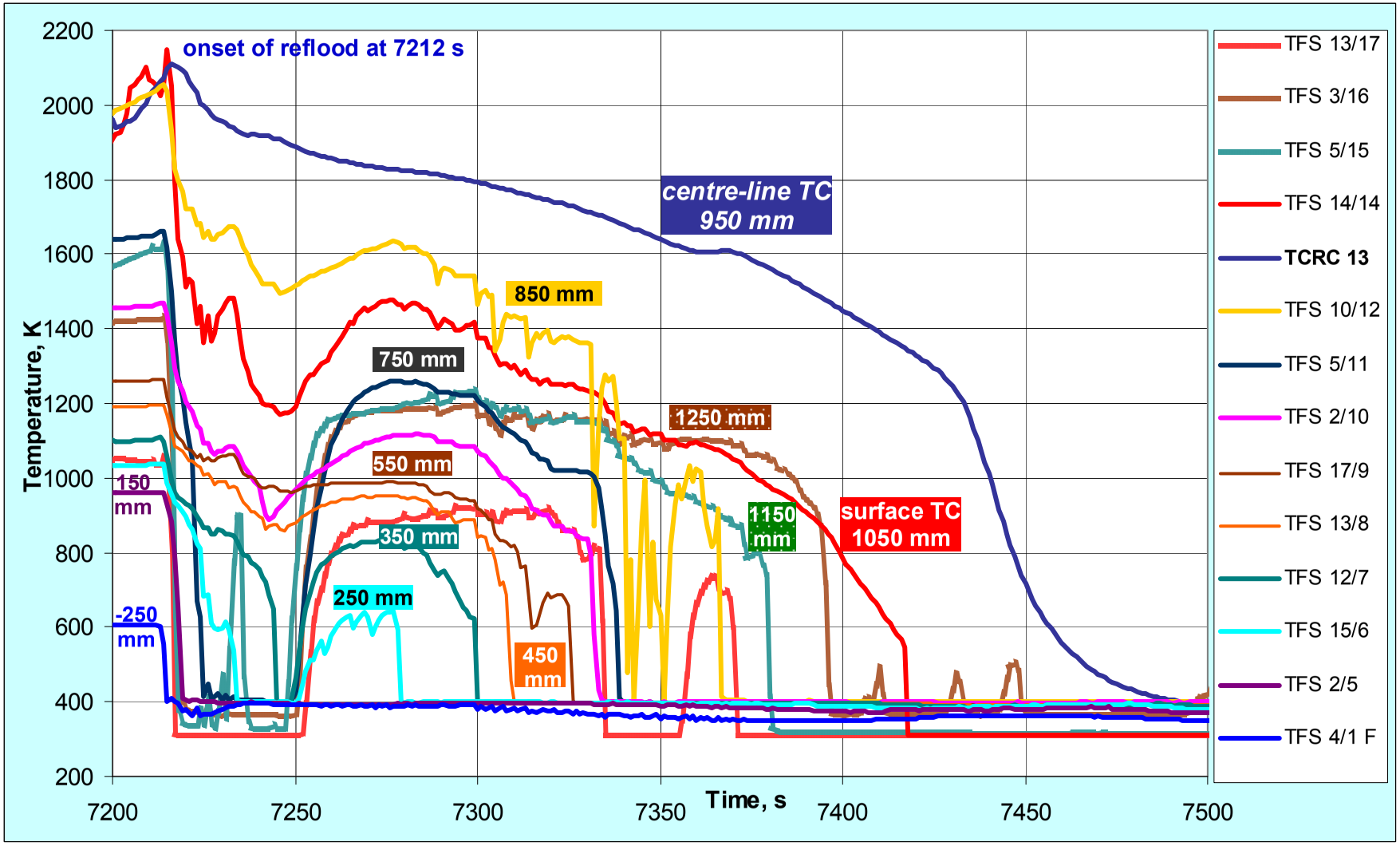

Fig. 27: Temperature response during the QUENCH-14 reflood phase depicting TC wetting at different bundle elevations and a duration of complete bundle cooling of ~300 s (the same duration as for QUENCH-06 and QUENCH-12).

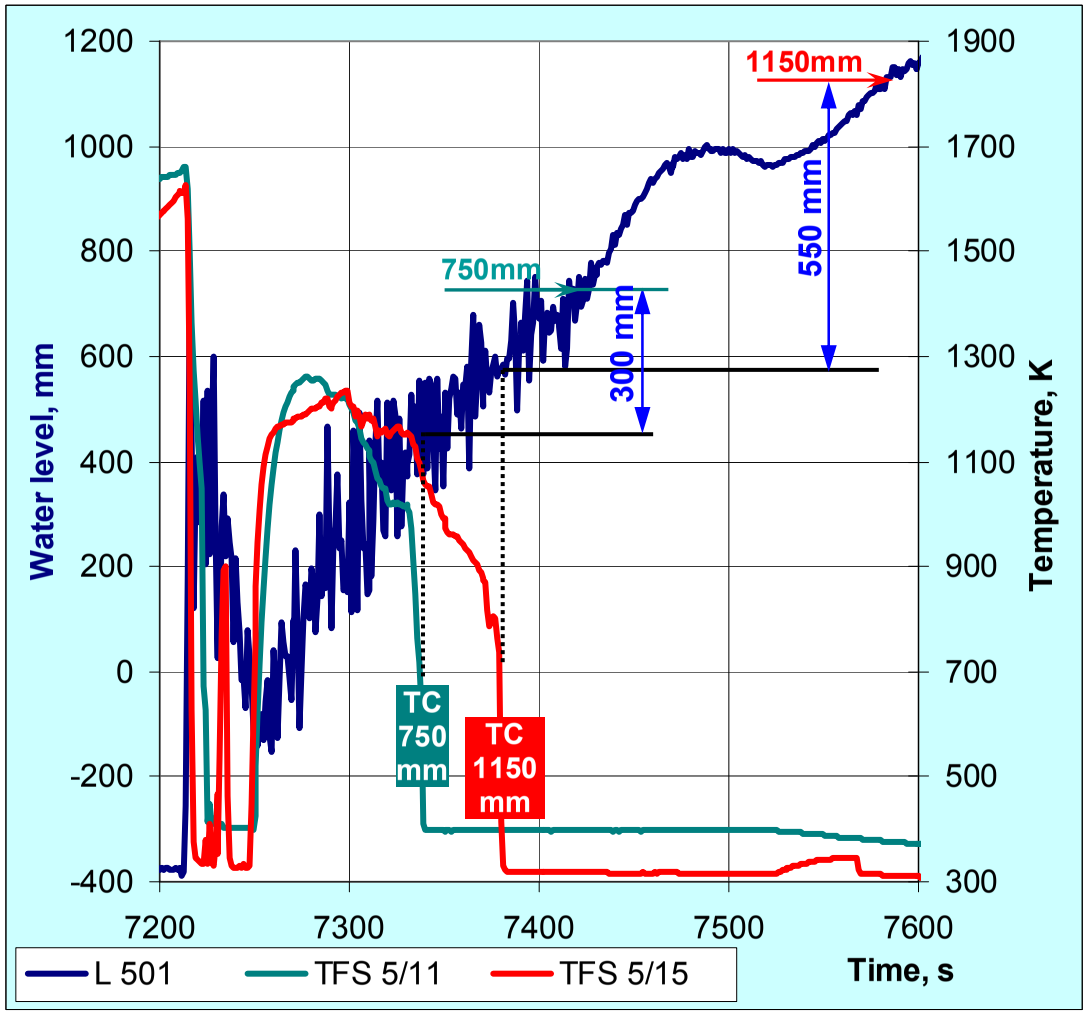

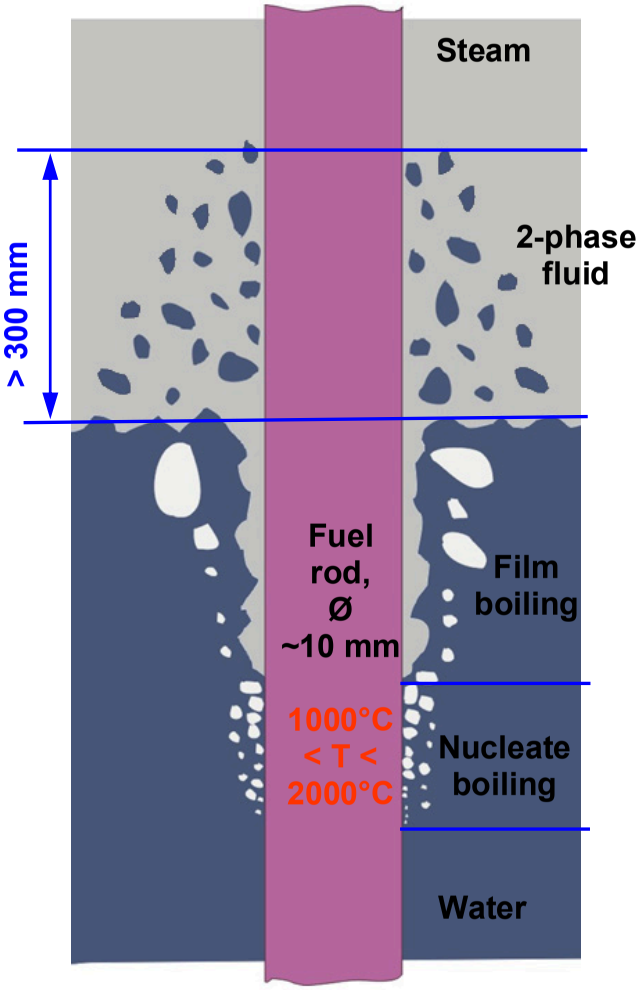

Fig. 28: QUENCH-14; reflood phase: cooling in 2-phase fluid above collapsed water surface.

Upper part of corner rods

Lower part of corner rods

Material of corner rods:
Zry-4: rods B (solid), D (solid), A (TC Instrumentation tube up to 940 mm)
E110: rod C (TC instrumentation tube up to 840 mm)

Time of withdrawal:
Corner rod B: before transient;
rod D: before reflood;
C and A rods: after end of the test

Fig. 29: QUENCH-14; Appearance of withdrawn corner rods B, D, C, and A depicting intensive breakaway for E110 (rod C).

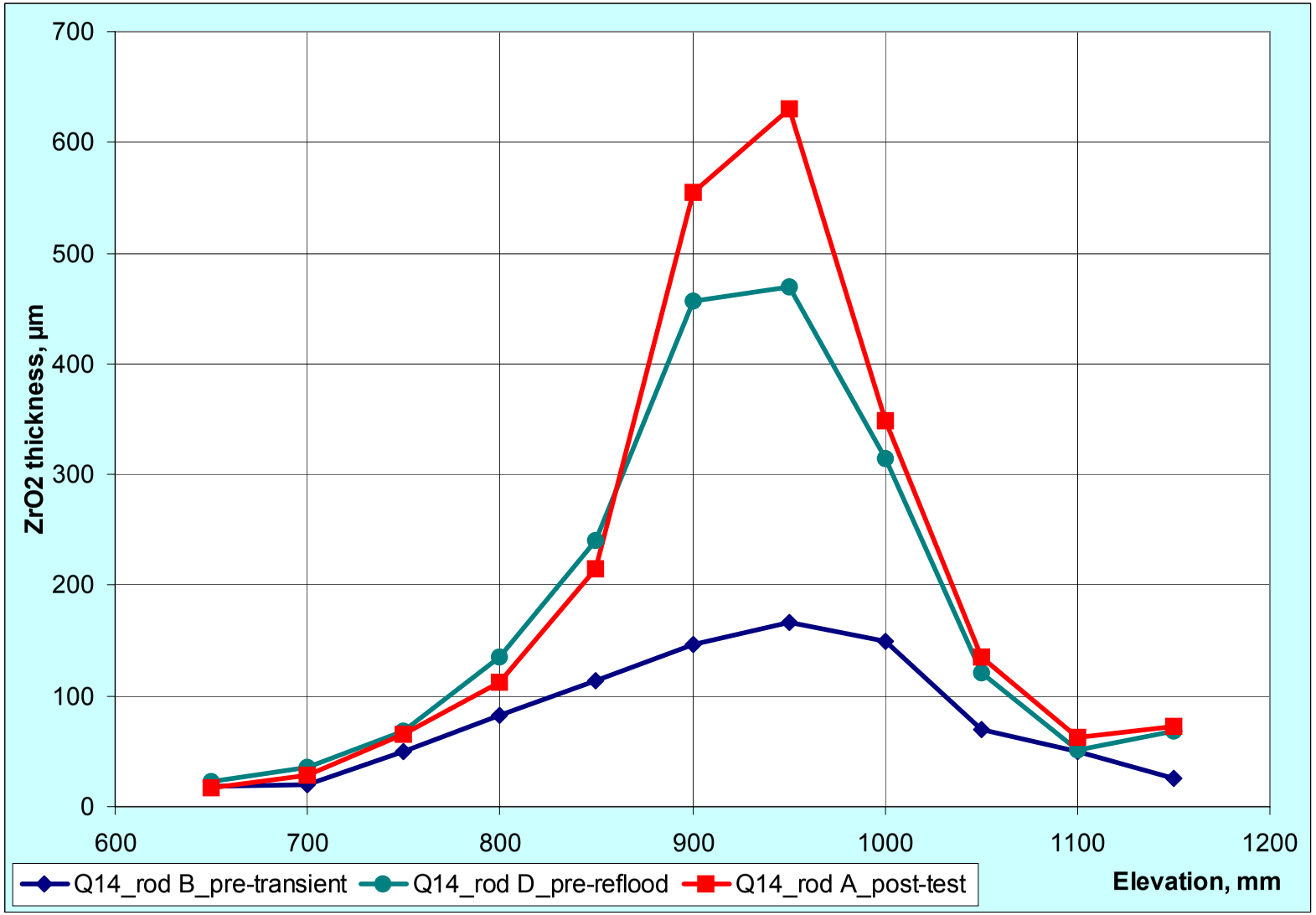

Fig. 30: QUENCH-14; Axial oxide layer thickness distribution of Zry-4 corner rods B (withdrawn at the end of pre-oxidation), D (at the end of the transient) and A (after the test), evaluated by metallography.

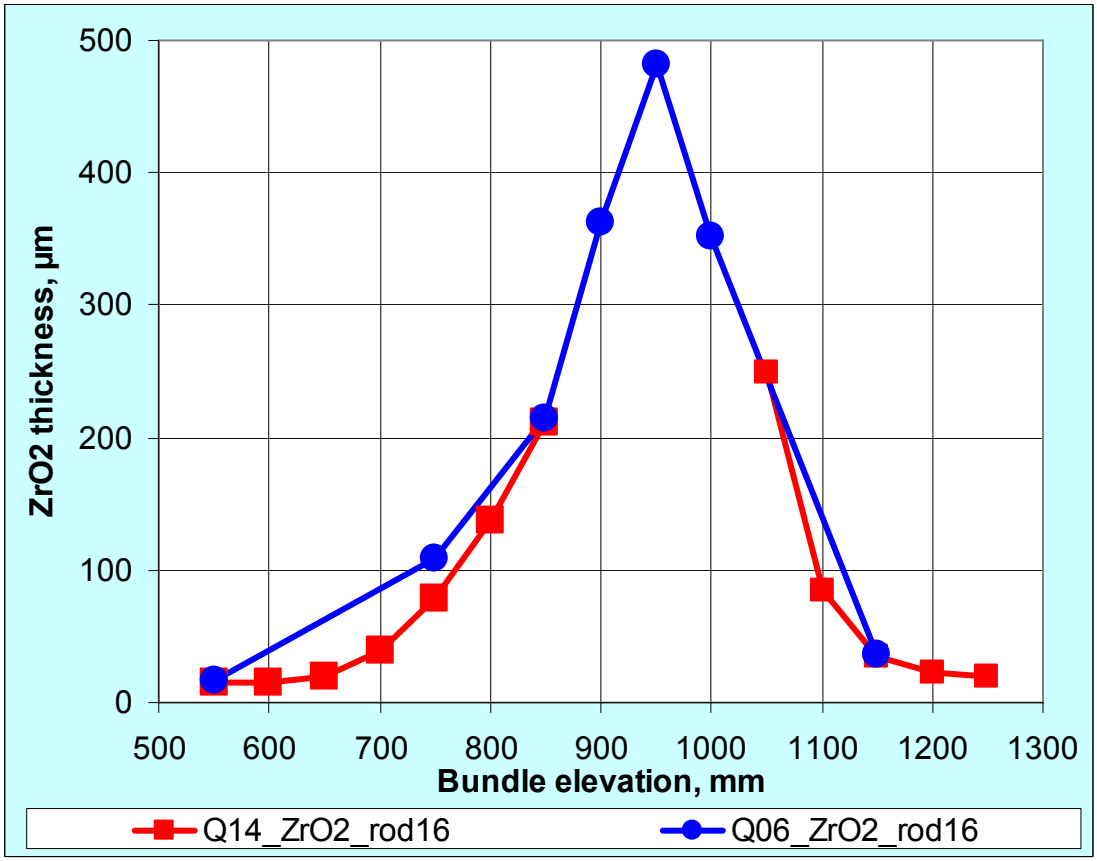

Fig. 31: Axial oxide layer profile of rod No. 16 of the QUENCH-14 test bundle (M5®) compared to the QUENCH-06 data (Zircaloy-4).

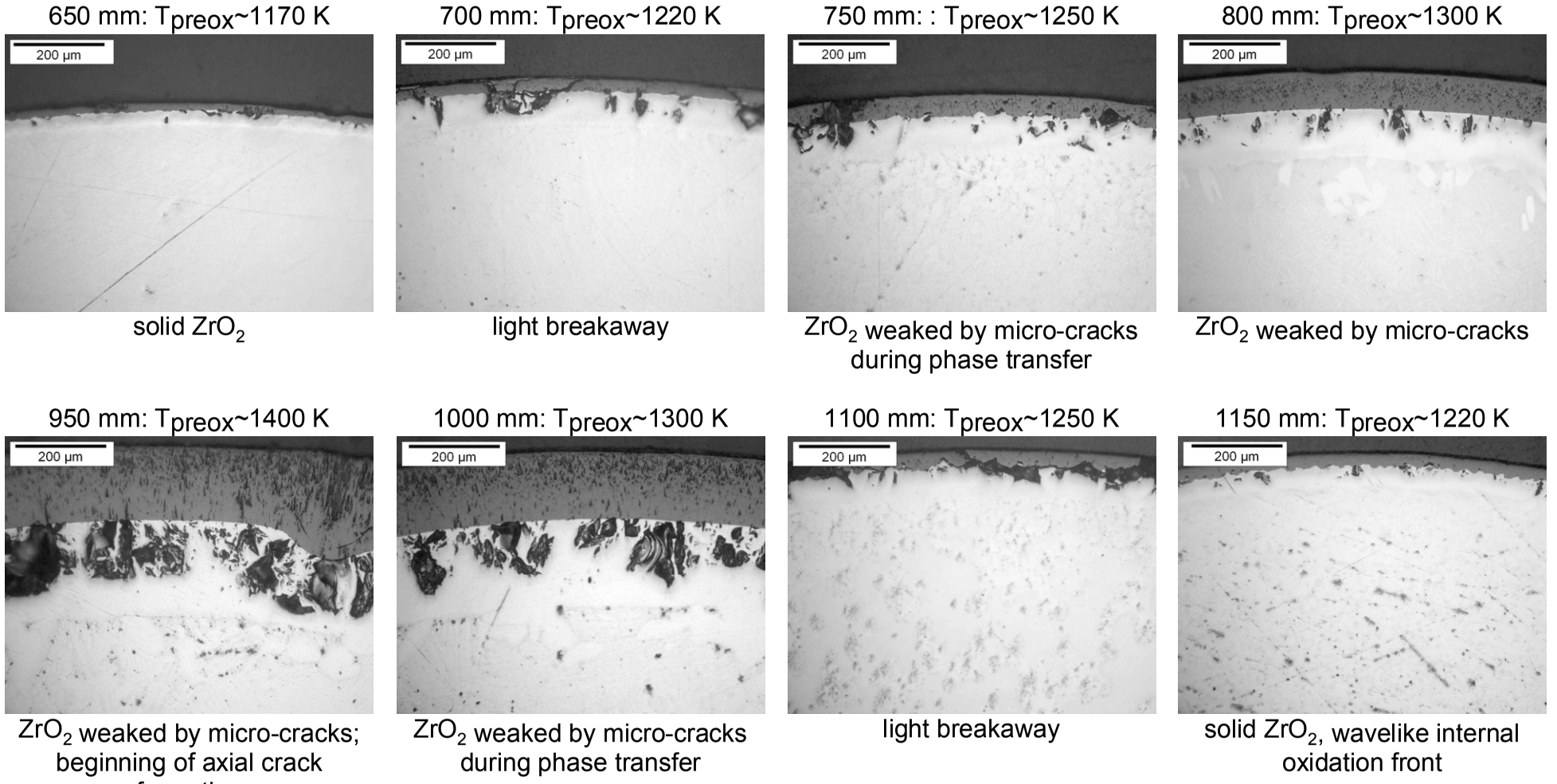

Fig. 32: QUENCH-14; ZrO_2 structure of solid corner rod B withdrawn at the end of preoxidation.

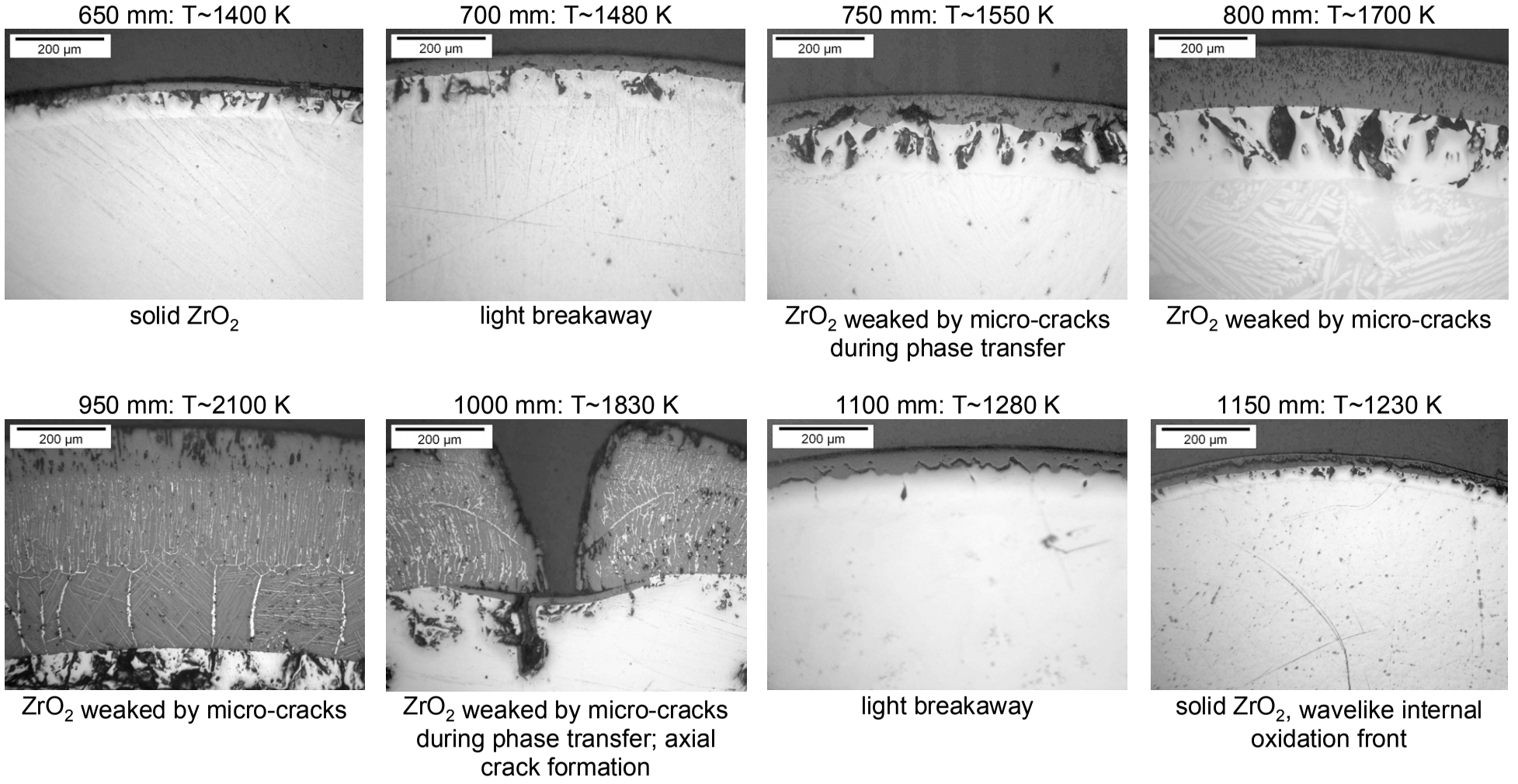

Fig. 33: QUENCH-14; ZrO_2 structure of solid corner rod D withdrawn at the end of transient.

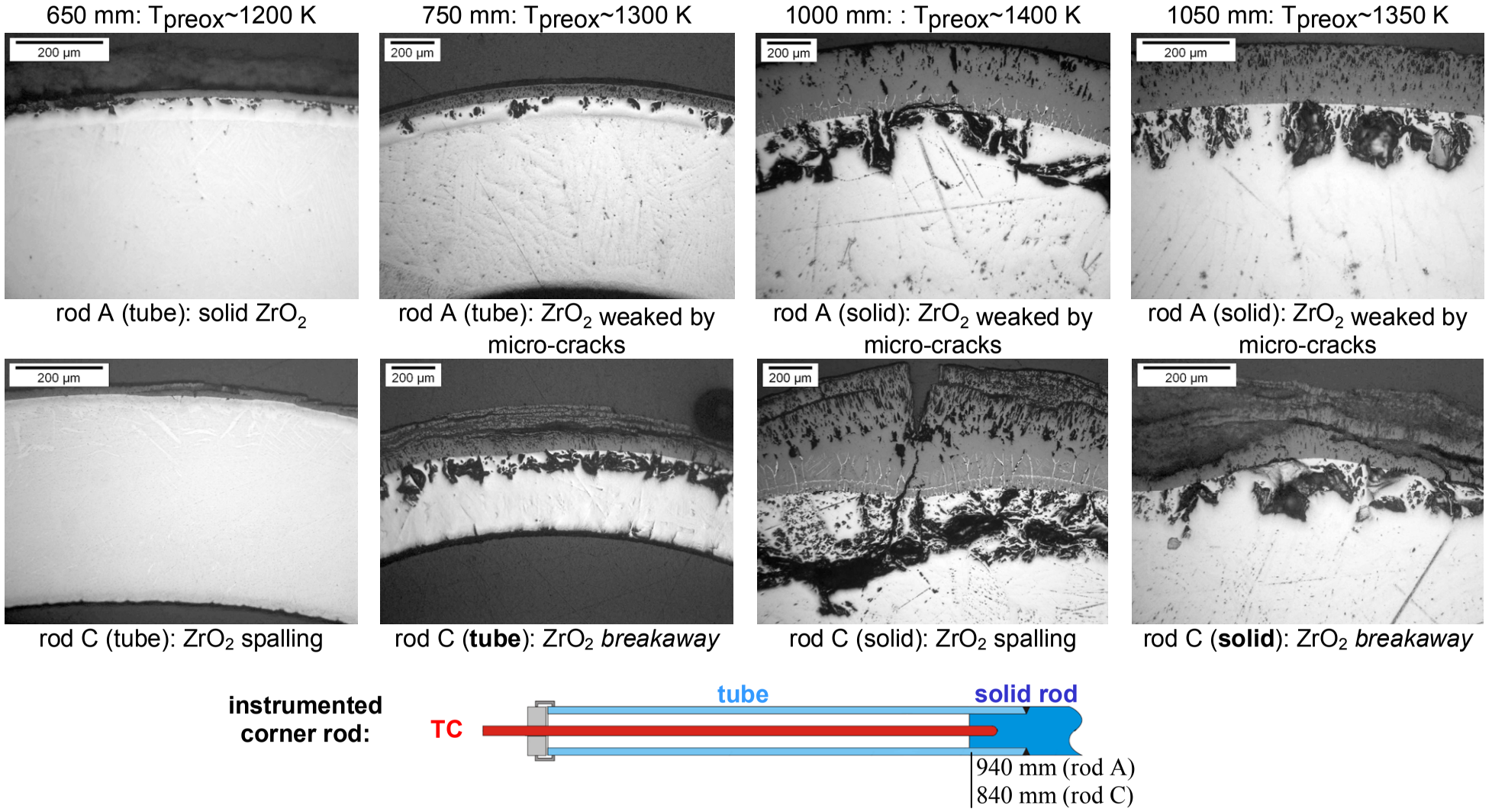

Fig. 34: QUENCH-14; Comparison of ZrO_2 structure of instrumented corner rods A (Zry-4) and C (E110) withdrawn after the test; breakaway for external ZrO_2 sub-layer formed during preoxidation on surface of rod C.

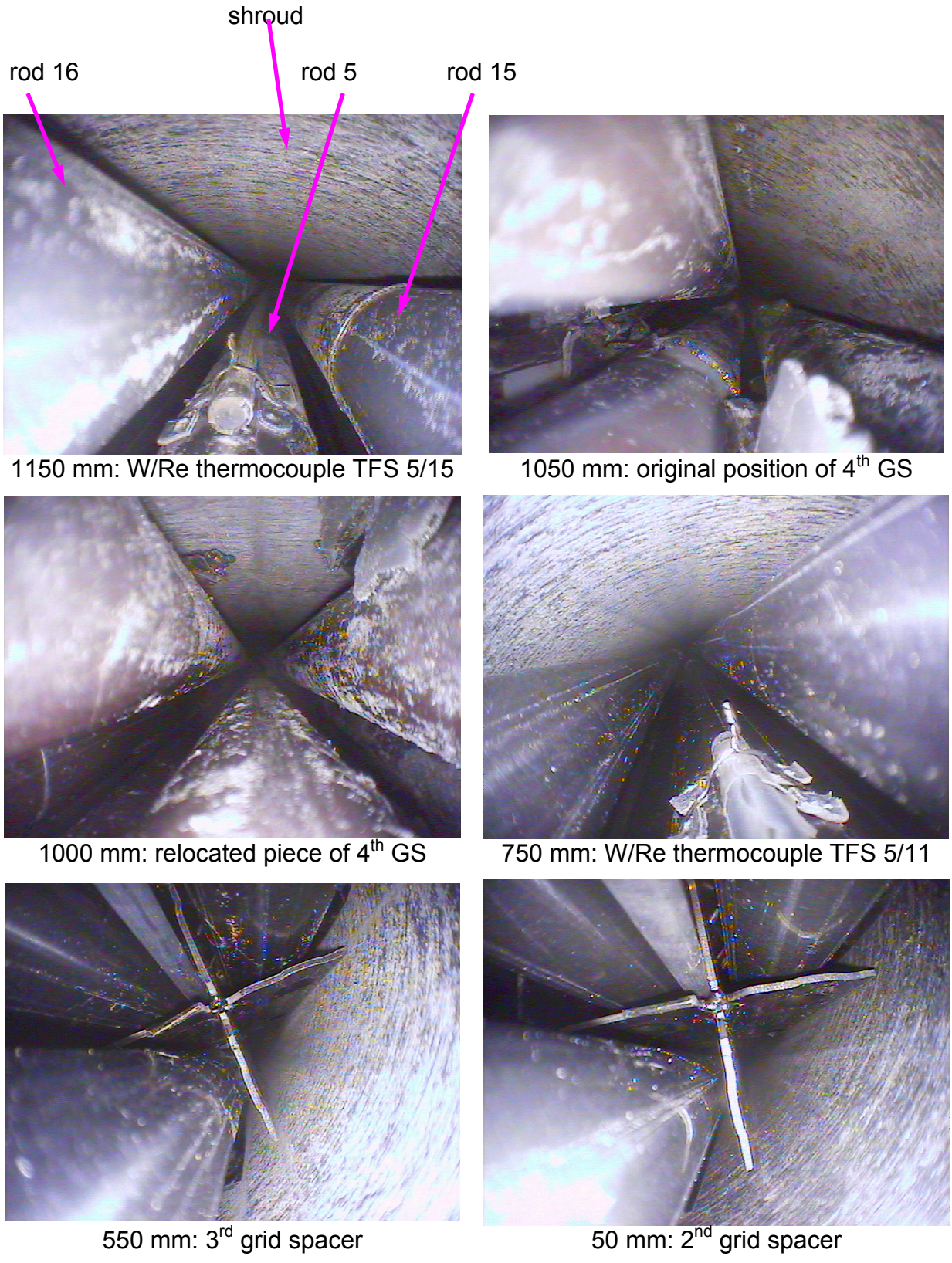

Fig. 35: QUENCH-14; Post-test videoscope observations at the position of the withdrawn corner rod B. View from bottom.

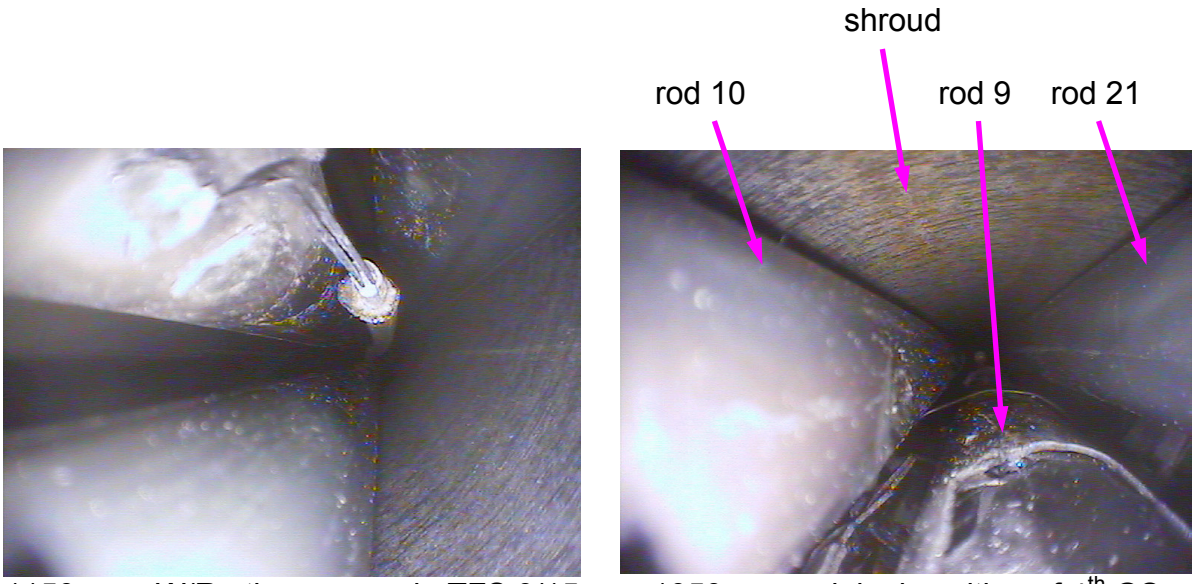

1150 mm: W/Re thermocouple TFS 9/15

1050 mm: original position of 4th GS

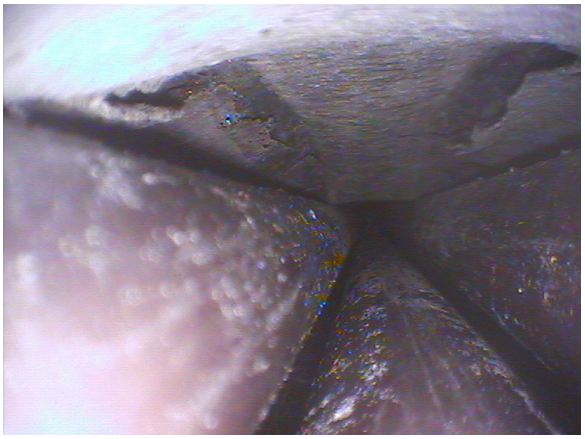

1000 mm: melt on shroud

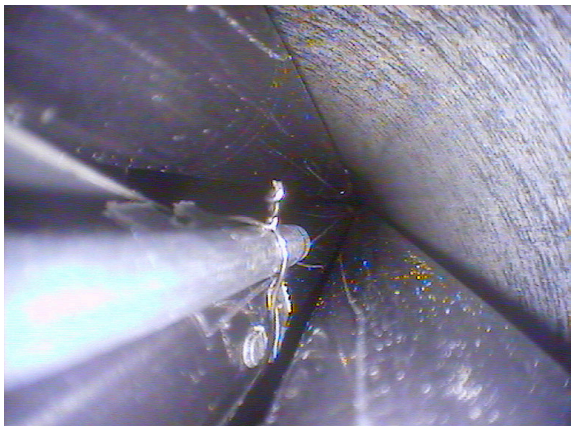

750 mm: W/Re thermocouple TFS 9/11

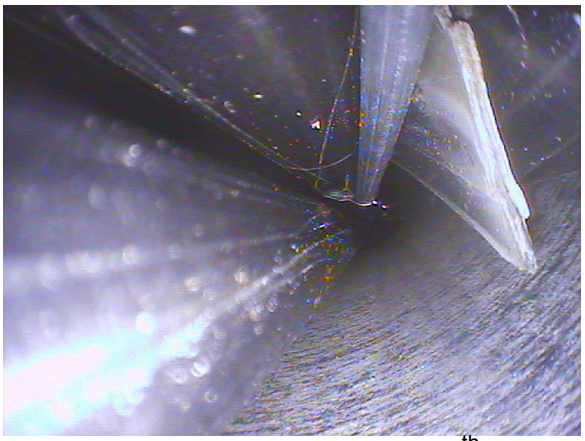

700 mm: relocated piece of 4th GS

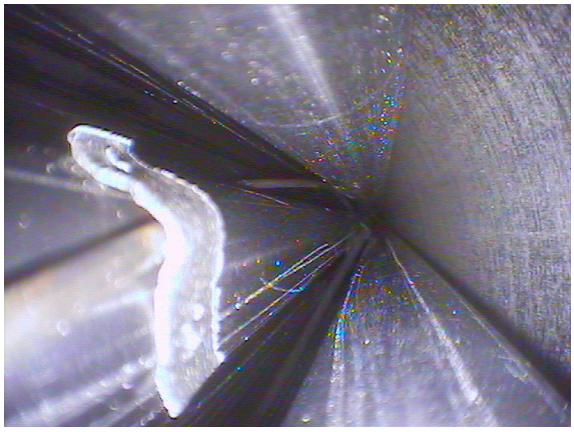

450 mm: NiCr/Ni thermocouple TFS 9/8

Fig. 36: QUENCH-14; Post-test videoscope observations at the position of the withdrawn corner rod D. View from bottom.

0° 90° 180° 270°

Fig. 37: QUENCH-14; Posttest view of the test bundle at elevations 500-800 mm.

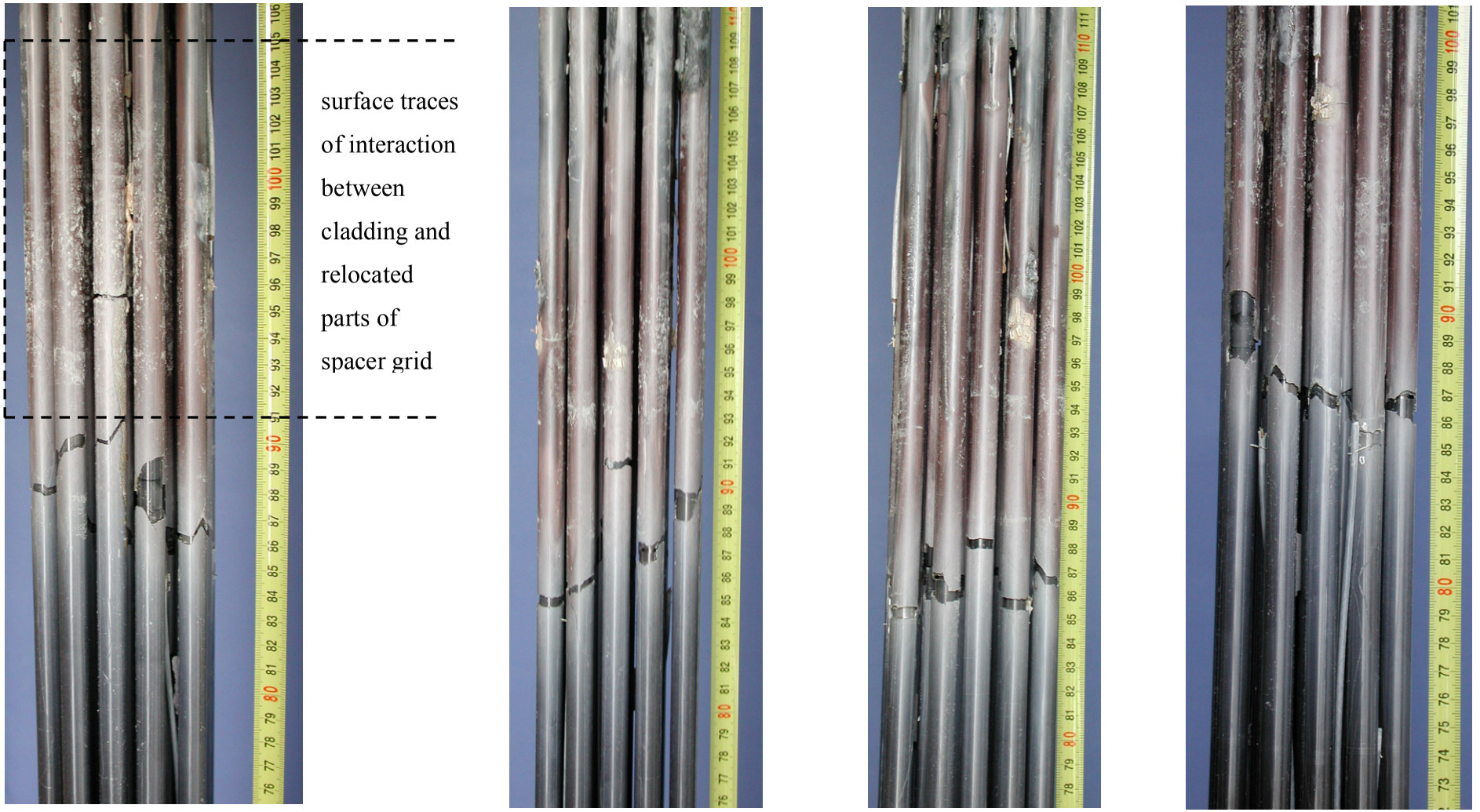

Fig. 38: QUENCH-14; Posttest view of the test bundle at elevations 800-1000 mm (cladding breaches caused by disassembly of test bundle and shroud).

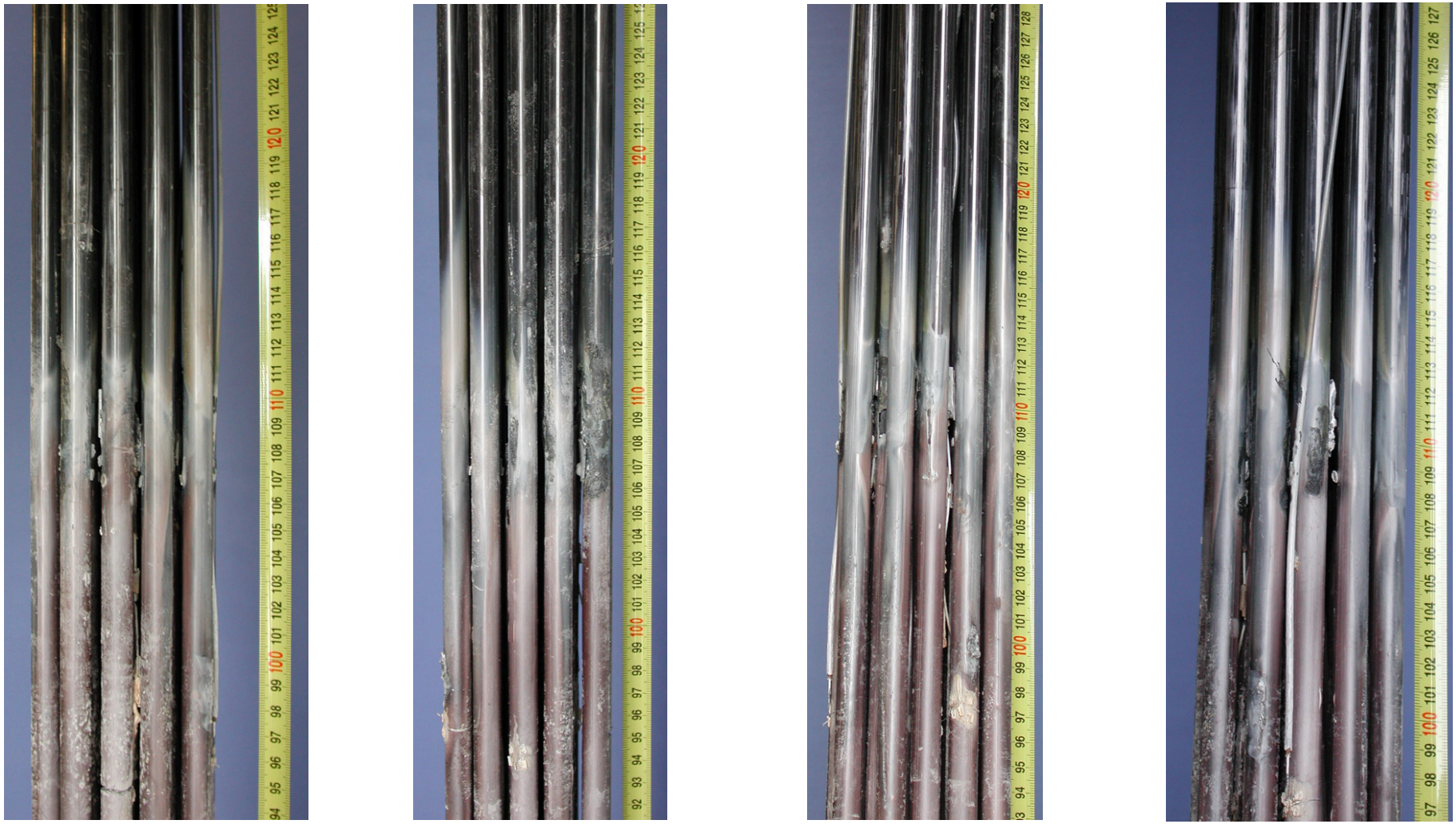

Fig. 39: QUENCH-14; Posttest view of the test bundle at elevations 1000-1200 mm.

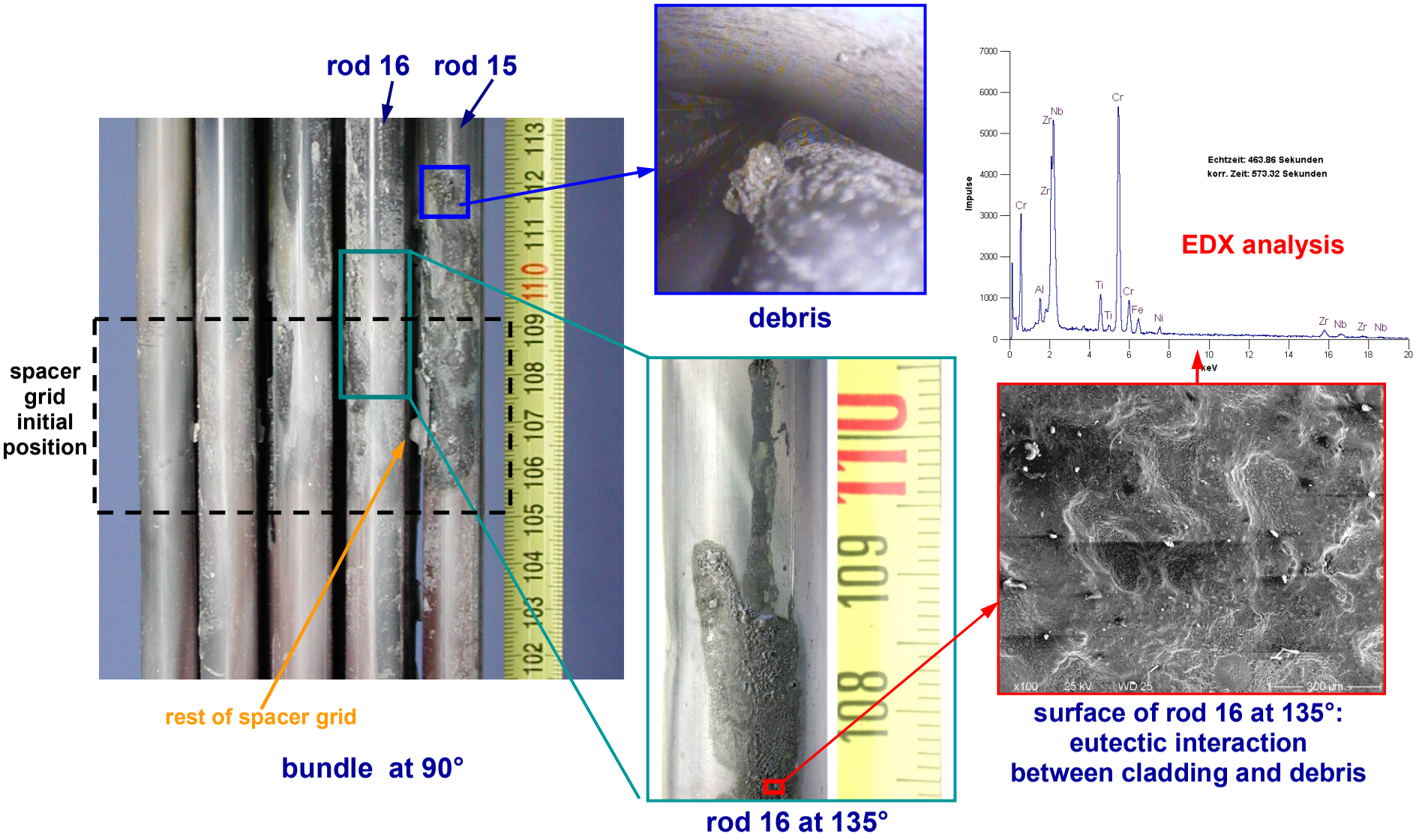

Fig. 40: QUENCH-14; debris buildup at spacer grid #4 (1050 mm).

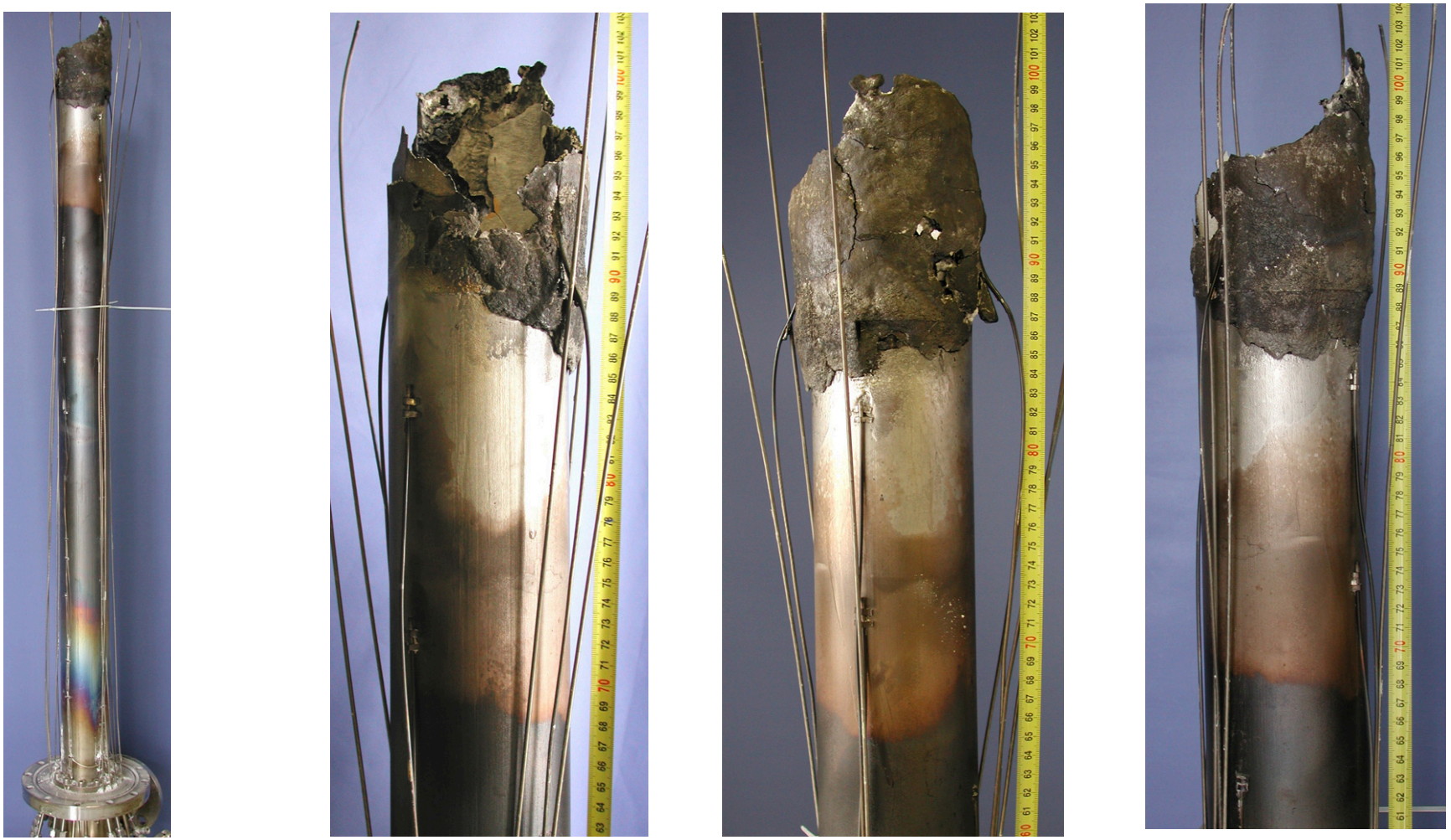

250° 0° 180° 250°

Fig. 41: QUENCH-14; Posttest appearance of the lower part of the shroud (viewed from different azimuthal positions) at elevations -300 to 1000 mm and 600-1000 mm, respectively.

0° 90° 180° 270°

Fig. 42: QUENCH-14; Posttest view of the upper part of the shroud at elevations 1000-1300 mm.

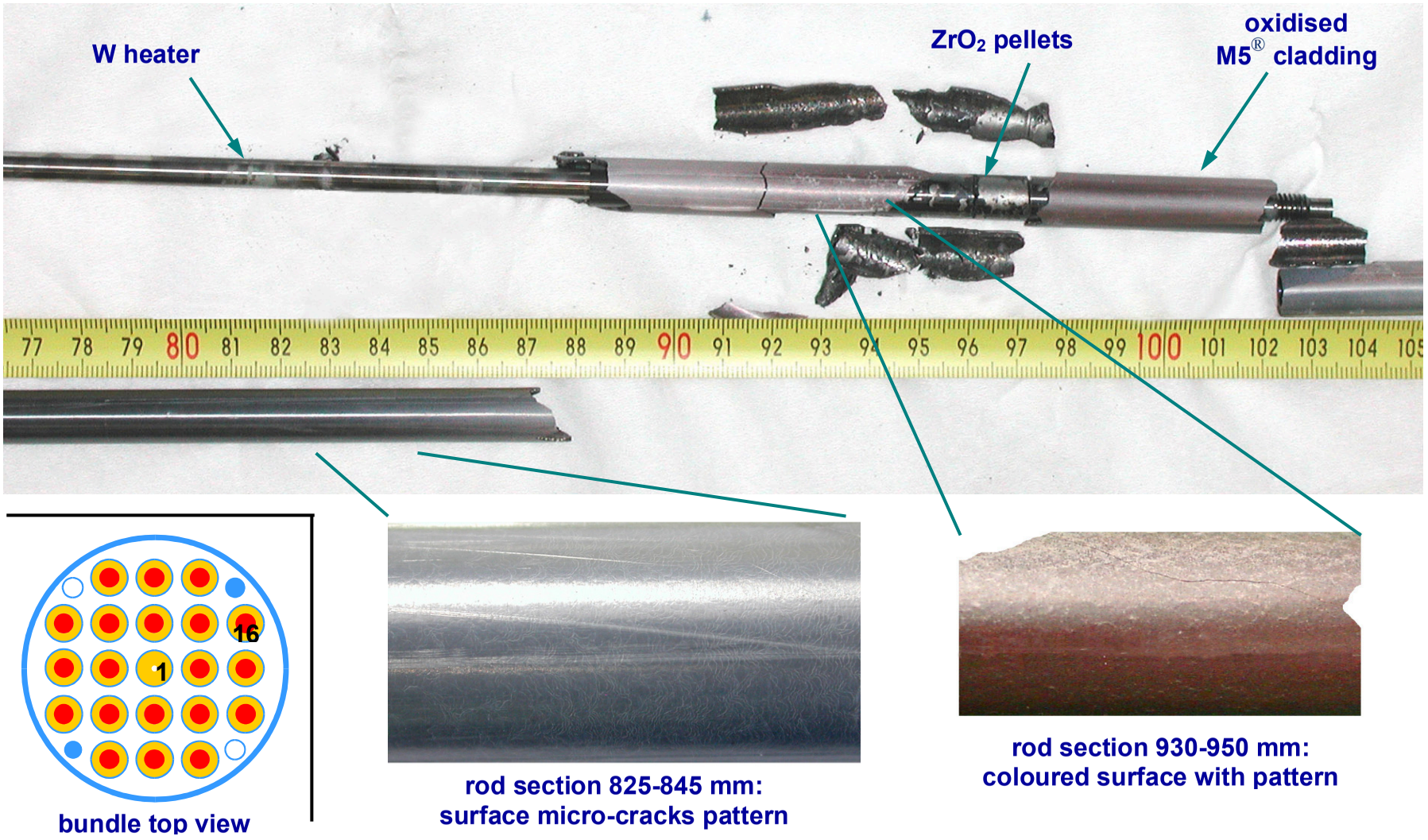

Fig. 43: Appearance of test rod No. 16 after removed from the QUENCH-14 test bundle.

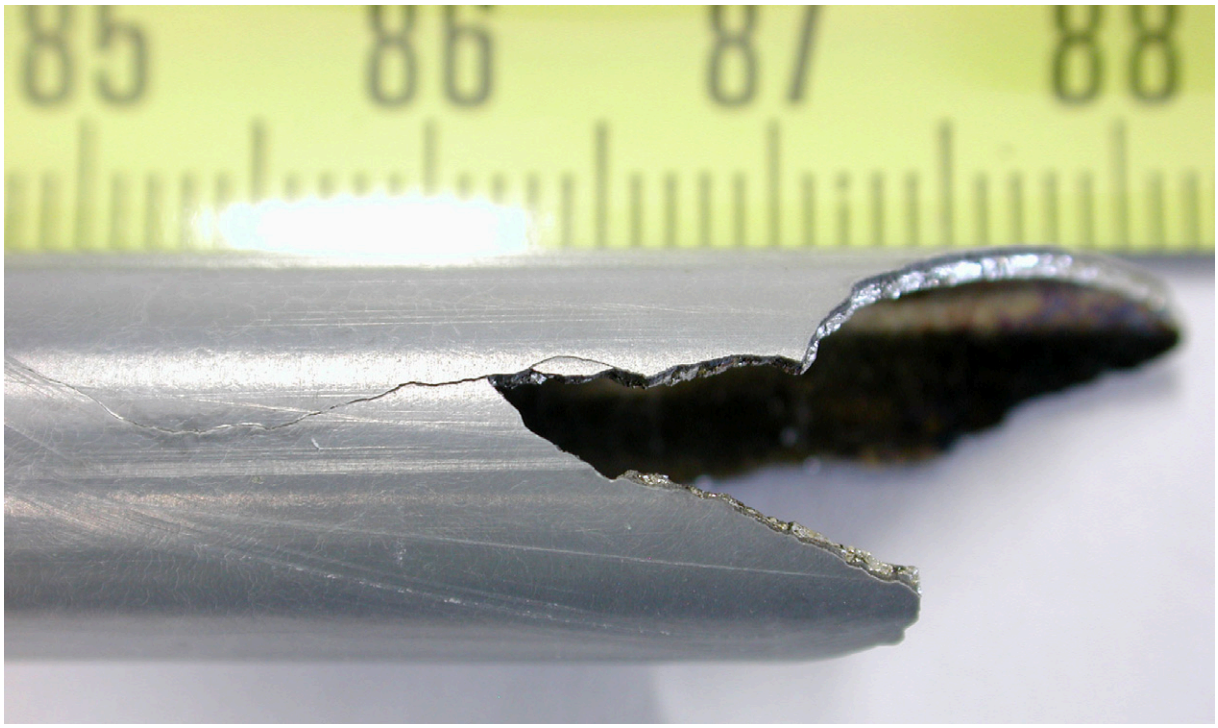

Upper position of lower part of cladding: 880 mm

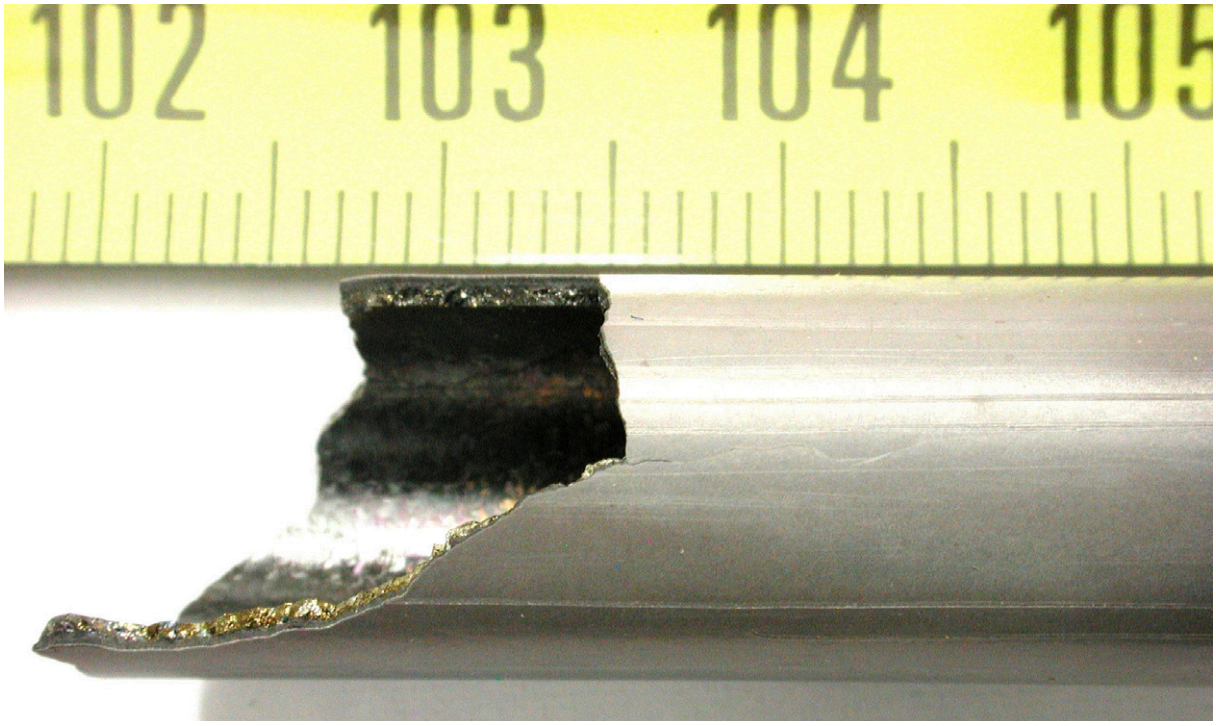

Lower position of upper part of cladding:1020 mm

Fig. 44: QUENCH-14; Cladding rupture of fuel rod simulator No. 16 during handling.

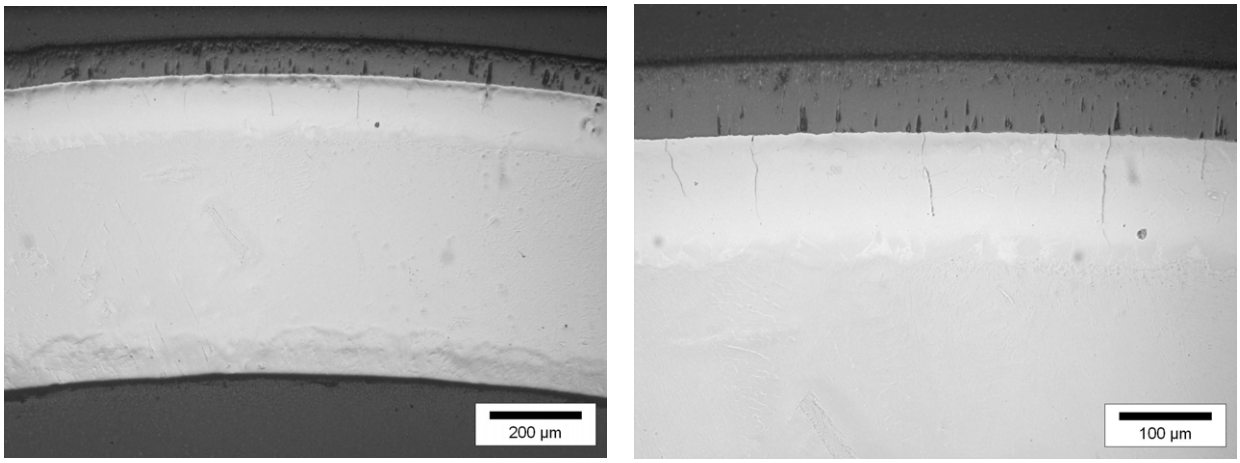

Elevation 750 mm

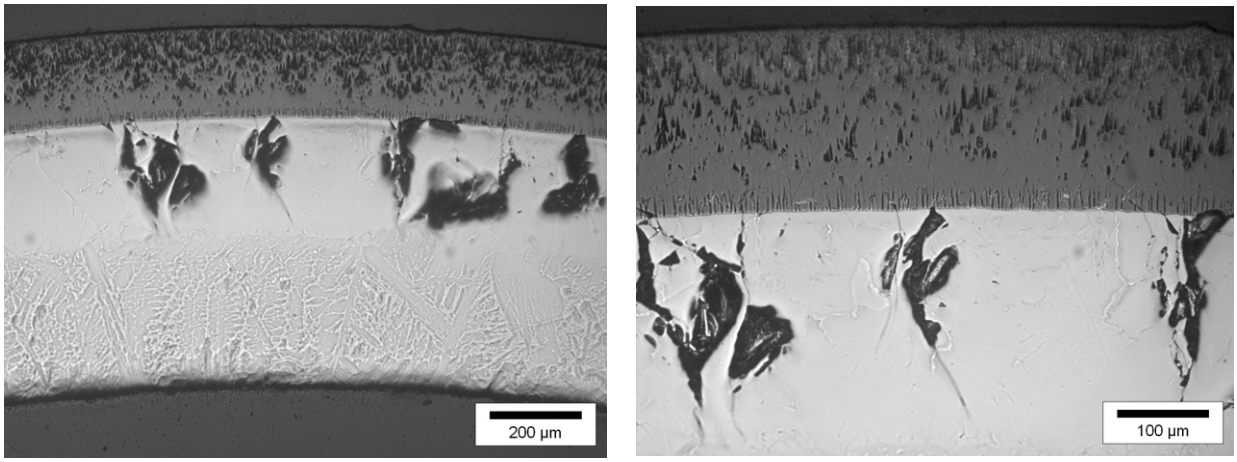

Elevation 850 mm

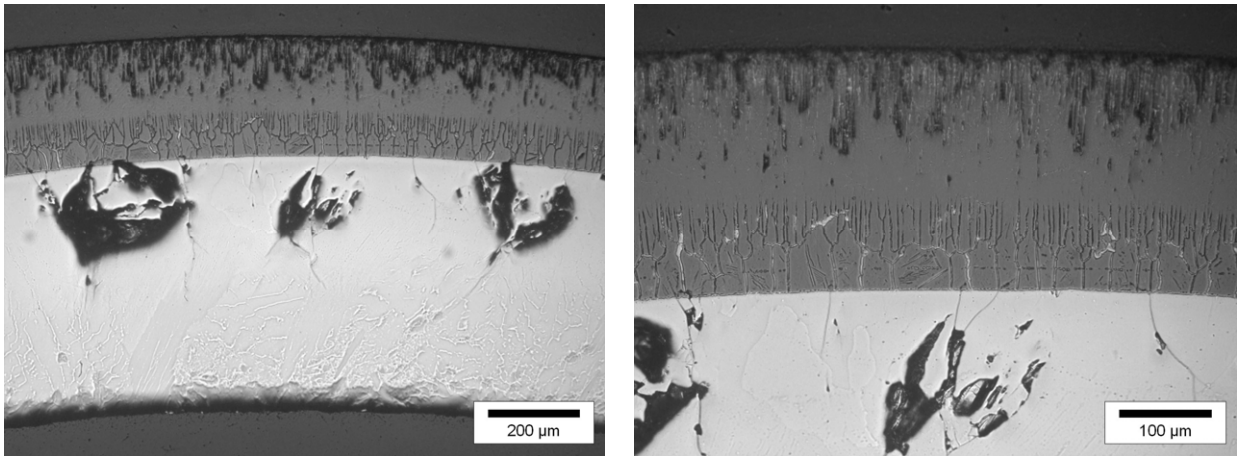

Elevation 1050 mm

Fig. 45: QUENCH-14; Microstructure of the cladding tube of rod No. 16 withdrawn after the test.

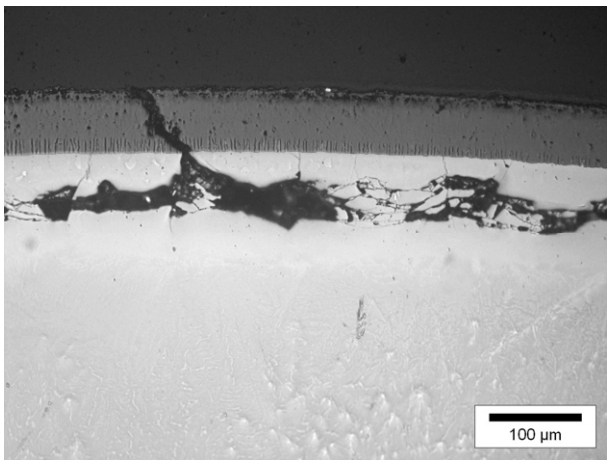

Elevation 1100 mm,
135° orientation: facing “cold” shroud side

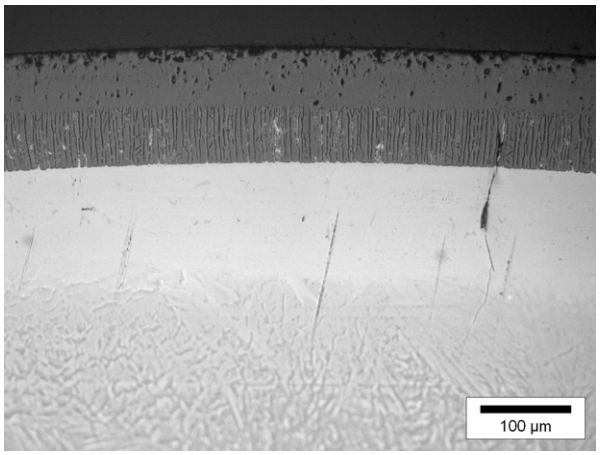

Elevation 1100 mm,
225° orientation: facing “hot” bundle side

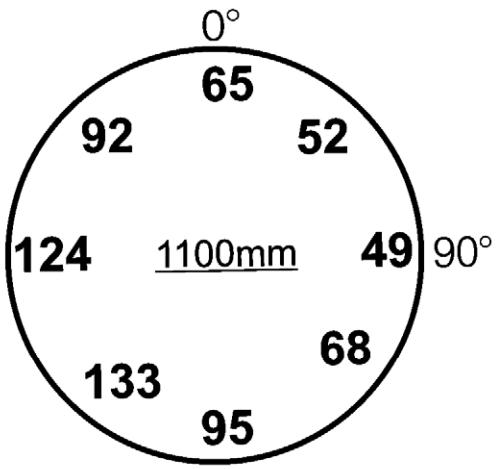

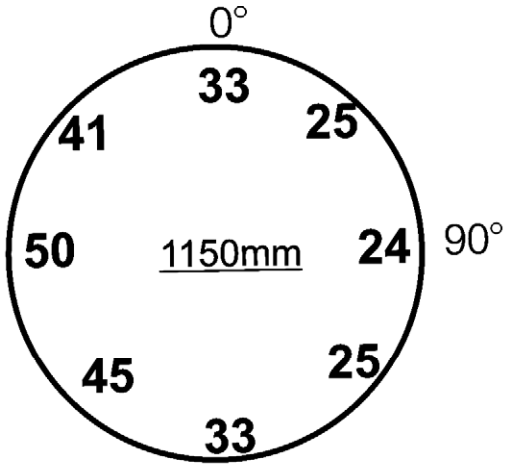

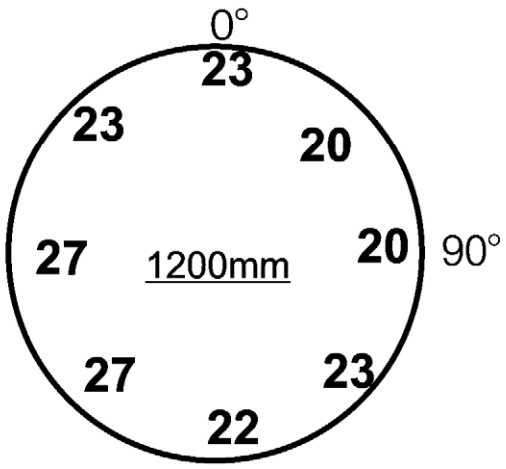

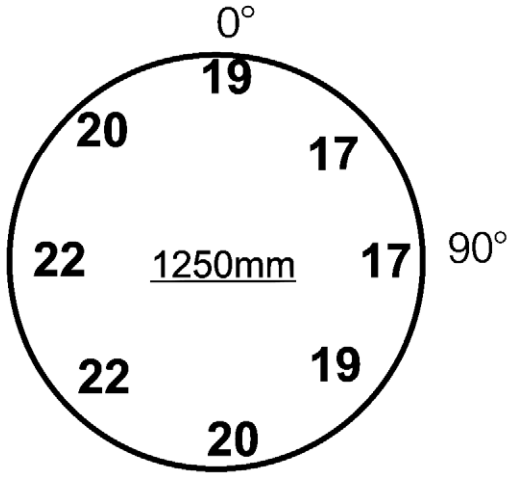

Fig. 46: QUENCH-14; Circumferential distribution of ZrO_2 thickness [µm] at different elevations of peripheral rod 16.

QUE-14-1 **550 mm**

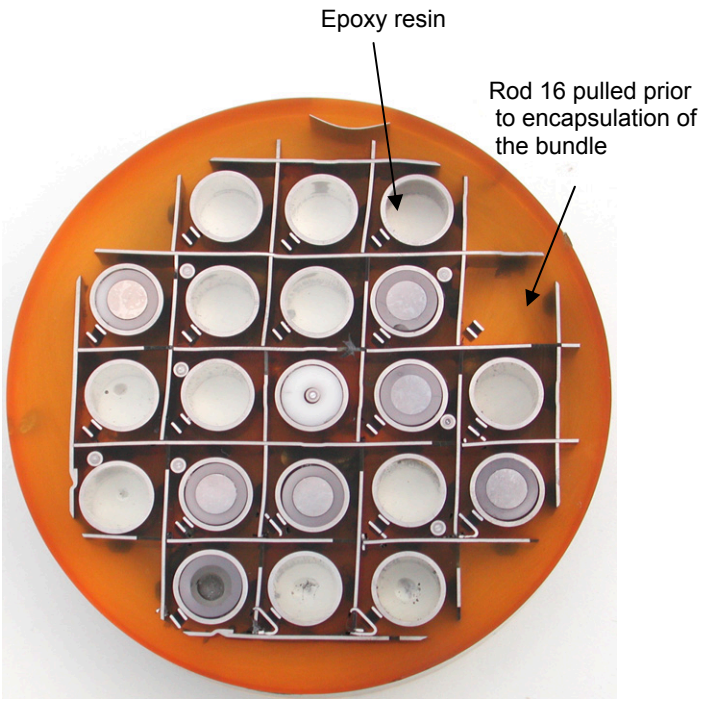

QUE-14-1 **570 mm**

QUE-14-2 **636 mm**

QUE-14-2 **650 mm**

Fig. 47: QUENCH-14; Bundle cross sections at 550 mm, 570 mm, 636 mm and 650 mm (top view).

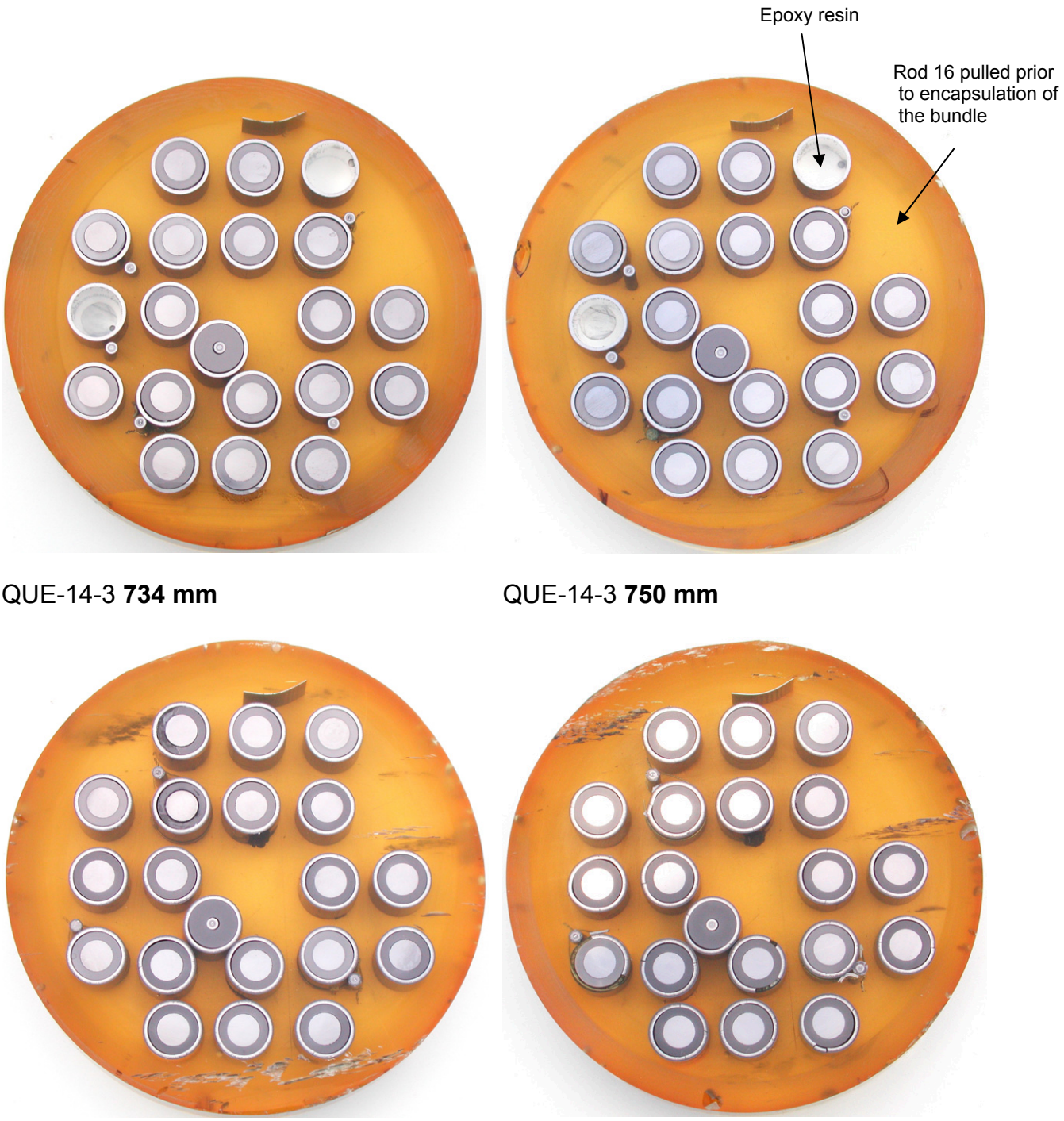

QUE-14-3 **734 mm**

QUE-14-3 **750 mm**

QUE-14-4 **834 mm**

QUE-14-4 **850 mm**

Fig. 48: QUENCH-14; Bundle cross sections at 734 mm, 750 mm, 834 mm and 850 mm (top view).

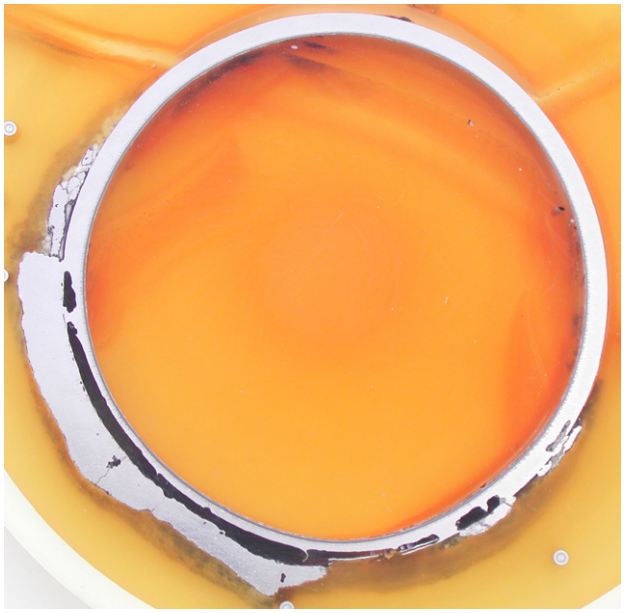

QUE-14-11 **885 mm**

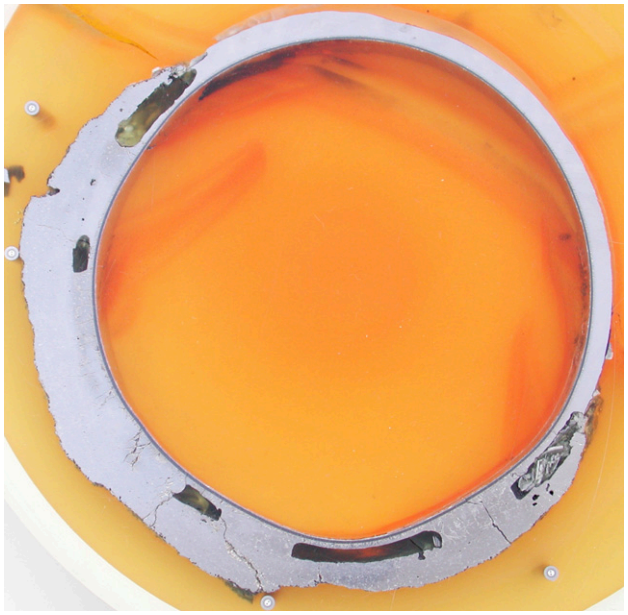

QUE-14-11 **900 mm**

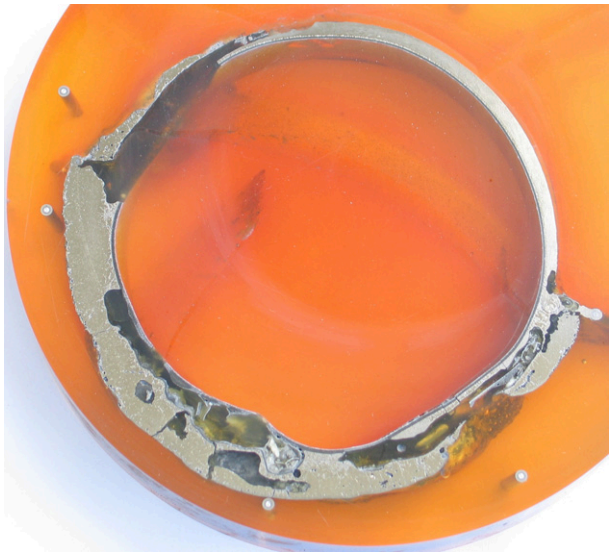

QUE-14-16 **925 mm**

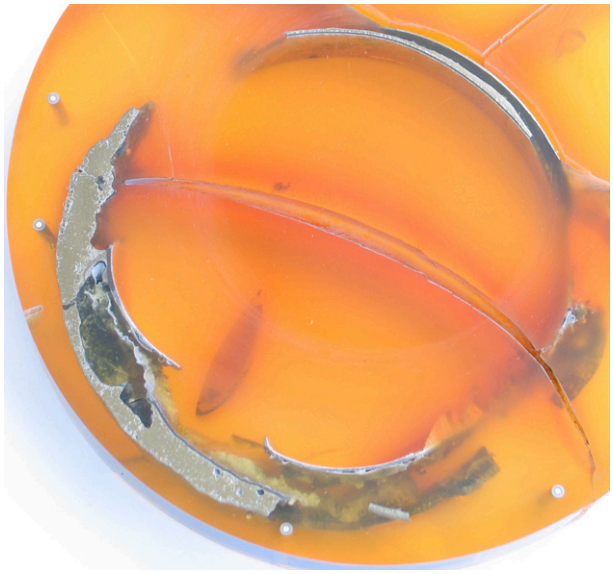

QUE-14-17 **950 mm**

Fig. 49: QUENCH-14; Shroud cross sections at 885 mm, 900 mm, 925 mm and 950 mm (top view).

QUE-14-9 **900 mm**

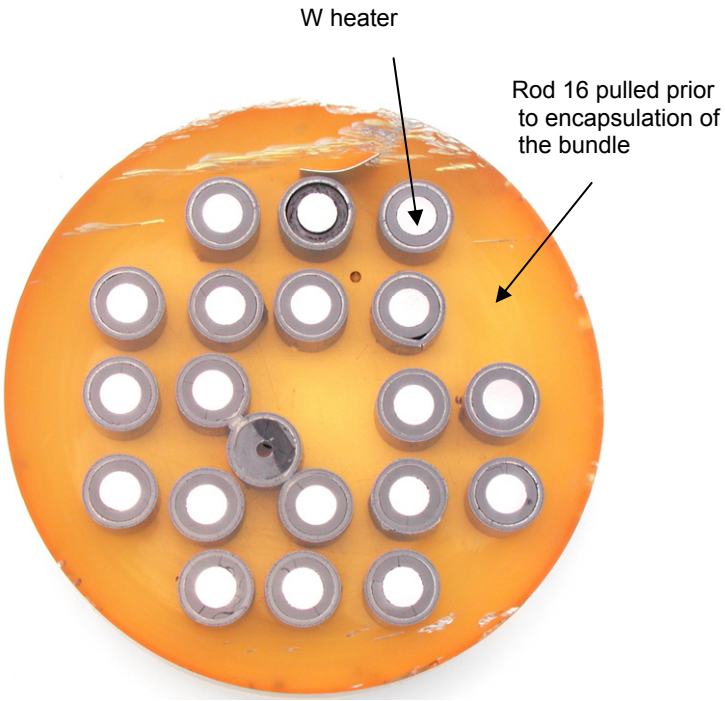

QUE-14-5 **934 mm**

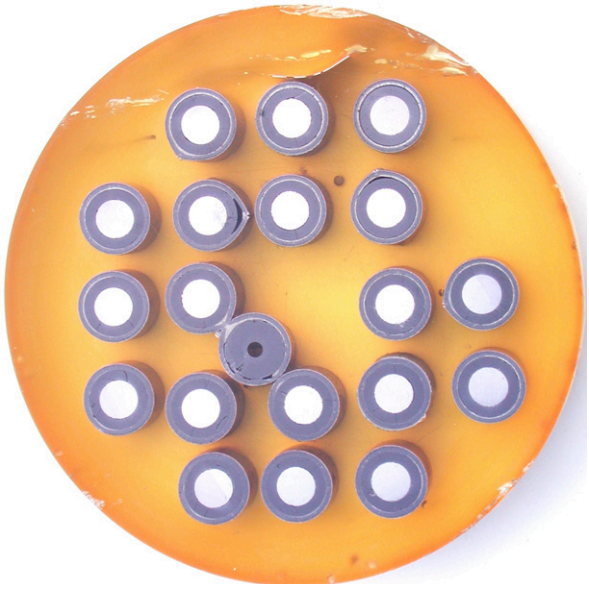

QUE-14-5 **950 mm**

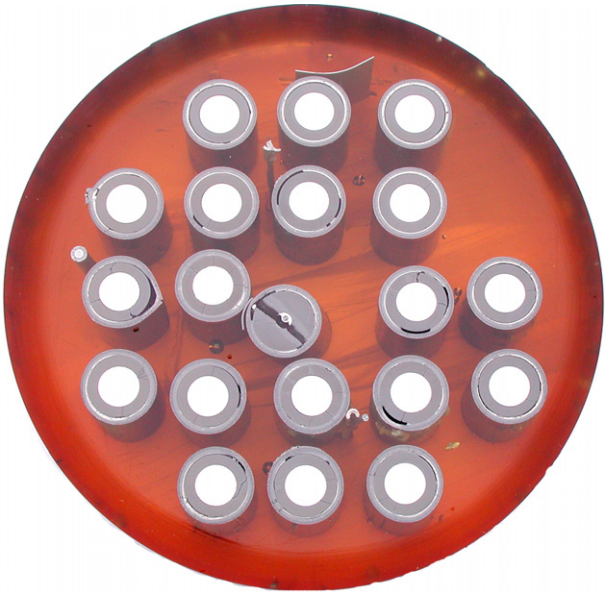

QUE-14-10 **1000 mm**

Fig. 50: QUENCH-14; Bundle cross sections at 900 mm, 934 mm, 950 mm and 1000 mm.

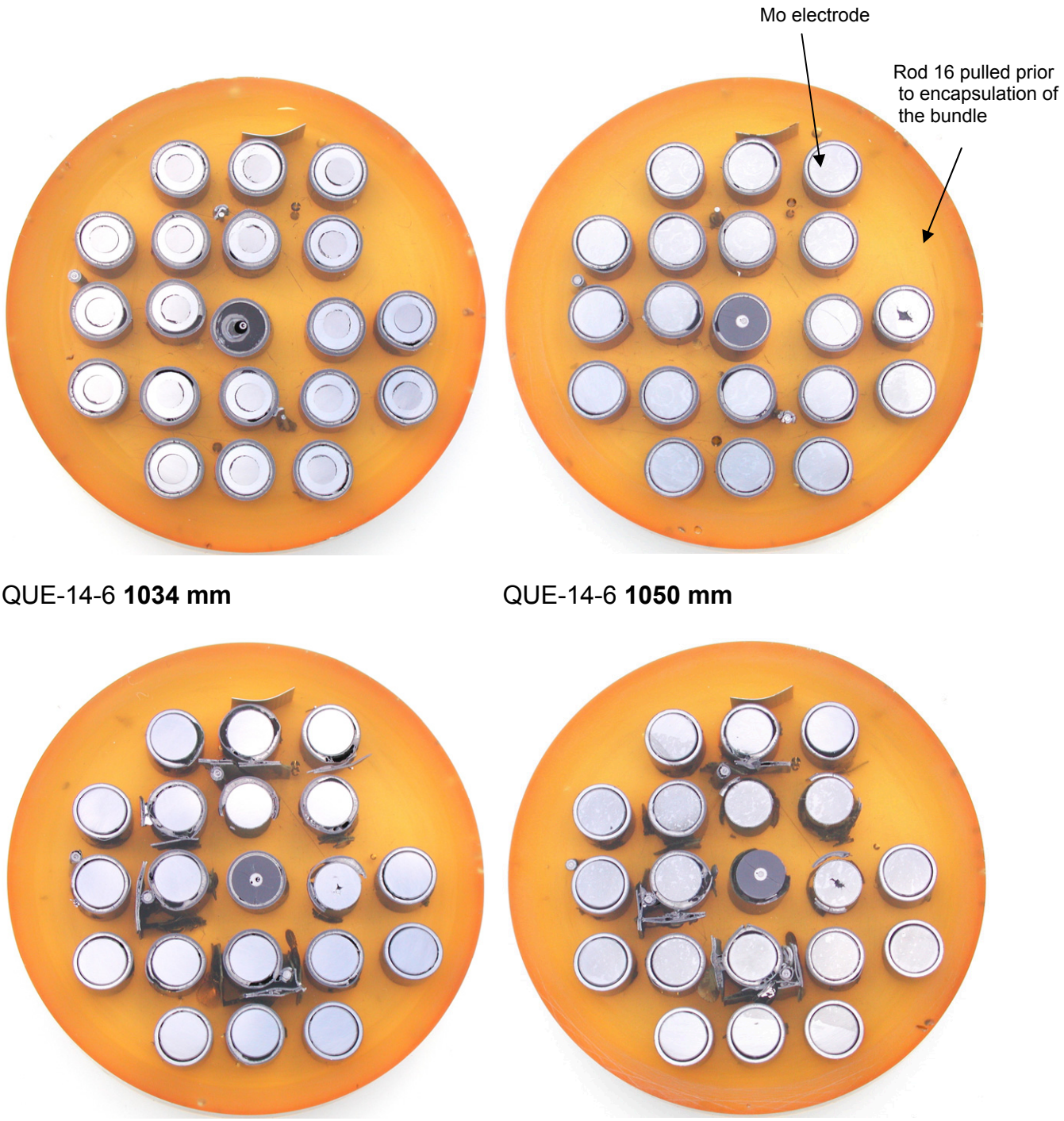

QUE-14-6 **1034 mm**

QUE-14-6 **1050 mm**

QUE-14-7 **1084 mm**

QUE-14-7 **1100 mm**

Fig. 51: QUENCH-14; Bundle cross sections at 1034 mm, 1050 mm, 1084 mm and 1100 mm (top view).

QUE-14-8 **1134 mm**

QUE-14-8 **1150 mm**

Fig. 52: QUENCH-14; Bundle cross sections at 1134 mm and 1150 mm (top view).

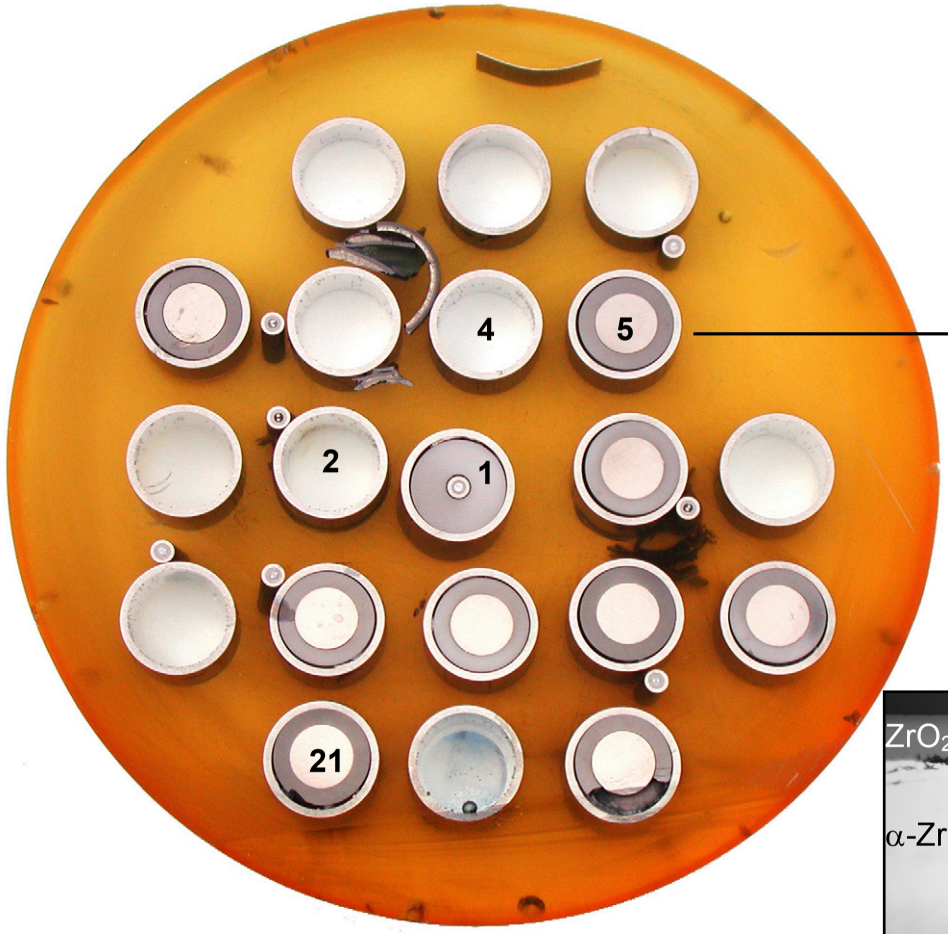

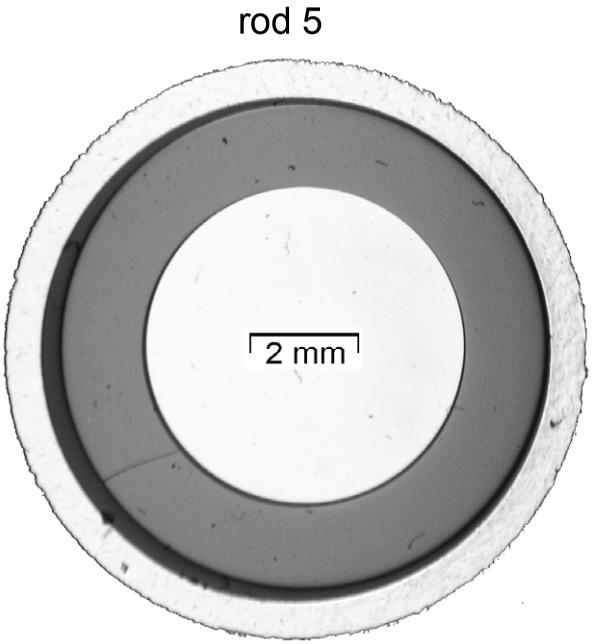

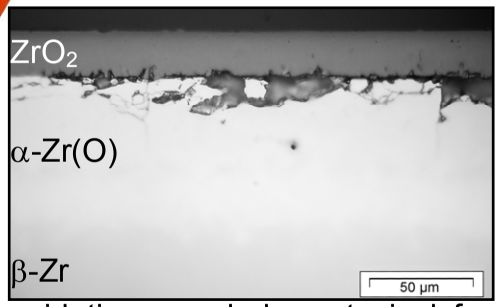

oxidation morphology, typical for long-term oxidation at moderate temperatures T<1473 K

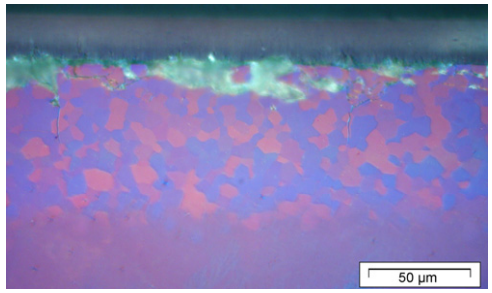

polarized light: relatively thick α-Zr(O) layer

Fig. 53: QUENCH-14: Cross section at 636 mm bundle elevation; overview, oxidation state of rod No. 5.

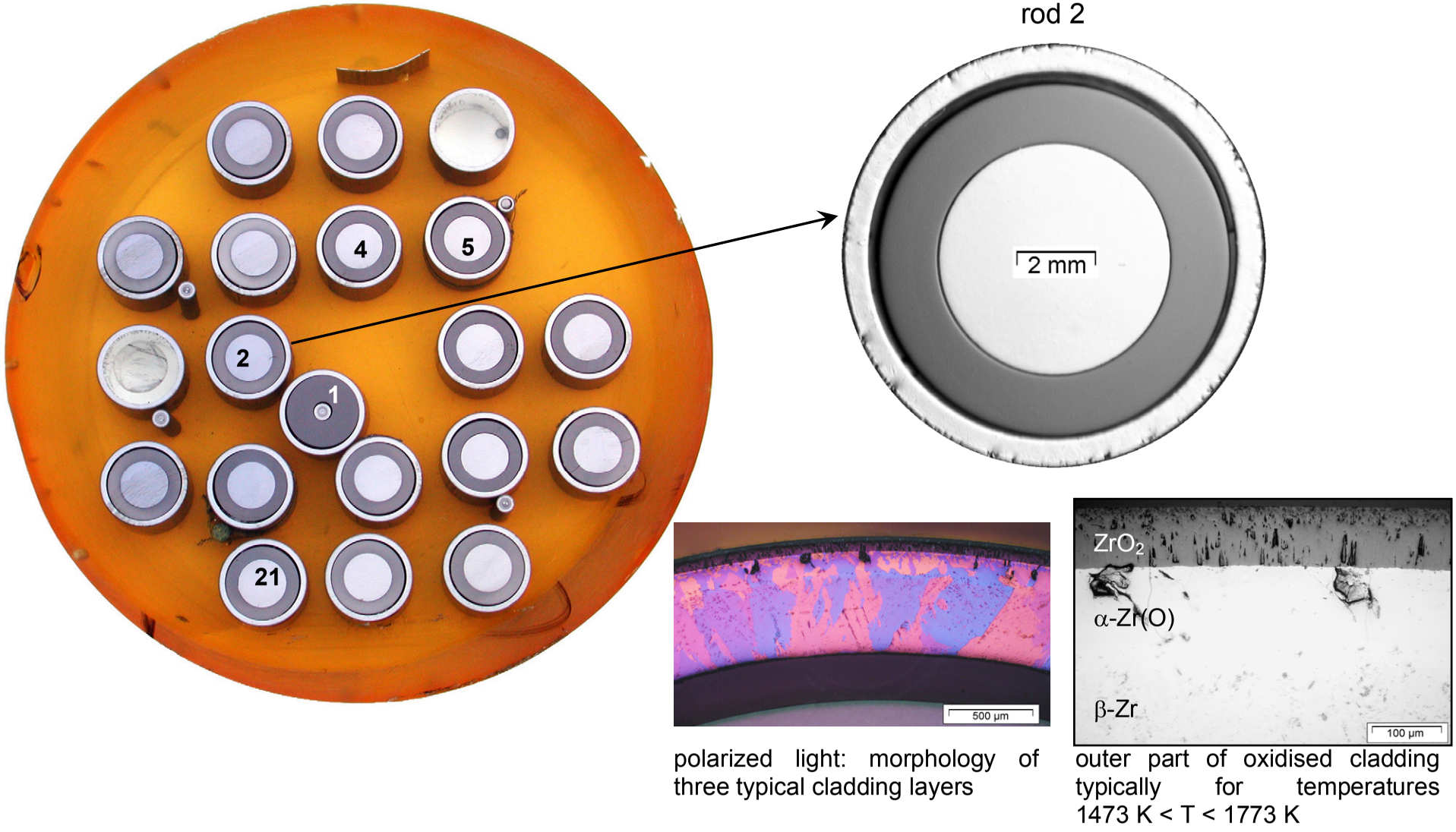

polarized light: morphology of three typical cladding layers

outer part of oxidised cladding typically for temperatures 1473 K < T < 1773 K

Fig. 54: QUENCH-14; Cross section at 750 mm bundle elevation; overview, oxidation state of rod No. 2.

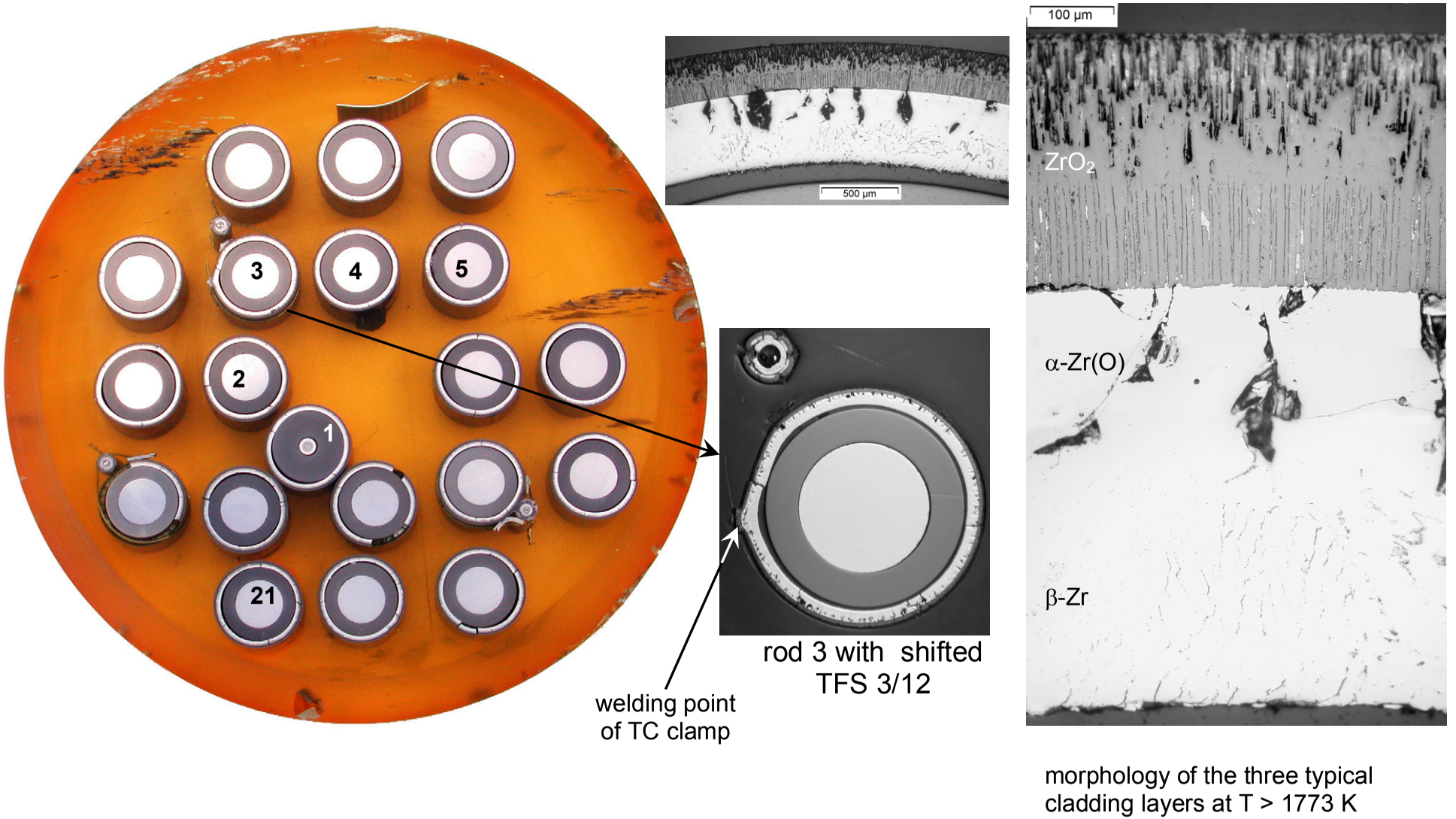

Fig. 55: QUENCH-14; Cross section at 850 mm bundle elevation; overview; oxidation state of rod No. 3.

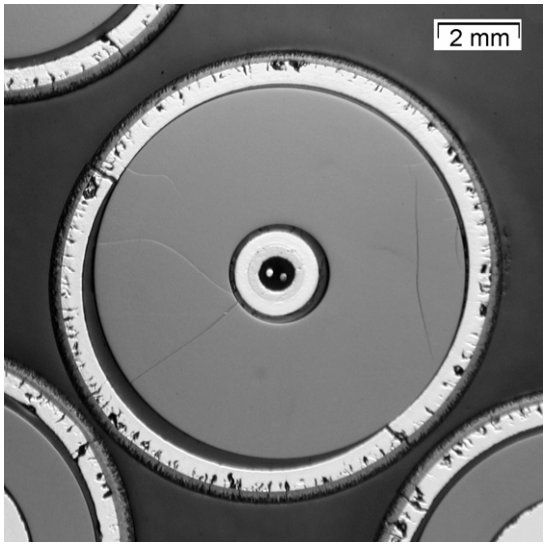

unheated rod 1 with internal TCRC 12

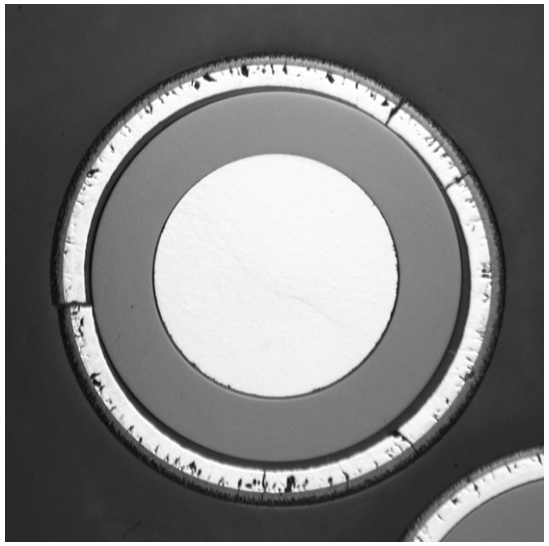

heated rod 2: 5 through going cladding cracks

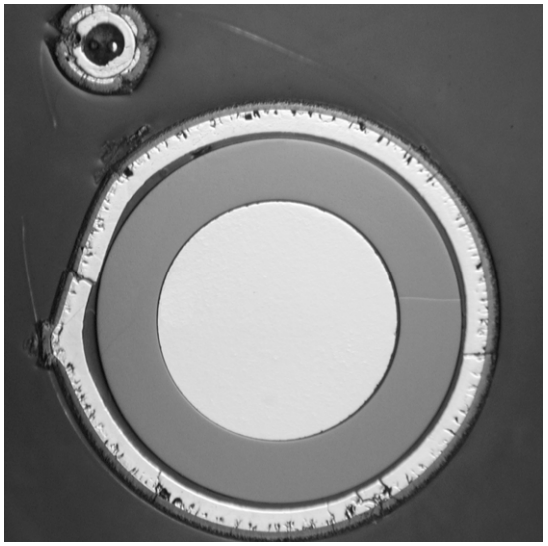

heated rod 3 with decoupled TFS 3/12

heated rod 4: 2 through going cladding cracks

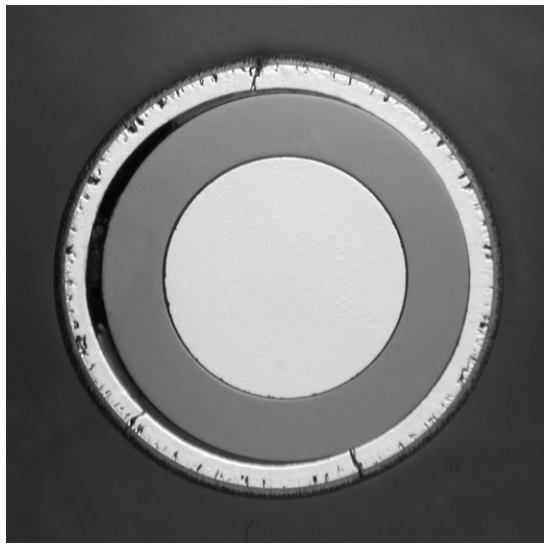

heated rod 5: 3 through going cladding cracks

heated rod 6: 3 through going cladding cracks

Fig. 56: QUENCH-14; Cross section at elevation 850 mm depicting separately test rods 1-6.

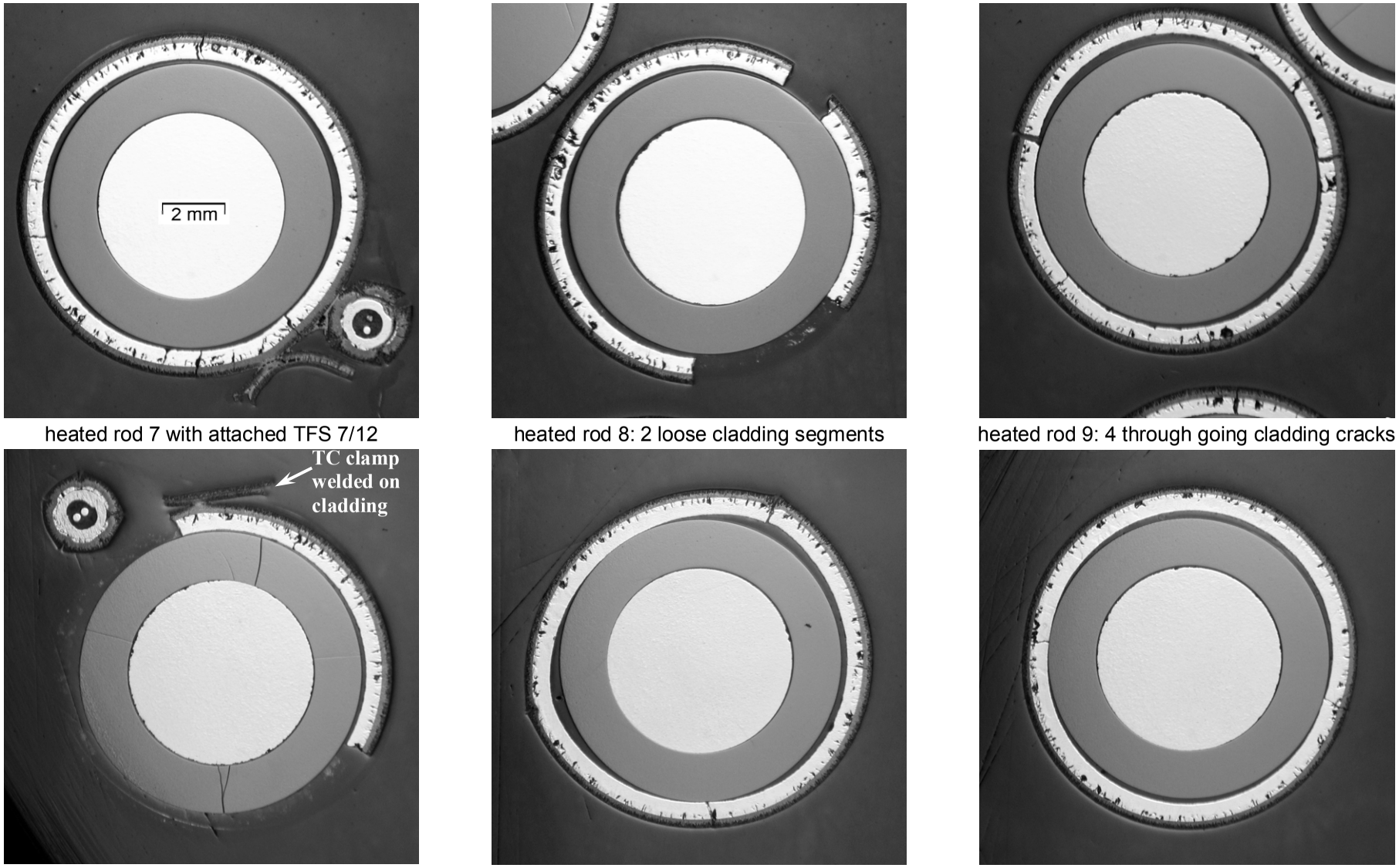

heated rod 7 with attached TFS 7/12 | heated rod 8: 2 loose cladding segments | heated rod 9: 4 through going cladding cracks

heated rod 10 with attached TFS 10/12 | heat. rod 11: deformation and cracking of cladding | heated rod 12: 2 through going cladding cracks

Fig. 57: QUENCH-14; Cross section at elevation 850 mm depicting separately test rods 7-12.

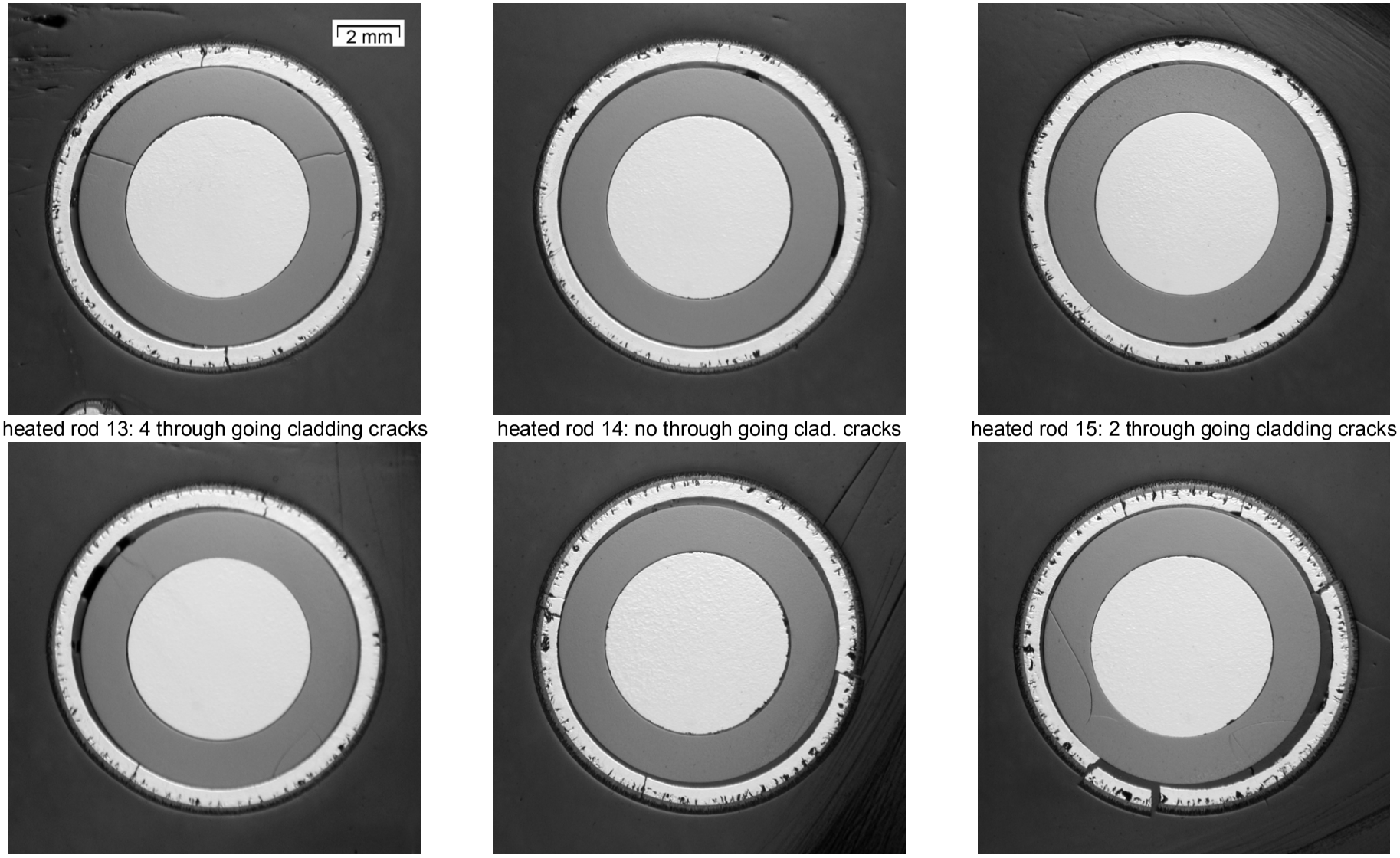

Fig. 58: QUENCH-14; Cross section at elevation 850 mm depicting separately test rods 13-19.

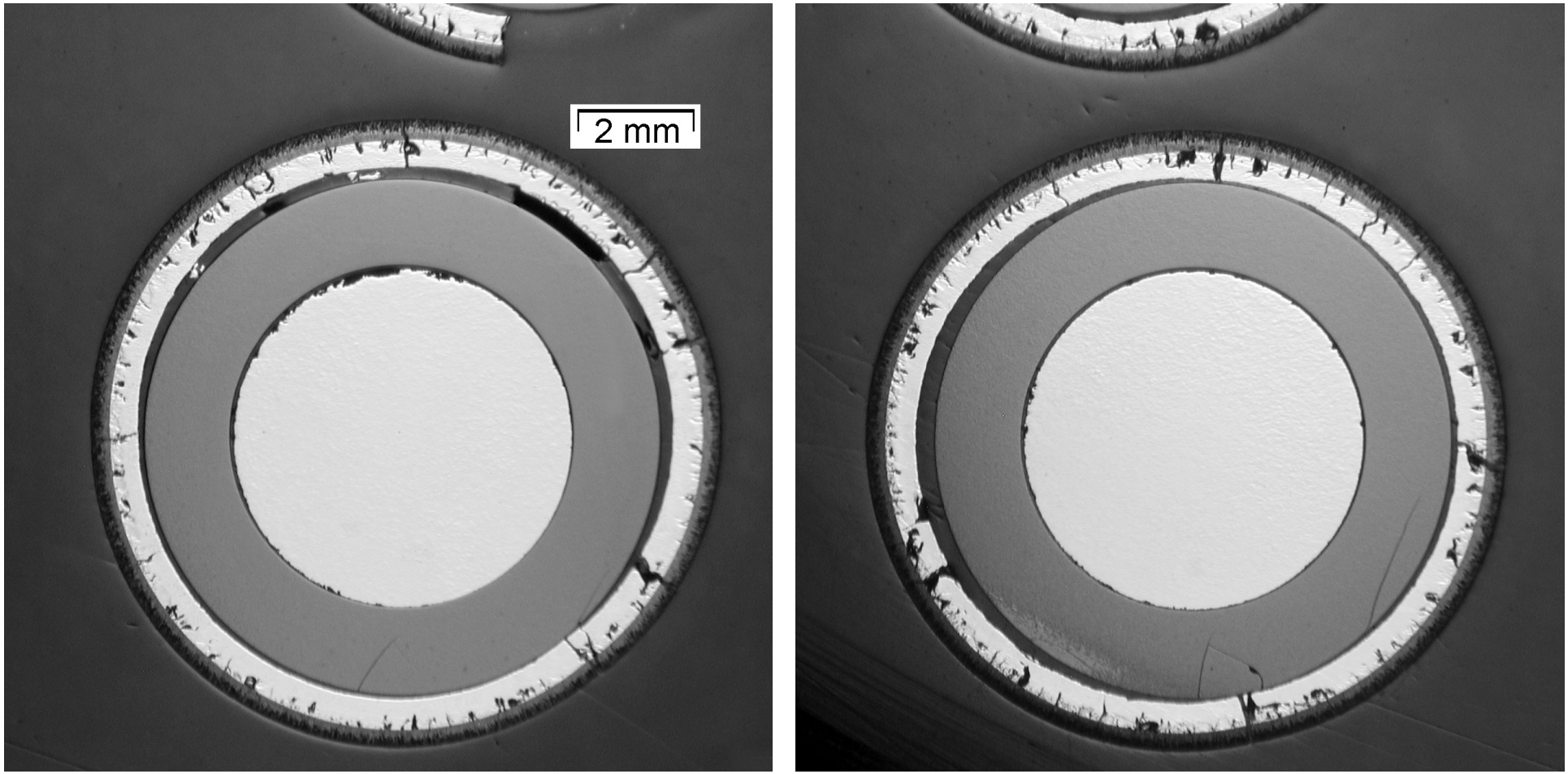

heated rod 20: 6 through going cladding cracks

heated rod 21: 8 through going cladding cracks

Fig. 59: QUENCH-14; cross section at elevation 850 mm depicting separately test rods 20, 21.

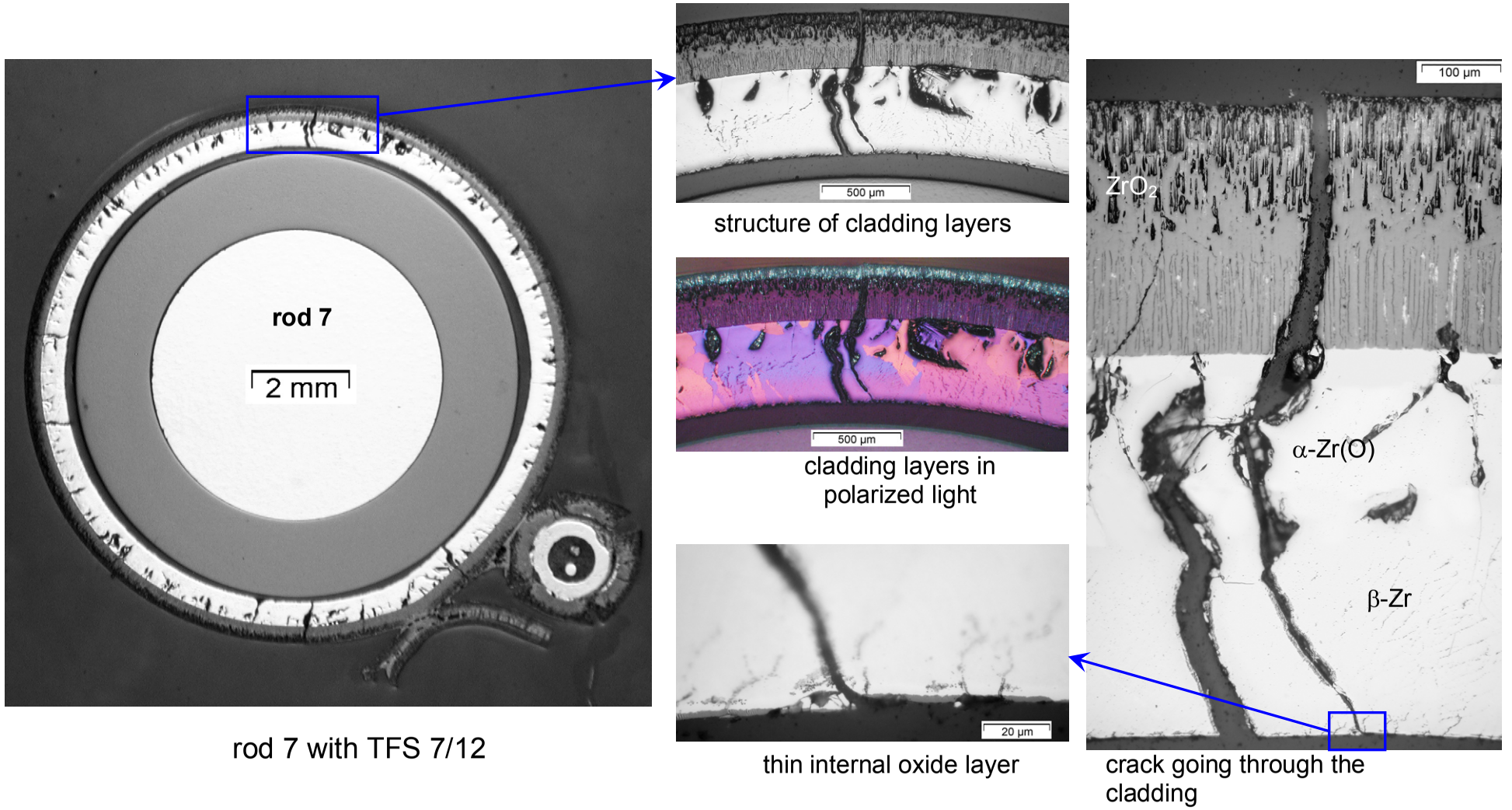

Fig. 60: QUENCH-14; Cross section at 850 mm bundle elevation; overview, oxidation state of rod No. 7.

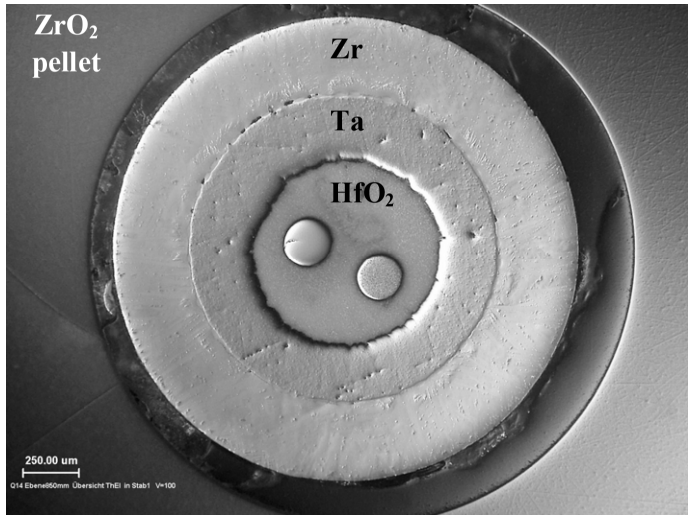

intact TCRC 12 inside pellet of rod #1

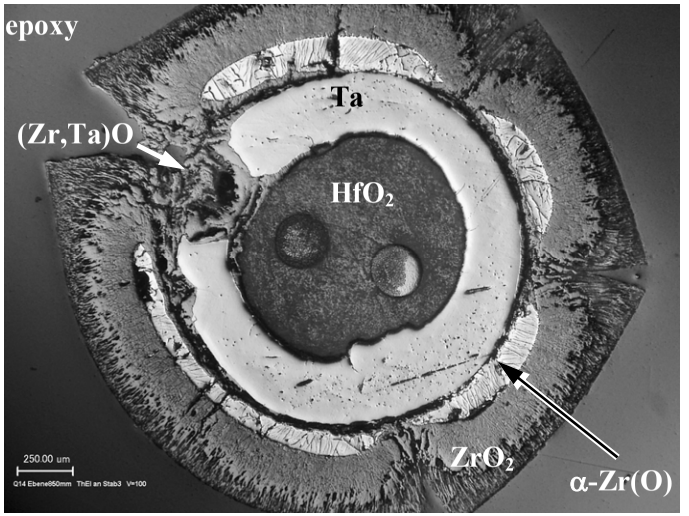

TFS 3/12 decoupled from surface of rod #3: intensive oxidised Zr-sheath, locally damaged Ta-sheath with foamy region of (Zr, Ta)O

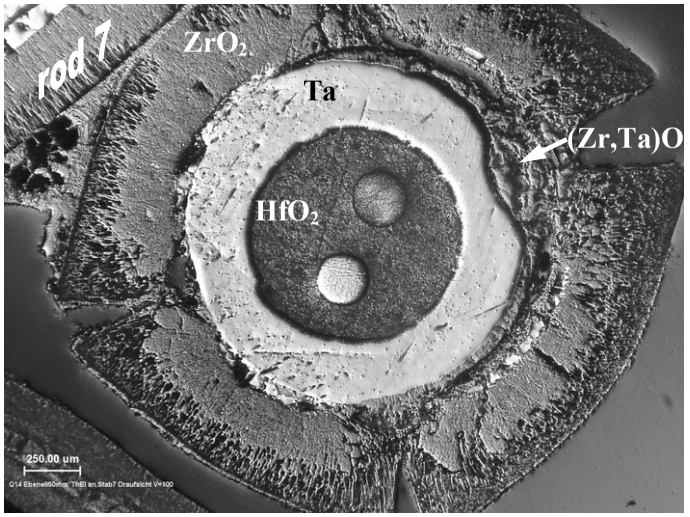

TFS 7/12 at surface of rod #7: completely oxidised Zr-sheath, locally steam attacked Ta-sheath with foamy region of (Zr, Ta)O

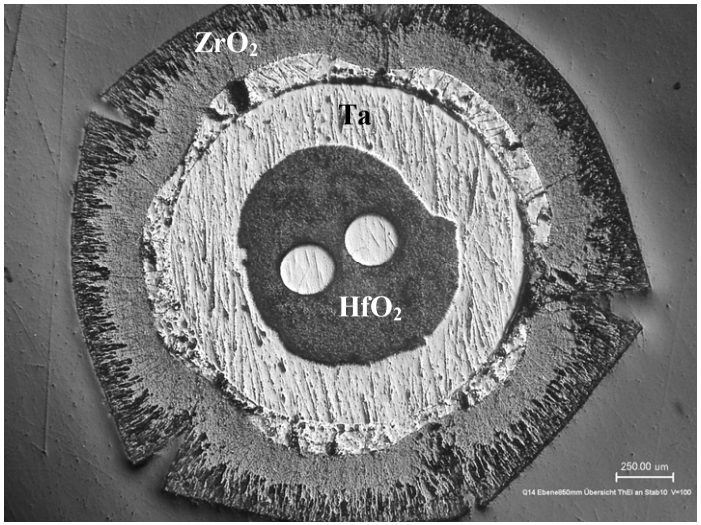

TFS 10/12 at surface of rod #10: intensive oxidised Zr-sheath, intact Ta-sheath

Fig. 61: QUENCH-14; Thermocouples state at elevation 850 mm.

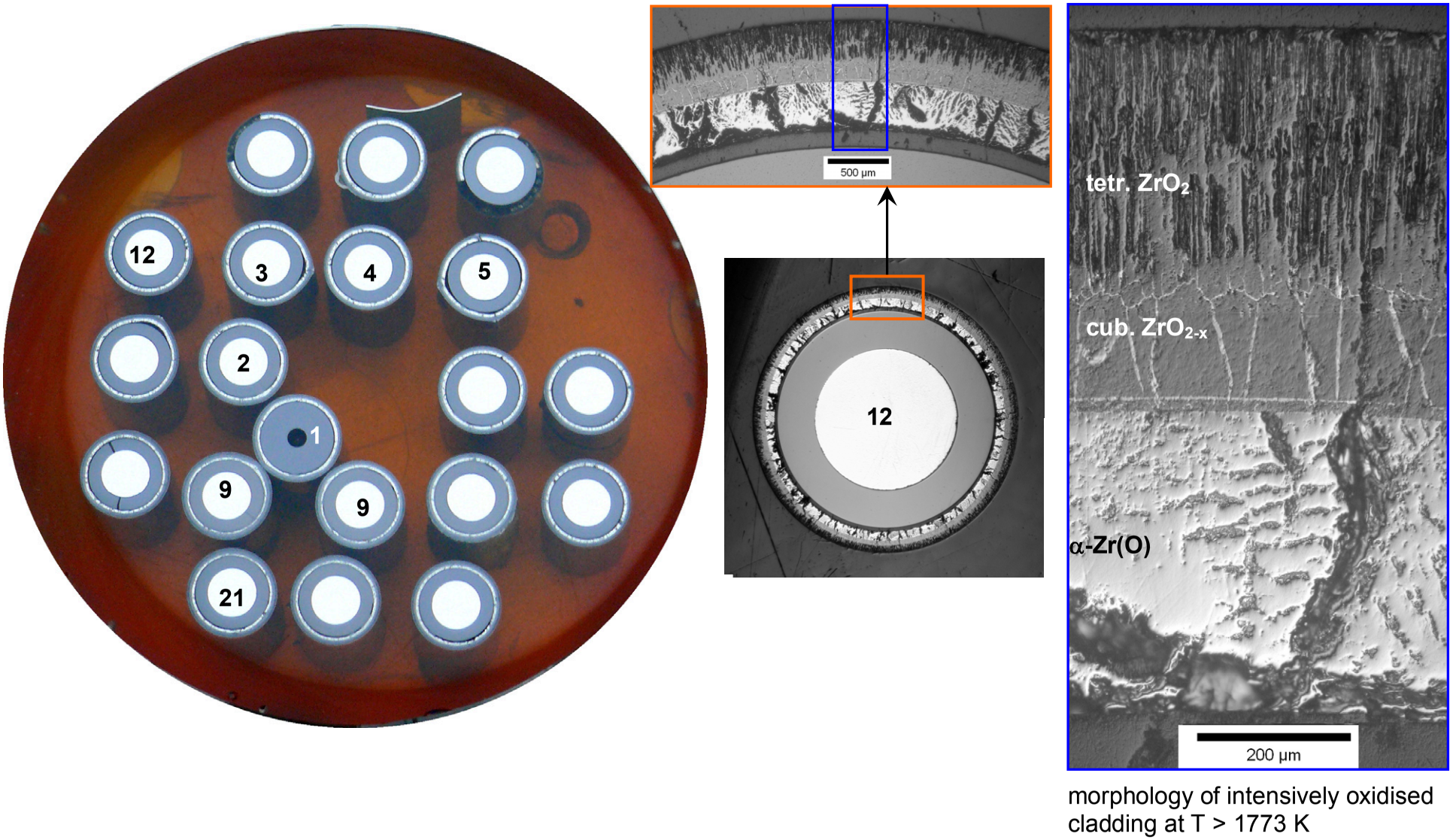

morphology of intensively oxidised cladding at T > 1773 K

Fig. 62: QUENCH-14; Cross section at 900 mm bundle elevation; overview, oxidation state of rod No. 12.

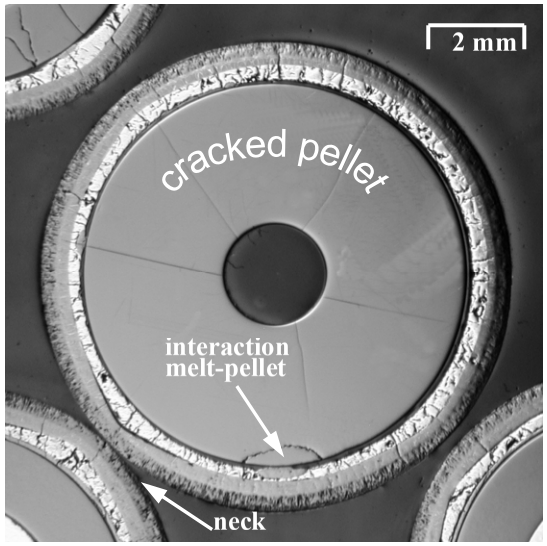

unh. rod 1: steam starvation at necking

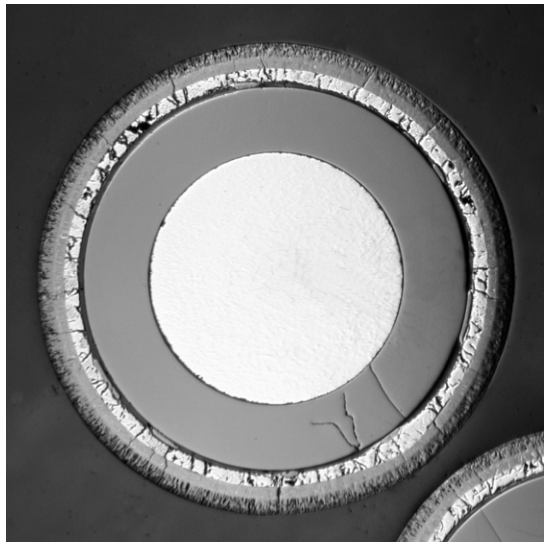

heat. rod 2: locally developed internal oxide layer

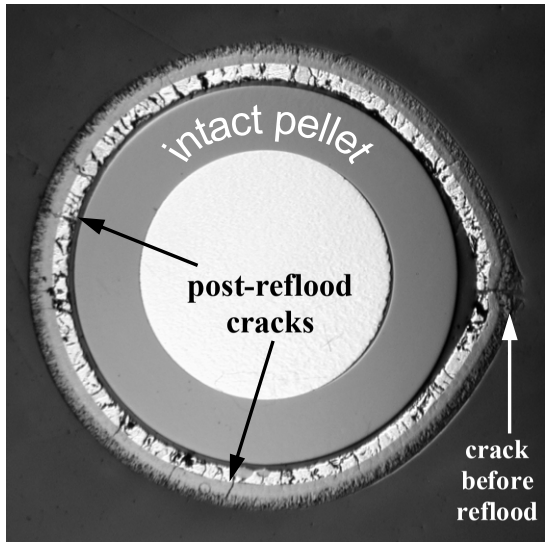

heated rod 3: pre-and post-reflood cracks

heat. rod 4: no internal oxidation of α-Zr(O) layer

heated rod 5: three pre-reflood cracks

heat. rod 6: locally developed internal oxide layer

Fig. 63: QUENCH-14; Elevation 900 mm; rods 1-6 with externally and internally oxidised cladding.

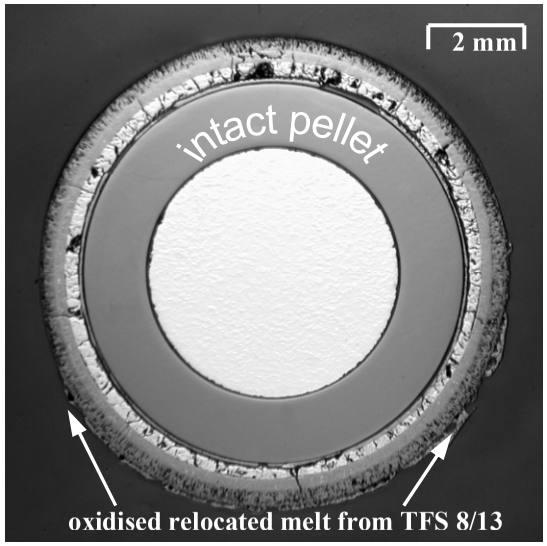

heat. rod 7: circumference internal oxide layer

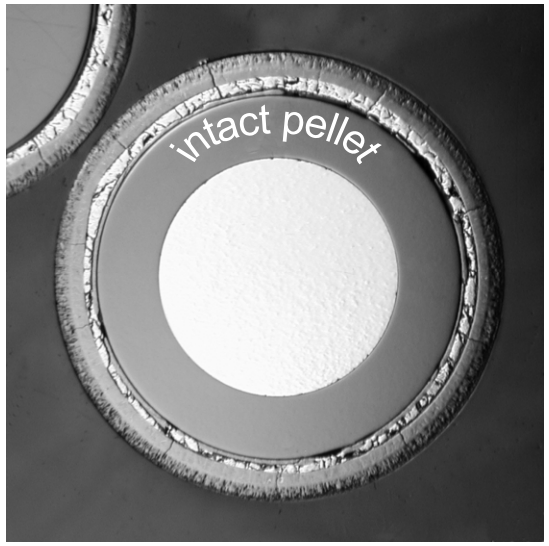

heat. rod 8: circumference internal oxide layer

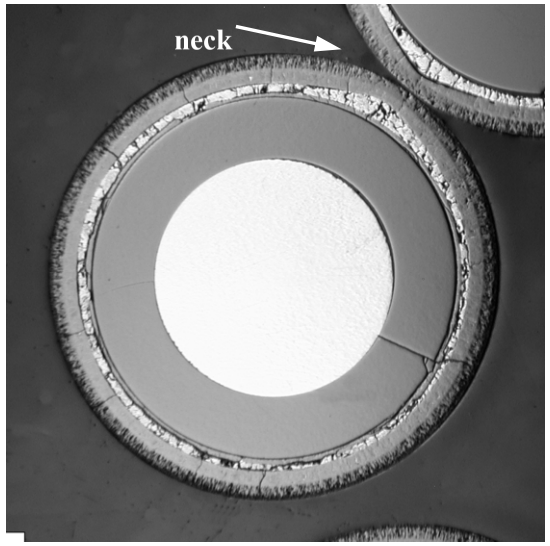

heated rod 9: circumference internal oxide layer

heat. rod 10: no internal oxidation of α-Zr(O) layer

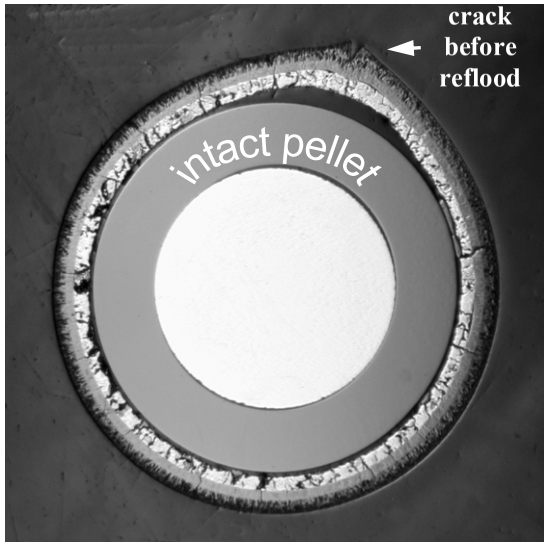

heat. rod 11: locally developed internal oxide layer

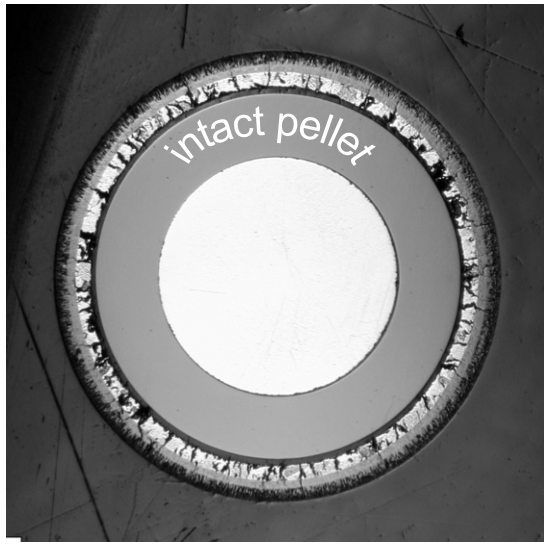

heat. rod 12: no internal oxidation of α-Zr(O) layer

Fig. 64: QUENCH-14; Elevation 900 mm; rods 7-12 with externally and internally oxidised cladding.

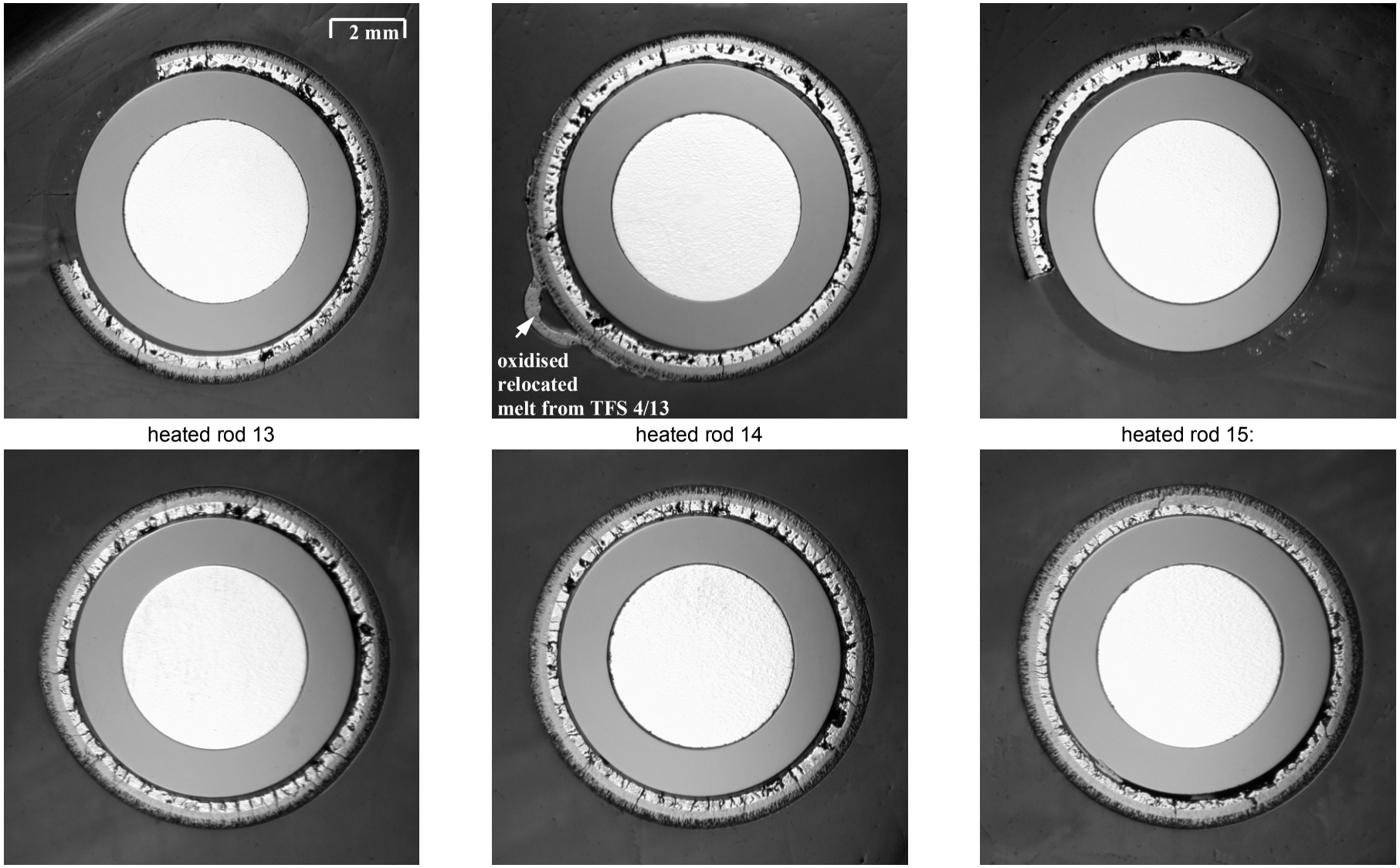

Fig. 65: QUENCH-14; Elevation 900 mm; rods 13-19 with externally oxidised cladding and intact pellets.

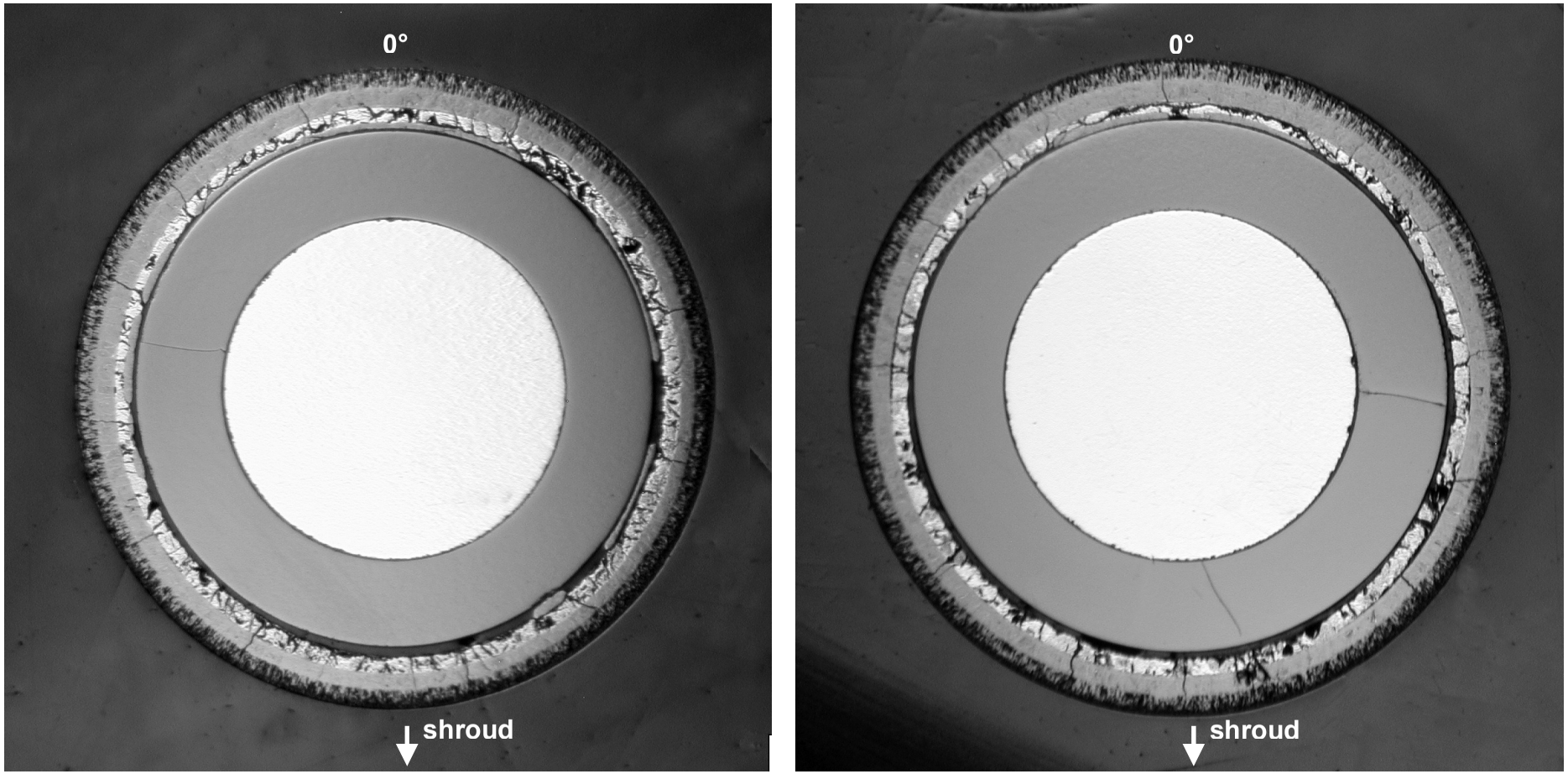

heated rod 20: internal oxide layer between 250° and 150°

heated rod 21: internal oxide layer between 315° and 60°

Fig. 66: QUENCH-14; Elevation 900 mm; rods 20, 21 with externally and internally oxidised cladding.

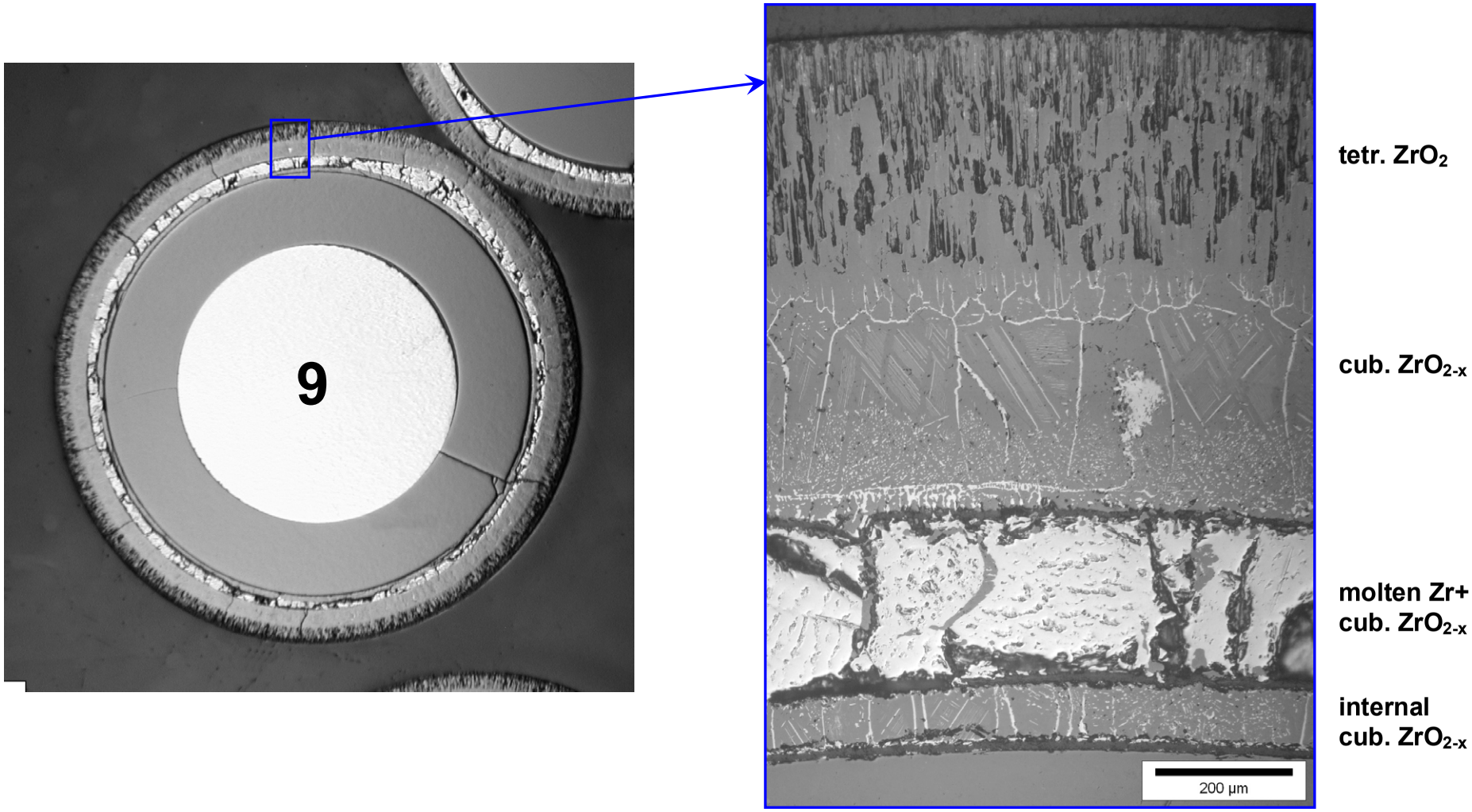

Fig. 67: QUENCH-14; Cross section at 900 mm bundle elevation; overview; oxidation state of rod No. 9 with partially liquefied metal layer and development of internal oxide layer.

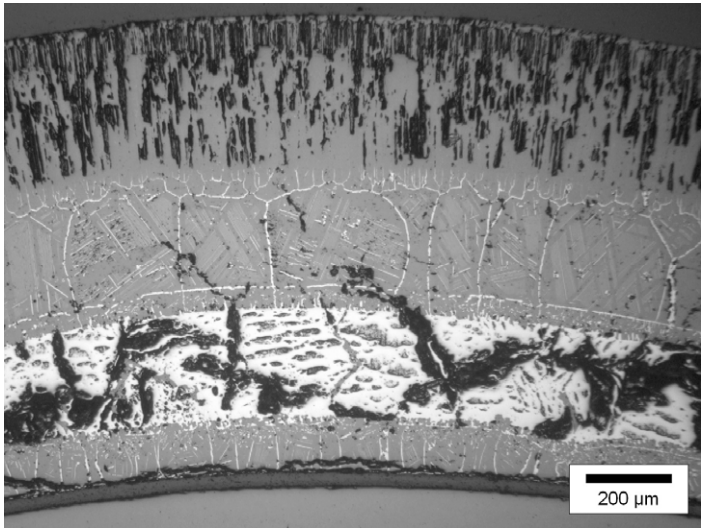

0°: homogeneous internal oxide layer

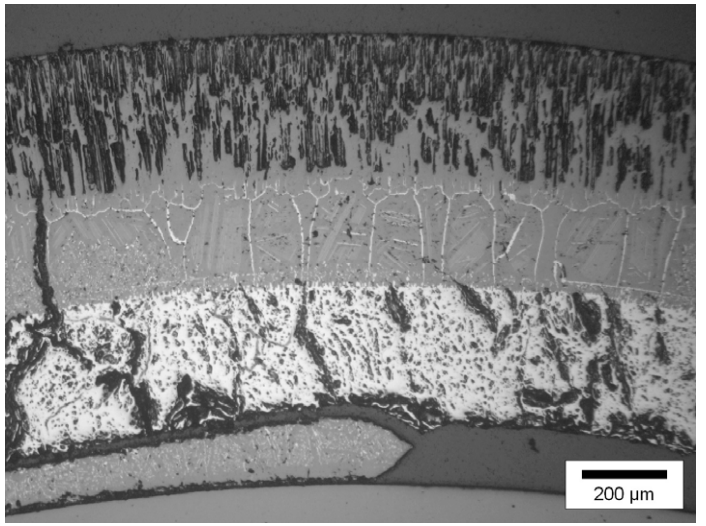

90°: interrupt of internal oxide layer development

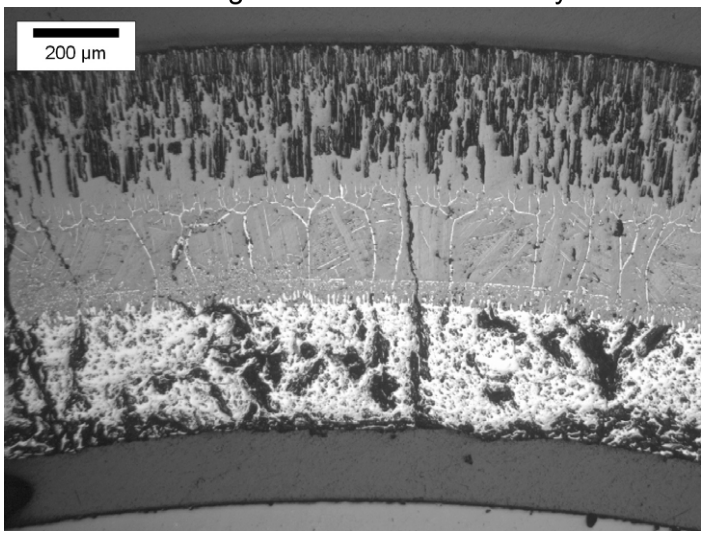

180°: absence of internal oxide layer

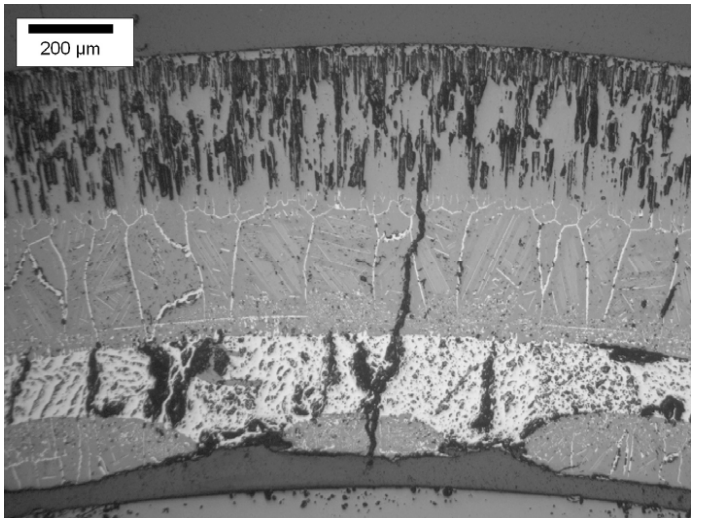

270°: local absence of internal oxide layer

Fig. 68: QUENCH-14; Elevation 900 mm; structure of oxidised cladding of rod No. 20 with frozen melt of metal layer.

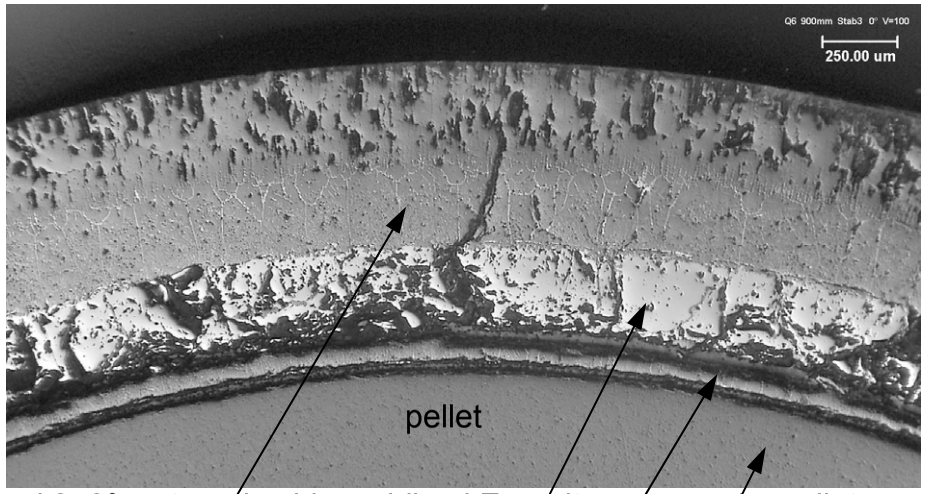

rod 3, 0°: external oxide, oxidised Zr-melt, epoxy resin, pellet

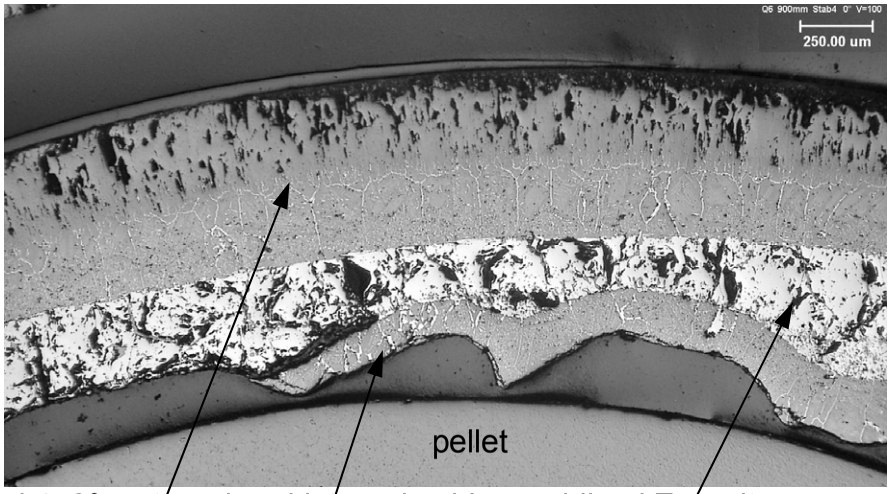

rod 4, 0°: external and internal oxides; oxidised Zr-melt

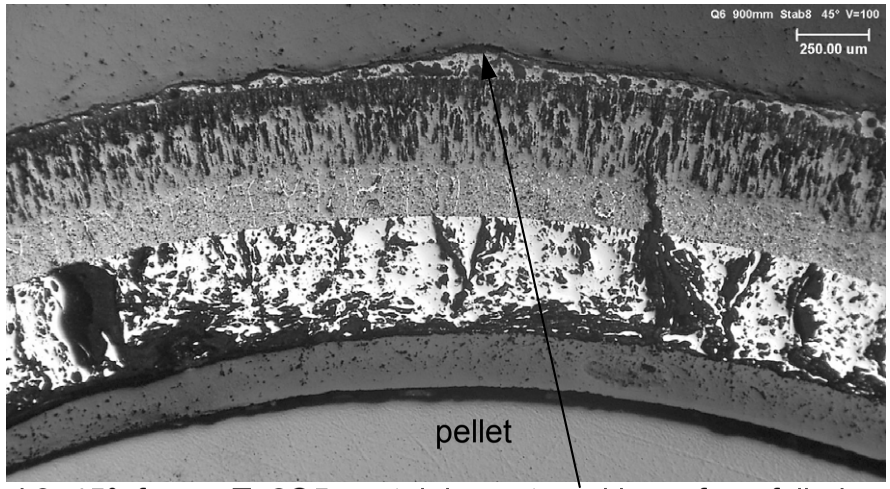

rod 8, 45°: foamy Ta2O5-containing external layer from failed thermocouple; external oxide, oxidised melt, epoxy, pellet

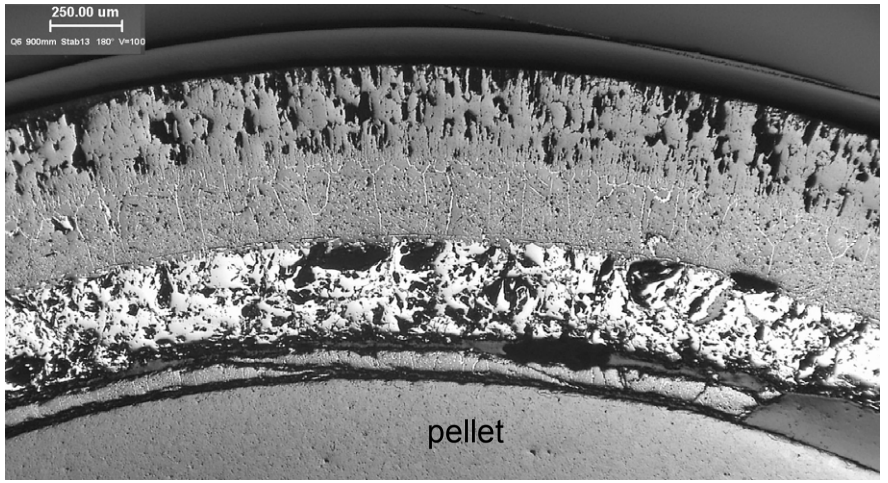

rod 13, 180°: external oxide, oxidised Zr-melt, epoxy resin, pellet

Fig. 69: Some fragments of cladding structures of the QUENCH-06 bundle at elevation 900 mm.

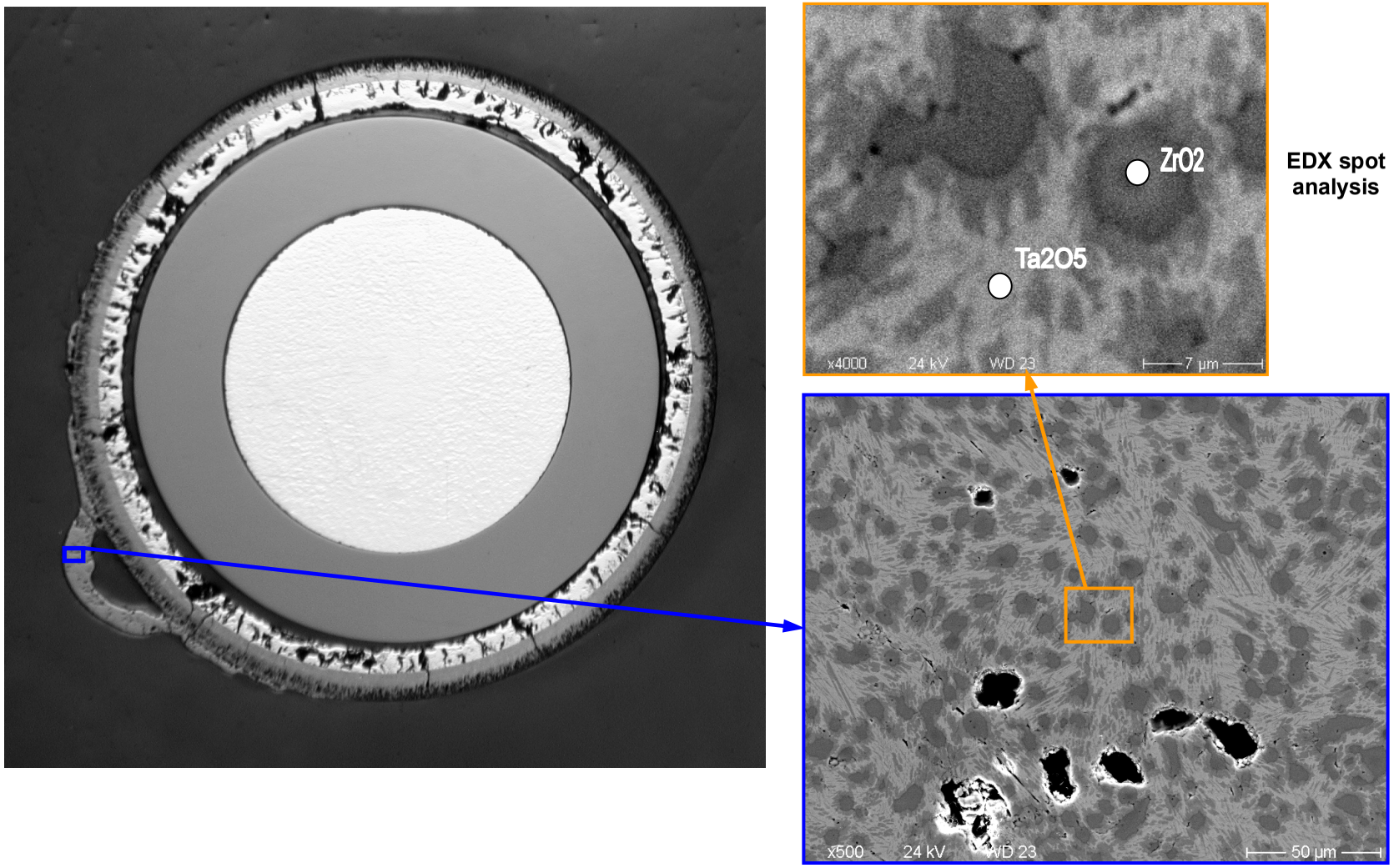

Fig. 70: QUENCH-14; EDX analysis of foaming material at surface of rod No. 14 at elev. 900 mm: part of oxidised, melted and downwards relocated TFS 4/13 duplex sheath.

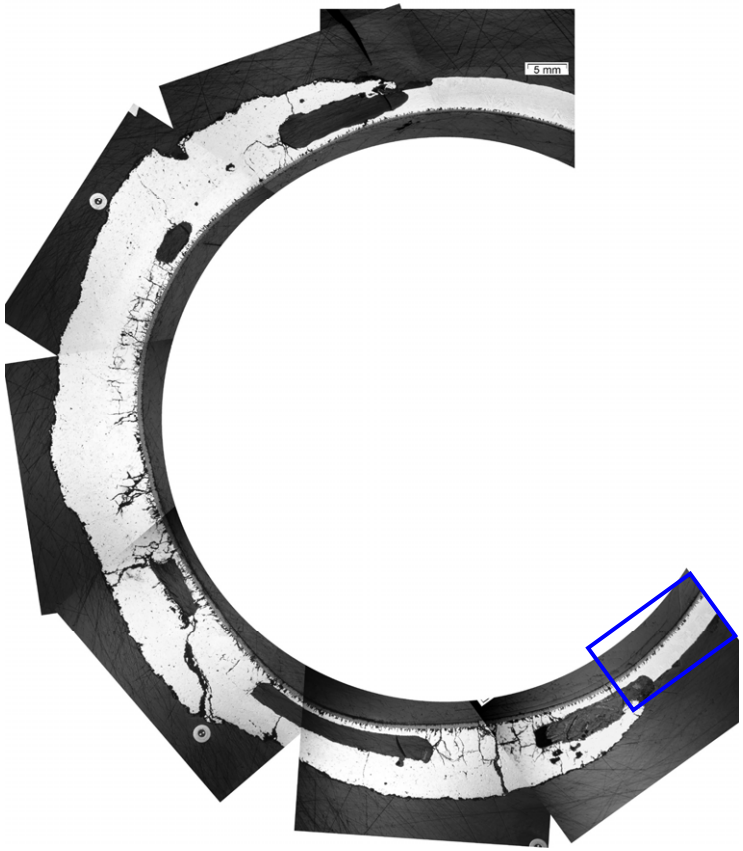

part of shroud, interacted with ZrO_2 heat insulation;
voids between insulation and shroud α-Zr(O) layer
as result of downwards relocation of molten β-Zr

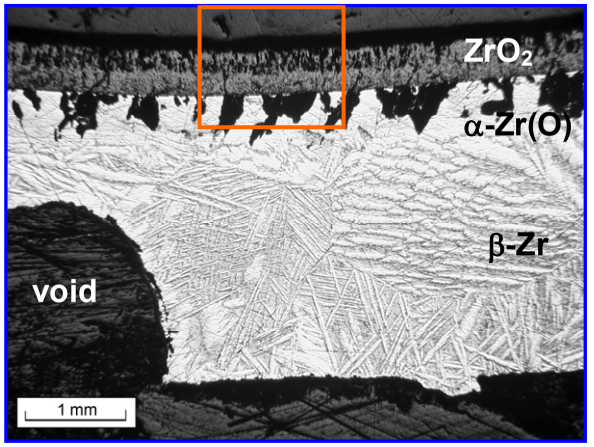

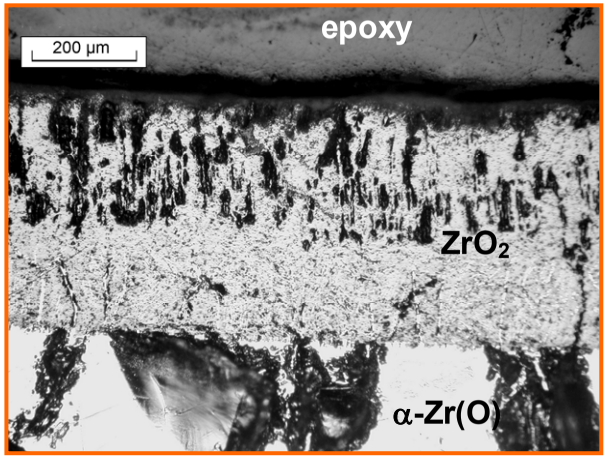

fragment of oxidised shroud at circumference
position without interaction with ZrO_2 heat insulation

Fig. 71: QUENCH-14; shroud cross section at 900 mm bundle elevation.

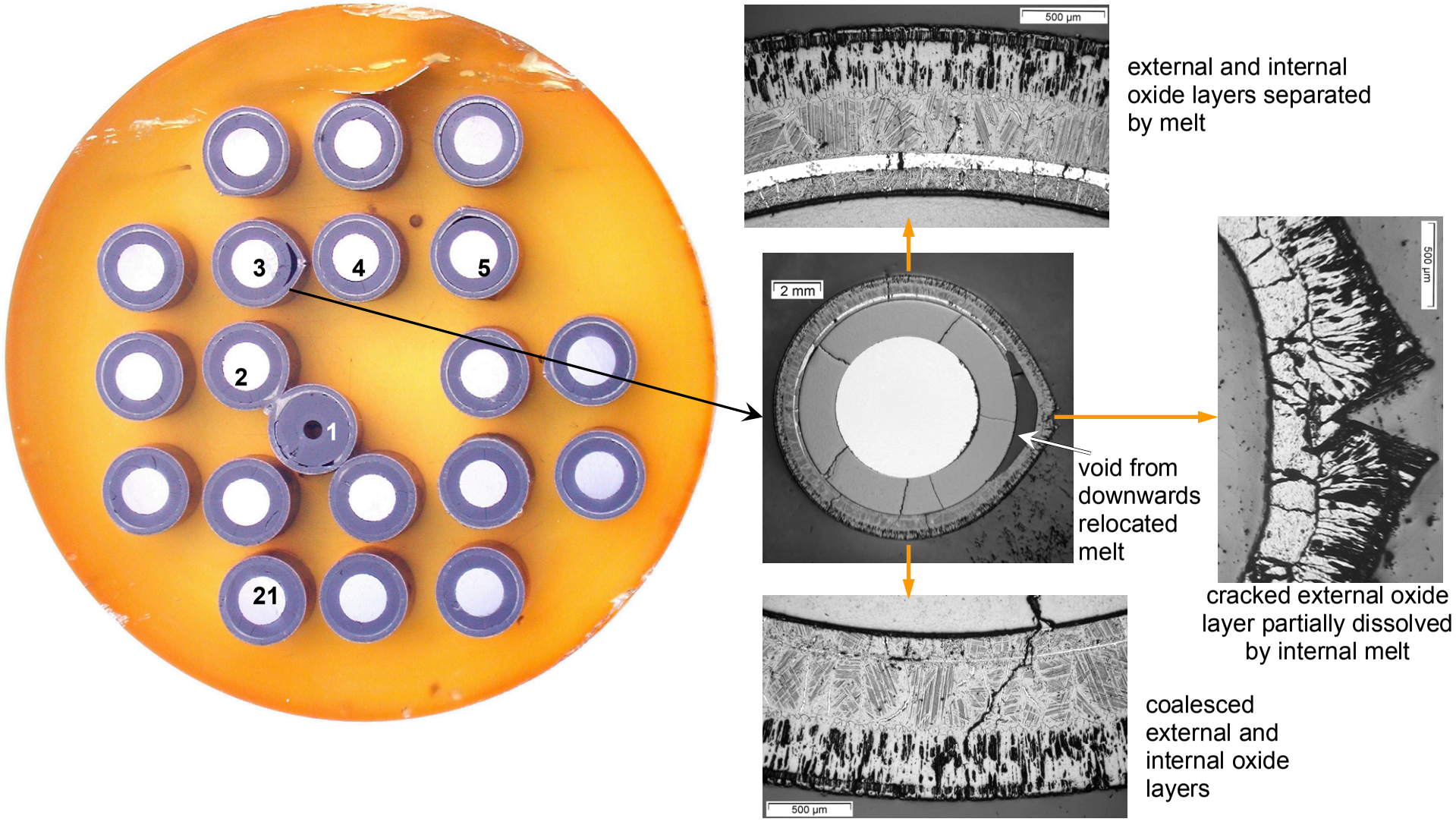

Fig. 72: QUENCH-14; Cross section at 950 mm bundle elevation; overview oxidation state of rod No. 3.

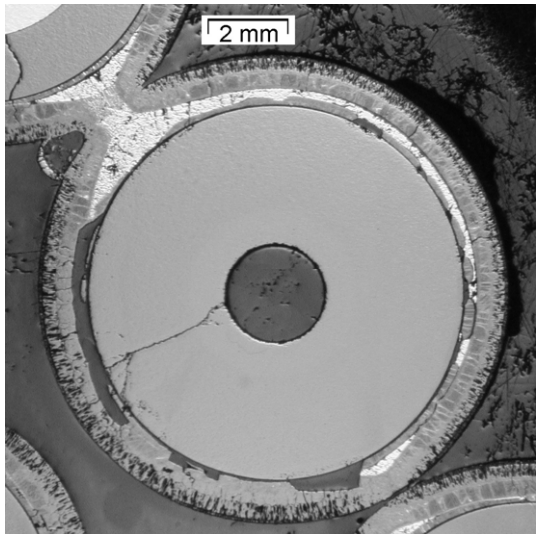

unh. rod 1: voids from relocated melt

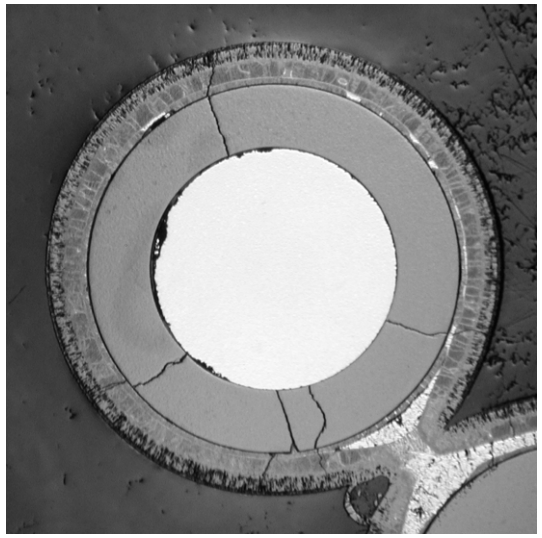

heat. rod 2: few oxidised melt at necking position

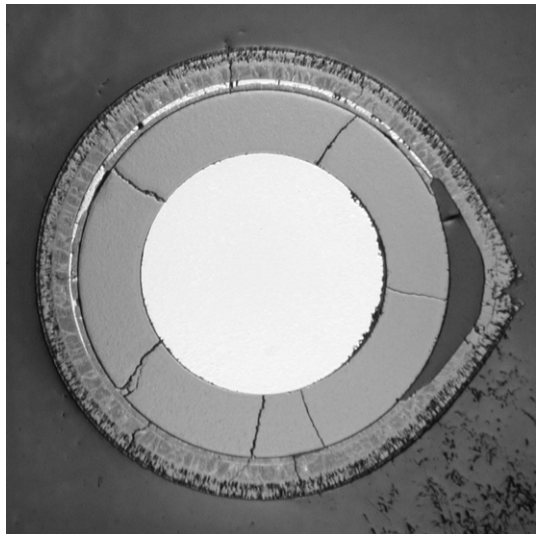

heated rod 3: void from relocated melt

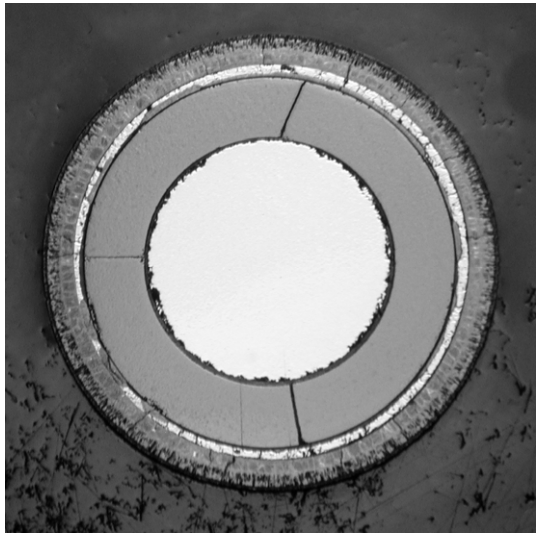

heat. rod 4: alternating thickness of internal oxide

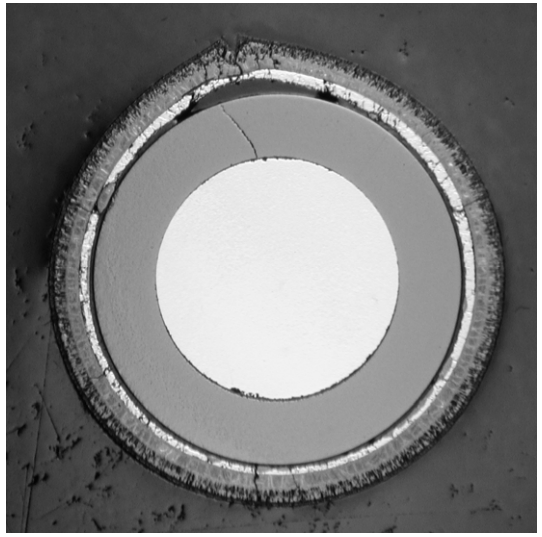

heated rod 5: spots of internal oxide

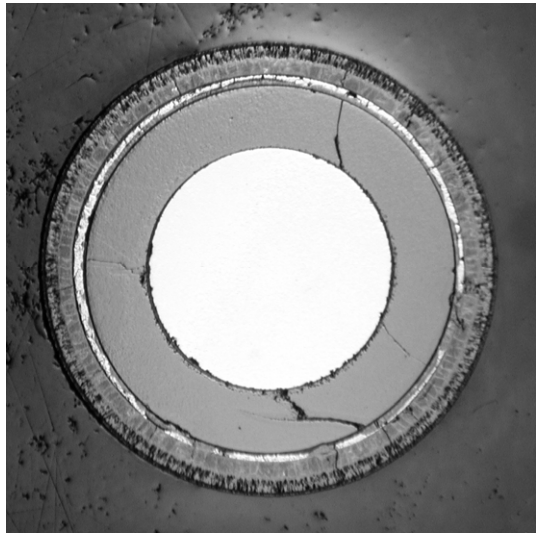

heated rod 6: alternating thickness of internal oxide

Fig. 73: QUENCH-14; Cross section at elevation 950 mm; rods 1-6 with externally and internally oxidised cladding.

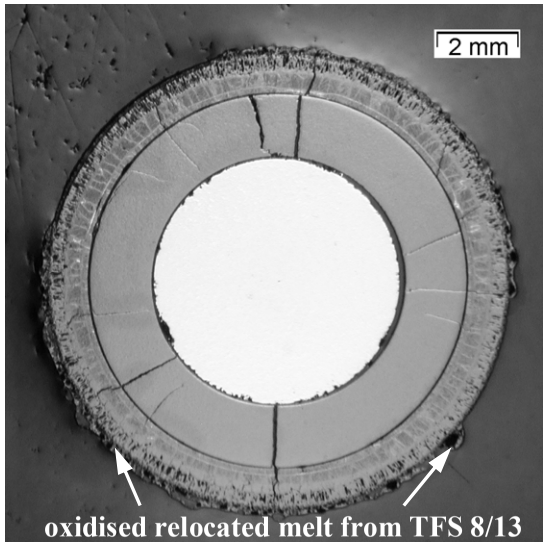

heat. rod 7: completely oxidised cladding

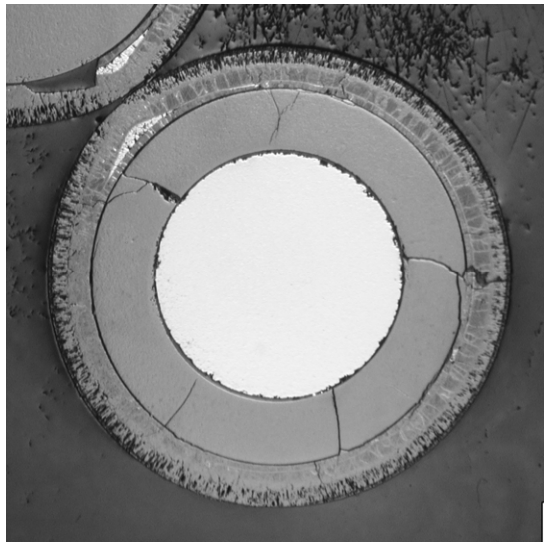
heat. rod 8: few oxidised melt at necking position

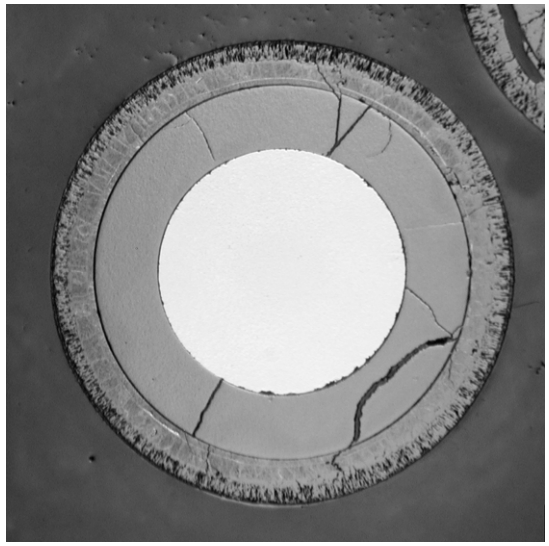
heat. rod 9: completely oxidised melt layer

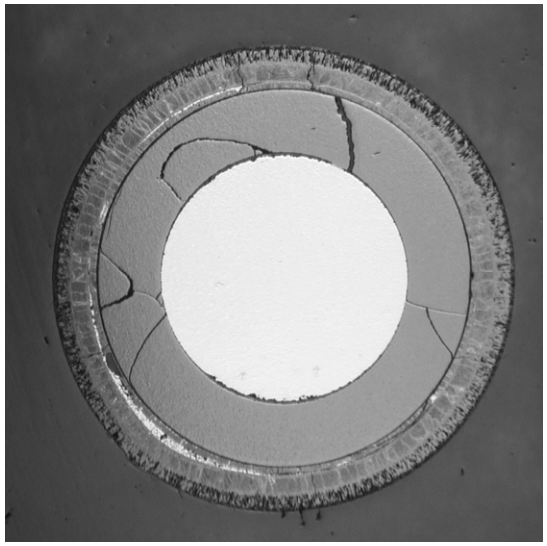
heat. rod 10: not completely oxidised melt layer

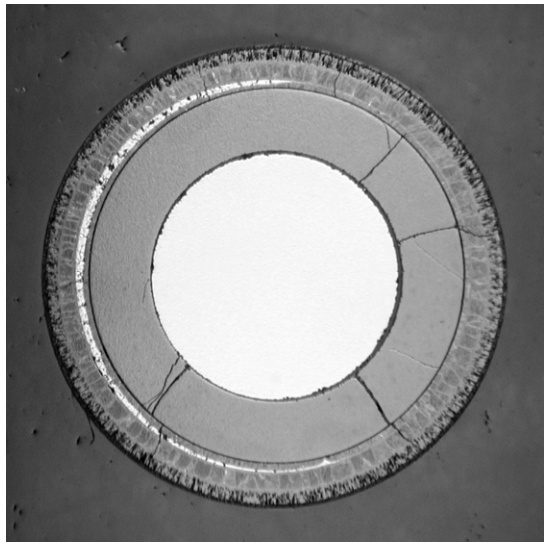
heat. rod 11: not completely oxidised melt layer

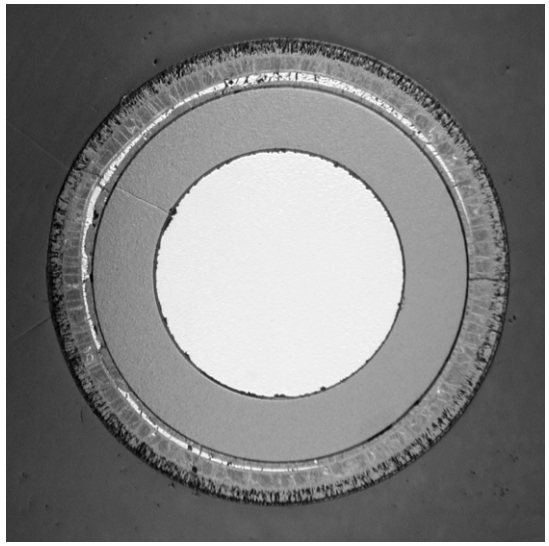
heat. rod 12: not completely oxidised melt layer

Fig. 74: QUENCH-14; Cross section at elevation 950 mm; rods 7-12 with externally and internally oxidised cladding.

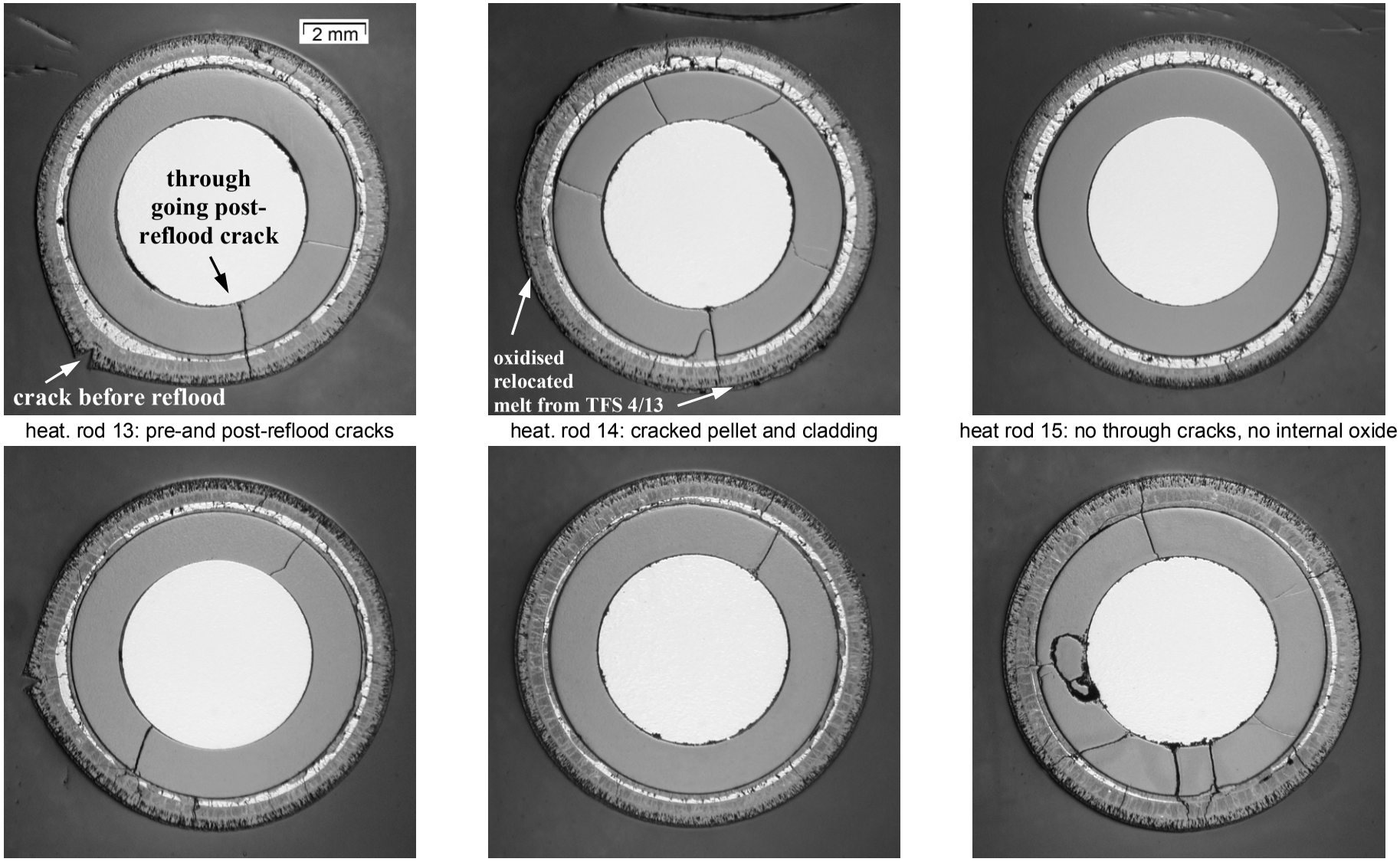

heat. rod 13: pre-and post-reflood cracks

heat. rod 14: cracked pellet and cladding

heat rod 15: no through cracks, no internal oxide

heat. rod 17: pre-and post-reflood cracks

heat. rod 18: cracks, partially oxidised melt layer

heat. rod 19: cracked pellet and cladding

Fig. 75: QUENCH-14; Cross section at elev. 950 mm; rods 13-19 with externally and internally oxidised cladding.

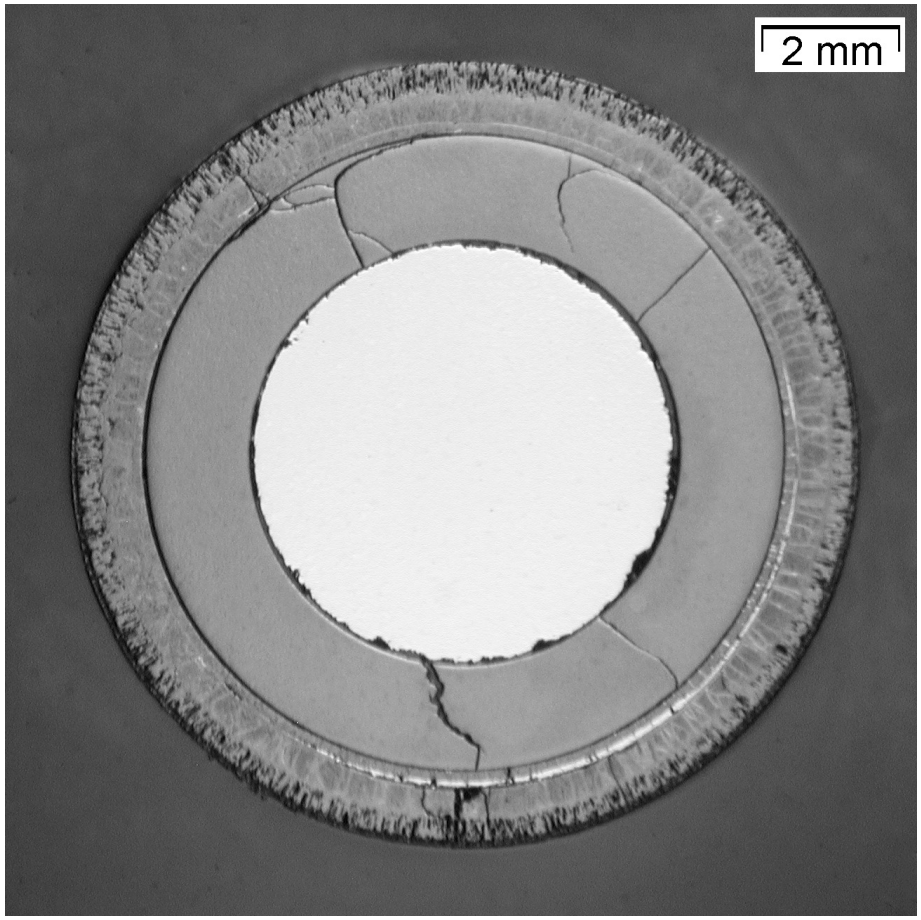

heated rod 20: cracked pellet and cladding, not completely oxidised melt layer at relatively cold position near to shroud

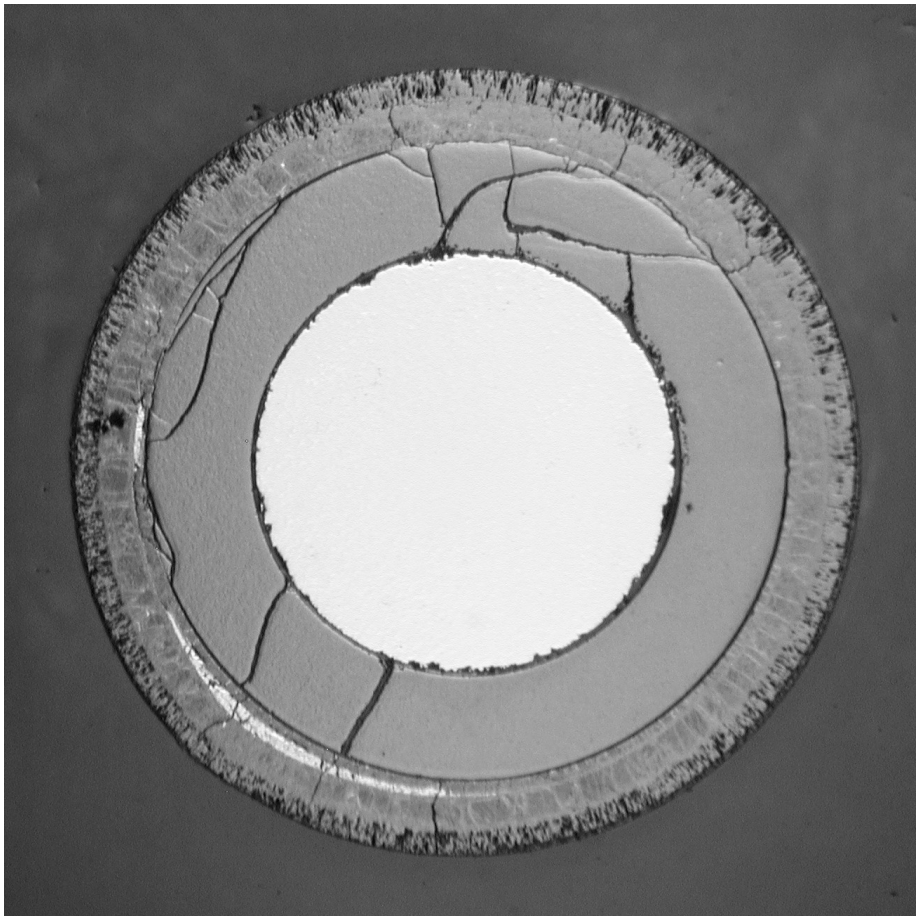

heated rod 21: cracked pellet and cladding, not completely oxidised melt layer at relatively cold position near to shroud

Fig. 76: QUENCH-14; Cross section at elevation 950 mm depicting separately test rods 20, 21.

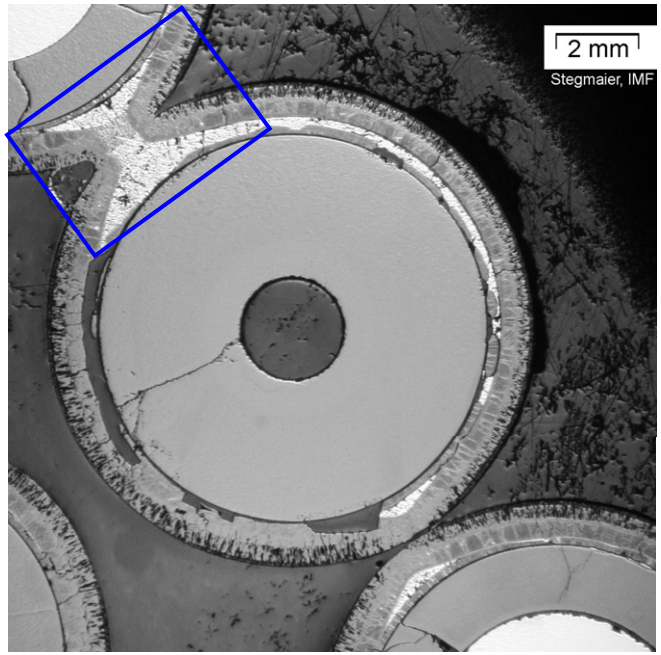

contact between rods 1 and 2

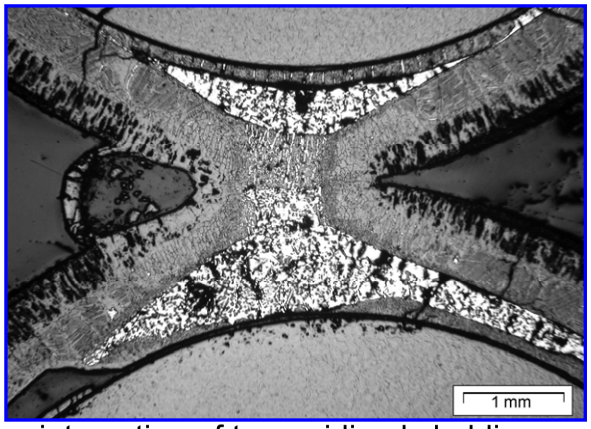

interaction of two oxidised claddings
with small molten pool formation

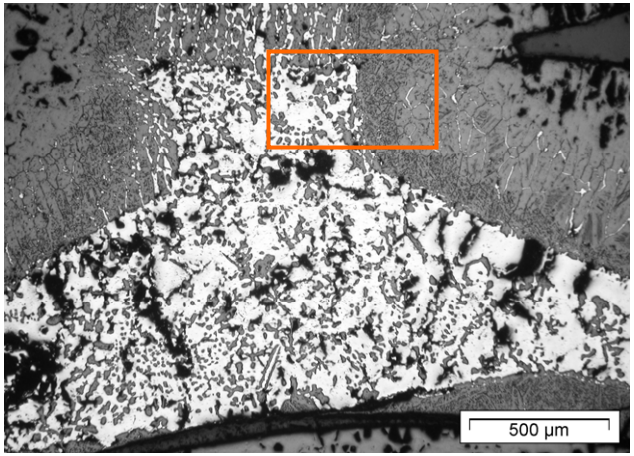

interaction of two oxidised claddings
with small molten pool formation

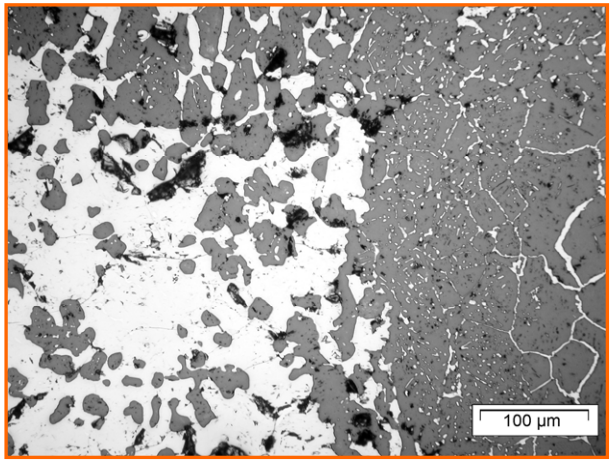

oxidation of melt by dissolution and
reduction of oxide layer

Fig. 77: QUENCH-14; Cross section at 950 mm bundle elevation; interaction of metal melt with oxide layers at necking position between rods 1 and 2.

cladding of rod 3 at 0°: external and internal oxide layers separated by molten metal

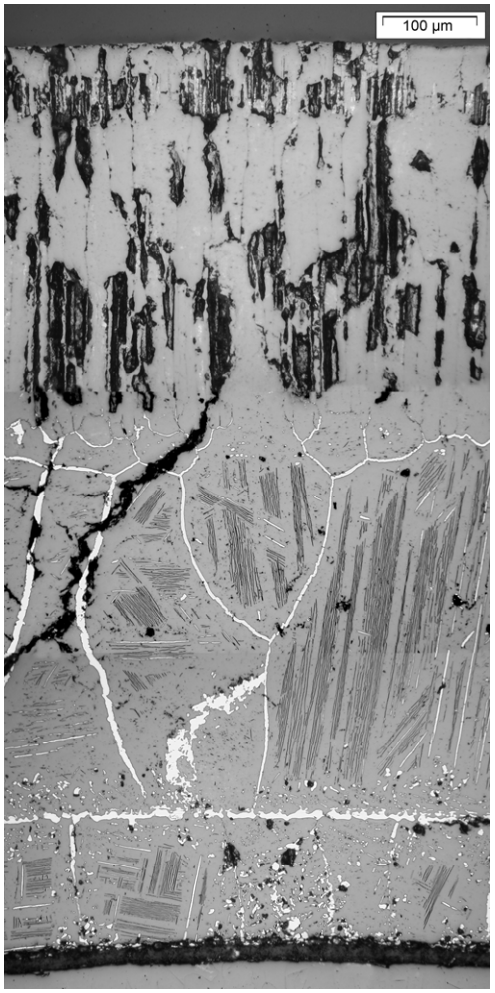

cladding of rod 3 at 180°: external and internal oxide layers separated by very thin molten layer

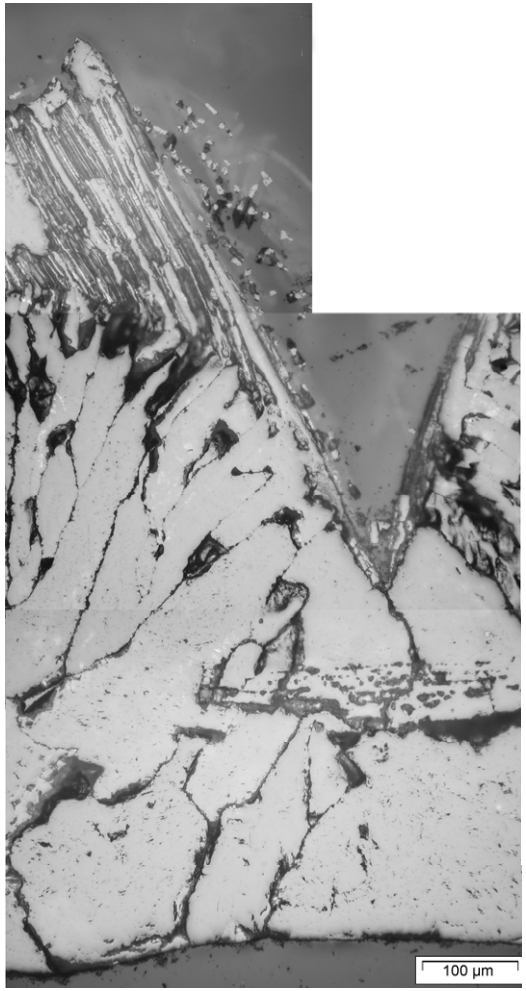

cladding of rod 3 at 90°: crack in external layer

Fig. 78: QUENCH-14; Cross section at 950 mm bundle elevation; oxidation state of rod No. 3.

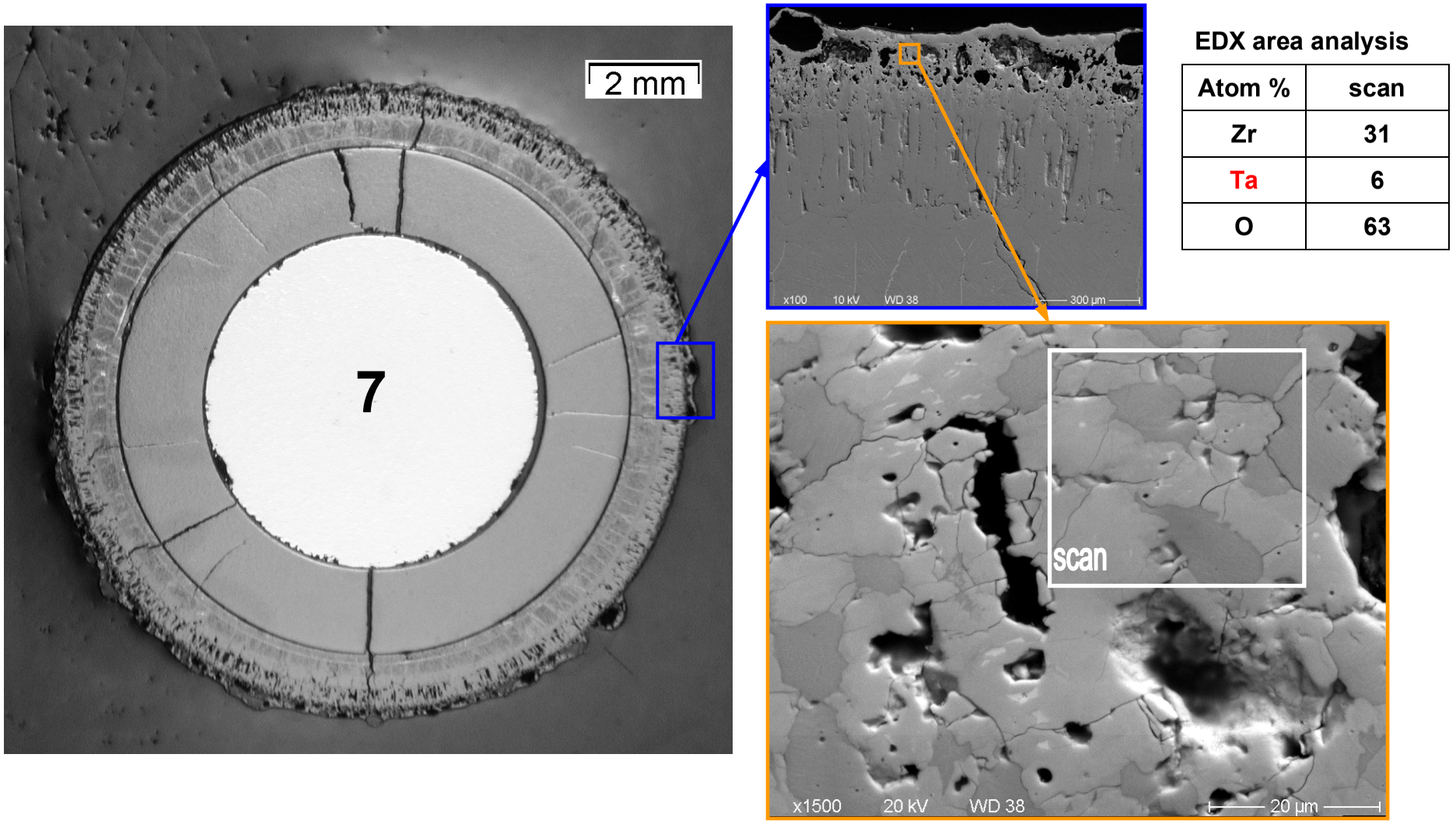

EDX area analysis

Atom %	scan
Zr	31
Ta	6
O	63

Fig. 79: QUENCH-14; EDX analysis of foaming material at surface of rod No. 7 at elev. 950 mm: interaction of oxidised cladding tube with melt of failed TFS 8/13.

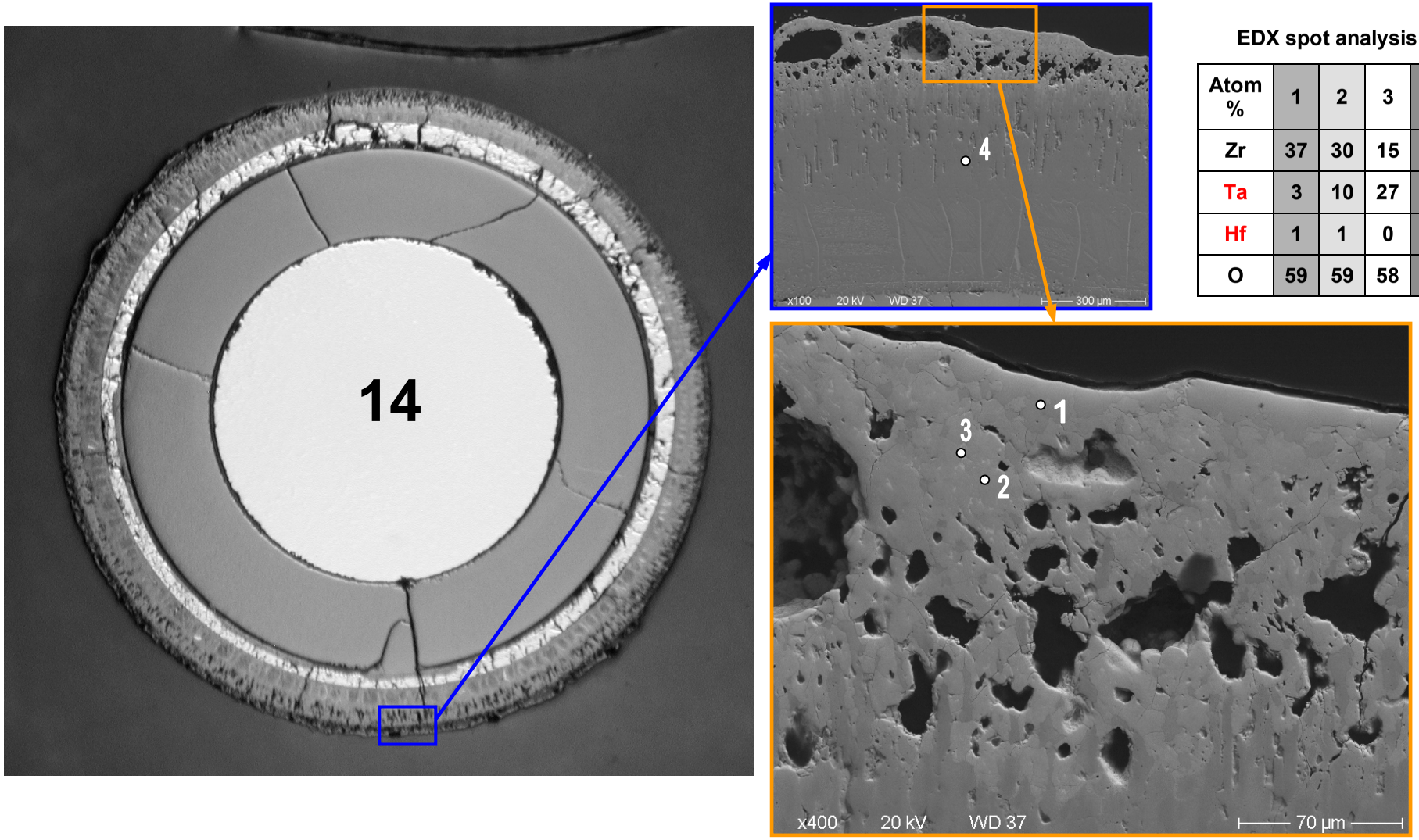

EDX spot analysis

Atom %	1	2	3	4
Zr	37	30	15	44
Ta	3	10	27	0
Hf	1	1	0	0
O	59	59	58	56

Fig. 80: QUENCH-14; EDX analysis of foaming material at surface of rod No. 14 at elev. 950 mm: interaction of oxidised cladding tube with melt of failed TFS 4/13

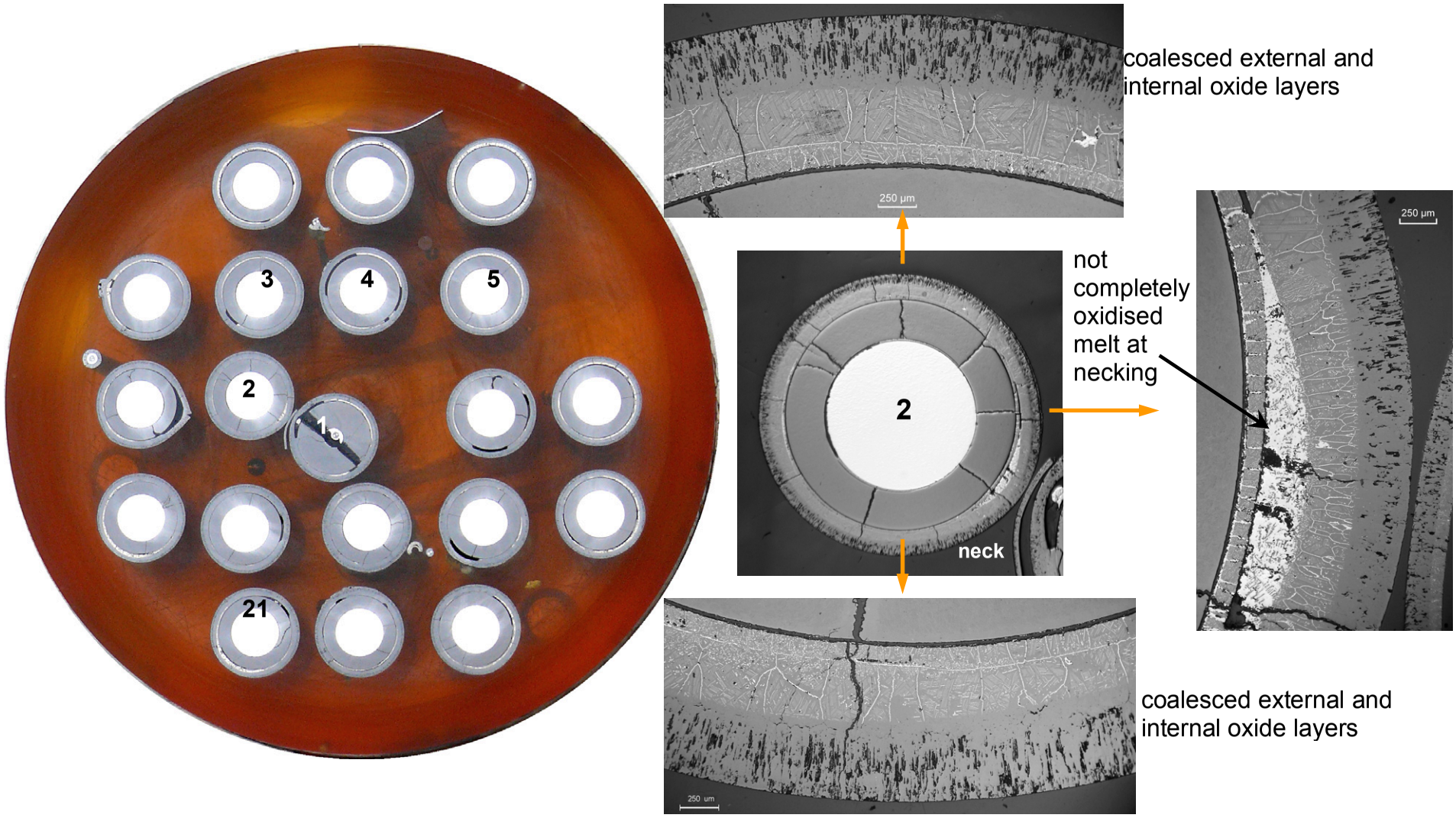

Fig. 81: QUENCH-14; Cross section at 1000 mm bundle elevation; overview, oxidation state of rod No. 2.

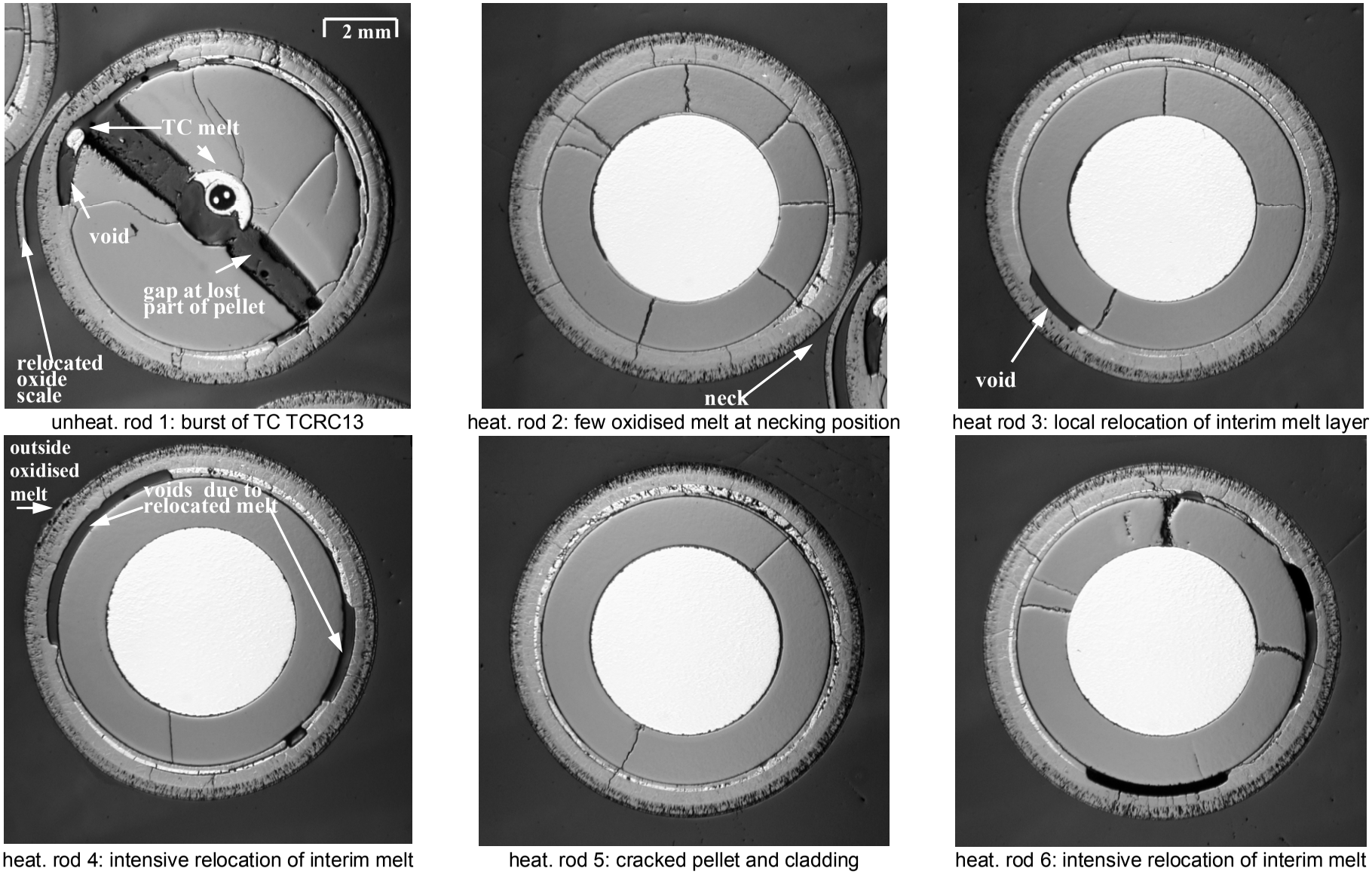

Fig. 82: QUENCH-14; Cross section at elev. 1000 mm; rods 1-6 with externally and internally oxidised cladding.

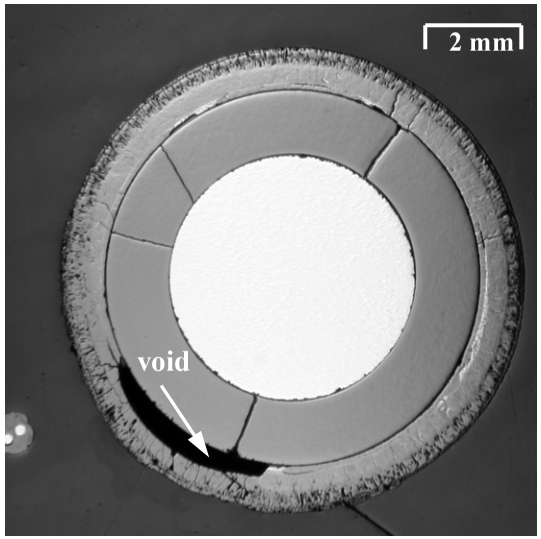

heat. rod 7: local relocation of interim melt layer

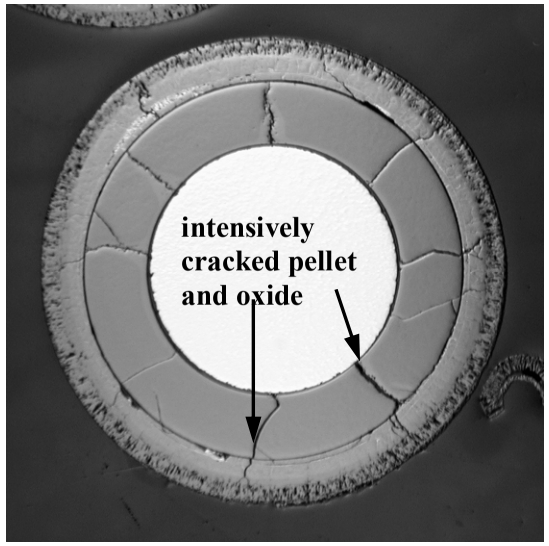

heat. rod 8: completely oxidised melt layer

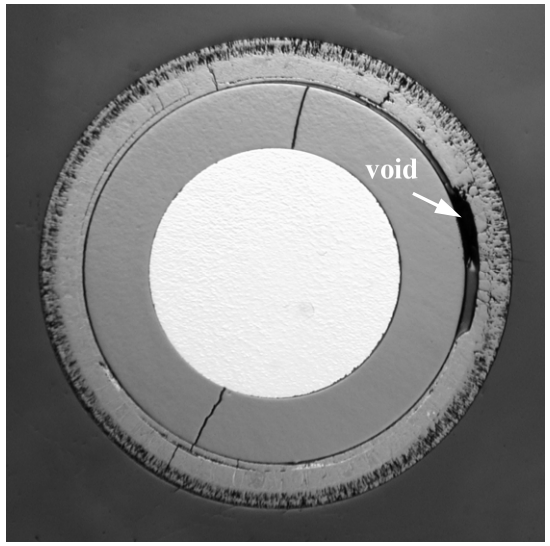

heat rod 9: local relocation of interim melt layer

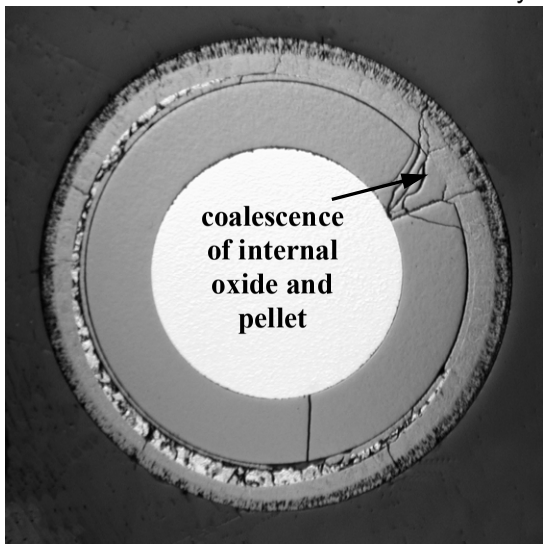

heat. rod 10: partially oxidised melt layer

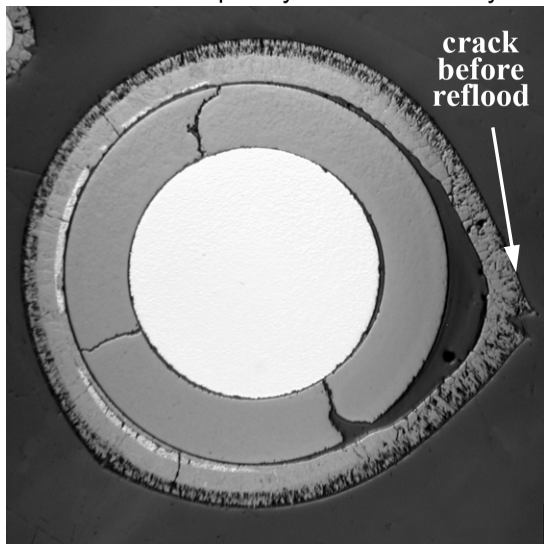

heat. rod 11: pre-and post-reflood cladding cracks

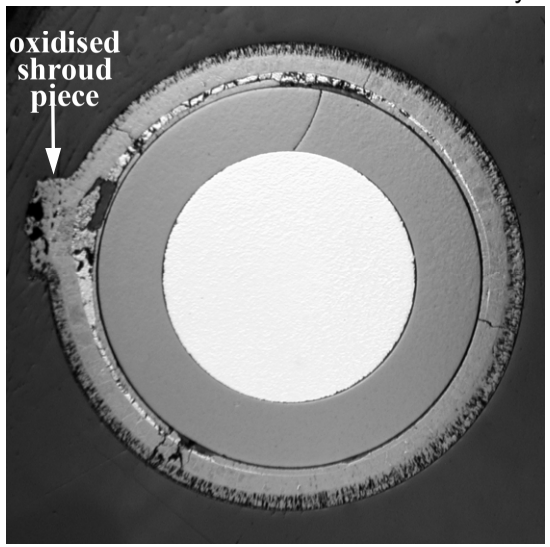

heat. rod 12: partially oxidised cladding melt layer

Fig. 83: QUENCH-14; Cross section at elev. 1000 mm; rods 7-12 with externally and internally oxidised cladding.

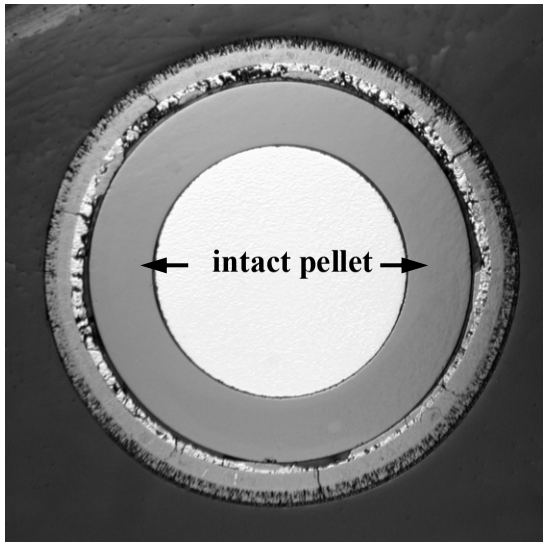

heat. rod 13: local development of internal oxide

heat. rod 14: partially oxidised metal melt

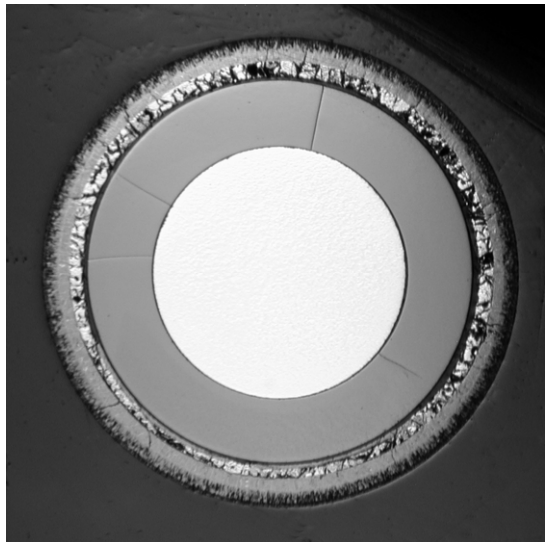

heat rod 15: partially oxidised metal melt

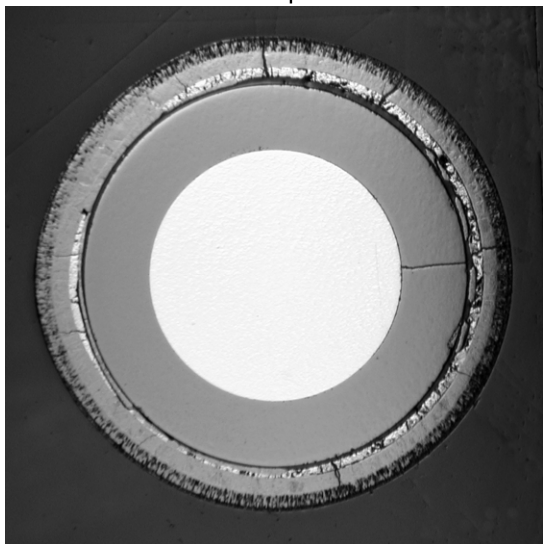

heat. rod 17: local complete oxidation of cladding

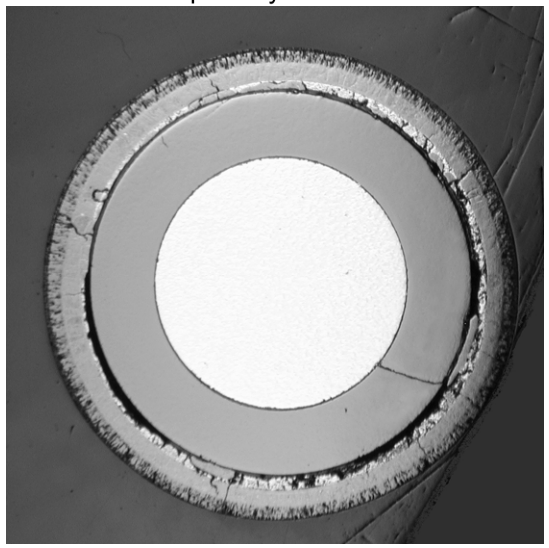

heat. rod 18: intensive oxidised metal melt

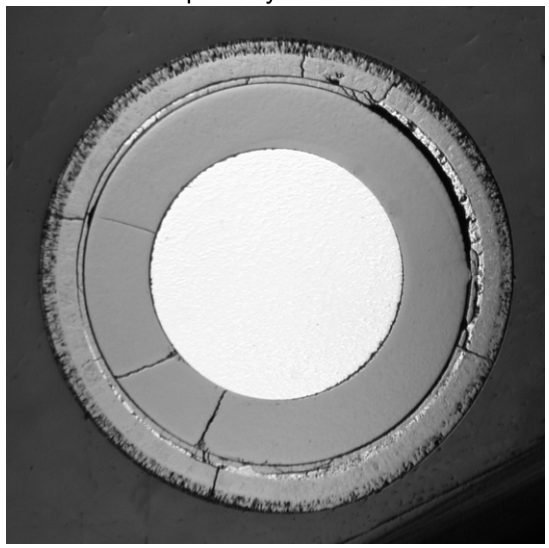

heat. rod 19: intensive cladding disruption

Fig. 84: QUENCH-14; Cross section at elev. 1000 mm; rods 13-19 with externally and internally oxidised cladding.

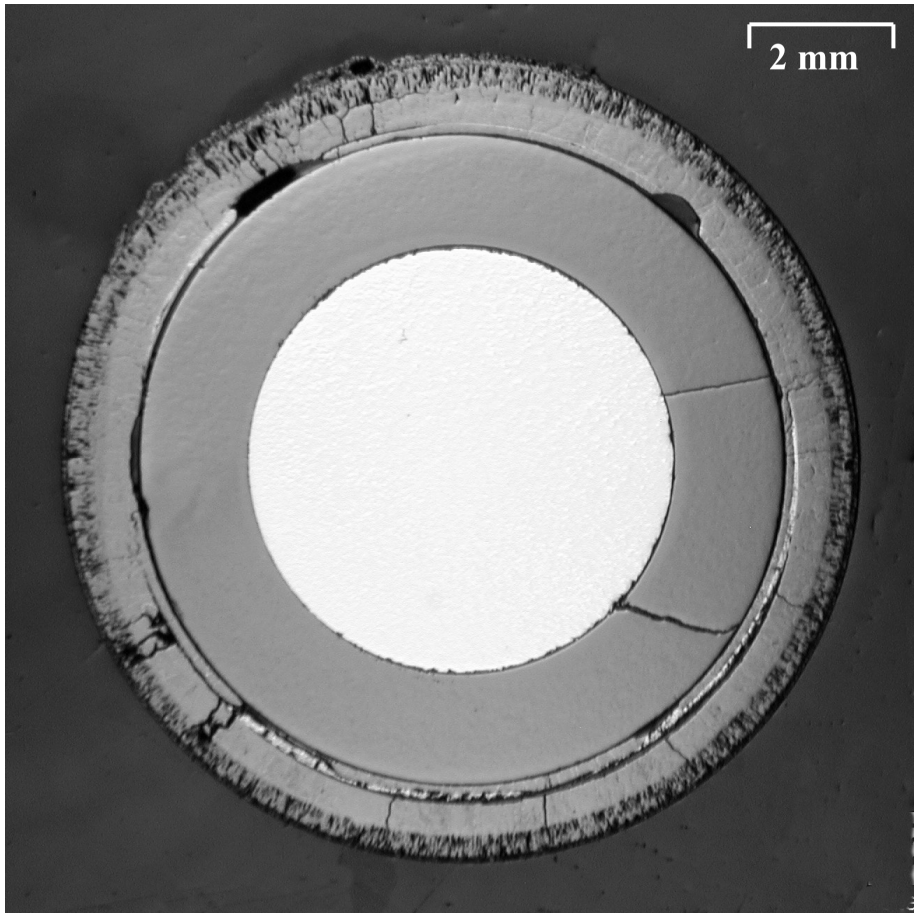

heated rod 20: intensive oxidation of molten melt layer; local melt relocation (voids)

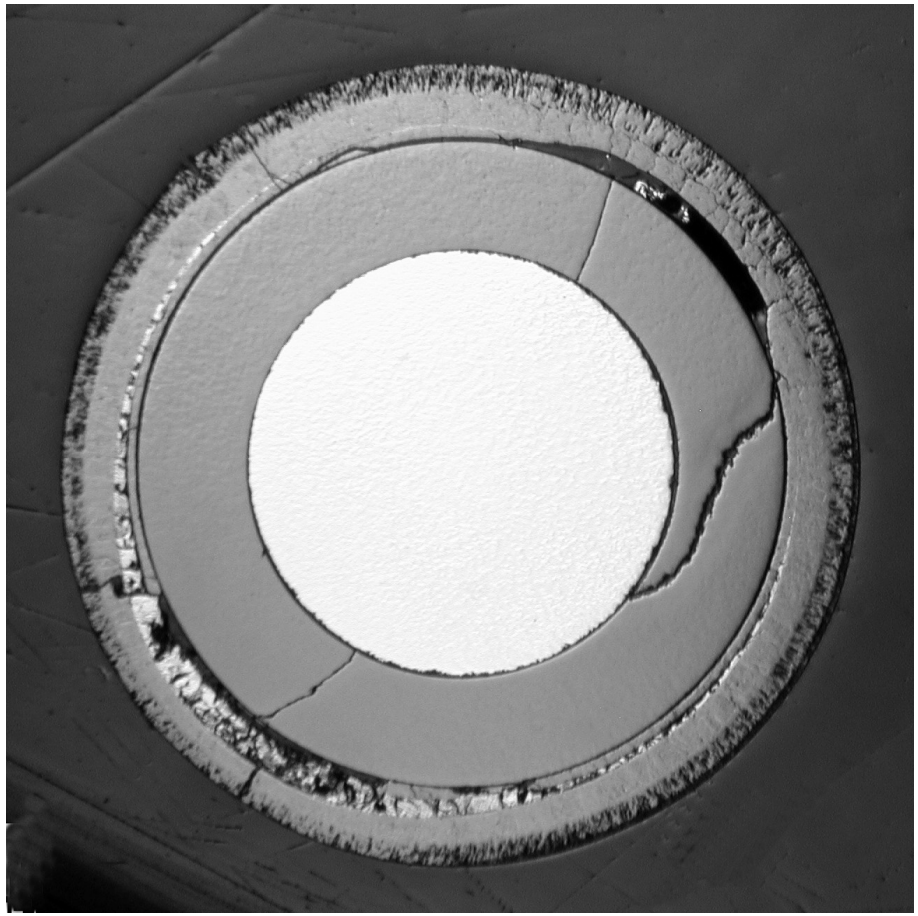

heated rod 21: not completely oxidised melt layer at relatively cold position near to shroud

Fig. 85: QUENCH-14; Cross section at elevation 1000 mm depicting separately test rods 20, 21.

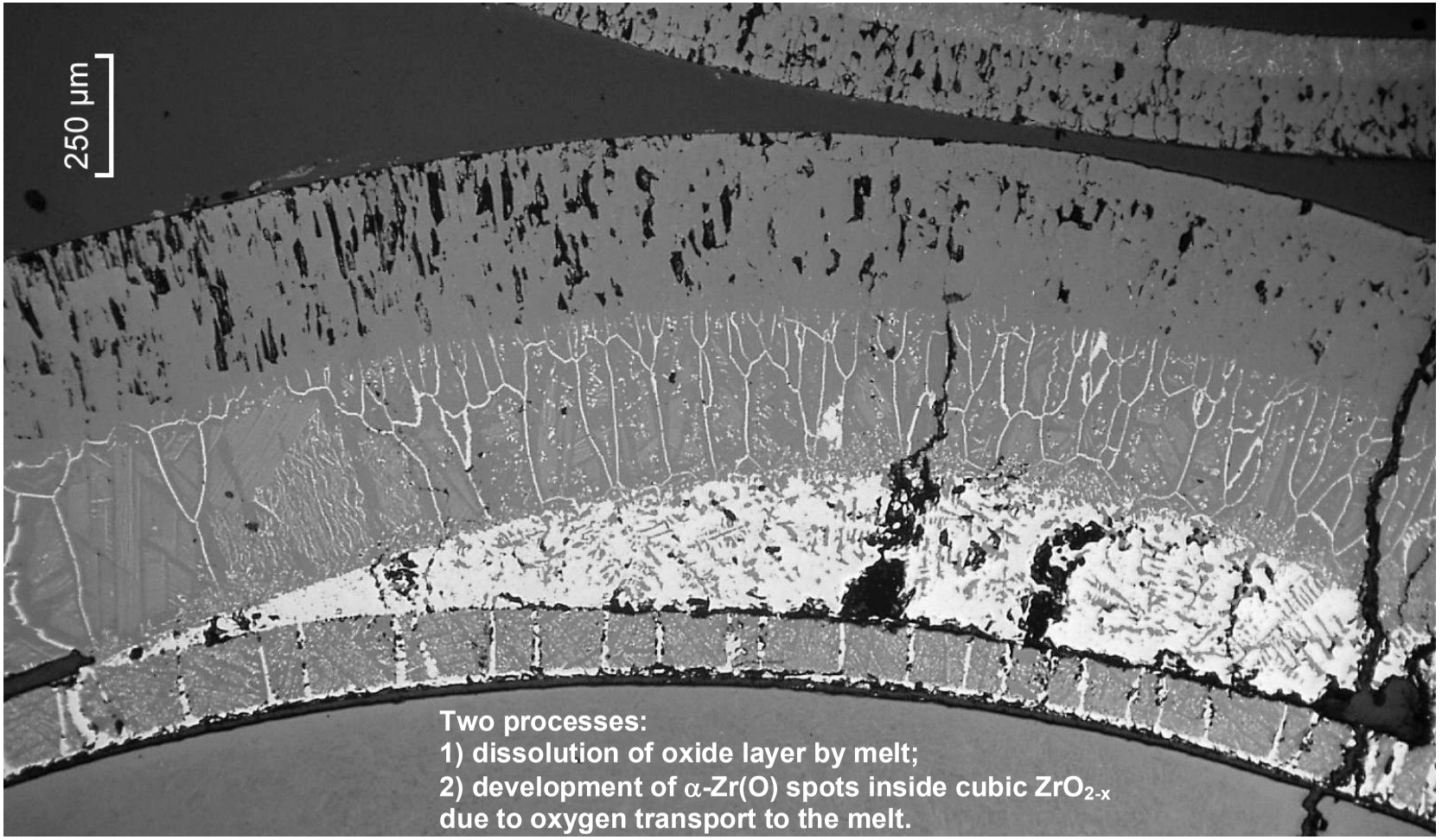

Fig. 86: QUENCH-14; Elevation 1000 mm, rod No. 2: interaction of melt with external oxide layer under steam starvation conditions.

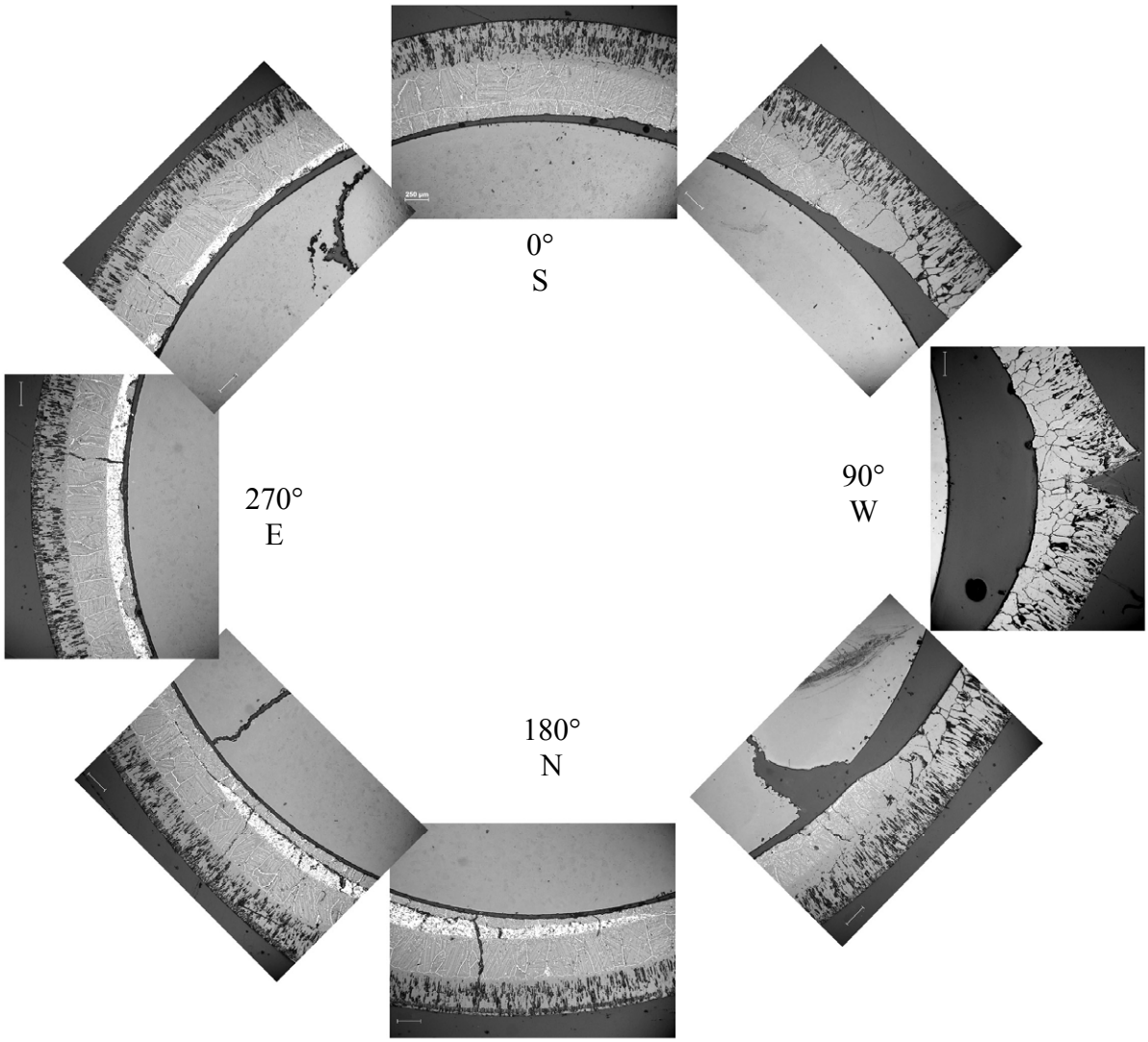

Fig. 87: QUENCH-14; Cladding of rod No. 11 at 1000 mm bundle elevation: oxidised melt and internal oxide layer between 170° and 340°.

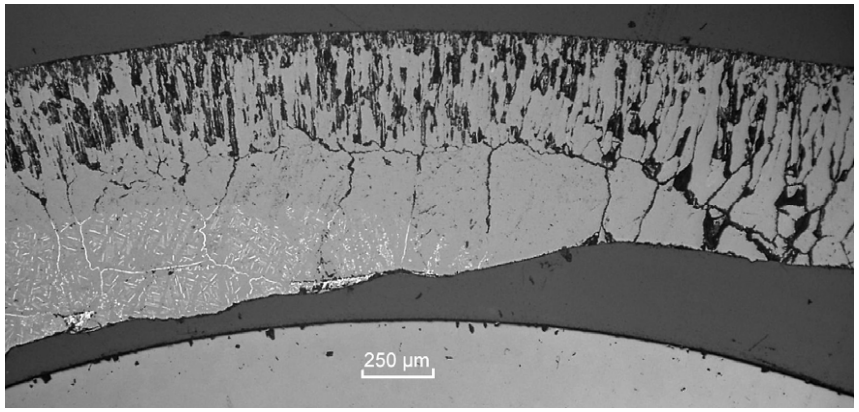

45°: transition from two oxide sub-layers to 1-phase oxide layer

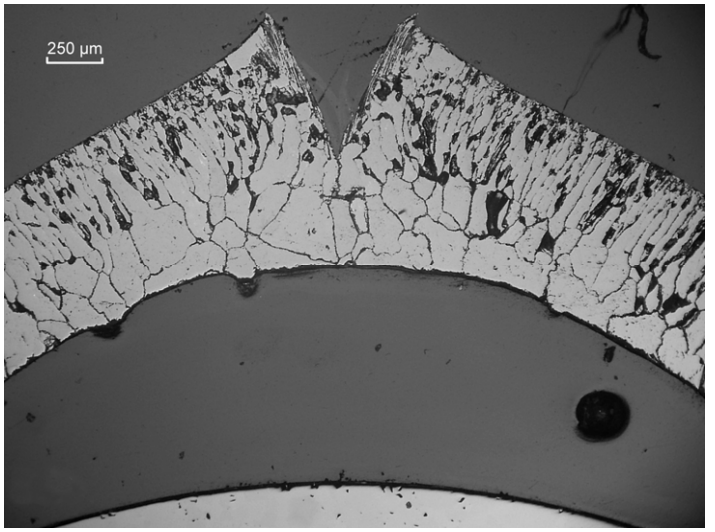

90°: absence of cubic ZrO_2-x phase in oxide layer; melt relocated downwards

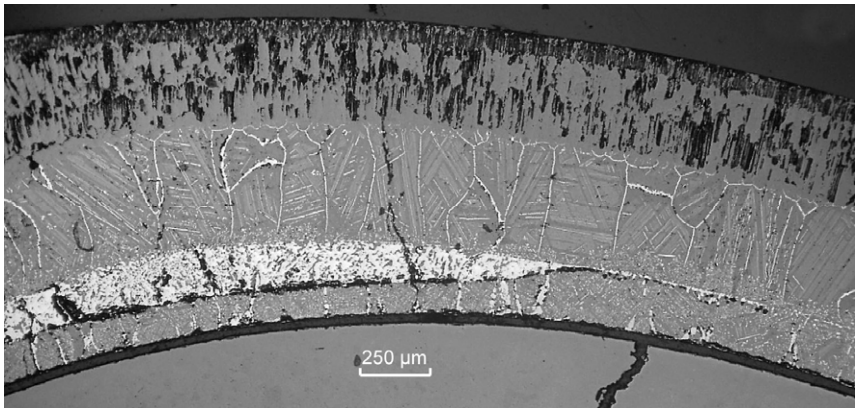

225°: transition from melt to completely oxidised cladding

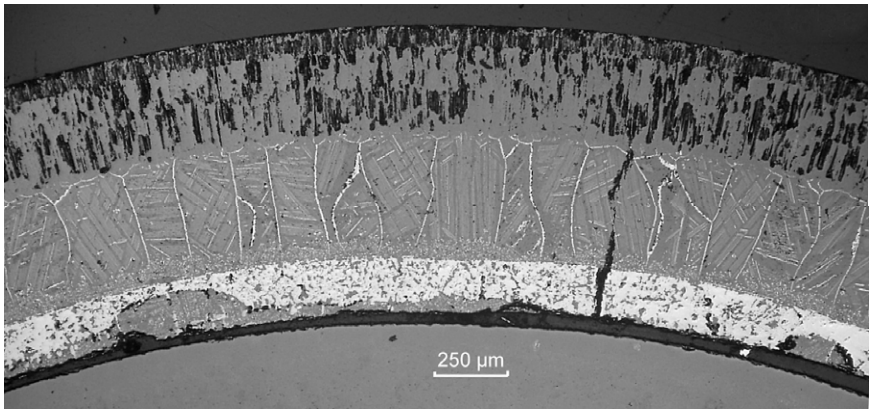

270°: non homogeneous internal oxide layer

Fig. 88: QUENCH-14; Elevation 1000 mm; structure of oxidised cladding of rod No. 11 with frozen and lost melt of metal layer.

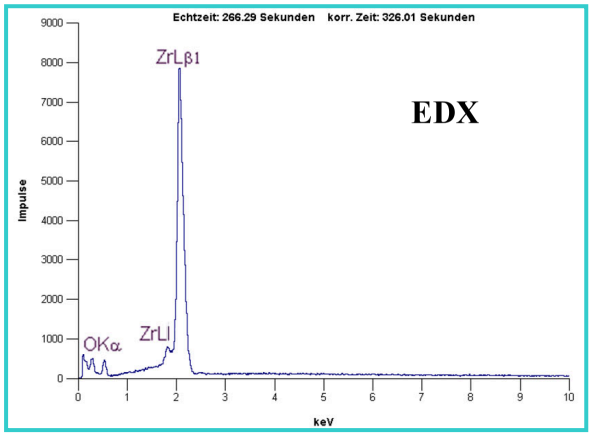

ZrO_2

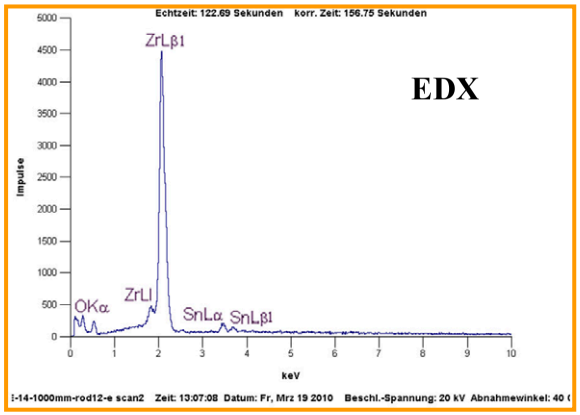

region with Sn precipitates

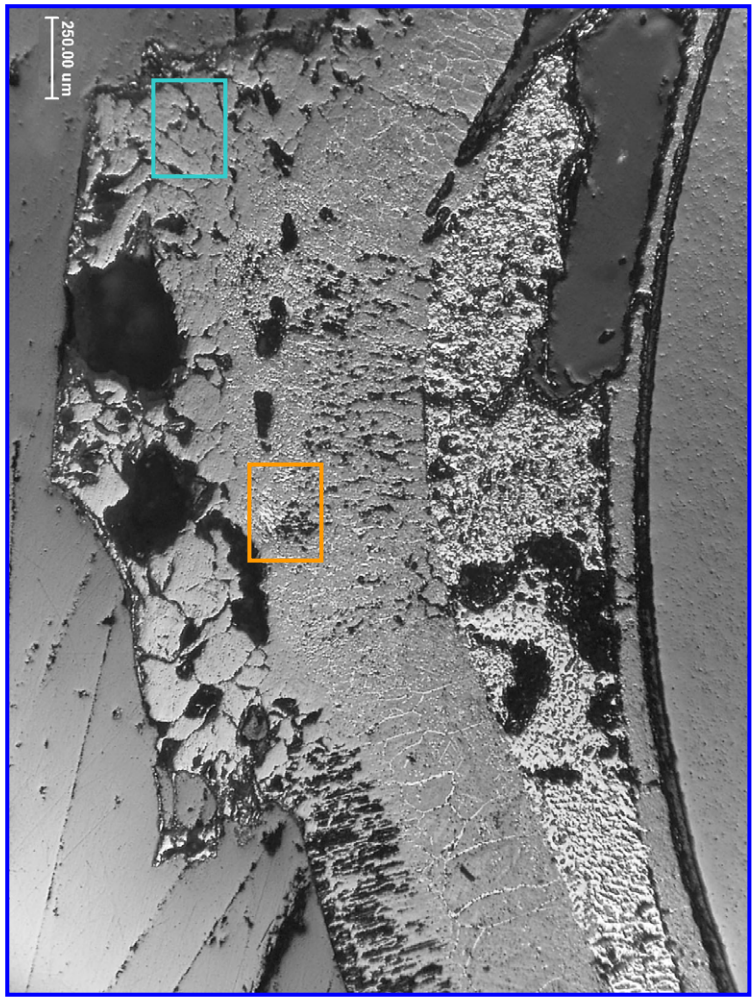

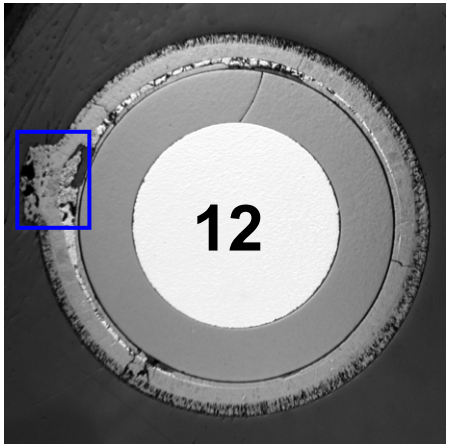

Fig. 89: QUENCH-14; cross section of rod No. 12 at elev. 1000 mm; interaction of oxidised cladding tube with relocated piece of Zry-4 shroud.

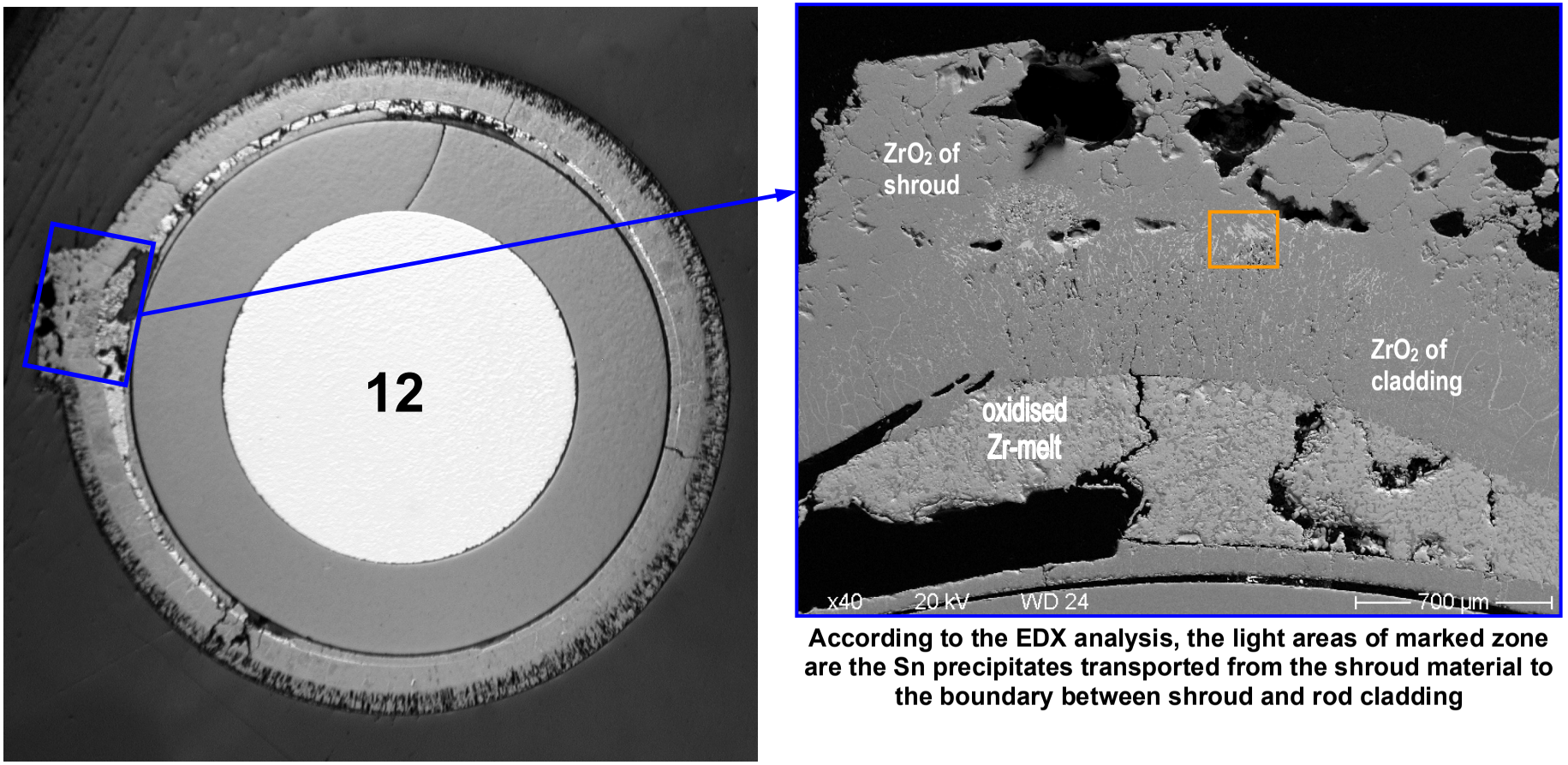

According to the EDX analysis, the light areas of marked zone are the Sn precipitates transported from the shroud material to the boundary between shroud and rod cladding

Fig. 90: QUENCH-14; EDX analysis of contact point between the Zry-4 shroud and the M5® cladding of rod NO. 12 at elevation 1000 mm.

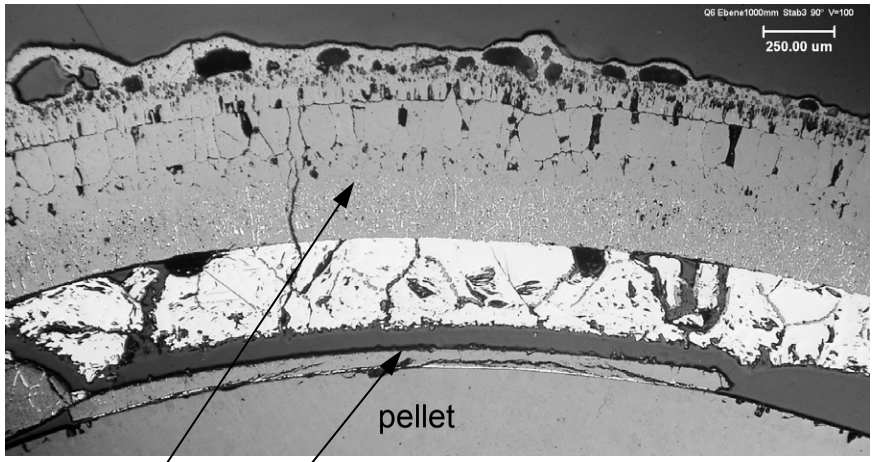

rod 3, 90°: outer and internal oxides; foamy Ta2O5-containing external layer from failed thermocouple

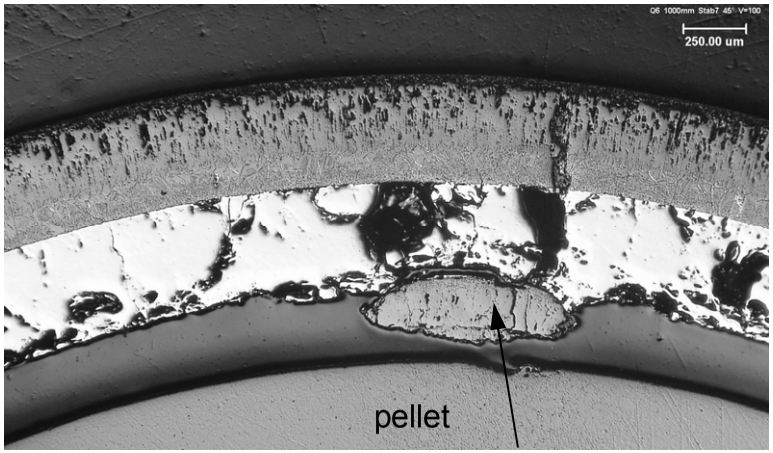

rod 7, 45°: external oxide, local internal oxide from relocated melt

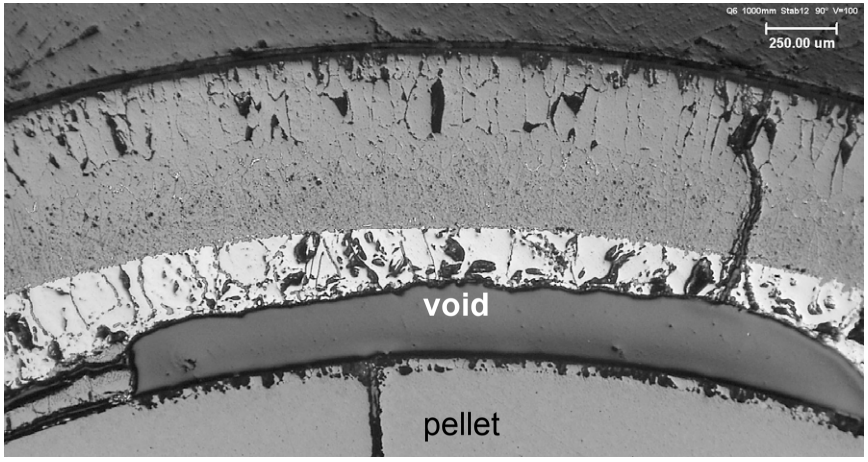

rod12, 90°: void from downwards relocated melt

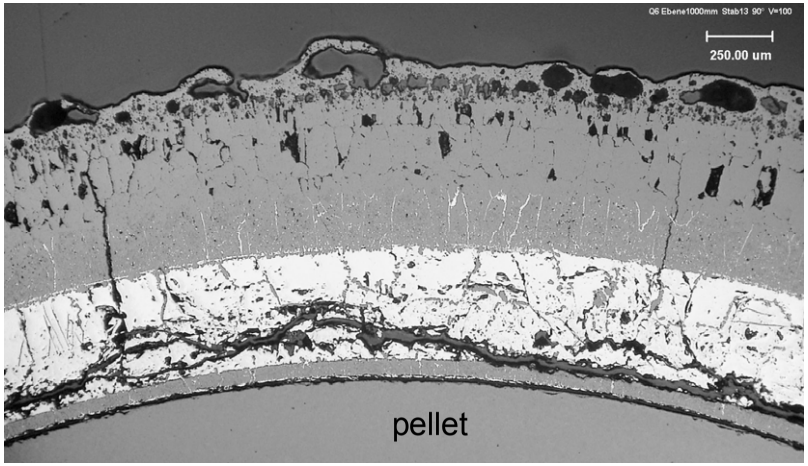

rod 13, 90°: outer and internal oxides; foamy Ta2O5-containing external layer from failed thermocouple

Fig. 91: Some fragments of cladding structures of the Quench-06 bundle at elevation 1000 mm.

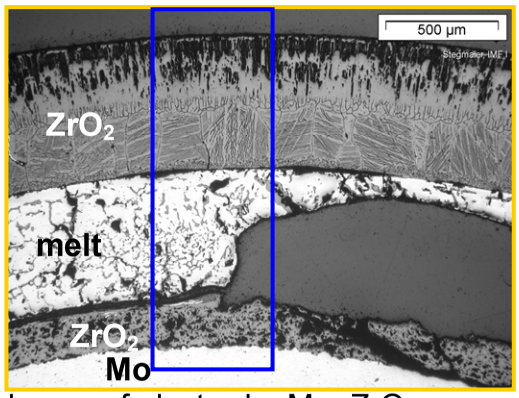

layers of electrode: Mo, ZrO_2 sprayed between Mo and clad. for insulation; layers of cladding: melt, oxide ZrO_2

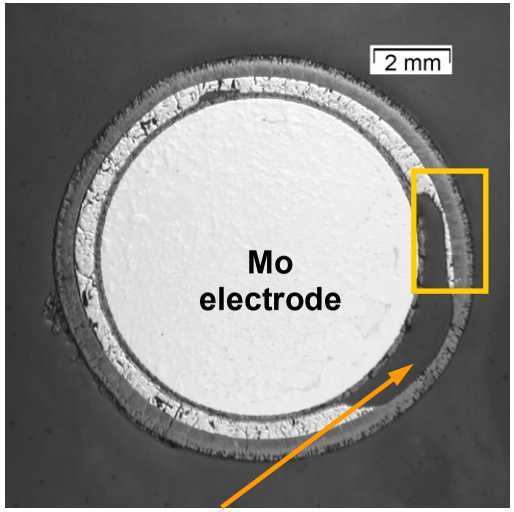

rod 2 with void from downwards relocated **melt**

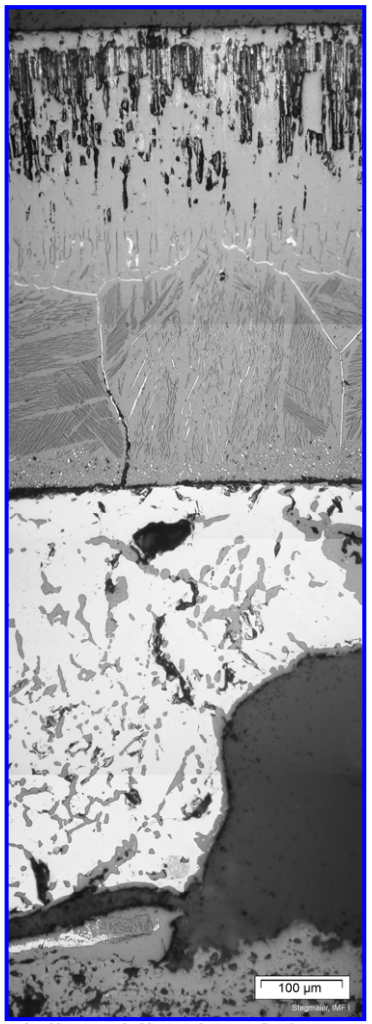

partially oxidised **melt** between ZrO_2 layers

Fig. 92: QUENCH-14; Cross section at elevation 1050 mm; oxidation state of rod No. 2 with moderate oxidised melt.

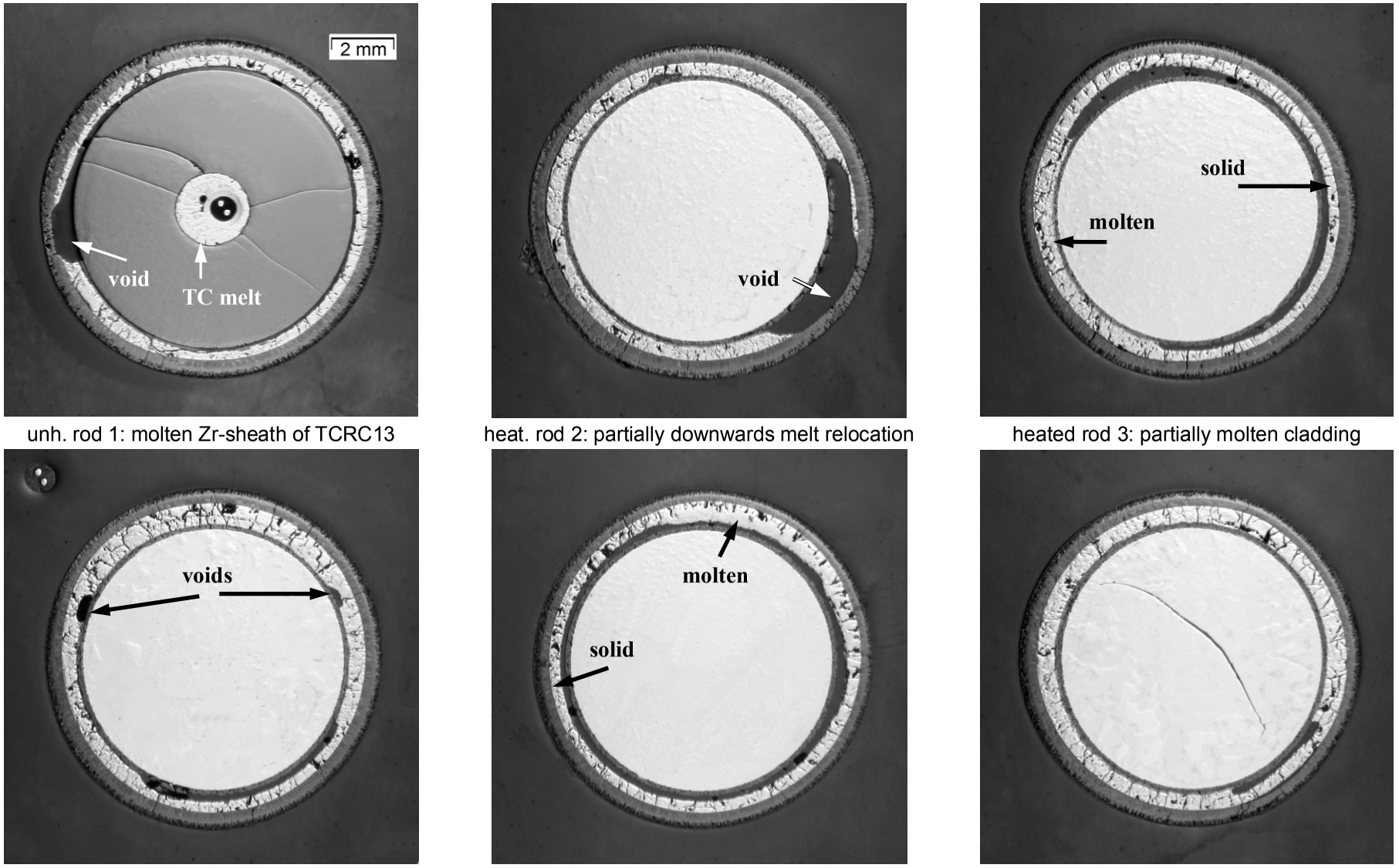

unh. rod 1: molten Zr-sheath of TCRC13

heat. rod 2: partially downwards melt relocation

heated rod 3: partially molten cladding

heat. rod 4: local downwards melt relocation

heated rod 5: partially molten cladding

heated rod 6: partially molten cladding

Fig. 93: QUENCH-14; Cross section at elevation 1050 mm; rods 1-6 externally and internally oxidised cladding.

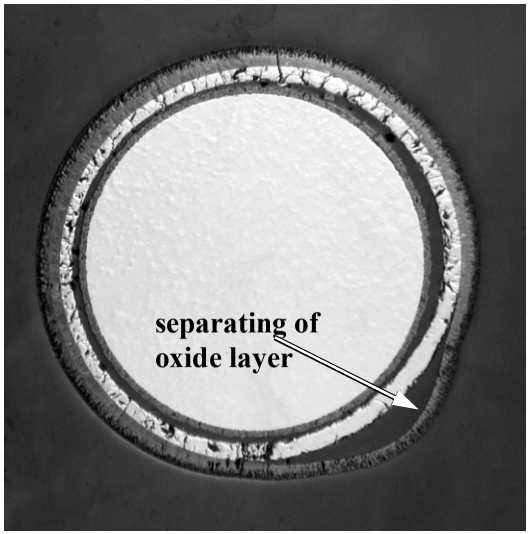

heat. rod 7: solid metal layer at temperature

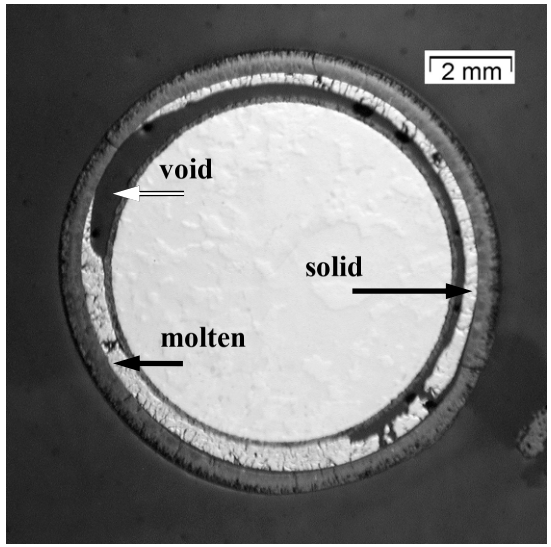

heat. rod 8: partially downwards melt relocation

heat. rod 9: solid metal layer at temperature

heat. rod 10: solid metal layer at temperature

heat. rod 11: deformation of solid cladding

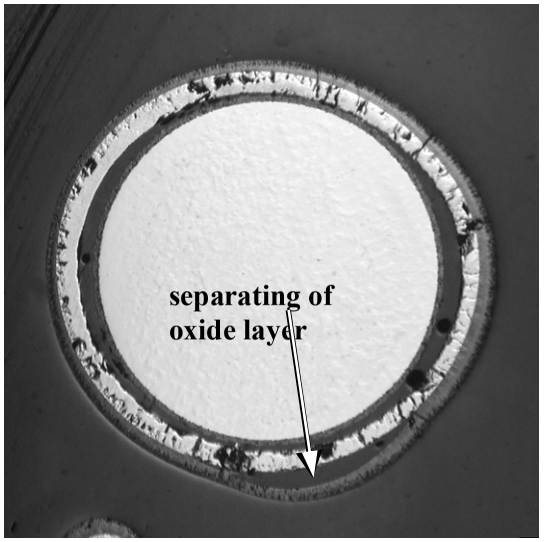

heat. rod 12: deformation of solid cladding

Fig. 94: QUENCH-14; Cross section at elevation 1050 mm; rods 7-12 with externally and internally oxidised cladding.

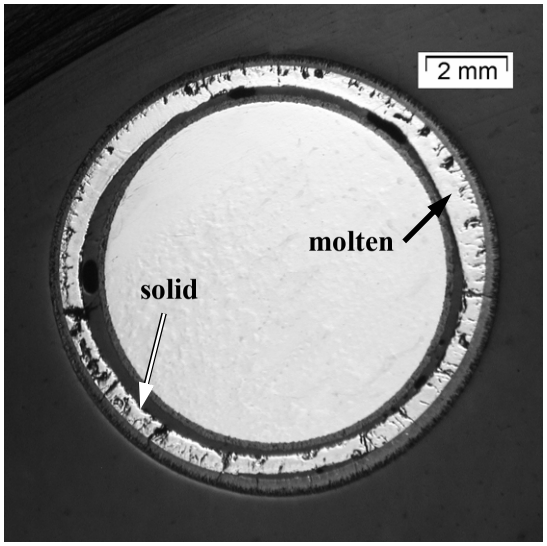

heat. rod 13: partially molten cladding

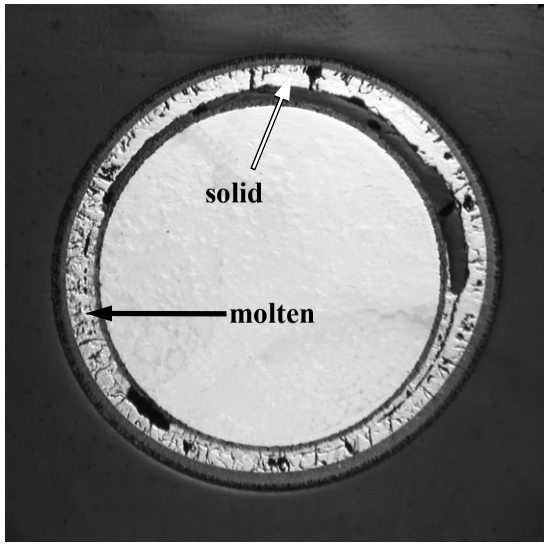

heat. rod 14: partially molten cladding

heat rod 15: solid metal layer at temperature

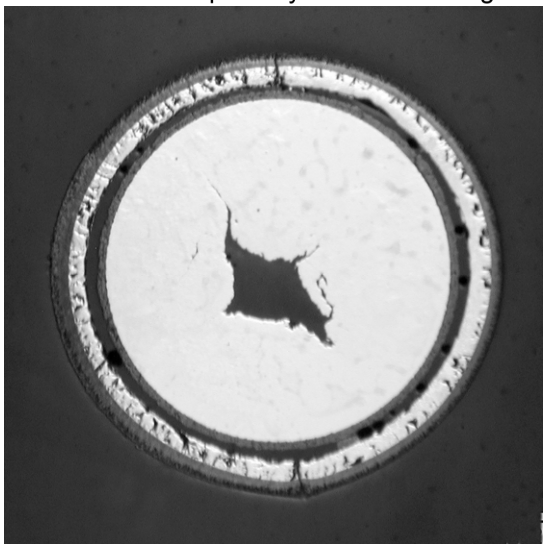

heat. rod 17: solid metal layer at temperature

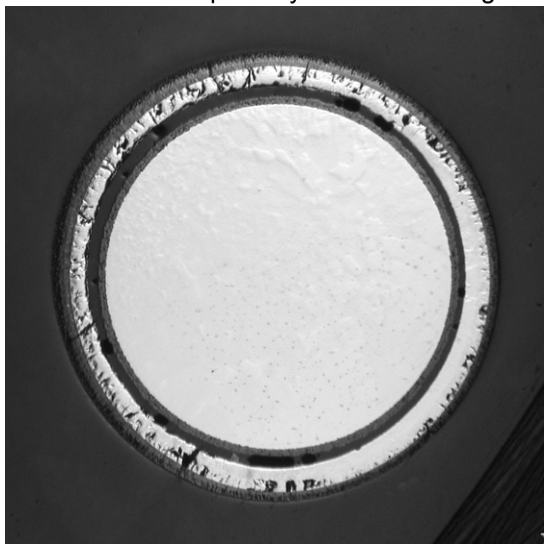

heat. rod 18: solid metal layer at temperature

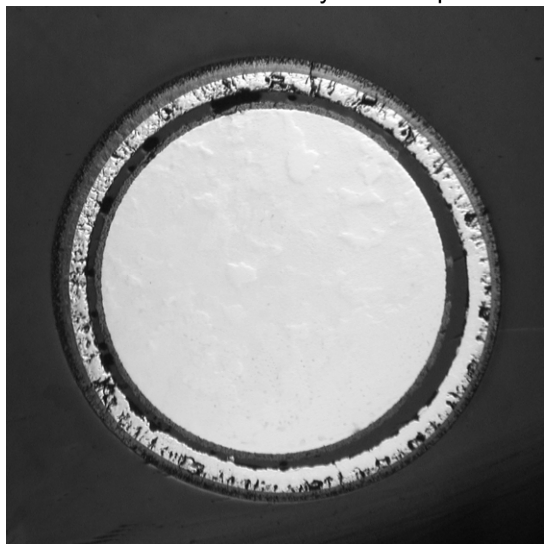

heat. rod 19: solid metal layer at temperature

Fig. 95: QUENCH-14; Cross section at elev. 1050 mm; rods 13-19 with externally and internally oxidised cladding.

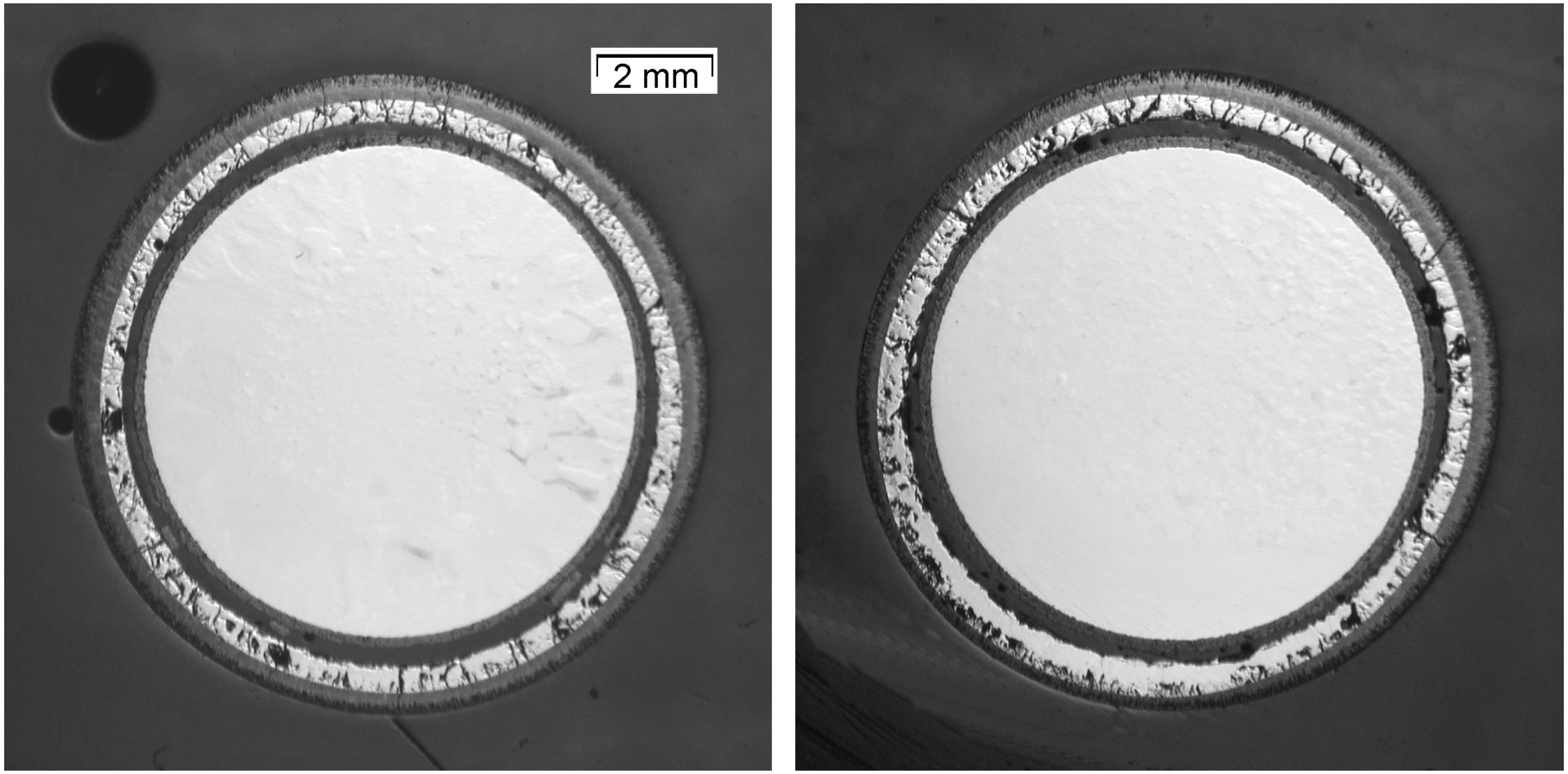

heated rod 20: solid metal layer at temperature

heated rod 21: solid metal layer at temperature

Fig. 96: QUENCH-14; Cross section at elevation 1050 mm depicting separately test rods 20, 21.

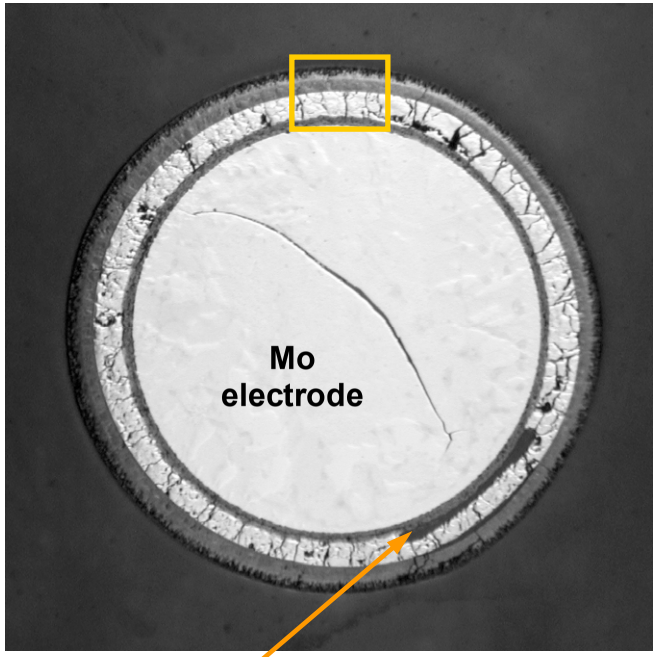

rod 6 with void from downwards relocated **melt**

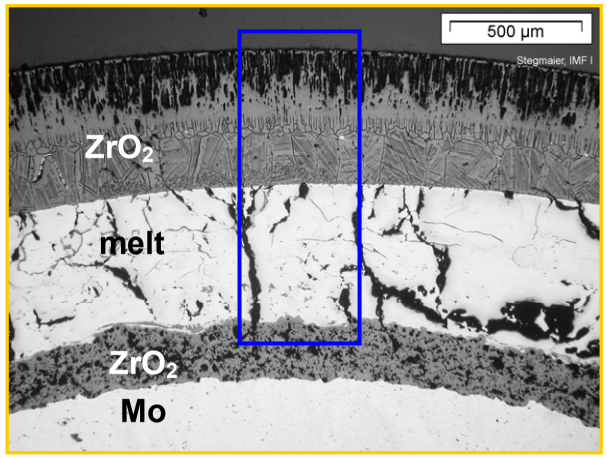

layers of electrode: Mo, ZrO_2 sprayed between Mo and clad. for insulation; layers of cladding: melt, oxide ZrO_2

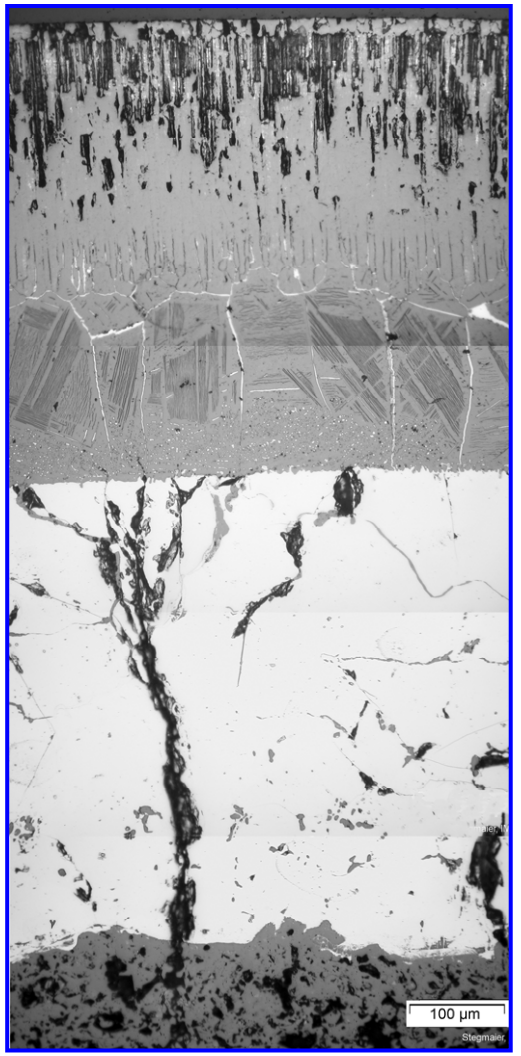

slightly oxidised **melt** between ZrO_2 layers

Fig. 97: QUENCH-14; Cross section at elevation 1050 mm; oxidation state of rod No. 6 with slightly oxidised melt.

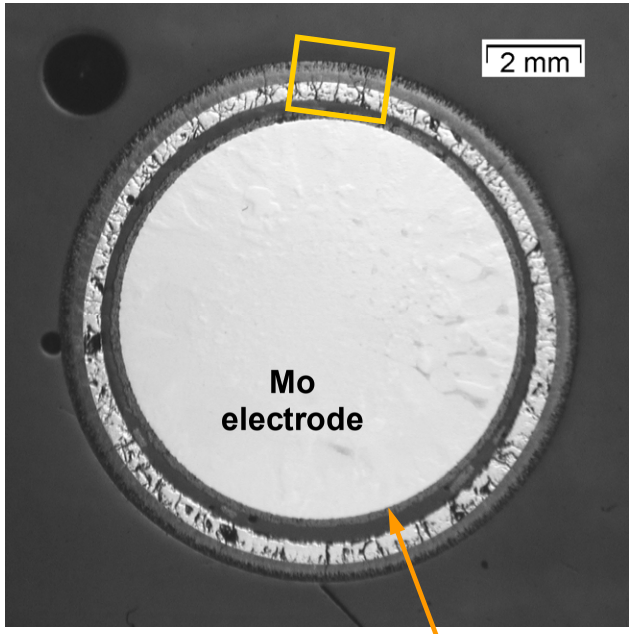

rod 20 with intact ZrO_2 layer
sprayed on the Mo electrode

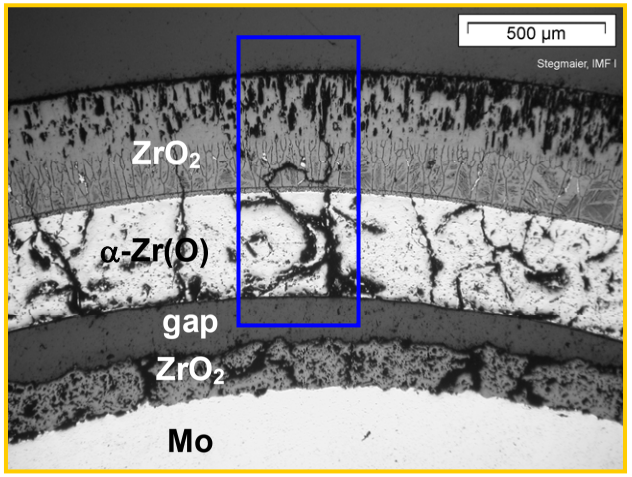

layers of electrode: Mo, sprayed ZrO_2; gap
between electrode and cladding;
layers of cladding: melt, oxide ZrO_2

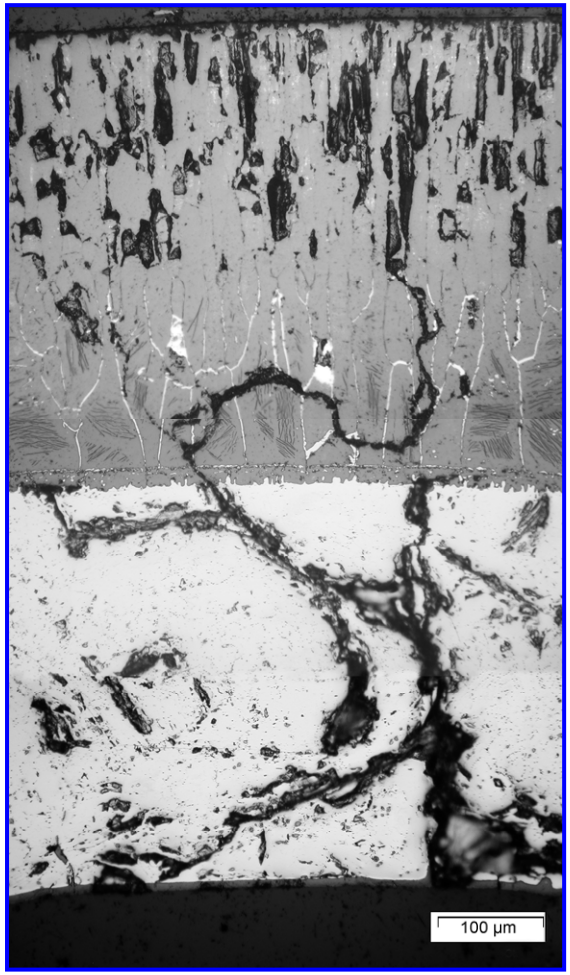

2 layers of cladding: ZrO_2
and α-Zr(O)

Fig. 98: QUENCH-14; Cross section at elevation 1050 mm; oxidation state of rod No. 20 without melt formation.

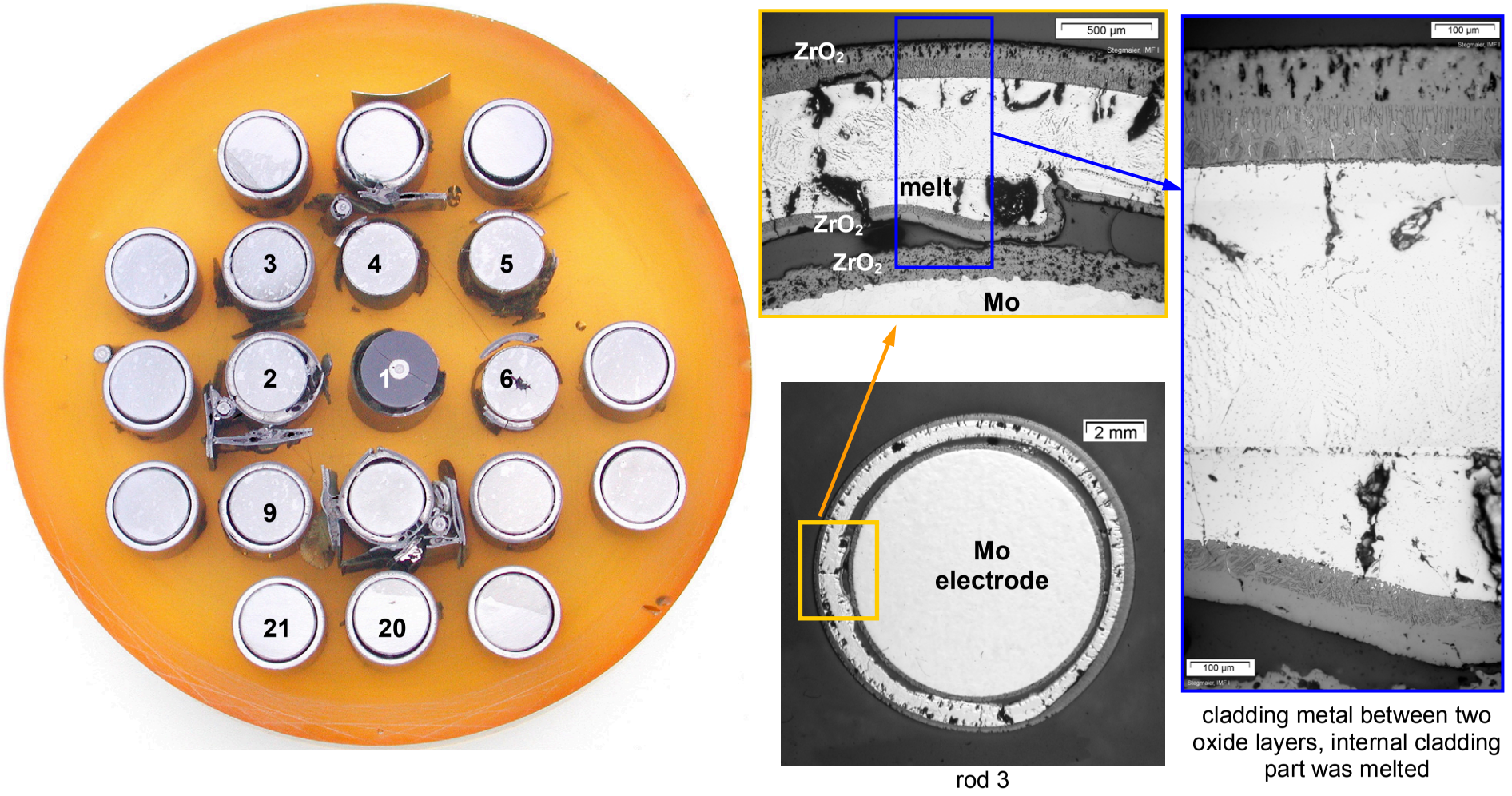

Fig. 99: QUENCH-14; Cross section at elevation 1100 mm; oxidation state of rod No. 3.

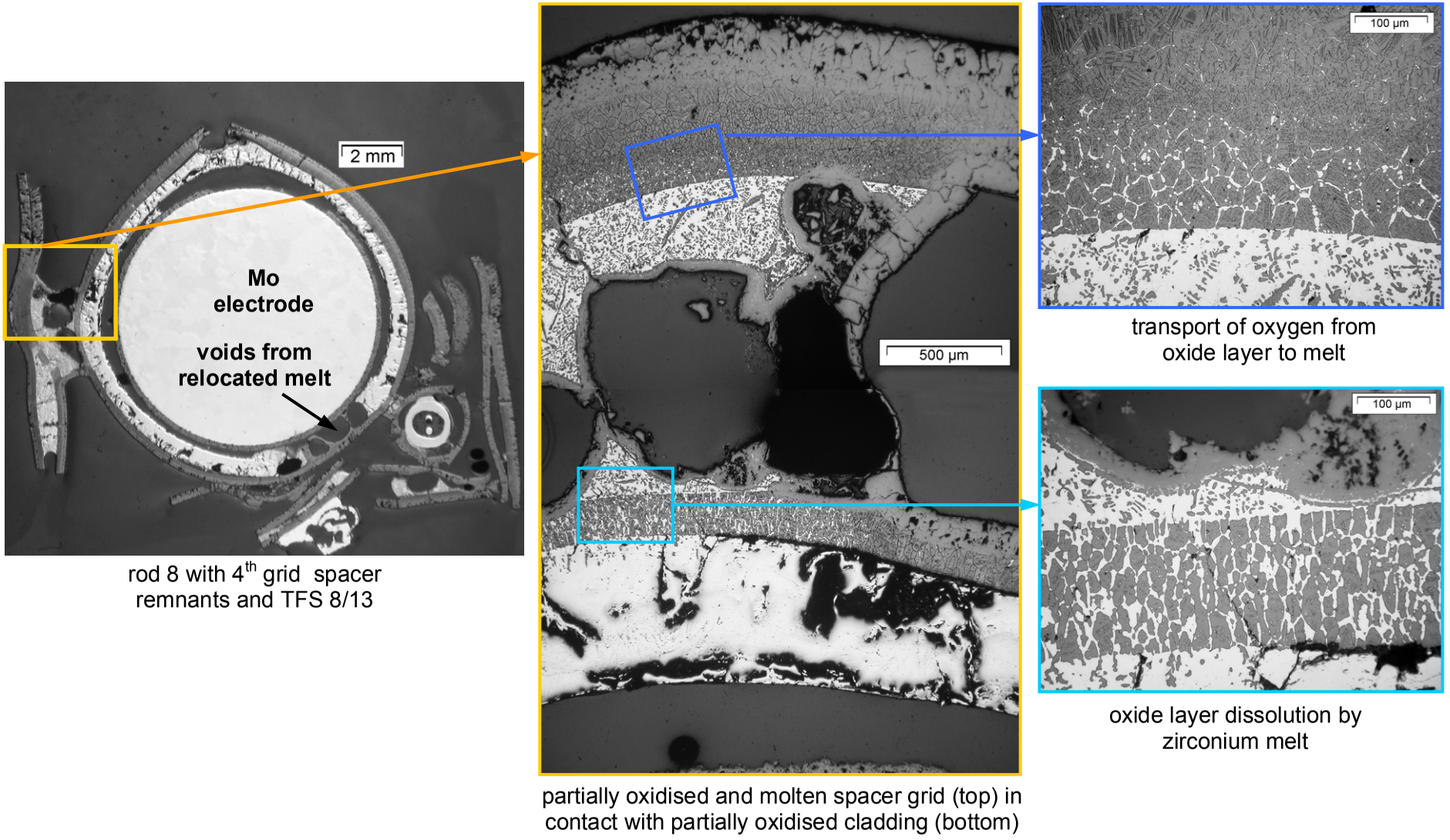

rod 8 with 4th grid spacer remnants and TFS 8/13

partially oxidised and molten spacer grid (top) in contact with partially oxidised cladding (bottom)

transport of oxygen from oxide layer to melt

oxide layer dissolution by zirconium melt

Fig. 100: QUENCH-14; Cross section at elevation 1100 mm; oxidation state of rod No. 8.

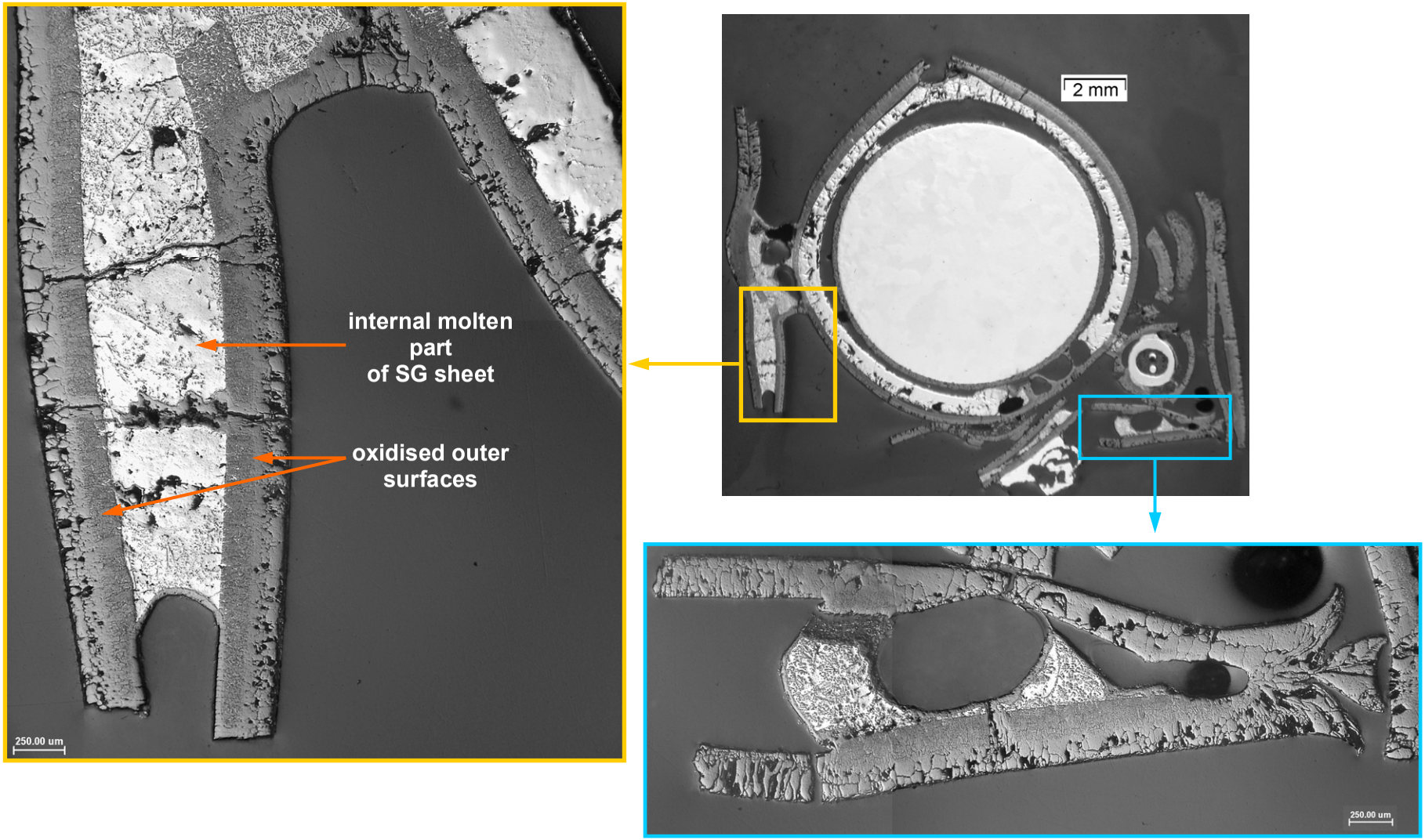

Fig. 101: QUENCH-14; Elevation 1100 mm; oxidation state of the Zry-4 spacer grid sheets at rod No. 8.

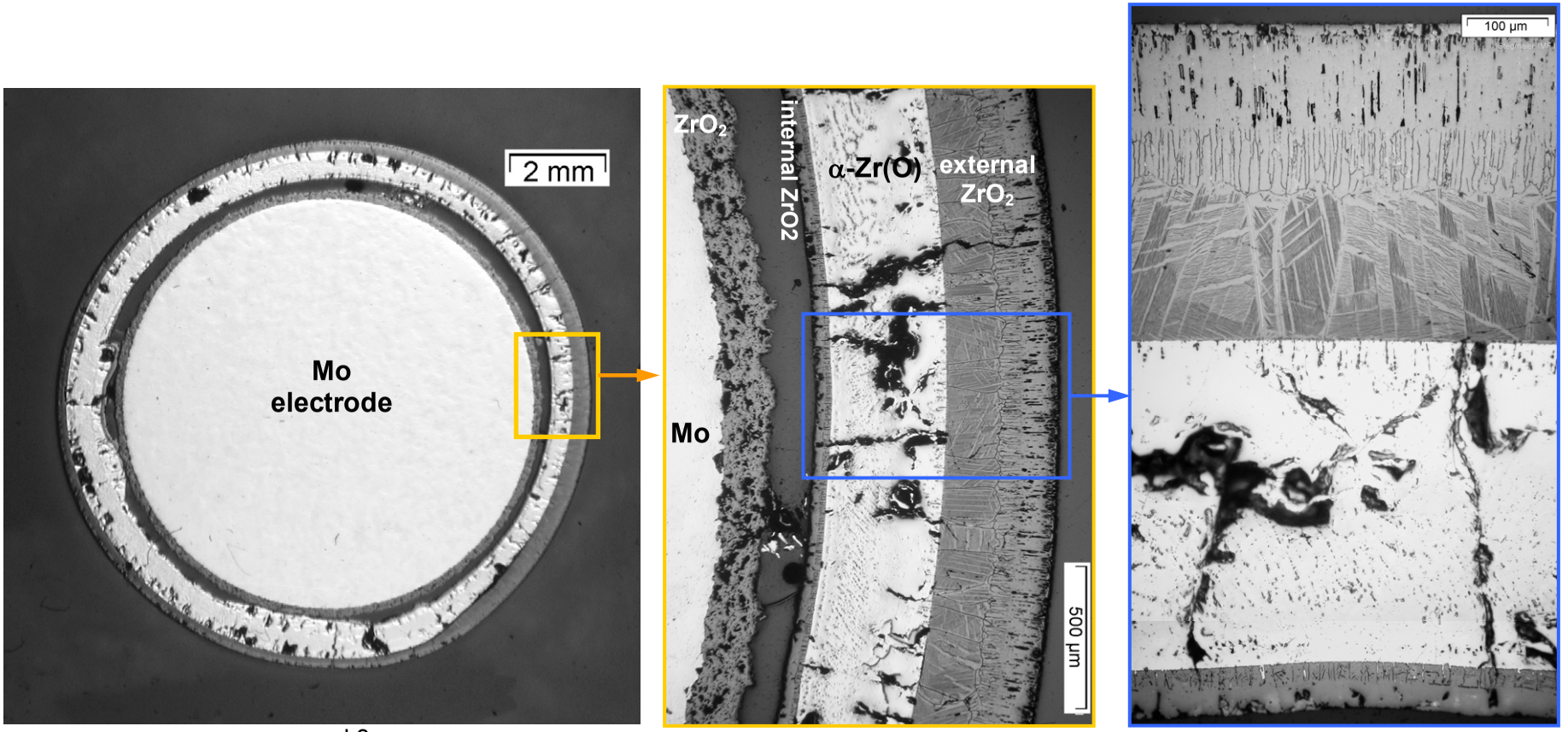

rod 3

cladding metal between two oxide layers; internal oxide layer developed in steam penetrated in the gap between electrode and cladding

Fig. 102: QUENCH-14; Cross section at elevation 1100 mm; oxidation state of rod No. 3 (continuation).

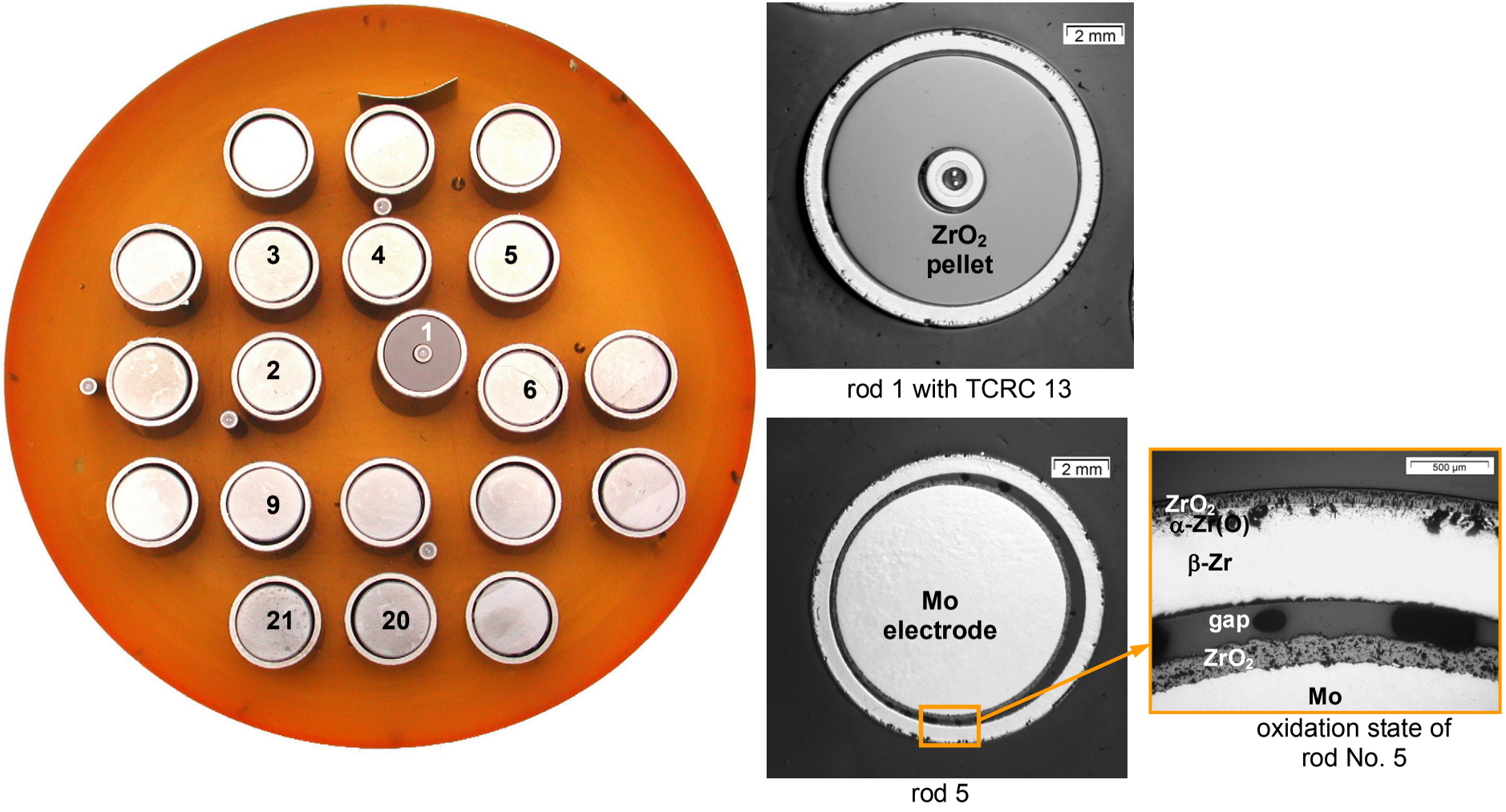

Fig. 103: QUENCH-14; Cross section at elevation 1150 mm; overview, oxidation state of rod No. 5.

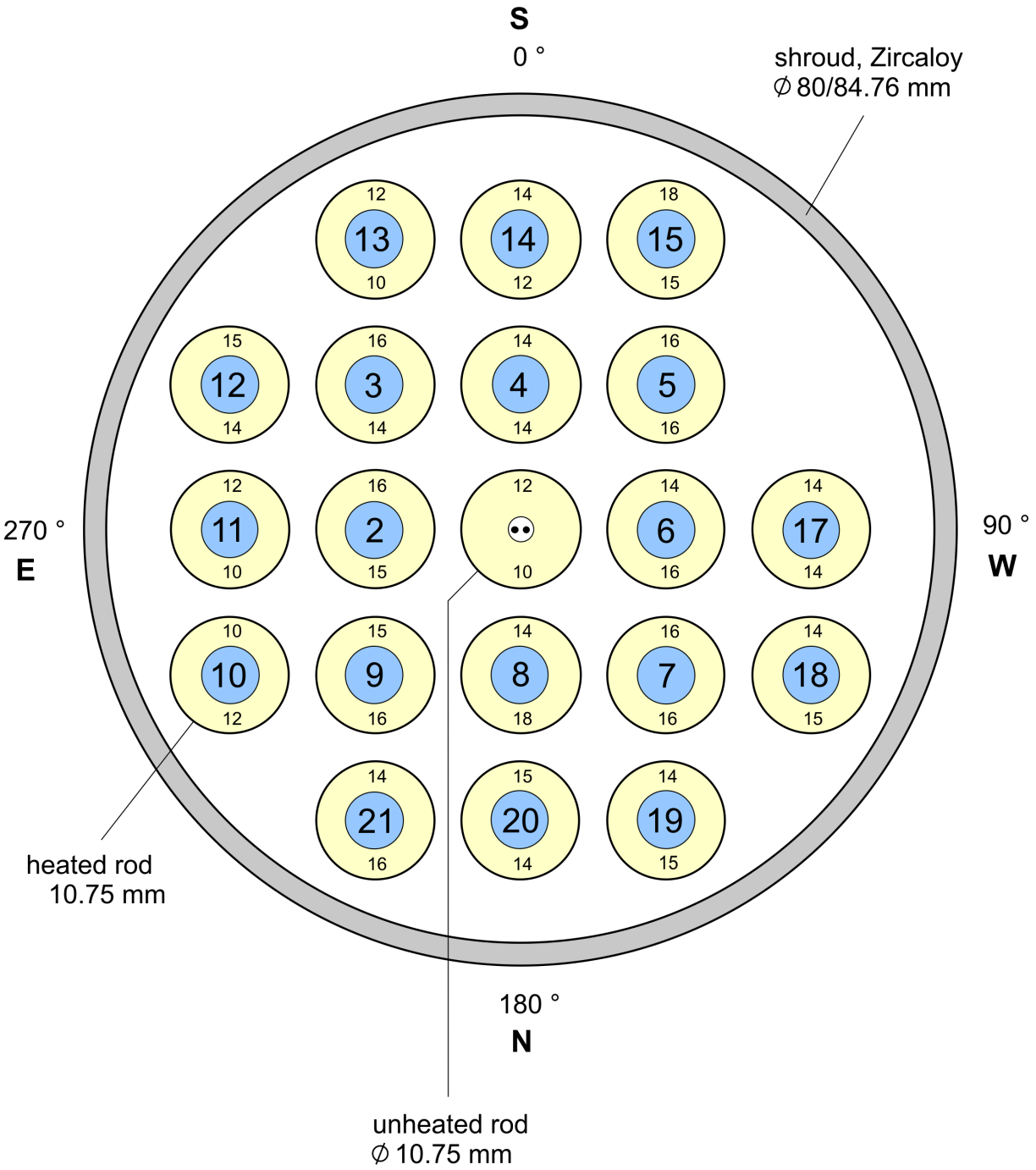

Fig. 104-QUE14 cross section 14-1.doc
12.05.10 - IMF

Fig. 104: QUENCH-14; Oxide layer thickness at bundle elevation 570 mm (Cross section QUE-14-1).

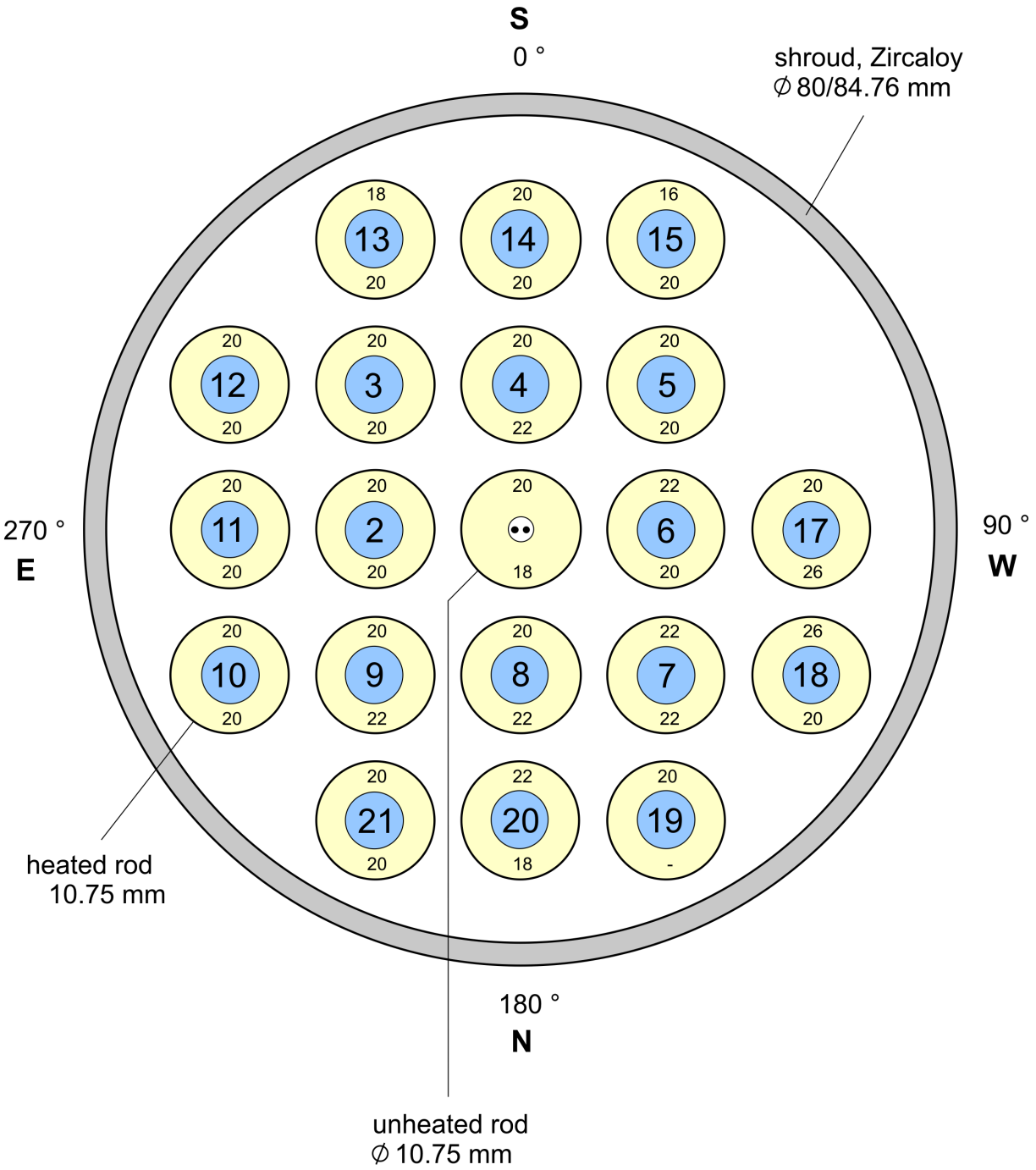

Fig 105 -QUE14 cross section 14-2.doc
12.05.10 - IMF

Fig. 105: QUENCH-14; Oxide layer thickness at bundle elevation 636 mm (Cross section QUE-14-2).

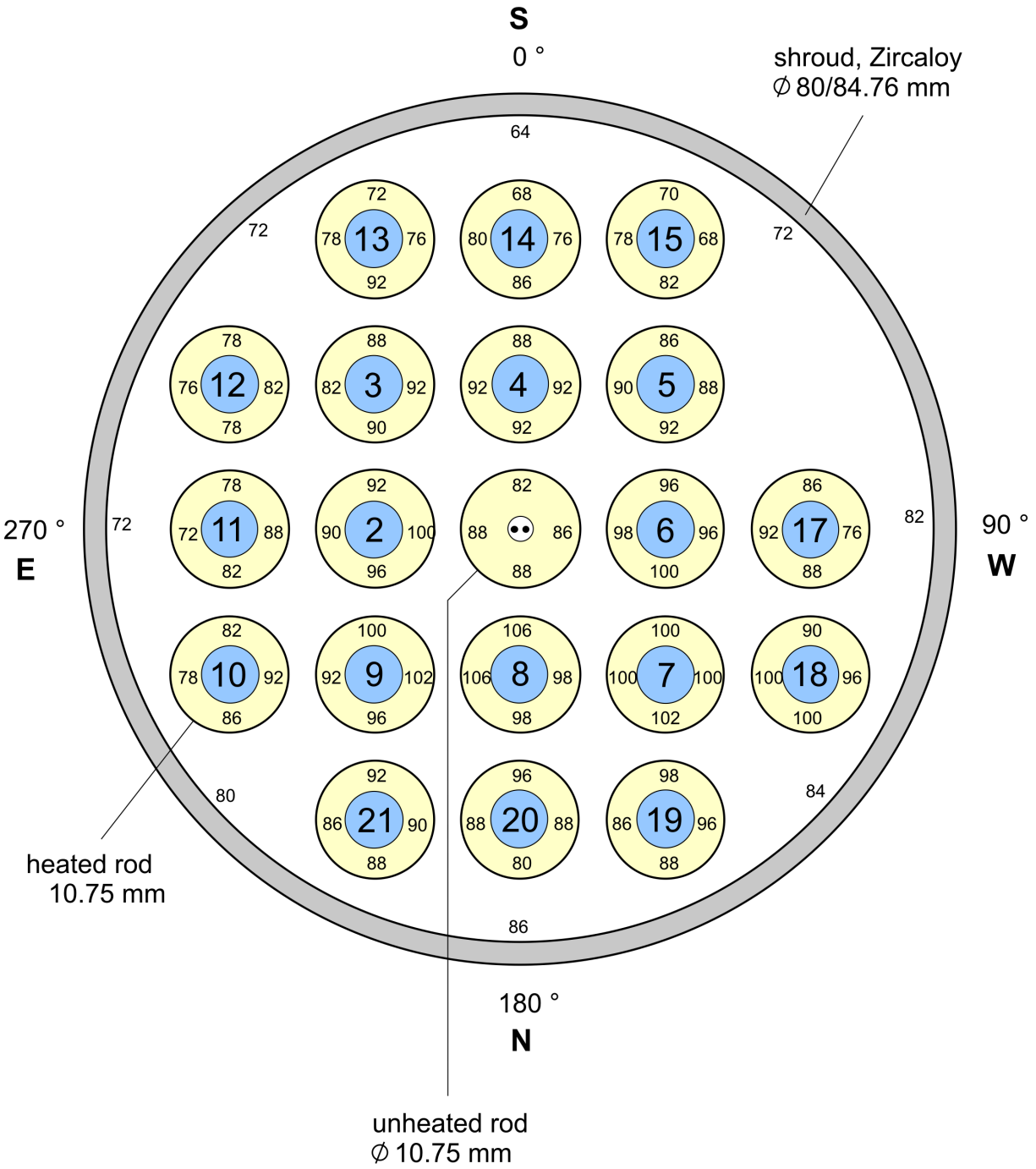

Fig.106 -QUE14 cross section 14-3.doc
12.05.10 - IMF

Fig. 106: QUENCH-14; Oxide layer thickness at bundle elevation 750 mm (Cross section QUE-14-3).

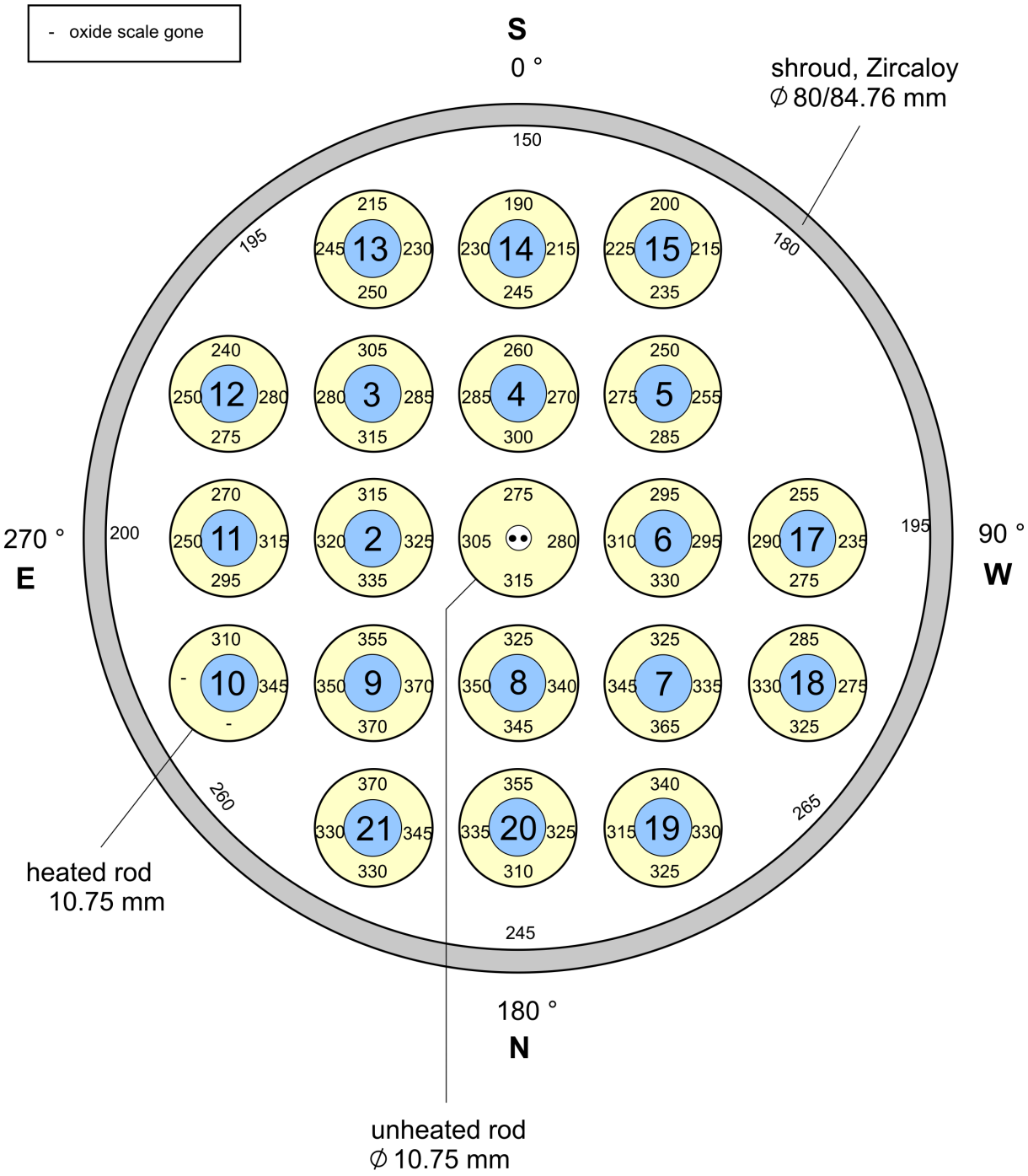

Fig 107 -QUE14 cross section 14-4.doc
112.05.10 - IMF

Fig. 107: QUENCH-14; Oxide layer thickness at bundle elevation 850 mm (Cross section QUE-14-4).

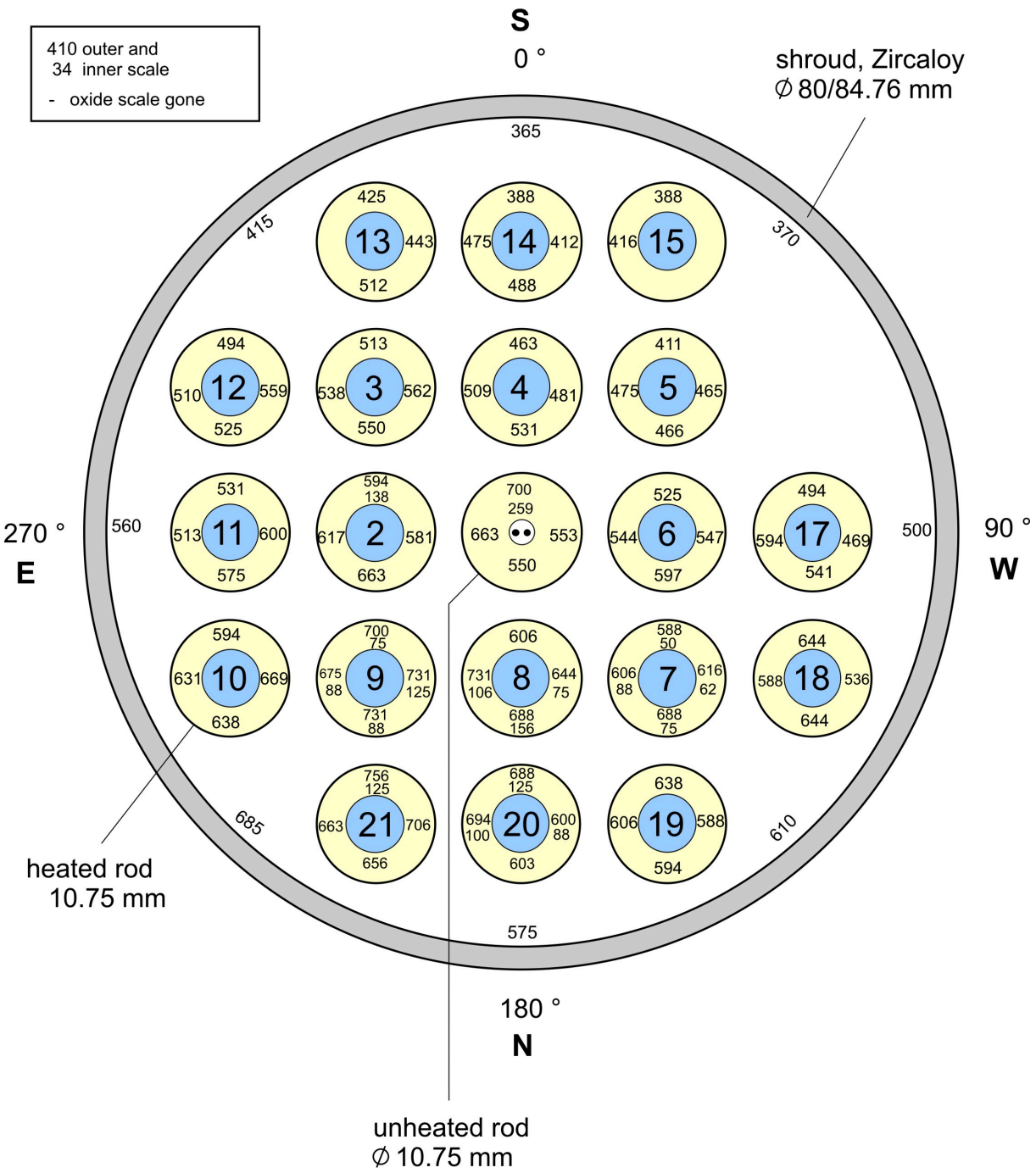

Fig 108 -QUE14 cross section 14-9.doc
12.05.10 - IMF

Fig. 108: QUENCH-14; Oxide layer thickness at bundle elevation 900 mm (Cross section QUE-14-9).

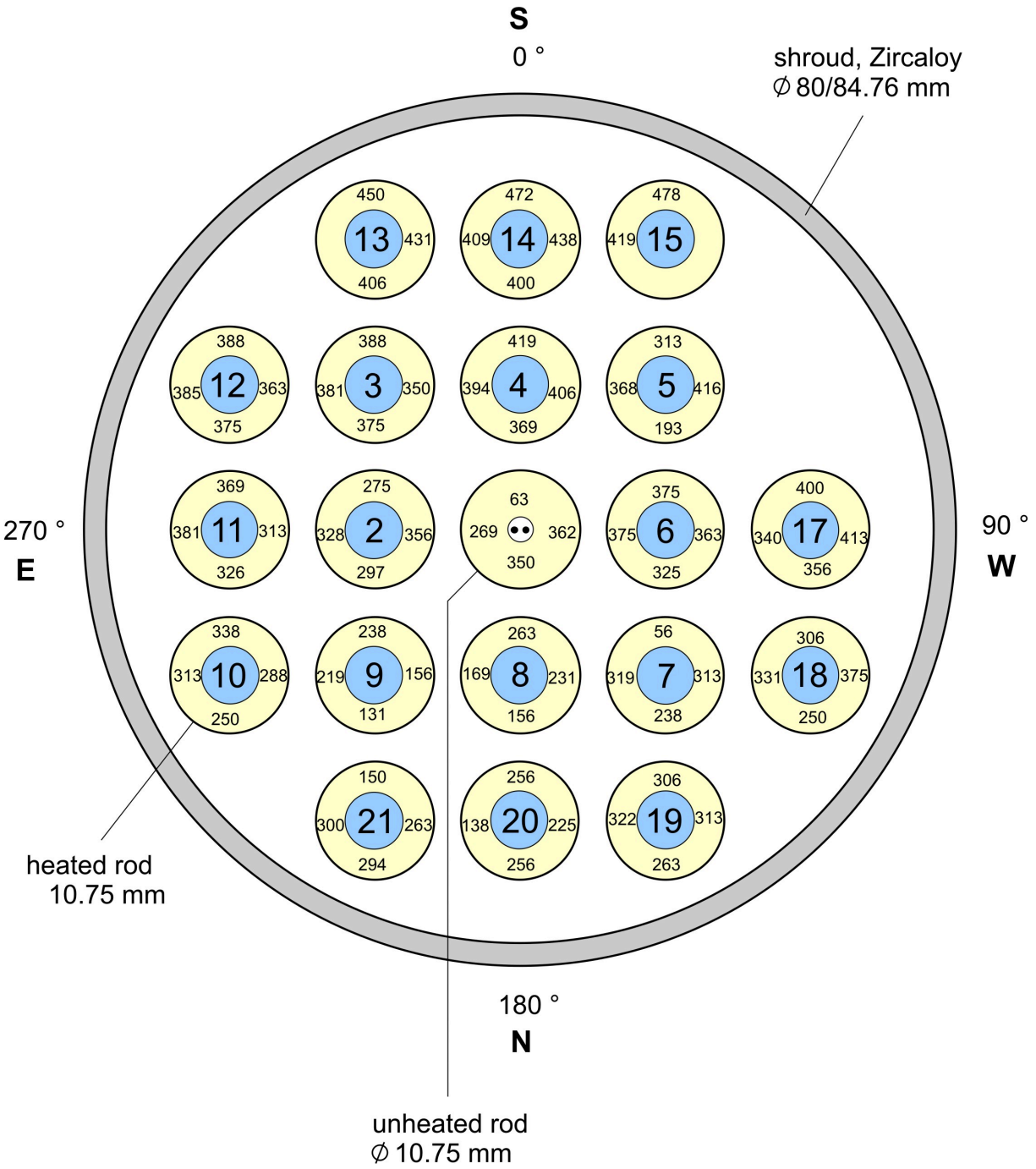

Fig 109 -QUE14 cross section 14-9-2.doc
12.05.10 - IMF

Fig. 109: QUENCH-14; α-layers at bundle elevation 900 mm (Cross section QUE-14-9).

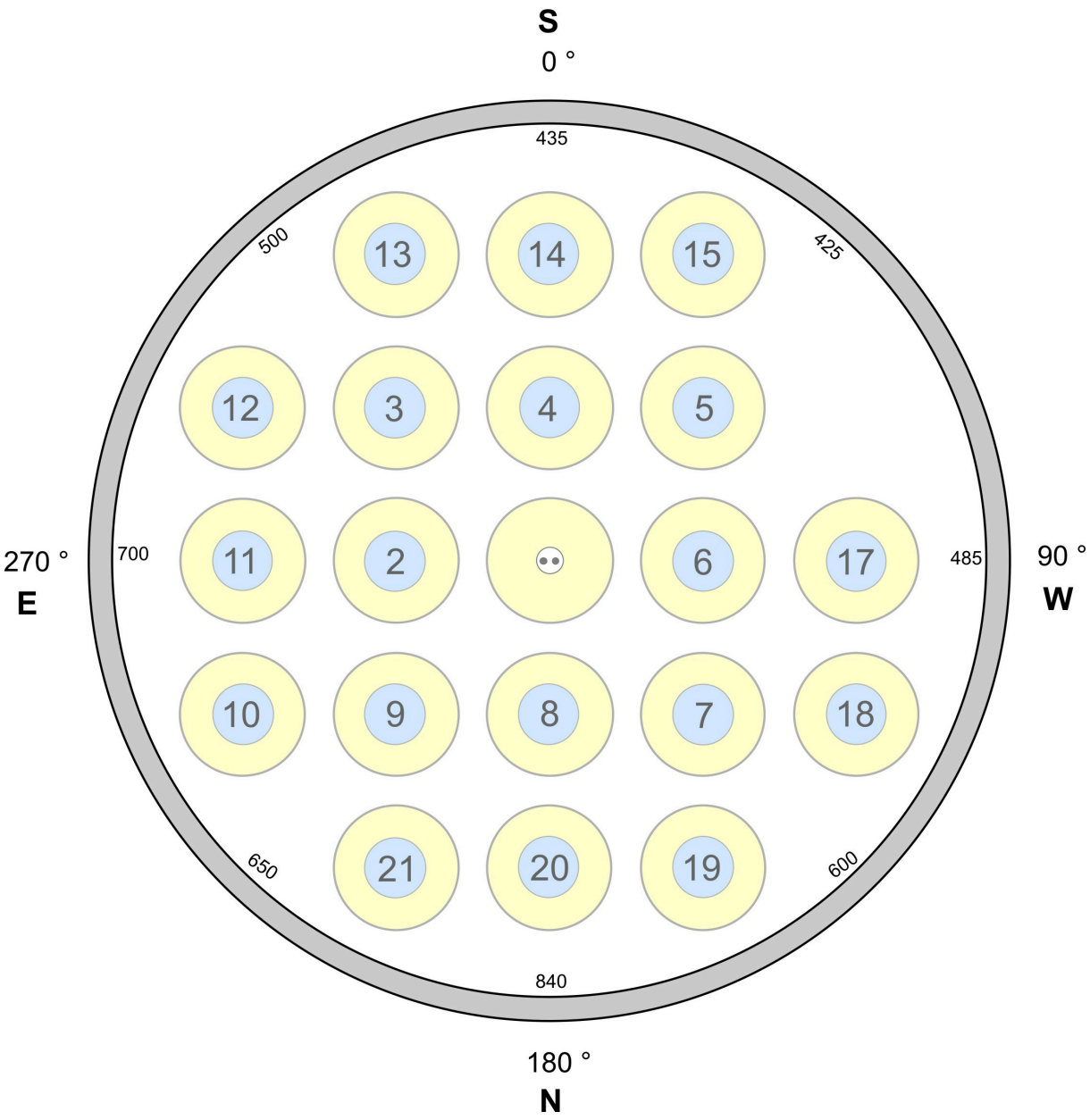

Fig 110 -QUE14 cross section 14-16 .doc
12.05.10 - IMF

Fig. 110: QUENCH-14; Oxide layer thickness of the shroud at bundle elevation 925 mm (Cross section QUE-14-16).

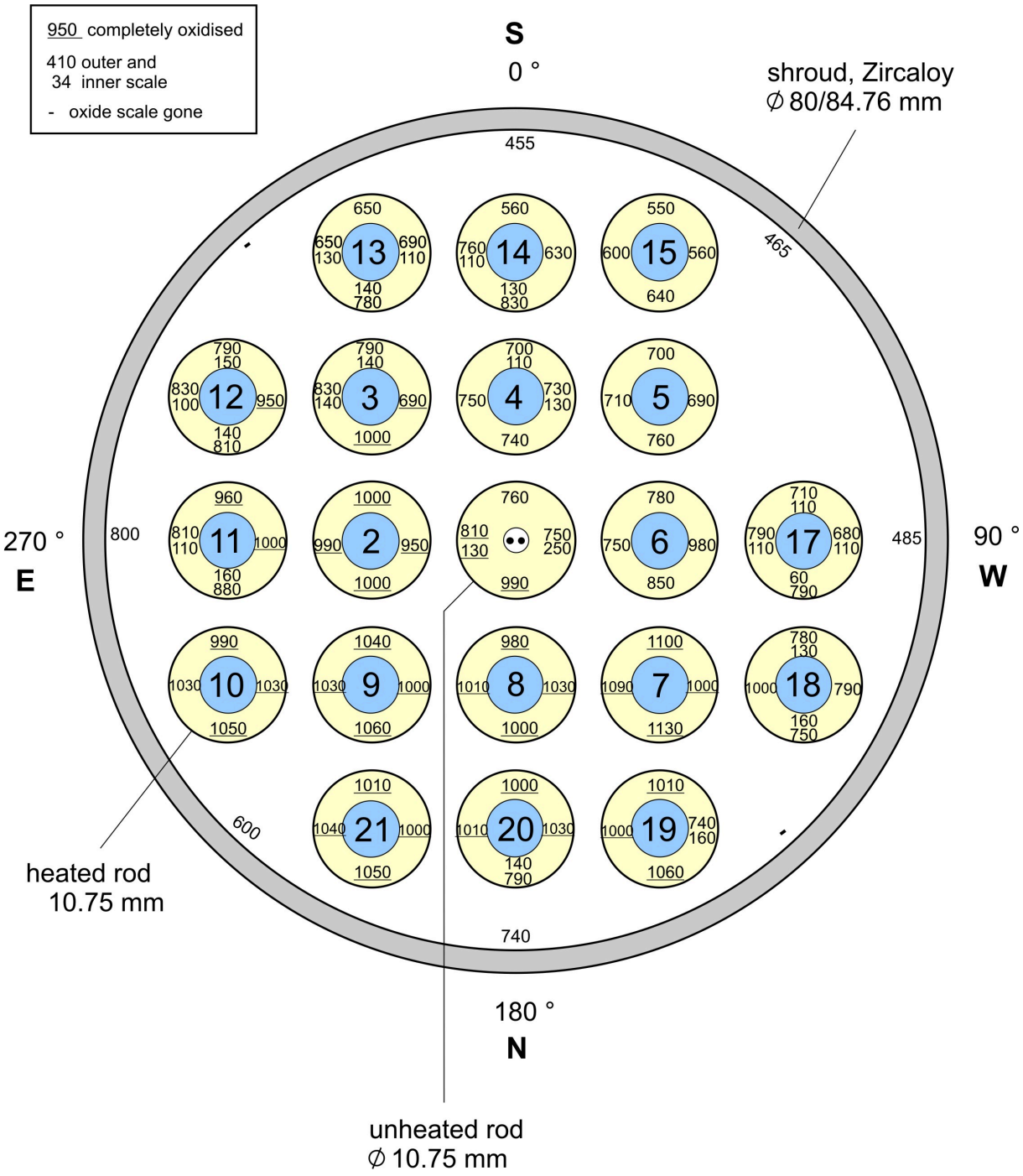

Fig 111 -QUE14 cross section 14-5.doc
12.05.09 - IMF

Fig. 111: QUENCH-14; Oxide layer thickness at bundle elevation 950 mm (Cross section QUE-14-5).

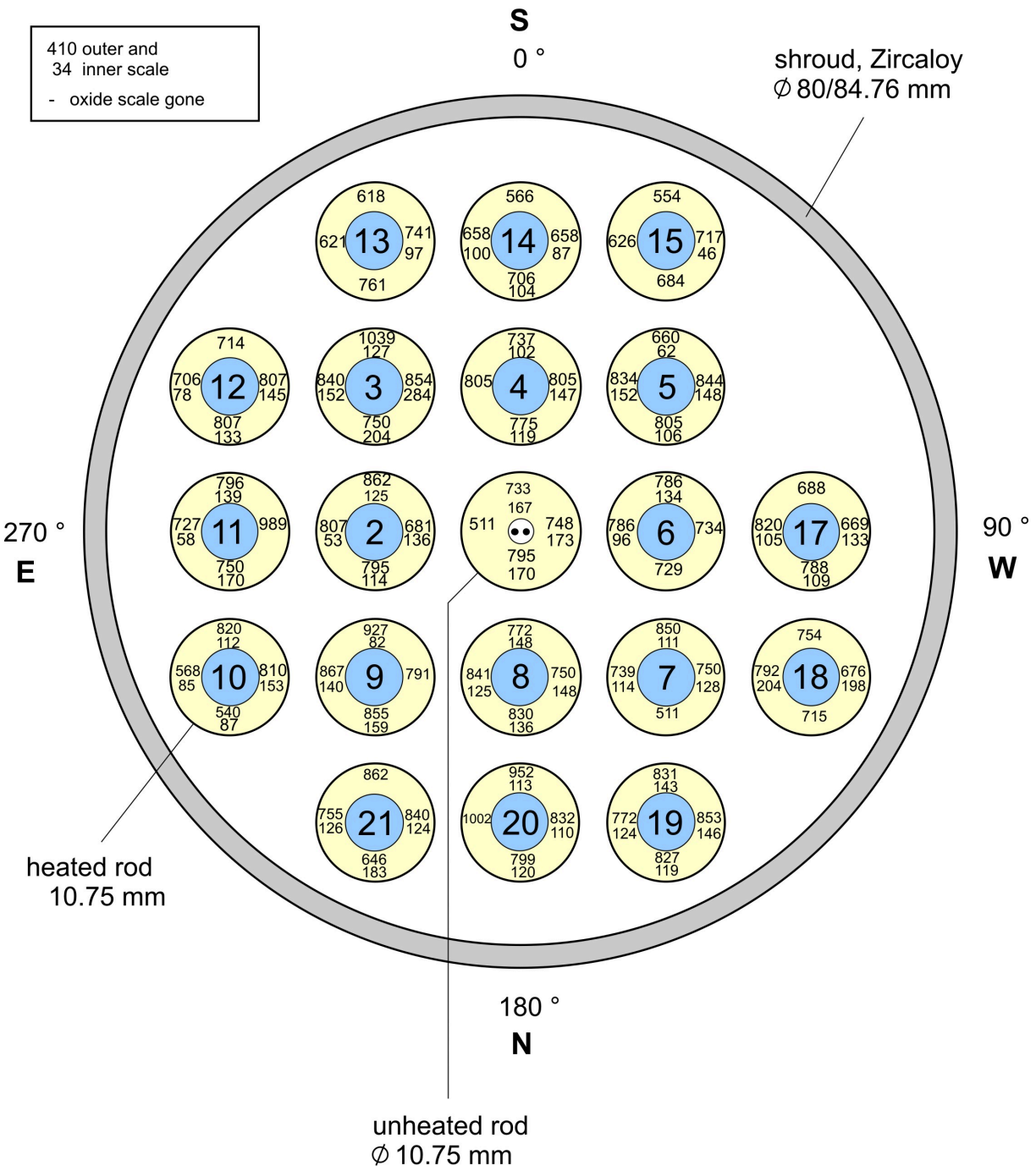

Fig 112 -QUE14 cross section 14-10.doc
12.05.10 - IMF

Fig. 112: QUENCH-14; Oxide layer thickness at bundle elevation 1000 mm (Cross section QUE-14-10).

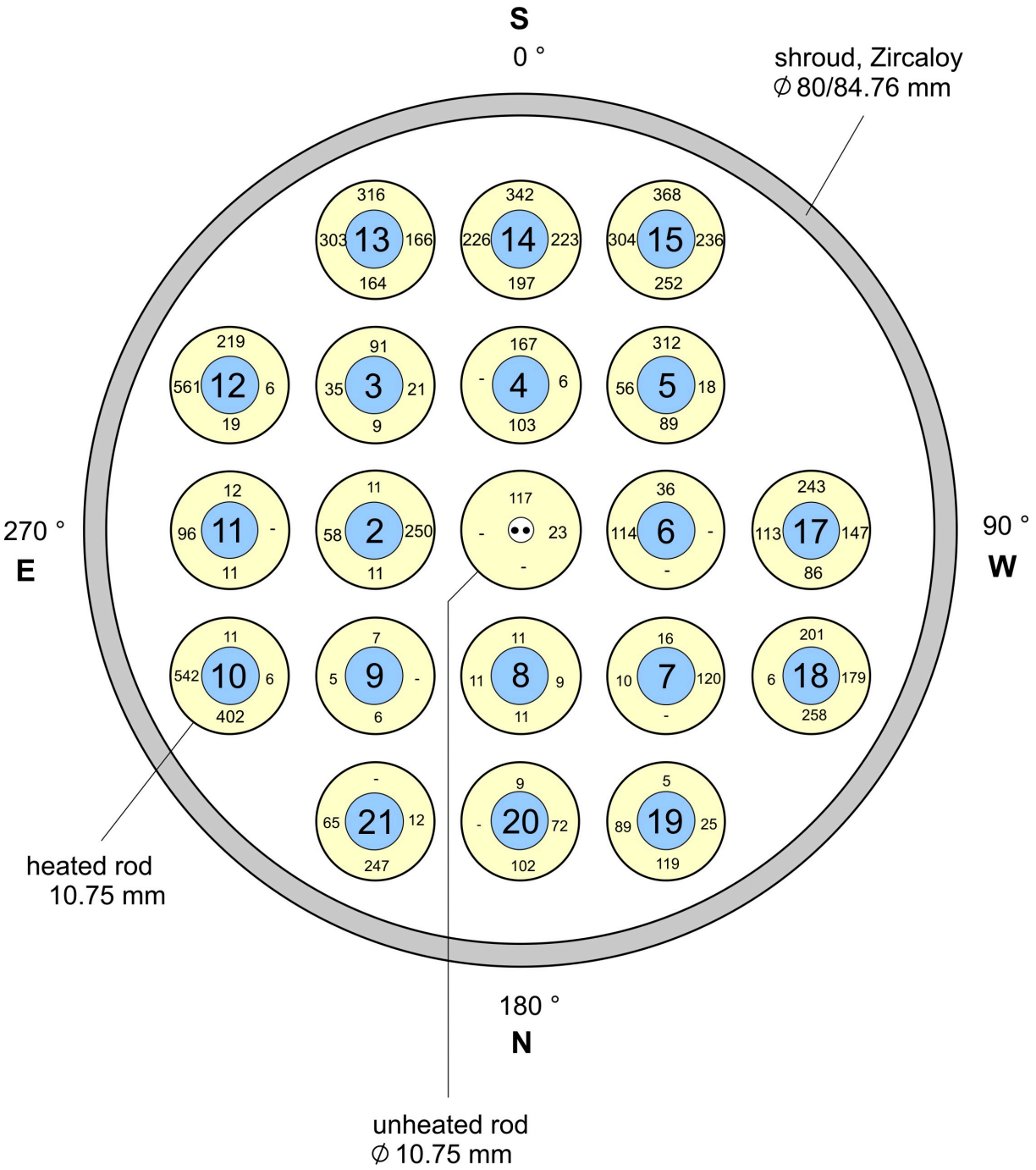

Fig 113 -QUE14 cross section 14-10-2.doc
12.05.10 - IMF

Fig. 113: QUENCH-14; α-layers at bundle elevation 1000 mm (Cross section QUE-14-10).

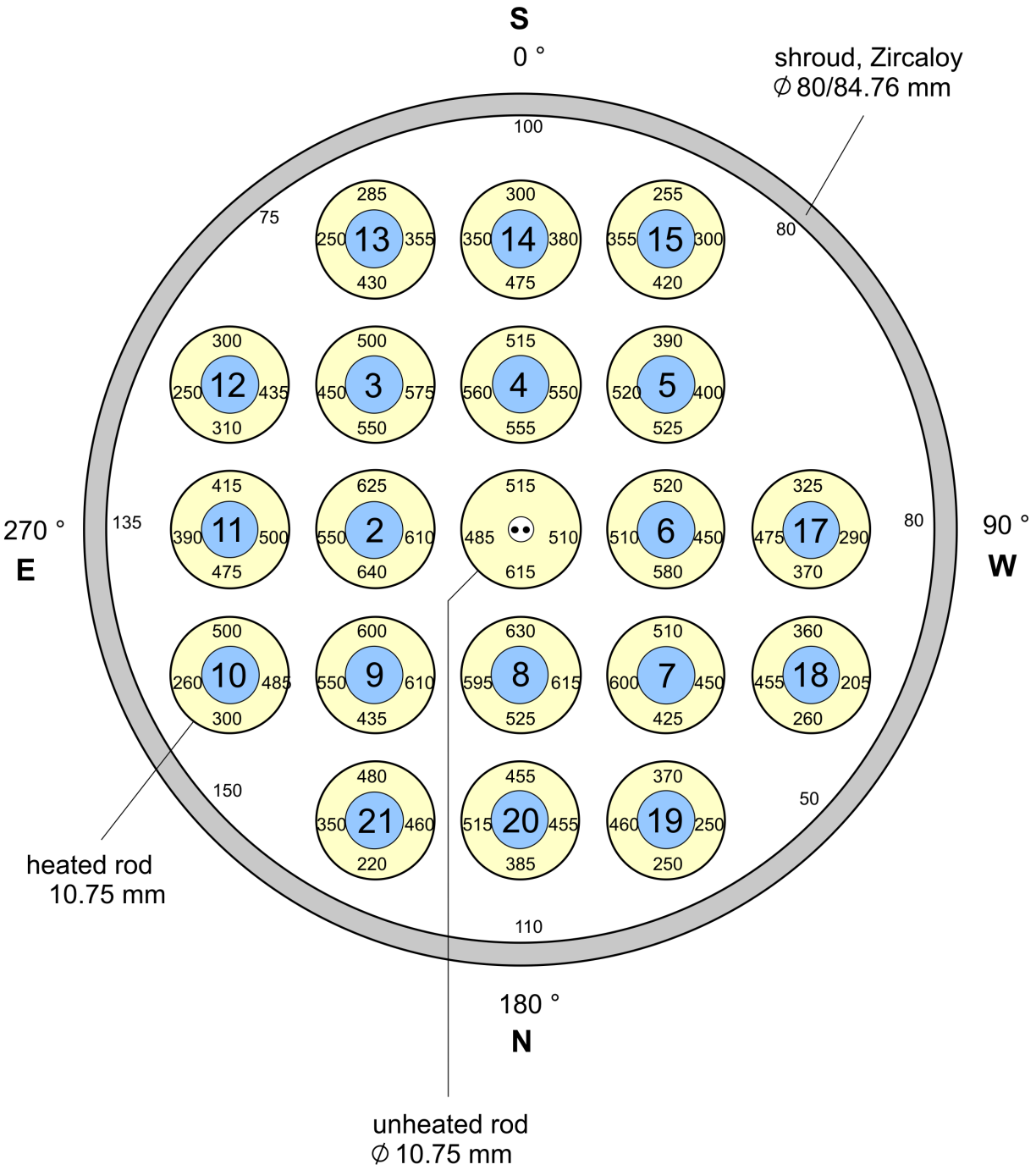

Fig 114 -QUE14 cross section 14-6.doc
12.05.10 - IMF

Fig. 114: QUENCH-14; Oxide layer thickness at bundle elevation 1050 mm (Cross section QUE-14-6).

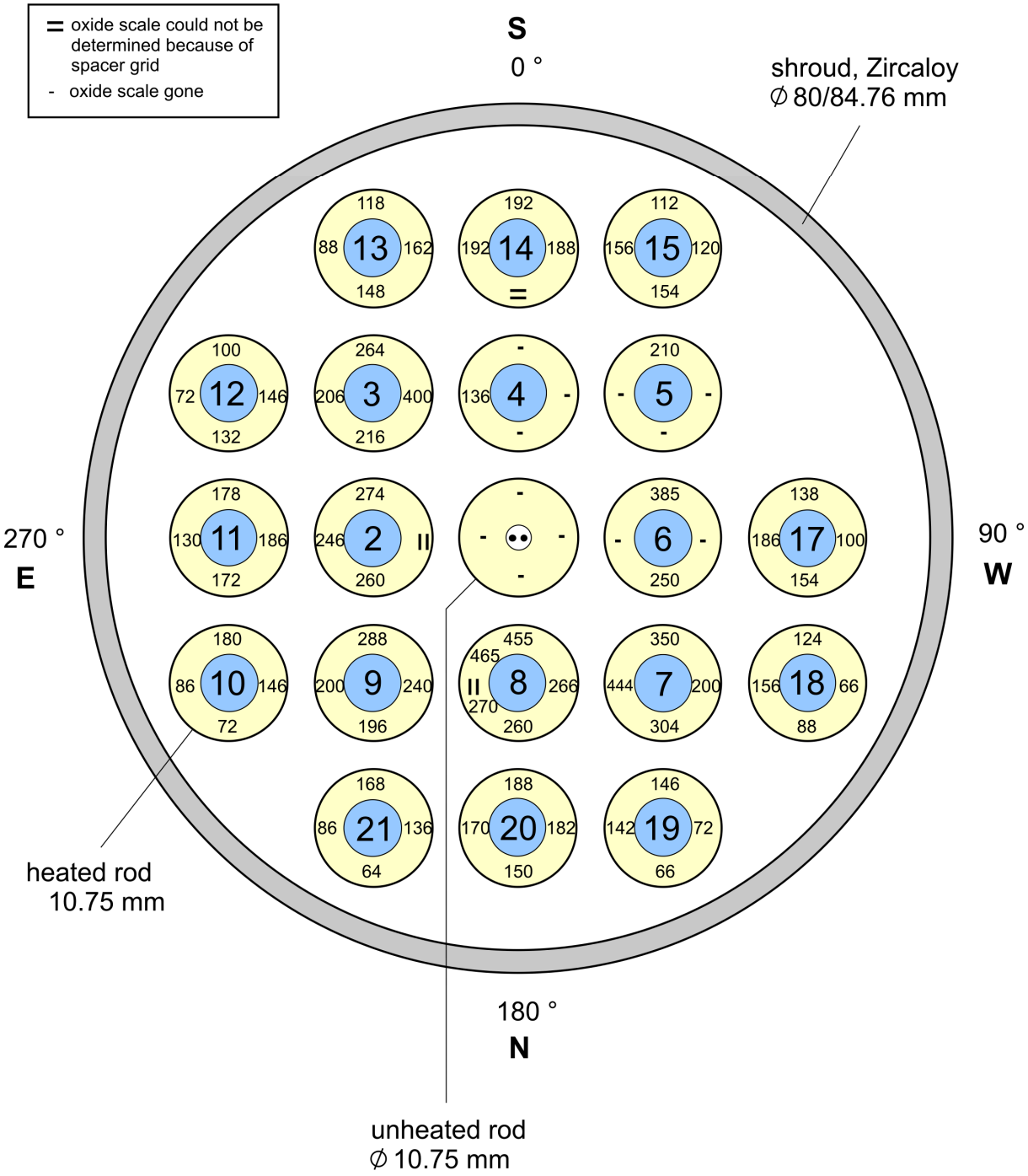

Fig 115-QUE14 cross section 14-7.doc
12.05.10 - IMF

Fig. 115: QUENCH-14; Oxide layer thickness at bundle elevation 1100 mm (Cross section QUE-14-7).

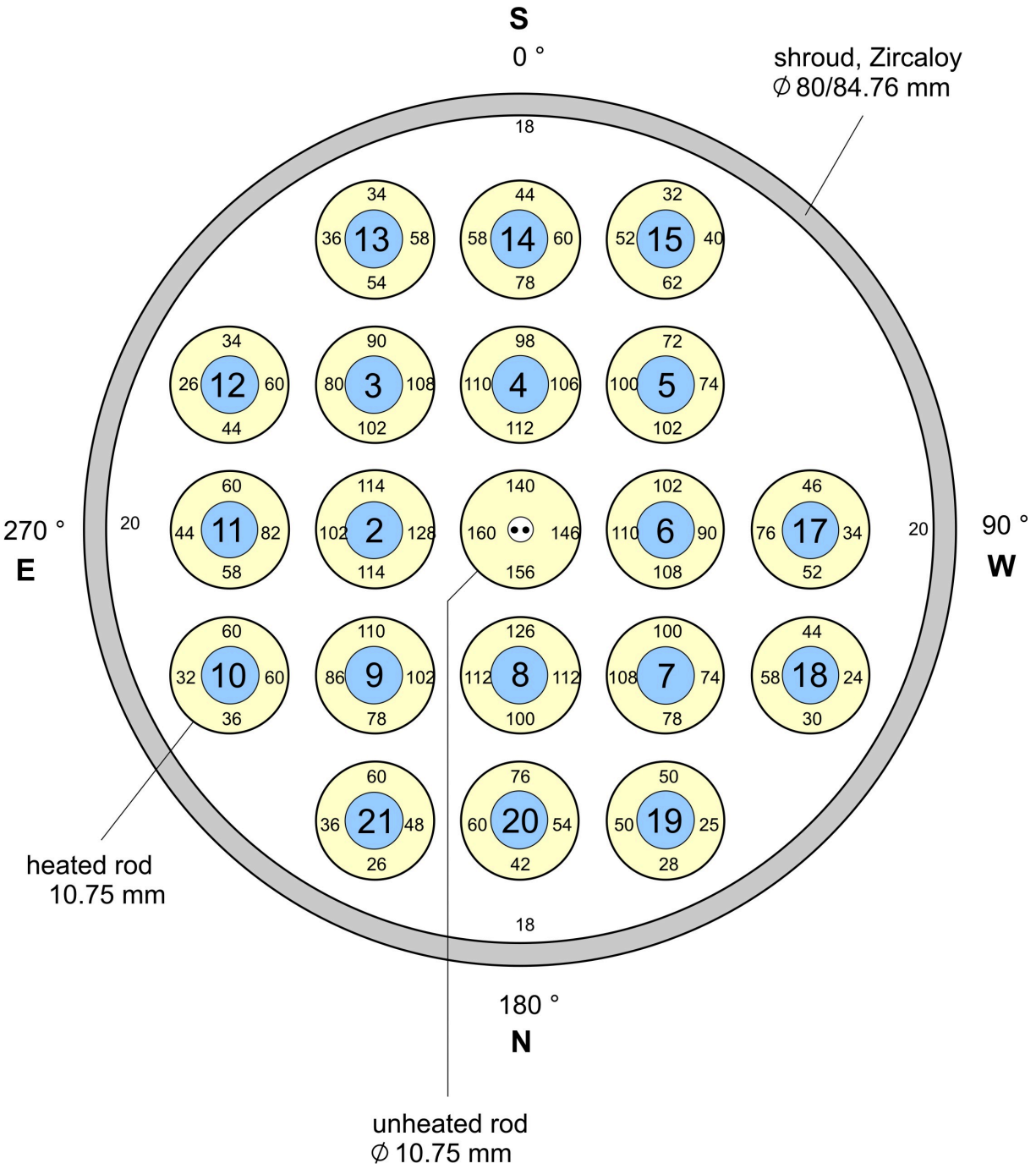

Fig 116 -QUE14 cross section 14-8.doc
12.05.10 - IMF

Fig. 116: QUENCH-14; Oxide layer thickness at bundle elevation 1150 mm (Cross section QUE-14-8).

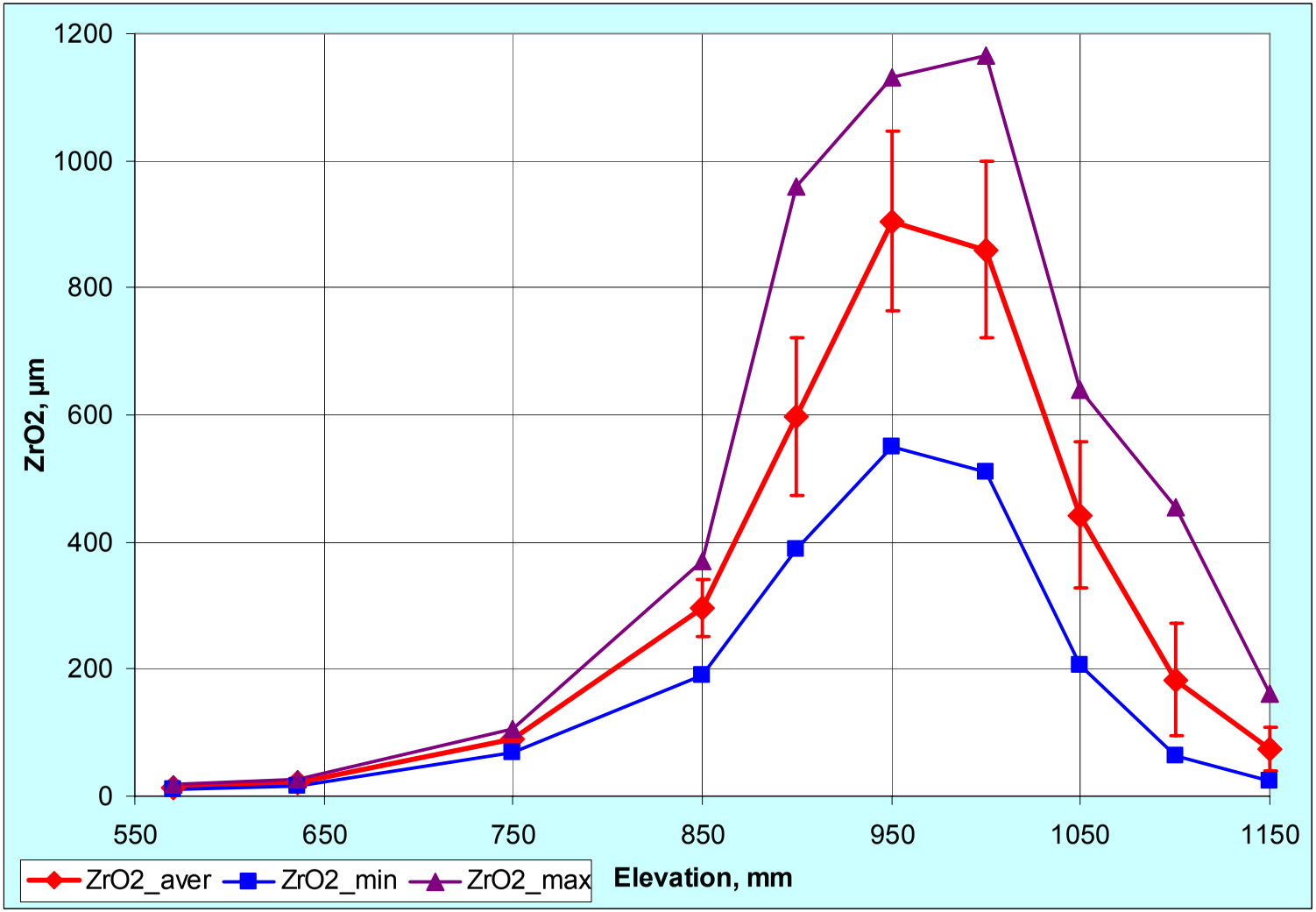

Fig. 117: QUENCH-14; axial distribution of summarized oxide thickness (external and internal oxide layers) for all rod simulators. Averaged, minimum and maximum values for each elevation. Evaluated by metallography.

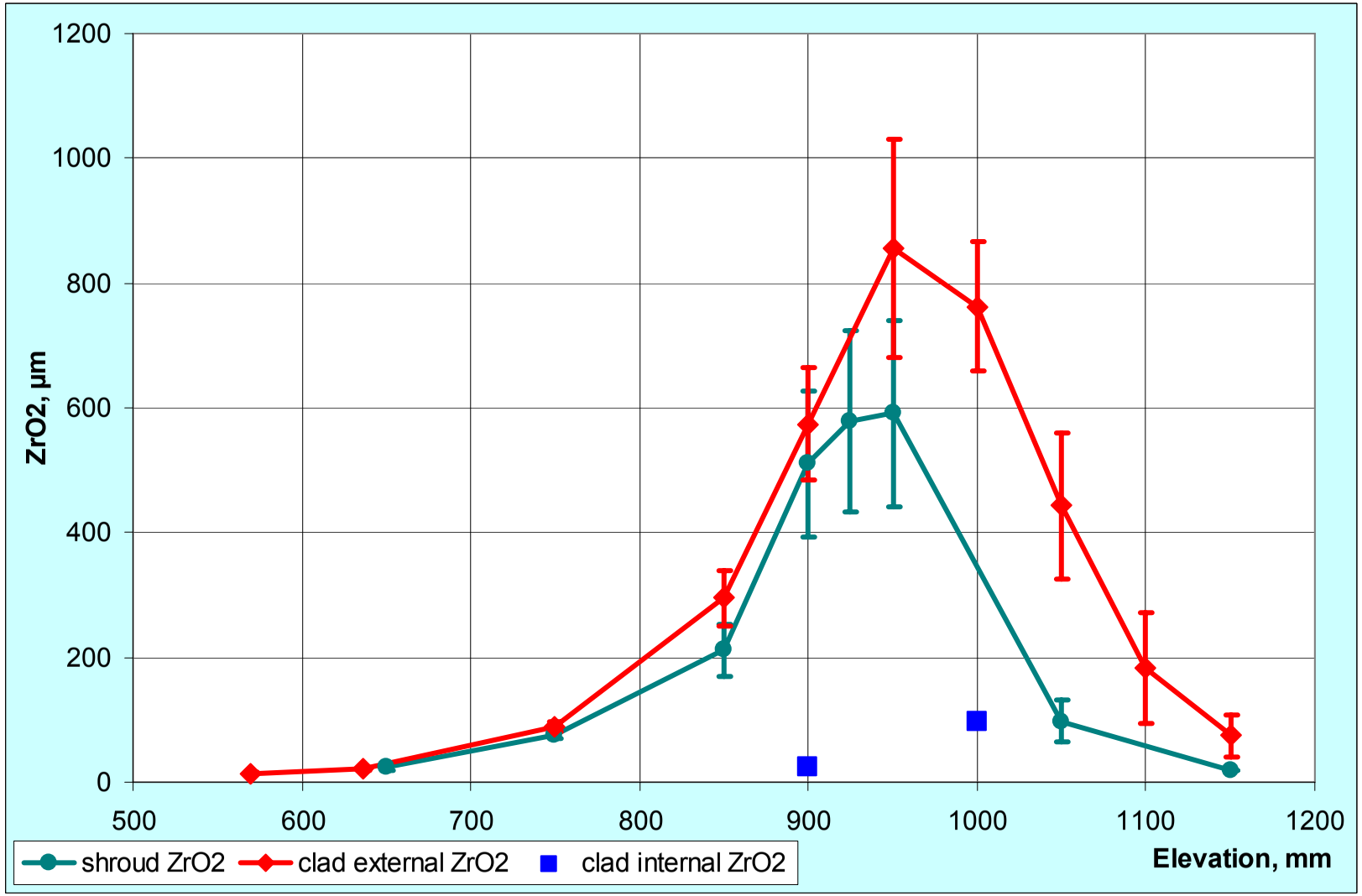

Fig. 118: QUENCH-14; axial distribution of oxide thicknesses for external and internal cladding oxide layers and shroud. Averaged values for each elevation. Evaluated by metallography.

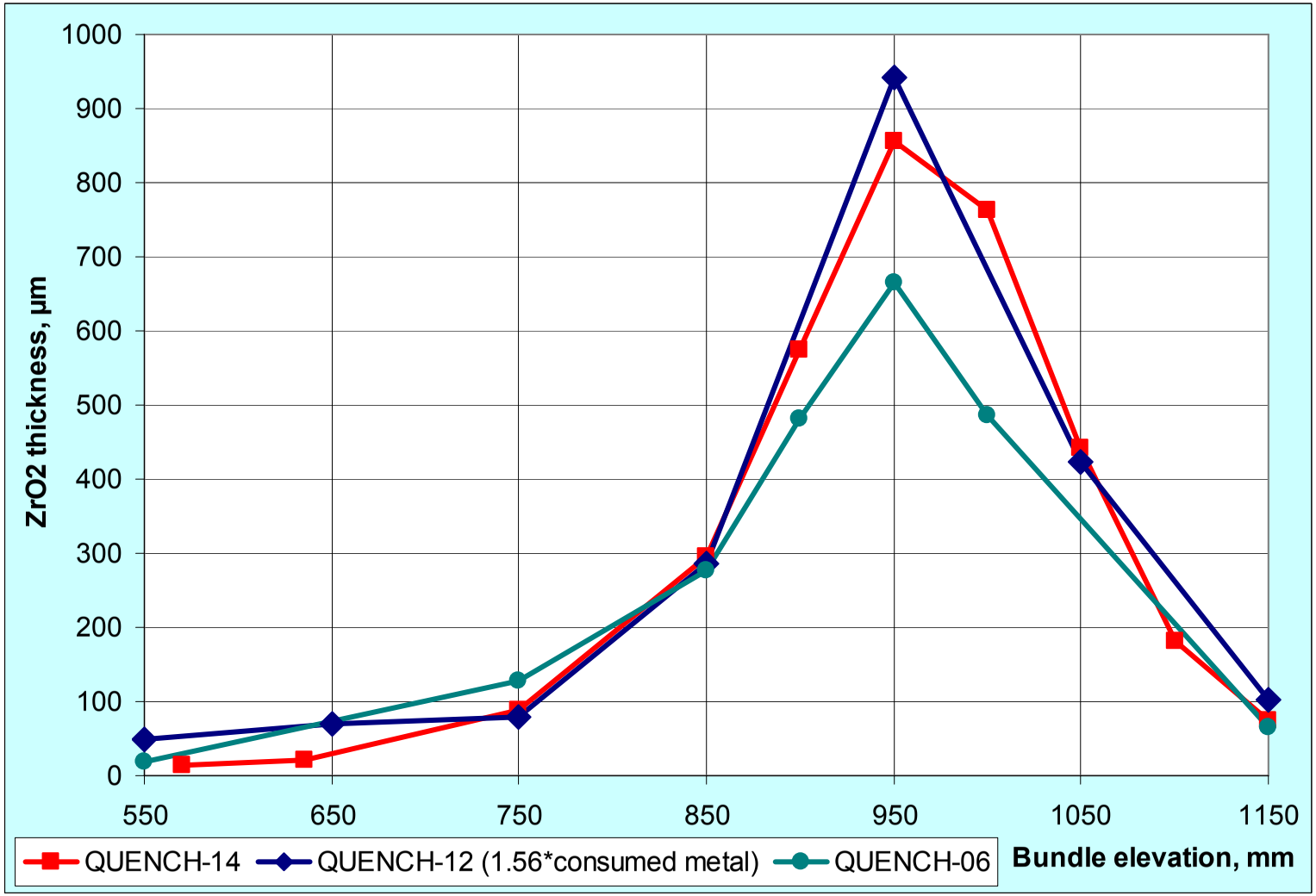

Fig. 119: Comparison of axial distribution of cladding external oxide thicknesses for the bundles QUENCH-06, QUENCH-12 and QUENCH-14.

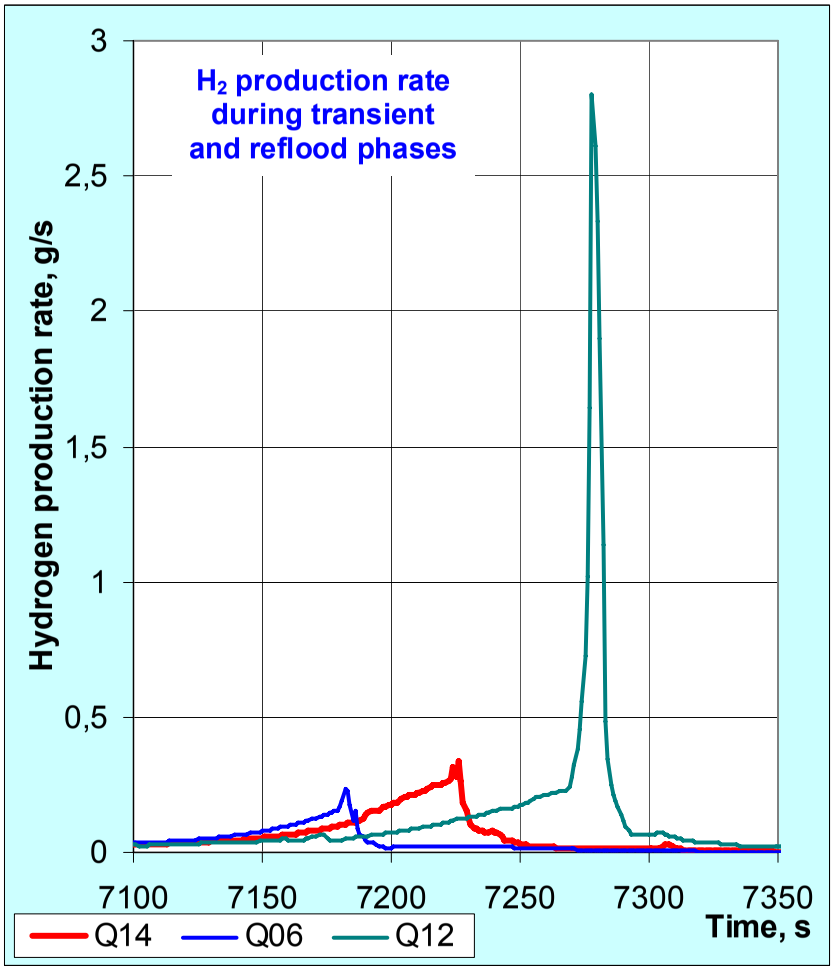

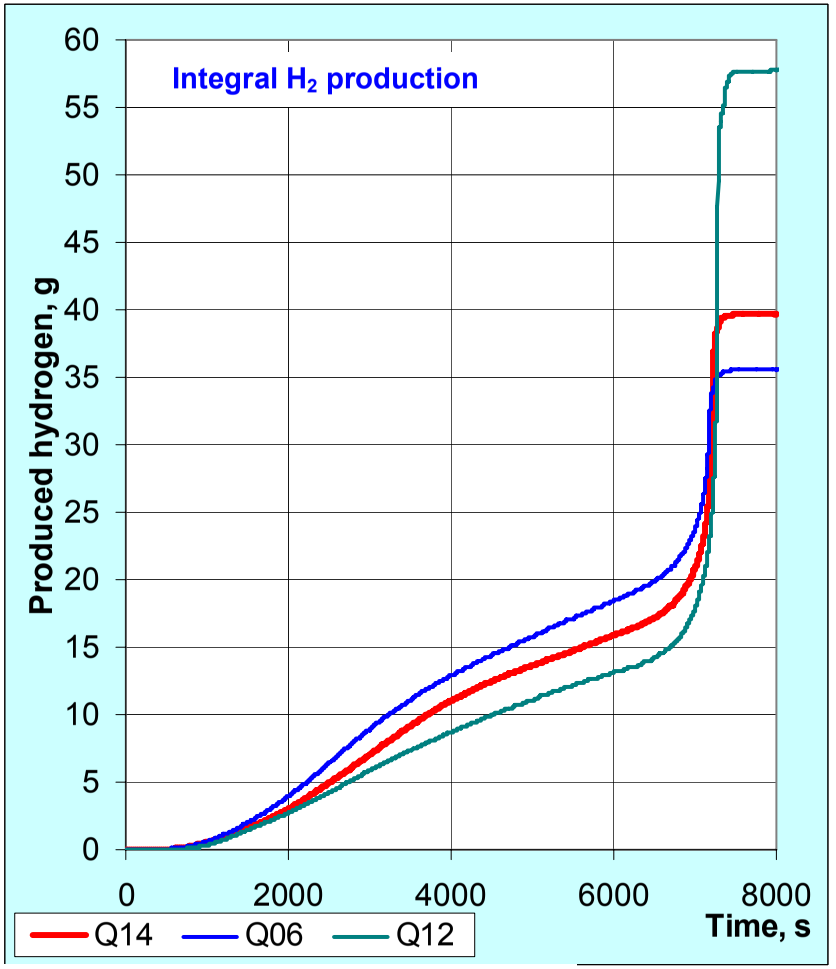

	Q-14	Q-06	Q-12
H_2 production before reflood (g):	34	32	34
H_2 production during reflood (g):	6	4	24

Fig. 120: Hydrogen production according to mass-spectrometer measurements. Comparison between QUENCH-06, QUENCH-12 and QUENCH-14.

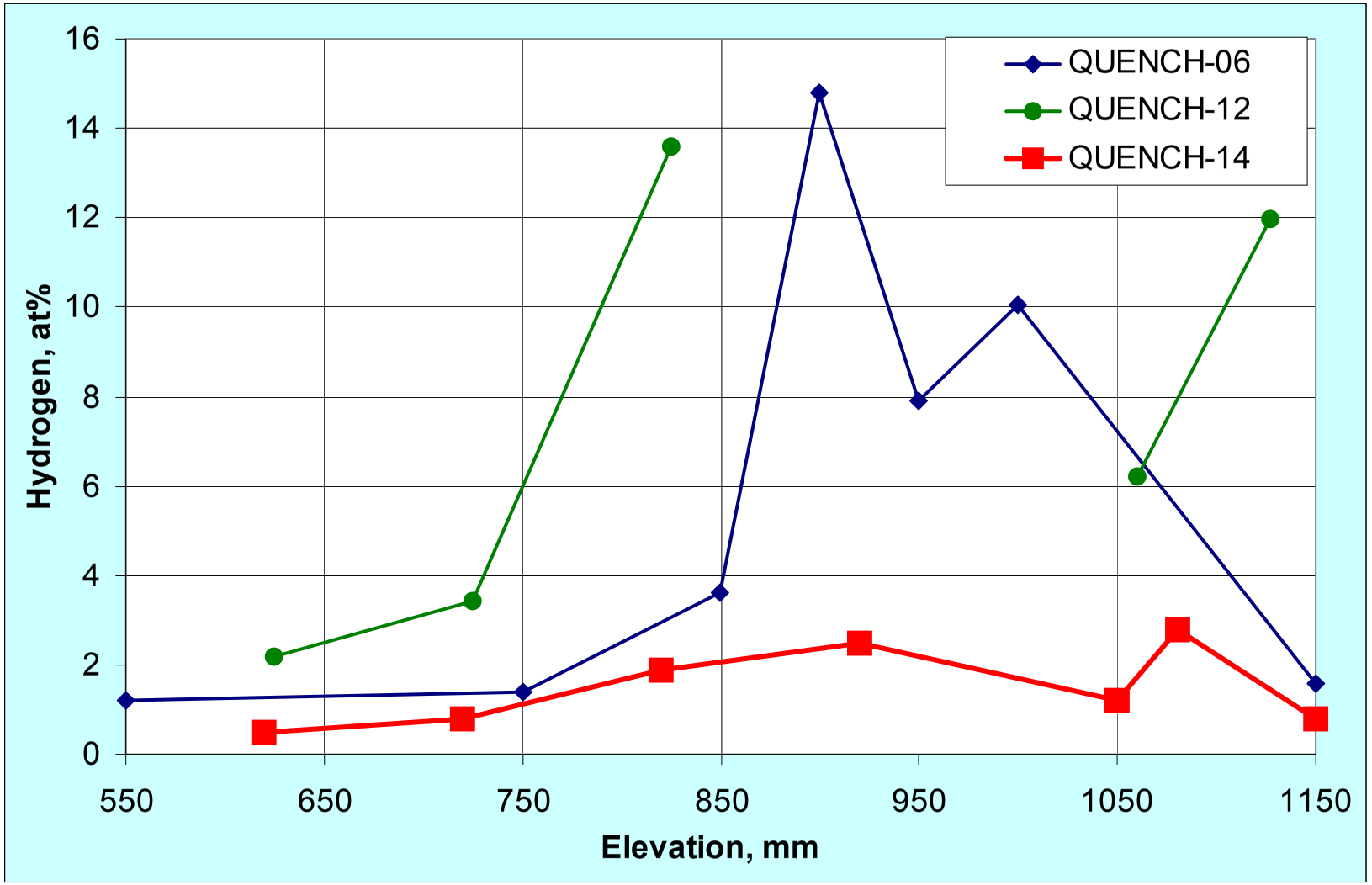

Fig. 121: Comparison of hydrogen uptake by claddings of QUENCH-14, QUENCH-12, and QUENCH-06 bundles; evaluation by hot extraction.

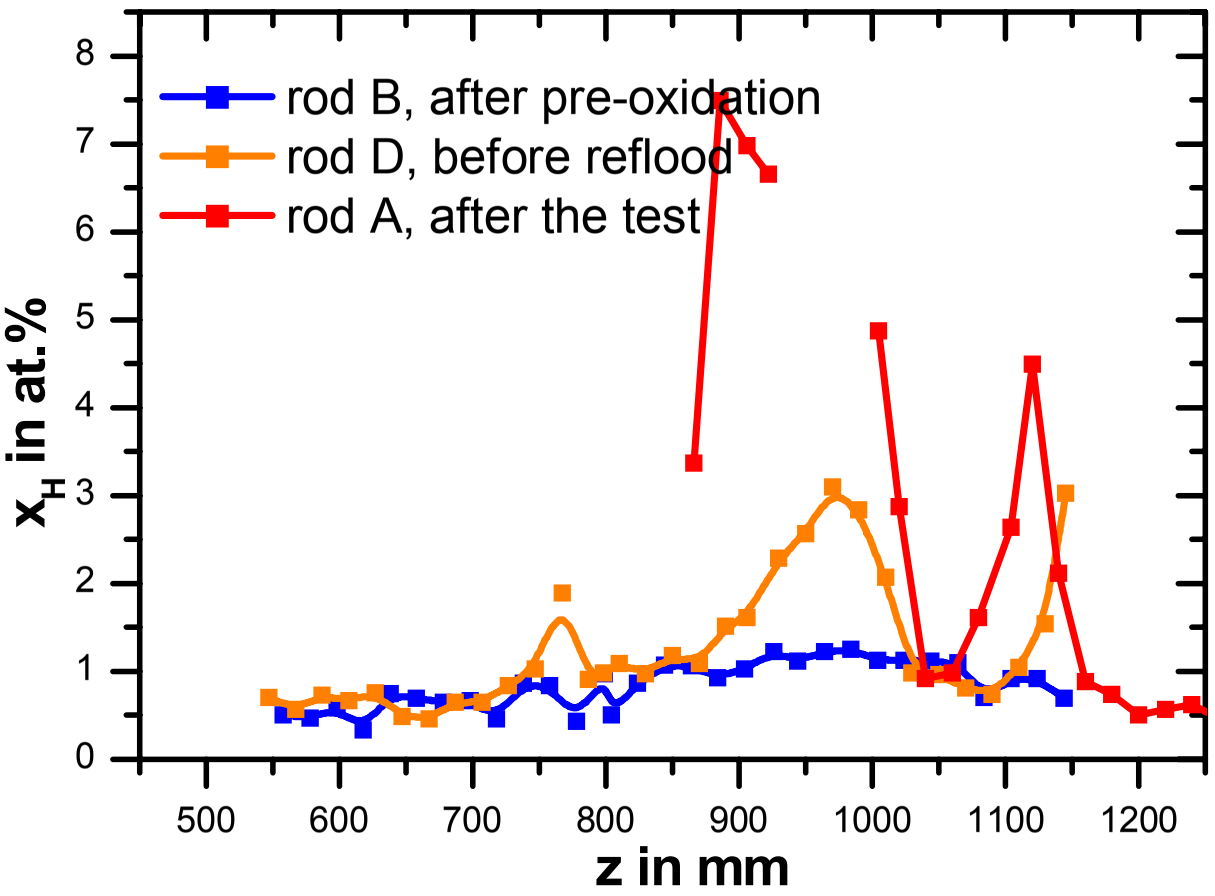

Fig. 122: QUENCH-14; Axial distribution of hydrogen absorbed in the Zry-4 corner rods at different experiment stages; evaluation by neutron radiography.

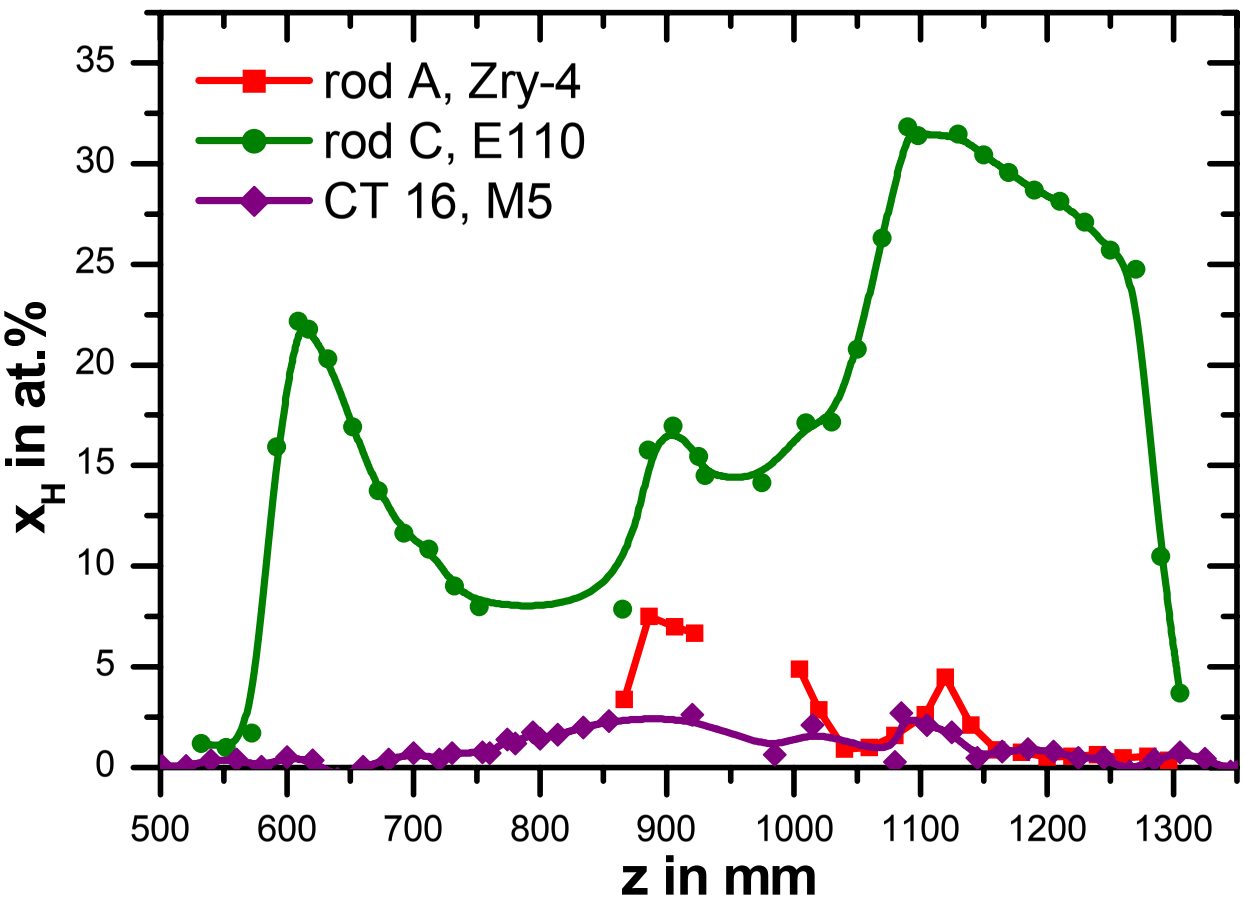

Fig. 123: QUENCH-14; Comparison of the hydrogen absorbed in the E110 and Zry-4 corner rods and M5® cladding tube of the rod simulator No. 16, which were withdrawn from the bundle after the test. Evaluation by neutron radiography.

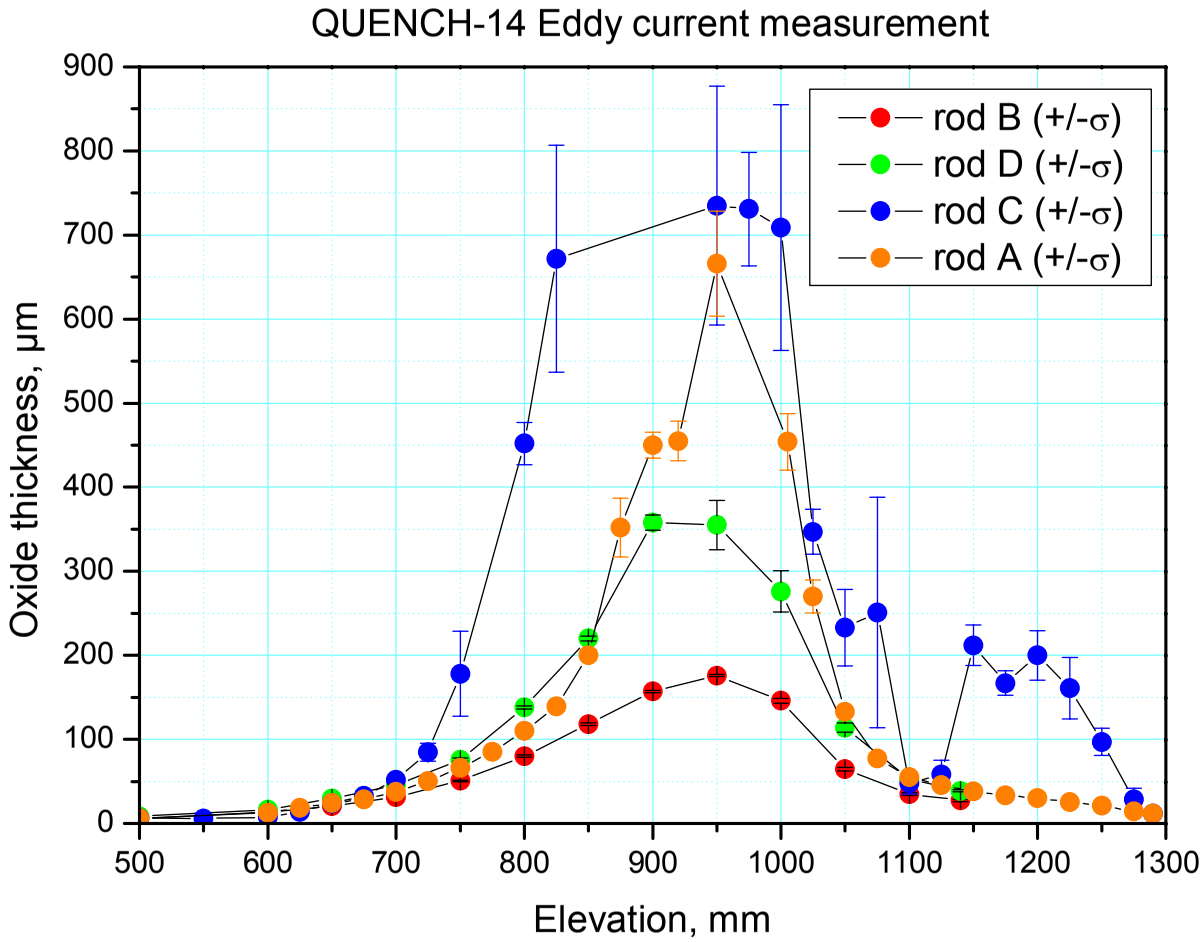

Fig. A-1: QUENCH-14; Eddy current measurement of oxide thickness at corner rod.

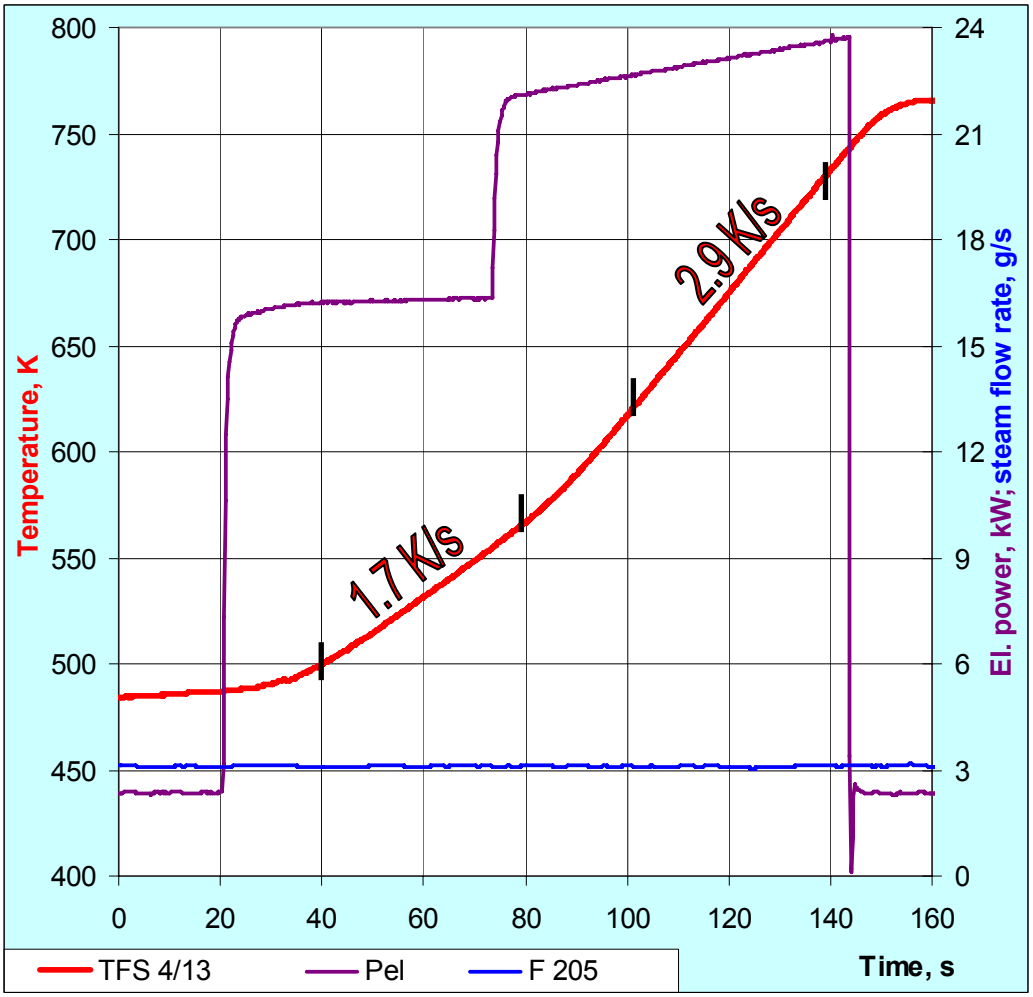

Fig. A-2: QUENCH-14; Pre-test with gradual increase of electrical power and constant steam flow rate of ~3 g/s.

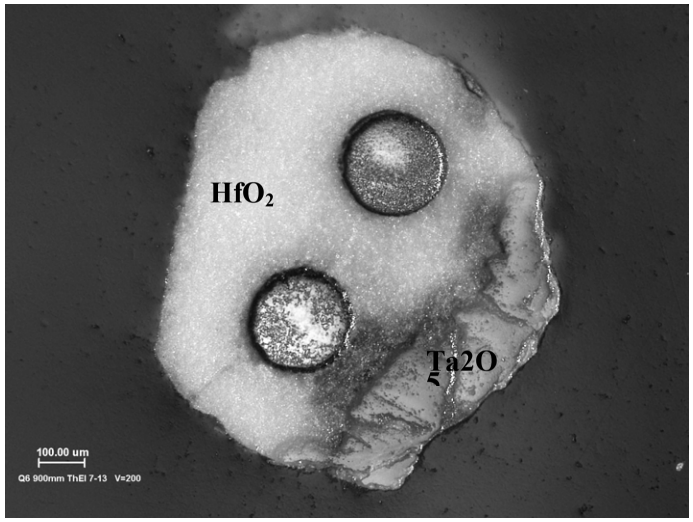

900 mm: TFS remnants

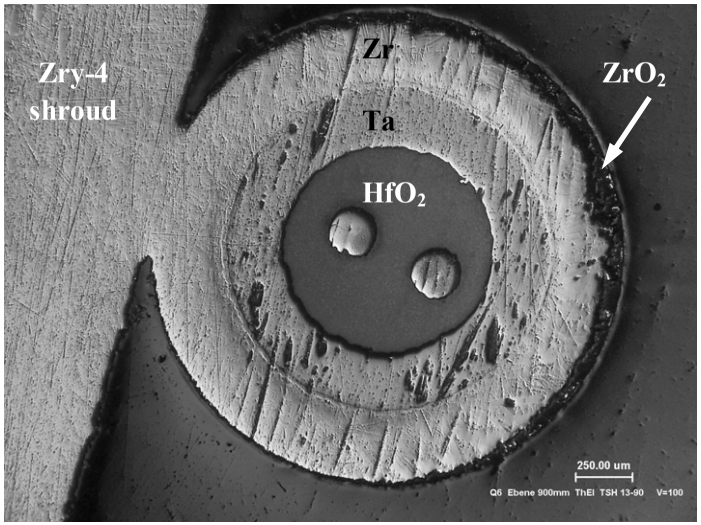

900 mm: TSH 13/90 contacted with shroud

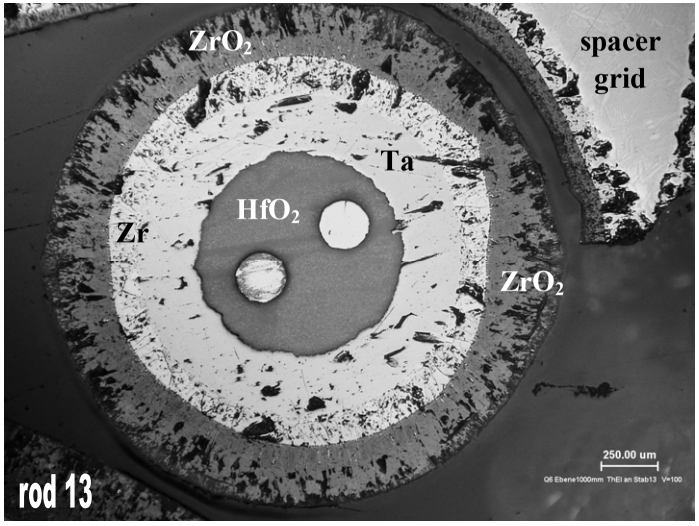

1000mm: TFS between rod No. 13 and spacer grid remnants: partially oxidised Zr-sheath

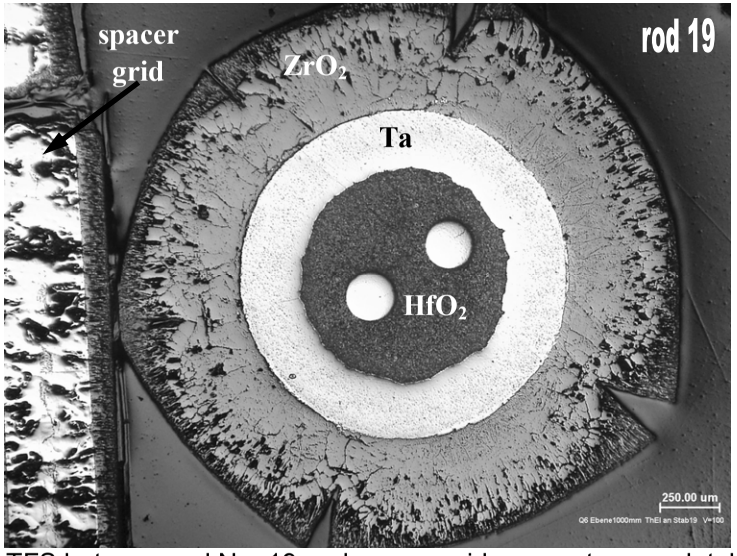

1000 mm: TFS between rod No. 19 and spacer grid remnants: completely oxidised Zr-sheath

Fig. A-3: QUENCH-06; thermocouples state at elevations 900 mm and 1000 mm.

The QUENCH experiments are to investigate the hydrogen release resulting from the water injection into an uncovered core of a Light Water Reactor as well as the high-temperature behaviour of core materials. The typical QUENCH test bundle consists of 21 fuel rod simulators with a total length of approximately 2.5 m.

The QUENCH-14 experiment investigated the effect of M5® cladding material on bundle oxidation and core reflood, in comparison with the tests QUENCH-06 that used standard Zircaloy-4 and QUENCH-12 that used VVER E110-claddings. The peak temperature of ~2300 K was measured shortly after quench initiation. Complete bundle cooling was reached in 300 s after reflood initiation. During reflood 6 g hydrogen were released which is similar to QUENCH-06 (4 g) but much less than during quench phase of QUENCH-12 (24 g). The reason for the different behaviour of the Zr1%Nb cladding alloys is the different oxide scale properties of the materials.

ISSN 1869-9669
ISBN 978-3-86644-535-2

ISBN 978-3-86644-535-2